Wanderson da Silva

NANOSTRUCTURED SURFACES FOR ELECTROCHEMICAL SENSORS AND BIOSENSORS AND APPLICATIONS

Tese no âmbito do Doutoramento em Química, Ramo de Especialização em Eletroquímica, orientada pelo Professor Doutor Christopher Michael Ashton Brett e apresentada ao Departamento de Química da Faculdade de Ciências e Tecnologia da Universidade de Coimbra.

Setembro de 2019

Universidade de Coimbra
Faculdade de Ciências e Tecnologia

Nanostructured surfaces for electrochemical sensors and biosensors and applications

Wanderson da Silva

Tese no âmbito do Doutoramento em Química, Ramo de Especialização em Eletroquímica, orientada pelo Professor Doutor Christopher Michael Ashton Brett e apresentada ao Departamento de Química da Faculdade de Ciências e Tecnologia da Universidade de Coimbra.

Setembro de 2019

“Science without religion is lame, religion

without science is blind.”

Albert Einstein

Acknowledgements

Throughout this academic course, I have always been surrounded by people who supported me and encouraged me to overcome every challenge that was proposed to me. I thank all these people and dedicate this work to them.

To my lovely and caring family: my sisters, cousins and uncles for all the prayers and positive thoughts. Special thanks to my mother (Maria Silva) and my grandmother Dona Eunice (*in memoriam*) for the continued support and believing in me throughout my academic studies, which helped me to reach this moment.

My sincere gratitude goes to my supervisor, Prof. Dr. Christopher M.A. Brett for the opportunity to work under his supervision, for all the scientific discussions, support and encouragement in these four years under his supervision.

And then, to all my colleagues from the Laboratory of Electrochemistry and Corrosion: Carolina Queiroz, Luciana Tomé, Madalina Bărsan, Ricardo Leote, Vanessa Baião I would like to express my special gratitude to Dr^{a} Mariana Ghica (Madi) for her availability for scientific discussions and guidance in my first years as a PhD student. To my colleagues António Aguiar, Carlos Murilo, José Malta, who provided me relaxing moments and friendship.

Thanks to Science Without Borders Mobility Programme (*Programa de Mobilidade Ciência Sem Fronteiras - CSF*) financed by the Conselho Nacional de Desenvolvimento Científico e Tecnológico (CNPq) - Brazil for the PhD grant, 232979/2014-6.

Resumo

O principal objetivo deste estudo foi desenvolver novos sensores e biossensores eletroquímicos com propriedades analíticas melhores pelo uso de diferentes nanomateriais condutores e mediadores redox para a modificação de elétrodos, além de seu uso como elétrodo suporte para a imobilização de enzimas.

Alguns dos aspetos mais relevantes na fabricação de sensores e biossensores eletroquímicos estão focados, o estado da arte em relação aos nanomateriais condutores, aos nanomateriais nanoestruturados como modificadores de elétrodos, e sobre as enzimas. Os principais fundamentos teóricos das técnicas eletroquímicas utilizadas, nomeadamente a voltametria cíclica, a voltametria de impulso diferencial e a espectroscopia de impedância eletroquímica também são descritos, bem como outras técnicas utilizadas para a caracterização das nanoestruturas, nomeadamente a microscopia eletrónica de varrimento, a microscopia eletrónica de transmissão e a difração de raios-X.

Um sensor eletroquímico de fácil fabricação para a determinação de teofilina foi desenvolvido baseado em uma nova plataforma preparada pela fixação direta de nanopartículas de ouro numa rede de nanotubos de carbono de paredes múltiplas, que foi depositado sobre um elétrodo suporte de carbono vítreo. Para este efeito, os nanotubos de carbono funcionalizados dispersos em quitosana foram misturados coma uma solução coloidal de nanopartículas de ouro. As técnicas de voltametria cíclica, voltametria de impulso diferencial e espectroscopia de impedância eletroquímica foram utilizadas para caracterizar os sistemas. Sob condições experimentais otimizadas, a plataforma com as melhores propriedades sensoriais foi utilizada para a determinação de teofilina, com um limite de detecção de 90 nM.

Numa segunda fase, novos sensores eletroquímicos para a detecção da tiramina, uma amina biogénica comumente encontrada em alimentos fermentados, foram desenvolvidos. Nanopartículas de ouro preparadas por um novo método de síntese verde foram misturadas com um derivado da anilina, o 8-anilino-1-naftaleno- ácido sulfónico. Eletropolimerização potenciodinâmica levou à formação de um filme polimérico com nanopartículas de ouro encapsuladas e estabilizadas, por este método simples e eficiente. Elétrodos modificados com o filme nanocompósito foram utilizados para a monitorização da tiramina por duas metodologias electroanalíticas. Na primeira, um sensor impedimétrico sensível usando um filme do polímero dopado com nanopartículas de ouro eletrodepositados sobre um elétrodo

suporte de ouro foi desenvolvido. A segunda consistiu no desenvolvimento de um biossensor amperométrico com a enzima tirosinase imobilizada sobre o filme nanocompósito de polimero dopado com nanopartículas de ouro em elétrodo suporte de carbono vítreo. Ambos os tipos de sensores foram testados para a determinação de tiramina e demonstraram excelentes parâmetros analíticos. Os limites de detecção foram estimados em 0,04 μM e 0,71 μM para o sensor impedimétrico e o biossensor, respectivamente. Os limites de detecção obtidos foram similares a arquiteturas de elétrodo mais complexas encontradas na literatura.

Um biossensor de inibição enzimática empregando poli(verde brilhante) como mediador foi desenvolvido para a determinação de vestígios de iões metálicos biotóxicos, Hg^{2+}, Cd^{2+}, Pb^{2+} e Cr^{VI}, por inibição enzimática. Filmes de poli (verde brilhante) foram preparados por eletropolimerização potenciodinâmica no solvente eutético etalina com adição de ácido dopante depositados sobre elétrodos de carbono vítreo modificados por nanotubos de carbono de paredes múltiplas; o melhor ácido dopante encontrado foi o ácido sulfúrico. A glucose oxidase foi imobilizada sobre estas superfícies e o novo biossensor foi utilizado com sucesso para a determinação de vestígios de catiões metálicos biotóxicos, com limites de detecção nanomolares e inferiores aos descritos na literatura, aproximadamente 2 nM para todos os iões metálicos. O mecanismo de inibição enzimática reversível foi investigado.

A tinta fenazínica azul de cresil brilhante também foi eletropolimerizada no solvente eutético etalina sobre elétrodos de carbono vítreo modificados por nanotubos de carbono de paredes múltiplas, em diferentes condições experimentais de acido dopante, pH e modo de deposição (potenciostática ou potenciodinâmica). Sob as melhores condições experimentais, o novo filme nanocompósito desenvolvido foi testado como electrodo suporte para a imobilização das enzimas glucose oxidase, tirosinase e colina oxidase, apresentando excelente desempenho como biosensores para a determinação de glicose, catecol e colina e para o pesticida diclorvos (este por inibição da colina oxidase), respectivamente. Os limites de deteção obtidos foram de 2,6 μM, 3,9 μM, 1,55 μM e 1,6 nM, respectivamente. Estes limites de detecção baixos demonstram que o novo filme nanocompósito proposta é muito promissor para futuras aplicações em biossensores eletroquímicos enzimáticos.

As conclusões resumem os principais resultados obtidos e vantagens das plataformas utilizadas como sensores e biosensores baseadas em superfícies nanoestruturadas

desenvolvidas neste trabalho. Alguns tópicos importantes e direções futuras relacionados com este trabalho são indicados.

Palavras chaves: camada-sobre-camada, filmes automontados, (bio)ssensores, enzimas, carbono, compostos biotóxicos.

Abstract

The main goal of this study was to develop novel electrochemical sensors and biosensors, with improved analytical properties, by using different conducting nanomaterials and redox mediators for electrode surface modification and as electrode support for enzyme immobilisation.

An overview is given of some relevant aspects in the fabrication of electrochemical sensors and biosensors, the state-of-the-art regarding conducting nanomaterials and nanostructured materials as electrode modifiers, and concerning enzymes. The basis of the electrochemical techniques used, namely cyclic voltammetry, differential pulse voltammetry and electrochemical impedance spectroscopy are described, as well as other techniques used for characterisation of the nanostructures, namely scanning electron microscopy, transmission electron microscopy, and X-ray diffraction.

An easy to prepare electrochemical sensor for theophylline determination was developed based on a novel platform prepared by direct attachment of gold nanoparticles on a multi-walled carbon nanotube network, which was then deposited on a glassy carbon electrode support. For this purpose, functionalised multi-walled carbon nanotubes dispersed in chitosan were mixed with gold nanoparticle colloidal solution. Cyclic voltammetry, differential pulse voltammetry, and electrochemical impedance spectroscopy were used to characterise the systems. Under the best experimental conditions, the platform with the best sensing properties was used for theophylline determination, with a detection limit of 90 nM.

Secondly, new electrochemical sensors were developed for the determination of tyramine, a biogenic amine commonly found in fermented food. Gold nanoparticles prepared by a new, green synthetic route were mixed with the aniline derivative 8-anilino-1-naphthalene sulphonic acid. Potential cycling electropolymerisation led to a polymer film with encapsulated and stabilised gold nanoparticles, by this simple and efficient method. The nanocomposite film modified electrodes were used for monitoring of tyramine, by two electroanalytical approaches. In the first, a sensitive impedimetric sensor using the gold nanoparticle doped-polymer film on a gold electrode support was developed. The second consisted of the development of an amperometric biosensor with the enzyme tyrosinase immobilised on a gold nanoparticle doped-polymer nanocomposite film modified glassy carbon electrode. Both types of sensor were tested for tyramine determination and showed excellent analytical parameters. The detection limits were estimated to be 0.04 μM and 0.71 μM for the impedimetric sensor and the biosensor, respectively. The detection limits obtained were similar to more complex architectures found in the literature.

An enzyme inhibition biosensor employing poly(brilliant green) as mediator was developed for the determination of the biotoxic trace metal ions, Hg^{2+}, Cd^{2+}, Pb^{2+}, and Cr^{VI}, by enzyme inhibition. Poly(brilliant green) films were formed by potential cycling electropolymerisation in ethaline–deep eutectic solvent with added acid dopant on multi-walled carbon nanotube modified glassy carbon electrodes; the best acid dopant was found to be sulfuric acid. Glucose oxidase was immobilised on these surfaces and the novel biosensor was successfully used for the determination of biotoxic trace metal cations with lower nanomolar detection limits than reported in the literature, around 2 nM for all trace metal ions. The mechanism of reversible enzyme inhibition was probed.

The phenazine brilliant cresyl blue was also electropolymerised in ethaline deep eutectic solvent on multi-walled carbon nanotube modified glassy carbon electrodes, under varying experimental conditions of acid dopant, pH, and deposition mode (potentiostatic or potentiodynamic). Under optimal conditions, the novel nanocomposite film developed was tested as electrode support for glucose oxidase, tyrosinase, and choline oxidase immobilisation, presenting excellent biosensing performance for glucose, catechol, and choline and dichlorvos pesticide (this by choline oxidase inhibition) determination, respectively. The detection limits obtained were 2.6 μM, 3.9 μM, 1.55 μM and 1.6 nM, respectively. These low detection limits demonstrate that the novel nanocomposite film proposed is very promising for future applications in electrochemical enzyme biosensors.

The conclusions summarise the main achievements and advantages of the sensing and biosensing platforms based on nanostructured surfaces developed in this work. Some important topics and future directions related to this work are indicated.

Keywords: layer-by-layer, self-assembled films, (bio)sensors, enzymes, carbon, biotoxic compounds

Table of Contents

Notation of symbols i
Abbreviations ii

1. Introduction

2. Experimental

3. AuNP decorated MWCNT modified electrodes for the electrochemical determination of theophylline (TP)

4. Impedimetric sensor and enzyme-based biosensor based on green gold nanoparticle doped poly(8-anilino-1-naphthalene sulphonic acid) modified electrodes for tyramine determination

5. Glucose biosensor based on poly(brilliant green) (PBG) - ethaline deep eutectic solvent (DES) /carbon nanotube modified electrode for biotoxic trace metal ions detection

6. Poly(brilliant cresyl blue) (PBCB) - ethaline deep eutectic solvent/carbon nanotubes and biosensing applications

Symbols notation

A	area	cm^2
C_{dl}	double layer capacity	F
CPE	constant phase element	$\mu F\ cm^{-2}\ s^{\alpha-1}$
e	electron charge	C
$E^{\ominus}$	electrode potential	V
ΔE_p	peak-to-peak separation	
$E^{\ominus}$	standard electrode potential	
$E^{\ominus\prime}$	formal potential	
E_p	peak potential	
$E_{p/2}$	half wave peak potential	
E_{mid}	midpoint potential	
E_0	amplitude of potential signal	
f	frequency	Hz
h	Hill constant	
I	electric current	A
I_p	peak current intensity	
I_0	current of the substrate without inhibitor	
I_1	current of the substrate with inhibitor	
I_{10}	current for 10% inhibition	
I_{50}	current for 50% inhibition	
$I\%$	percentage inhibition	
j	electric current density	$A\ cm^{-2}$
k_i	constant of inhibition	
	rate constant: first order	s^{-1}
	rate constant: second order	$L\ mol^{-1}\ s^{-1}$
k_0	standard electron transfer rate constant	$cm\ s^{-1}$
K_M	Michaelis-Menten constant	$mol\ L^{-1}$
LoD	Limit of detection	$mol\ L^{-1}$
n	number of electrons transferred	
Q	electric charge	C
R	resistance	Ω
R_{ct}	charge transfer resistance	

R_{Ω}	cell solution resistance	
SD	Standard deviation	
t	time	s
T	temperature	K
v	scan rate	$\mathrm{V\ s^{-1}}$
$W_{1/2}$	peak width at half-height	mV
Z	impedance	Ω
Z'	real part of impedance	
Z''	imaginary part of impedance	
Z_{w}	Warburg impedance element	
α_a	anodic charge transfer coefficient	
α_c	cathodic charge transfer coefficient	
α	constant phase element exponent	
Γ	surface concentration of adsorbed specie	$\mathrm{mol\ cm^{-2}}$
[S]	concentration of enzyme substrate	$\mathrm{mol\ L^{-1}}$

Abbreviations

AuNP	gold nanoparticles
AuE	gold electrode
BSA	bovine serum albumin
BR	Britton-Robinson buffer
CV	cyclic voltammetry
ChOx	choline oxidase
DPV	differential pulse voltammetry
DES	deep eutectic solvent
EIS	electrochemical impedance spectroscopy
EDS	energy dispersive X-ray spectroscopy
EDTA	ethylenediamine tetra-acetic acid
GA	glutaraldehyde
GCE	glassy carbon electrode
GOx	glucose oxidase
HBA	hydrogen bond acceptor

HBD	hydrogen bond donor
MWCNT	multi-walled carbon nanotubes
SEM	scanning electron microscopy
OPS	organophosphorus pesticide
PANSA	poly(8-aniline-1-naphalene sulphonic acid)
PBCB	poly(brilliant cresyl blue)
$PBCB^{PDD}$	potentiodynamically formed PBCB
$PBCB^{PTD}$	potentiostatically formed PBCB
PB	phosphate buffer solution
$PBCB_{ethaline}$	PBCB formed by electropolymerisation in ethaline DES
$PBCB_{aq}$	PBCB formed by electropolymerisation in aqueous solution
PBG	poly(brilliant green)
$PBG_{ethaline}$	PBG formed by electropolymerisation in ethaline DES
PBG_{aq}	PBG formed by electropolymerisation in aqueous solution
RSD	relative standard deviation
TEM	transmission electron microscopy
TP	theophylline
Tyr	tyramine
Tyr_{ase}	tyrosinase
XRD	X-ray diffraction

This page intentionally left blank

Chapter 1

Introduction

This chapter gives an overview at electrochemical sensors, electrochemical biosensors, and conducting nanomaterials used as electrode modifiers and their intrinsic electrochemical properties. Some relevant aspects related to enzymes and their immobilisation methods are also presented. Furthermore, it also describes the basis of electrochemical techniques used in this work – cyclic voltammetry (CV), differential pulse voltammetry (DPV) and electrochemical impedance spectroscopy (EIS) - as well as other techniques used for the characterisation of the nanostructures, scanning electron microscopy (SEM), transmission electron microscopy (TEM), and X-ray diffraction (XRD).

1.1 Electrochemical sensors and biosensors

Sensors are devices, modules, or systems composed of an active sensing surface with a signal transducer. These two components play an important role, that is, to transmit the signal generated by a selected compound or from a change in the physical parameters (for example, temperature, blood pressure, humidity, etc.). The devices produce signals as electrical, thermal, or optical output information, which may be converted into a measurable electrical signal for further processing. Sensors are classified based on essential criteria, such as (1) primary input quantity, (2) transduction principles (physical changes and chemical reactions), or (3) properties and applications [1–3].

Among these, electrochemical sensors have special advantages, because they can sense chemical species without causing damage to the host system. Moreover, electrochemical sensors are especially attractive because of their high sensitivity, experimental simplicity, and low cost. They have a leading position among the currently available commercial sensors with a wide range of important applications in the areas of clinical, industrial, environmental, and agricultural monitoring, as summarised in **Fig. 1.1** [4,5].

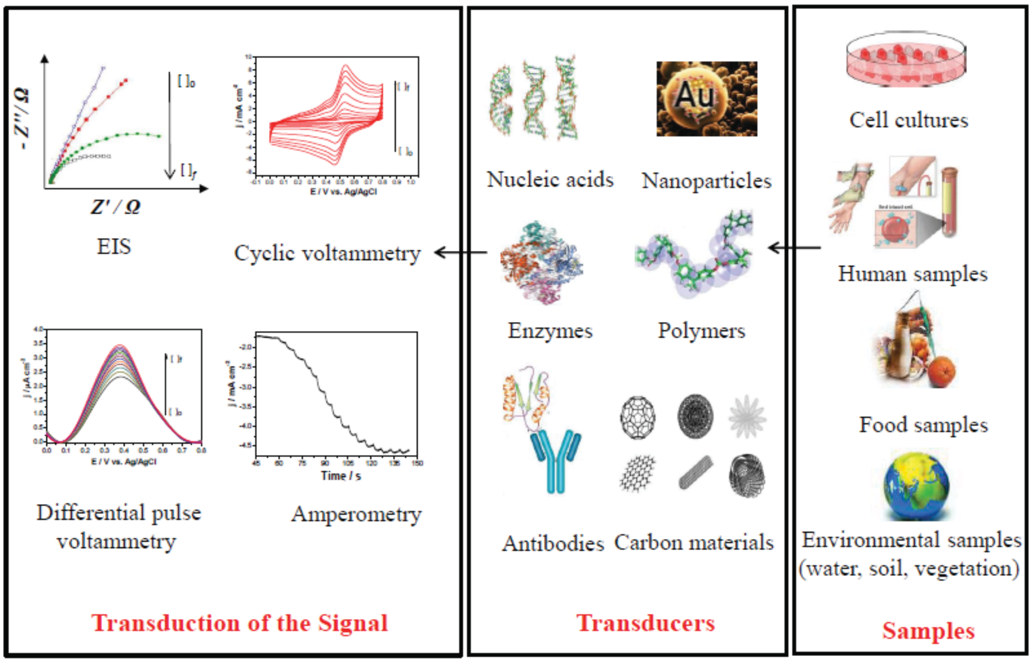

Fig. 1.1 Illustration of typical sensor and biosensor applications.

A useful distinction has been made between electrochemical sensors and biosensors. An electrochemical biosensor is a self-contained integrated device capable of providing specific quantitative or semi-quantitative information using a biologically-derived or biomimetic recognition element (enzyme, antibody, acid nucleic, cell, or tissue). The biological element is retained in direct spatial contact with an electrochemical transduction element for detecting an electroactive species. In the electrochemical sensor, the biological elements are not present. This useful distinction is not always used; the biosensor is sometimes defined as any sensor measuring a chemical concentration in a biological system [2,6,7]. This work will describe electrochemical sensors and biosensors based on the presence or not of the biological recognition element. The interest in the development of novel electrochemical (bio)sensors continues to be large, stimulated by the wide range of applications in daily life, where they continue to meet the expanding need for rapid, simple, and economic methods of determination of numerous analytes as an alternative to traditional analytical approaches. Traditional approaches include high-performance liquid chromatography (HPLC), ultra-performance liquid chromatography (UPLC), gas chromatography (GC), thin-layer chromatography (TLC), ion-pair liquid chromatography (IPLC), capillary electrophoresis (CE), etc., which require extensive sample pre-treatment, expensive equipment, and the necessity of sample clean up. In general, this is more time-consuming [8,9].

In order to construct a reliable (bio)sensor, some essential characteristics must be met [10,11]:

(i). *High sensitivity*: sensitivity is defined as the slope of the analytical calibration curve for a given analyte. A sensor is considered "sensitive" when a small change in analyte concentration causes a significant difference in the response.

(ii). *High degree of selectivity*: selectivity is the ability of a (bio)sensor to detect one specific species, even in the presence of many other interferent species. This characteristic has an important role for applications in real samples.

(iii). *Low limit of detection (LoD)*: LoD is the value of concentration or the quantity that can be detected with an acceptable degree of certainty for a given analytical procedure.

(iv). *Acceptable repeatability and reproducibility*: repeatability is the relative agreement between successive measurements carried out in the same conditions related to operators, apparatus, laboratories, and/or intervals of time between analyses. Reproducibility is the closeness of the agreement between successive measurements of the same parameter, performed in different conditions in terms of operators and apparatus, laboratories, and/or intervals of time between analyses. These two parameters are indicative of the stability of the sensing device.

(v). *Wide linear range*: the linear range should be large enough and over a concentration range considered critical, for example, for the detection of toxic compounds or biomarkers indicative of some disorder in living organisms.

Electrochemical (bio)sensors can use a range of modes of detection and may be divided into conductimetric, potentiometric, amperometric, voltammetric and, impedimetric sensors. Each electrochemical sensing principle depends on the exact mode of signal transduction and whether they are used under equilibrium or dynamic condition modes. For sensors at equilibrium, no current flows between the electrodes and the analyte and there is no change in the concentration profile over time. This regime is controlled by diffusion and possibly Brownian motion. In contrast, dynamic sensors are characterised by a current, which flows as a result of an oxidation or reduction reaction [12,13].

Potentiometry is the most important non-dynamic method, and its measurements are carried out based on measuring the potential difference between a working (indicator) electrode and a reference electrode.

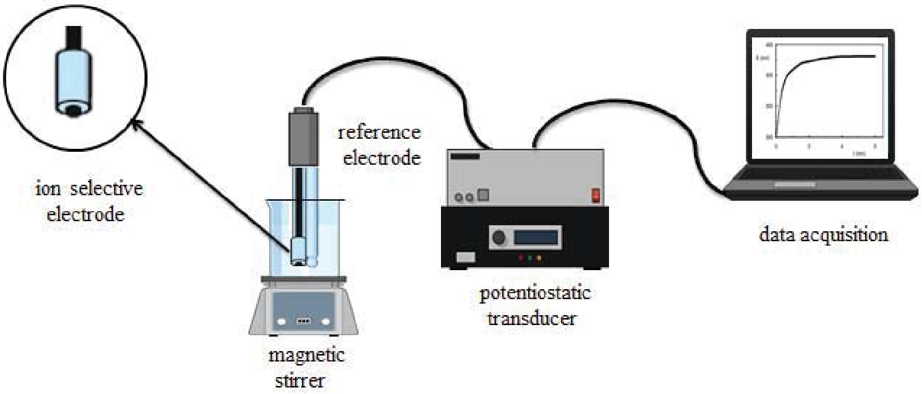

Fig. 1.2 Schematic illustration of a potentiometric sensor system.

Measurements are performed under equilibrium conditions and monitor the separation of charge, at zero current, created by a selective reaction or binding at the electrode surface. The electrode (membrane) surface often has a perm-selective outer layer, and, in the case of the biosensors, a bioactive material may be present, such as enzyme, DNA, or antibodies, at which the biomaterial-catalysed reaction generates or consumes a chemical species that is detected by an ion-selective electrode. The transducer is normally the ion-selective electrode (ISE) itself, which is based on a thin film or a selective membrane as recognition element [14,15], as illustrated in **Fig.1.2.**

Ion-selective electrodes can detect ionic species such as Na^+, K^+, H^+, F^-, I^-, CN^-, NH_4, or gases (CO_2 and NH_3) by sensing changes in the electrode potential when the ions bind to an appropriate ion exchange membrane. The analytical information obtained by converting the recognition process into a potential signal is logarithmically proportional to the concentration of species generated or consumed, as described by the Nernst equation [16]. Two main drawbacks are that the signal depends on temperature and that the membrane potential is sometimes influenced by the adsorption of other components in solution. Additionally, potentiometric-based sensors can detect only free species and require frequent calibration, and there may be errors from the existence of traces of the analyte or interfering ions in the reagents [15,17].

In amperometric sensors the analyte is oxidised or reduced. A chosen value of potential is applied between a working and a reference electrode, and the electroactive species passing over the working electrode is reduced or oxidised, leading to a current flow, this being the principle of the detection method [2,18]. The choice of applied potential must consider the material of the sensing electrode, the target analyte, and the environmental conditions (pH, ionic strength, temperature, etc.). Thus, to be suitable for this type of measurement detection, the compound or species of interest has to be electroactive within the potential range available for the working electrode in the particular electrolyte solution used and at the prevailing pH. A limitation is that only electroactive species are detectable, but the detection can be more selective [13,19]. The use of a sensing array with different applied potentials can make it possible to discriminate between several electroactive species, which also permits distinguishing between the target analyte and interferent species [20].

The basic instrumental arrangement requires controlled-potential equipment (potentiostat) and an electrochemical cell consisting of three electrodes immersed in a suitable electrolyte (see **Fig. 1.3**). One of the electrodes is used as a reference electrode, whilst the working electrode is where the reaction of interest occurs. The reference electrode (e.g., Ag/AgCl) provides a stable reference potential compared to the working electrode. An inert conducting material is used as an auxiliary/counter electrode (e.g., Pt, graphite, etc.) [21].

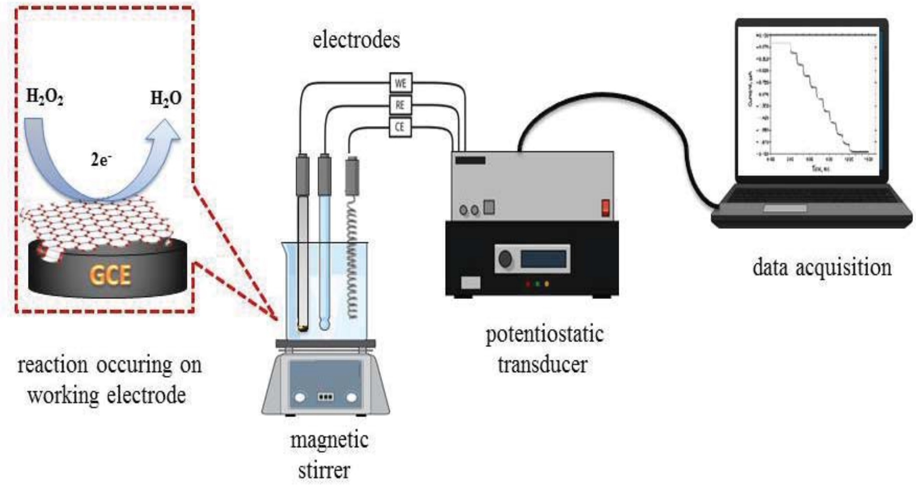

Fig. 1.3 Diagram of a typical amperometric sensor system

Voltammetric sensors are similar to amperometric sensors except that the applied potential is changed during the measurement process [22]. A linear potential ramp gives rise to linear sweep voltammetry (LSV). Cycling the potential between defined limits at a chosen scan rate is cyclic voltammetry (CV). Using potential pulses superimposed on a staircase waveform gives rise to square wave voltammetry (SWV) and differential pulse voltammetry (DPV). Voltammetric pulse techniques are generally more sensitive than scan techniques, and normally the range in which the electrochemical current response is linearly dependent upon the concentration of the electroactive species that is probed is used [23].

In impedimetric-based sensors, a small sinusoidal voltage is superimposed on a fixed applied potential with different frequencies, and the resulting current response is measured. The impedance is then calculated as the ratio of voltage to current in the frequency domain. By using small amplitude sine wave perturbation, linearity in the electrochemical system can be ensured [3]. The impedance is measured over a wide frequency range and its value depends on the reaction that occurs on the electrode surface. Generally, there is a decrease in the resistance to charge transfer as the concentration at electroactive species increases. The impedance spectra can be analysed by fitting to an equivalent electrical circuit to get the values of the electrical components which model the interfacial phenomena [24,25].

1.2 Nanomaterials and applications in electrochemical (bio)sensors

Modifying the surface of the electrode support with various conducting nanomaterials (such as metal oxides, redox polymers, carbon materials, biological molecules, etc.), results in a new surface that can have improved sensitivity and selectivity towards an analyte of interest.

Nanomaterials provide huge advantages for many applications—such as catalysis, imaging, biotechnology, and sensors applications—because of their particular properties. For sensor applications, the high surface area-to-volume ratio of the nanomaterials allows enhanced catalytic and sensing properties at nanomaterial modified electrodes. The physical and catalytic properties of the nanomaterial can be tuned or altered by reduction of the size, shape, the extent of agglomeration, as well as tailoring the nanostructure surfaces with chosen crystallographic faces [26,27].

The main advantages of nanomaterial modified-electrodes for sensing applications include [28]:

(i) Higher electroactive area.

(ii) Faster electrochemical reaction through improved electrode surface kinetics (electrocatalysis).

(iii) The use of carbon-based materials, such as graphene and carbon nanotubes, can significantly enhance the adsorption of analytes on the electrode surface, which can help lower trace level quantification.

(iv) Nanomaterials provide stable modified electrode supports, as well as highly active sites for functionalisation to improve the selectivity of the modified electrode.

Although nanomaterials can provide numerous advantages in electrochemical (bio) sensing, proper immobilisation on the electrode support and further functionalisation with the desired moieties are critical factors in improving performance. The methods commonly employed for electrode modification include electrodeposition, physical adsorption, electrostatic attraction, polymerisation, and chemical bonding [29]. Possible electrode modifiers include metal nanoparticles (e.g., gold, platinum, silver, titanium, zinc, cerium, iron, etc.), carbon materials (e.g., graphite, carbon fibre, carbon nanotubes, graphene, carbon black, etc.), conducting polymers (e.g., conjugated conducting or redox polymers such as polyphenazines).

1.2.1 Noble metal nanoparticles

Owing to the unique size and shape-dependent variables of physical, chemical, and electrochemical properties, noble metallic nanoparticles—such as gold (AuNP), silver (AgNP), platinum (PtNP), and palladium (PdNP) —bimetallic alloys, and core-shell nanoparticles are attractive for numerous technological applications [30]. These nanostructures are mostly prepared by in situ synthesis, such as electrodeposition [31], chemical vapour deposition [32], and more commonly by hydrothermal (chemical and green) synthesis [24,33]. The modification of the surface electrode with NP has been extensively employed for the development of novel electrochemical (bio)sensors. In general, metal nanoparticle (MNP) modified electrodes exhibit the attractive advantages compared to bulk metal electrodes alluded to above, such as higher surface area and increased electron and mass transfer rate, as well as improved selectivity and sensitivity [34,35]. Often their biocompatibility makes them a good choice for the fabrication of DNA, enzyme, and immunosensors [36], and well-dispersed nanoparticles with small size have better electrochemical performance than the larger size and aggregated particles [37]. In hydrothermal synthesis, aggregation of NP can be minimised by introducing an extra substance to disperse nanoparticles that have physical or chemical interaction, which can also stabilise the NP. Examples are functionalisation with citrate or hybridisation of NP with a stabiliser agent, such as chitosan hydrogel, polyvinyl pyrrolidone (PVP), or diethylene glycol providing sufficient structural stability. The introduction of a stabiliser or reactant together with metal nanoparticle precursors before synthesis has become the main method to protect shape and size [38,39].

1.2.2 Conducting and redox polymers

Conducting polymer systems can be reversibly reduced or oxidised and can change their electrochemical properties via losing electrons (oxidation) or gaining electrons (reduction). Examples of conducting conjugated polymers are polypyrrole, polyaniline, and polythiophene. Examples of redox conducting polymers are poly(phenazines).

Conjugated conducting polymers consist of alternating single and double bonds along the polymer chain. Both single and double bonds include a localised σ-bond, which forms a strong chemical bond. Additionally, each double bond also contains an initially localised π-bond, which is weaker than the σ–bond, **Fig. 1.4**.

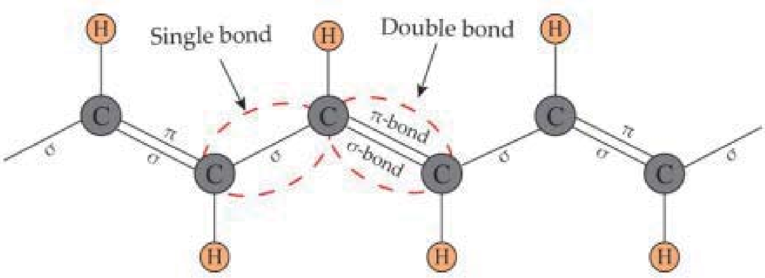

Fig. 1.4 The structure of a conjugated polymer [40].

Conjugated conducting polymers can be categorized into degenerate and non-degenerate systems based on their bond structures in the ground state. Degenerate polymers possess two identical geometric structures in the ground state while non-degenerate polymers exhibit two different structures with different energies in the ground state (e.g., benzenoid and quinoid structures, where the energy of the benzenoid is lower than that of the quinoid). Solitons are known to be the charge carriers in degenerate systems such as polyacetylene. Conversely, polarons and bipolarons serve as the charge carriers in both degenerate and non-degenerate systems such as polypyrrole and polythiophene. The movement of these charge carriers along polymer chains produces conductivity. In solid-state physics terminology, the oxidation and reduction processes correspond to p-type and n-type doping, respectively. In p-type doping, the electron moves directly from the HOMO of the polymer to the dopant species and creates a hole in the polymer backbone. Conversely, in n-type doping, electrons from the dopant species move to the LUMO of the polymer, resulting in increased electron density. Hence, the density and mobility of charge carriers can be tuned by doping [41,42].

Redox conducting polymers contain groups that can be oxidised or reduced, allowing movement of charge along the polymer chain. In other words, these polymers can change their electrochemical properties via losing electrons (oxidation) or gaining electrons (reduction). Redox polymers are also known by the names oxidation-reduction polymers, electron-transfer polymers or electron-exchange polymers.

The most common organic chemical groups with redox properties include nitroxyl, phenoxyl, quinones, viologens, carbazol or hydrazyl and they have been successfully applied in chemical sensing, biosensing, batteries, supercapacitors, etc., due to improved electronic properties, sensitivity, and biocompatibility [41,42]. The sensing mechanism of redox conducting polymers can involve redox reactions, ion adsorption and desorption, volume and mass changes, chain conformational changes, or charge transfer. Compared to inorganic counterparts, conducting polymers have advantages in achieving high sensitivity and selectivity, due to their chemical and structural diversity [43].

Conducting polymers can normally be obtained by chemical or electrochemical methods. The overall process usually involves the oxidation of monomers, to form cation radicals followed by chain growth. Chemical synthesis is advantageous for large-scale production at low cost, while electrochemical polymerisation offers the possibility of in-situ formation directly on the electrode surface for the development of sensing devices [43].

The controlled preparation of redox conducting polymer films by electrochemical synthesis involves optimising polymerisation parameters such as applied potential, potential cycling scan rate, pH, and electrolyte used for polymerisation [44,45].

1.2.3 Deep eutectic solvents (DES)

Deep Eutectic Solvents (DES) have emerged as a sustainable and “green” alternative solvent medium for electropolymerisation, due to the possibility of formation of a polymer material with superior sensing properties than its analogue formed in aqueous solution [46]. DES are produced from an eutectic mixture of solid Lewis or Brønsted acids and bases, which can contain a variety of anionic and cationic ionic species. They incorporate a hydrogen bond acceptor (HBA) and a hydrogen bond donor (HBD) and form a mixture with a melting point lower than either of the individual constituents [47]. DES have properties in common with ionic liquids (ILs), namely a broad working temperature range, excellent chemical stability, and a wide electrochemical window that is important for polymer electrosynthesis, which often requires a high potential for the generation of radicals. Additionally, the preparation of DES is easier than that of ILs, is at lower cost, and they do not require exhausting steps of preparation and/or purification and are usually biodegradable [48–50].

DES can be described by the general formula Cat^{+}-X^{-} zY with Cat^{+} being ammonium, sulfonium, or phosphonium and X^{-} a Lewis base, normally a halide. The HBD, a Lewis or Brønsted acid, Y, forms a “complex” with X^{-}. DES are commonly divided into four types, see **Table 1.1**. Type I, II and Type IV (e.g., ChCl:2$ZnCl_2$, ChCl:2$CrCl_3 \cdot 6H_2O$, $ZnCl_2$:3.5urea, respectively) and Type III (e.g. ChCl: oxalic acid). Common examples of the Type III HBD are urea, ethylene glycol, and glycerol, and when choline chloride (ChCl) is used as HBA, this gives rise to DES with the common names of reline, ethaline and glyceline, respectively [48,51].

Table 1.1 The most common DES types.

Type	**Formula**	**Terms**
I	$Cat^{+}X^{-}{}_{z}MCl_{x}{}^{-}$	M: Zn, Sn, Fe, Al, Ga, In
II	$Cat^{+}X^{-}{}_{z}MCl_{x}.{}_{y}H2O$	M: Cr, Co, Cu, Ni, Fe
III	$Cat^{+}X^{-}{}_{z}RZ$	Z: $CONH_2$, COOH, OH
IV	$MCl_{x} + RZ=MCl_{x-1}{}^{+}.\ RZ^{+}MCl_{x+1}{}^{-}$	M: Al, Zn; Z: $CONH_2$, OH

Two special classes of DES have been recently gaining increasing attention. These are natural deep eutectic solvents (NADES) and therapeutic deep eutectic solvents (THEDES).

NADES are mixtures which contain combinations of metabolites that occur in large amounts in cells, with a crucial role in cryoprotection, drought resistance, germination and dehydration. They have been considered as the third liquid phase in living organisms, the solubility of many natural products being greater in NADES than in water [52]. It has been shown that there is hydrogen bonding between the constituents in mixtures of ChCl with a variety of natural products such as organic acids (lactic acid, acetic acid, citric acid and, etc.), alcohols (hexanediol, butanediol, glycerol and, etc), sugars (fructose, glucose, sucrose and, etc.) or amino acids (citrulline, arginine, proline) and the future role of NADES in the food, cosmetic and pharmaceutical industries and in extraction and separation processes has been assessed [53].

THEDES are bioactive eutectic systems composed of an active pharmaceutical ingredient as one of the DES constituents [54]. The interest is due to their potential use as improved pharmaceutical formulations, to increase drug solubility and permeability and thence provide more efficient drug delivery. It has been established that the dominant interactions are of a hydrogen bond nature [55].

1.2.4 Carbon nanomaterials

Many carbon nanomaterials exhibit unique properties such as a high surface-to-volume area, high electrical conductivity, good chemical stability, biocompatibility, and robust mechanical strength [56,57]. Carbon nanomaterial-based electrochemical (bio)sensors generally have a high sensitivity and low limit of detection. The morphologies of carbon-based materials constitute an additional critical factor that enables their functionalisation, which can have a significant influence on electrode kinetics [58]. Their nanostructures have exposed surface groups for the binding between analyte molecules and transduction materials, leading to remarkable electroanalytical performance [59]. The most commonly used carbon nanomaterials for (bio)sensing applications are graphene oxide (GO), carbon nanotubes (CNT) and their derivatives—such as carbon quantum dots (CQD)—and graphene quantum dots (GQD) [60].

Graphene oxide (GO) is a 2D nanomaterial of sp^2 hybridised carbon nanosheets decorated with epoxy and carboxyl groups assembled in a honeycomb lattice, resulting in an extremely high surface area [26,61]. These functional groups can be used for a variety of surface-functionalisation reactions, which can be exploited in GO-based (bio)sensors. However, the existence of oxygen-containing groups in the GO nanostructure can cause defects and compromise the electrochemical performance. Decreasing the oxygen functional group content of GO is essential for the enhancement of its conductivity. Thus, the use of reduced GO (rGO) with fewer oxygen-containing groups and higher electrical conductivity than GO is desirable for the design of more sensitive electrochemical sensors [62,63].

Carbon nanotubes (CNT) can be visualised as cylindrical tubes ‘rolled up’ from sp^2 hybridised graphene sheets, exhibiting 100 times the tensile strength of steel, similar electrical conductivity to copper, and excellent electrocatalytic ability [64]. CNT have a diameter that typically varies from 0.4 to 40 nm with some microns in length. Both ends of the CNT are generally capped with fullerene-like structures. They can be exist as single-walled carbon nanotubes (SWCNT) and multi-walled carbon nanotubes (MWCNT), according to the number of rolled layers [28]. Both SWCNT and MWCNT are important nanomaterials as electrode modifier for (bio)sensing applications. However, a factor that limits utilisation and compromises the excellent properties of CNT is their inherent insolubility and tendency to agglomerate. In such cases, chemical functionalisation can be used to fine-tune CNT properties. Better dispersion can be achieved through functionalisation with, for example, carboxyl or amino groups, also causing some significant defects in the carbon nanotube structures and improving their conductivity [65,66].

Carbon quantum dots (CQD) are zero-dimensional carbon nanoparticles less than 10 nm in size. Their size and edge crystallography govern their electrical, magnetic, optical, and chemical properties. Due to their easy functionalisation, biocompatibility, good solubility, quantum confinement, and edge effects, CQD are used to construct nanoscale electronic devices [67,68]. CQD can be synthesised by many methods that include graphite laser ablation, pyrolysis, thermal annealing, strongly acidic and electrochemical oxidation, hydrothermal treatment, and microwave-assisted synthesis. These carbon nanoparticles display physical and chemical properties substantially different from bulk carbon, due to their smaller size. CQD has received much attention in spectroscopic applications, due to very good optical properties, photoluminescence behaviour, and high resistance to photobleaching. They have also been used in electroanalysis [69]. For example, a CQDs-chitosan film on a glassy carbon electrode has been reported to improve the electrochemical performance in relation to the bare electrode towards dopamine determination [70].

Graphene quantum dots (GQD) and CQD surface modifications of basal plane pyrolytic graphite electrodes, towards the electrochemical response of redox marker ferro/ferricyanide and two important biomarkers, uric acid and ascorbic acid. It was found the CQD have superior electrocatalytic properties in the presence of these species [71], even better than fluorescence detection [72].

GQD are different from CQD, as they possess the graphene structure. The edge and the quantum confinement effect become more prominent when the size of the graphene nanosheets becomes less than 100 nm and are especially evident when the dimensions are below 10 nm [73]. GQD properties can be tuned by controlling the size and surface chemistry properties. Compared with conventional semiconductor quantum dots, GQD have advantages of excellent biocompatibility, ease of combining with biomolecules and low biological toxicity [74]. They are easy to be chemically modified with superior conductivity [75,76]. These properties enable their extensive application in biosensing, biomedicine, energy-related devices and nanodevices [76].

1.2.5 Nanocomposites

The use of conducting nanocomposites is a breakthrough in the field of modified electrodes for sensing applications. The term nanocomposite refers to a novel nanomaterial that combines two or more nanomaterials with significantly different physical or chemical properties, due to the synergetic effect of the individual components, leading to improved sensitivity and lower limit of detection. The nanocomposites mostly include the combination of nanomaterials, such as polymers, metal or semi-conductors as nanomaterial matrix. Metal nanoparticles, carbon-based materials, and, more recently, ILs have also been reported [77].

1.3 Nanomaterials used as modifiers in this work

1.3.1 Gold nanoparticles (AuNP)

Metallic nanoparticles have recently become the focus of intense research due to their altered properties compared to the bulk metal [78]. One of the most used types of metal nanoparticle is gold nanoparticles (AuNP). Applications include therapeutic treatments, detection and diagnostics, biolabeling, drug delivery, chemical and biological sensing, imaging, nonlinear optics, photovoltaics, and catalysis [79]. The dominant features of AuNP include shape-related optoelectronic properties, large surface-to-volume ratio, excellent biocompatibility, and low toxicity. These properties make them excellent tools in biotechnology [80].

To date, there are numerous preparative methods for the synthesis of AuNP, including top-down and bottom-up procedures. Recent efforts have been dedicated to controlling size, shape, solubility, stability, and functionality [79].

Procedures for the synthesis of AuNP can be divided into physical, chemical, and biological methods.

(i) Methods such as γ-irradiation, microwave (MW) irradiation, sonochemical, ultraviolet (UV) radiation, laser ablation, thermolytic or photochemical process are categorised as physical procedures [81].

(ii) In chemical methods, chemical reactions are performed in an aqueous medium by a reduction agent. Citrate and sodium borohydride are the common reducing agents used. Among the conventional methods of chemical synthesis of colloidal gold, the Turkevich procedure, see more details in chapter 2, is widely utilised, due to the simplicity and ease of synthesis, stability and controllable size [82].

(iii) Biological synthesis, regarded as environmentally friendly, is another route of synthesis. Reducing hazardous generated wastes and assisting "green chemistry" are the main objectives of biosynthesis. The solvent medium, the reducing, and the stabiliser agents should be non-toxic and safe. Plant-based compounds and derivatives, bacteria, fungi, algae, yeast, and viruses are employed as common resources. Various shapes and sizes of nanoparticles may be obtained in this way, which has excellent properties for applications in nanotechnology [83].

1.3.2 Multi-walled carbon nanotubes (MWCNT)

Multi-walled nanotubes (MWCNT) are formed from the folding of graphene layers into carbon cylinders [84]. Their excellent intrinsic properties, lead to their wide potential applications in nanoelectronics, composite materials, energy research, and biomedicine [85] as well as in electrochemical sensors and biosensors [86–88]. Additionally, MWCNT as electrode modifiers enhance the electrochemical reactivity of important biomolecules and can promote the direct electron-transfer reaction of proteins, whilst limiting surface fouling effects. Their unique structure provides an exceptional electric current-carrying capacity along their length (1000 times higher than copper wires) [86–88].

For synthesising MWCNT, several different routes have been demonstrated in recent years. High-temperature preparation techniques, such as arc discharge or laser ablation, were the first methods used to produce MWCNT. However, these methods have been replaced by low-temperature chemical vapour deposition (CVD) (<800°C), since the orientation, alignment, nanotube length, diameter, purity, and density of the carbon nanotubes can be precisely controlled [89].

Most of these methods require supporting gases or are done under vacuum. Gas-phase methods are suitable for the production of large quantities of nanotubes in industrial-scale synthesis in an economically feasible way. On the other hand, gas-phase synthesis methods have low catalyst yields, since only a small percentage of catalysts form nanotubes, plus short catalyst lifetimes and low catalyst number density [89].

The main disadvantage of the majority of the synthetic methods is that they produce MWCNT with a mixture of diameters and chiralities and are usually contaminated with metallic and amorphous impurities, whose type and amount depend on the method used. Therefore, a fundamental challenge is efficient and simple purification. Post-synthesis chemical purification is necessary, that also improves the electronic and mechanical properties of these materials [90].

Another drawback in the utilisation of CNT is the poor solubility in most solvents, which limits applications. Hence, the functionalisation of nanotubes is extremely important, as it increases their “solubility” and processability. Several modification approaches—physical, chemical, or combined modifications—have been exploited for achieving uniform dispersion in common solvents to enhance performance and broaden their applications, [91,92]. For example, organic functionalisation of CNT (the edges or ends) with chemical groups enables the binding of CNT to other molecules or to surfaces, such as oxygen functional groups, small organic molecules, polymers and biomolecules (e.g. DNA and enzymes).

The addition of functional groups to the nanotubes usually takes place at defect sites in the CNTs or at the end caps. This is due to the lower activation energy for chemical reactions at defect sites (vacancy, non-hexagonal arrangement of C atoms, etc.). The defect concentration in carbon nanotubes is normally of the order of 1-3% of the carbon atoms, so the functional group concentration will have a similar value. Thus, before the functionalisation reactions are carried out, more defect sites are generated by oxidation. The nanotube sidewalls can be functionalised by a variety of chemical groups, a very common option being carboxylic groups, which can be introduced by exposing the carbon nanotubes to concentrated nitric acid [93,94]. Only very harsh conditions, such as fluorination, allow the addition of chemical species directly to the sidewalls.

During functionalisation, as in the specific case of carboxyl group addition, the sp^2 carbon in the tube sidewall transforms into a sp^3 type atom. This change in the hybridisation has a significant influence on the charge transport properties of the CNT. More localised types of perturbation are changes induced by specific chemical groups in the local electronic structure of the nanotubes. The addition of functional groups creates additional states in the CNT band structure. Such changes are specific to the kind of functional group producing them and are localised around the chemical group [95,96]. As a result, the intrinsic conductivity of the MWCNT is improved, making them better materials to be used as electrode modifiers for (bio)sensing applications.

1.3.3 Polymers

1.3.3.1 Poly(8-anilino-1-naphthalene sulphonic acid)

Poly(8-anilino-1-naphthalene sulphonic acid) (PANSA) is a derivative of polyaniline (PANI) with electronic properties that have much in common with PANI.

PANI is a mixed oxidation state polymer composed of reduced benzoid units and oxidised quinoids. It has three readily accessible oxidation states: fully reduced leucoemeraldine, half-oxidised emeraldine, and fully oxidised pernigraniline (see **Fig. 1.5**). Only the emeraldine salt, which is the protonated form of emeraldine base, is electrically conductive.

The basic sites (amine and imine groups) in the polymer backbone of emeraldine base can be protonated with sufficiently strong acids to produce emeraldine salt; thus, polyaniline is sensitive to pH changes. PANI is redox active at pH values lower than 4. At higher pH values, PANI deprotonates and loses its redox activity [97,98].

PANI is prepared by chemical or electrochemical oxidative polymerisation of the respective aniline monomers in strongly acidic solution. Other polymerisation techniques that have been used to prepare polyaniline include photochemically-initiated polymerisation and enzyme-catalysed polymerisation. Both chemical and electrochemical polymerisation of aniline proceeds via several steps as a radical propagation reaction. The steps are [99]:

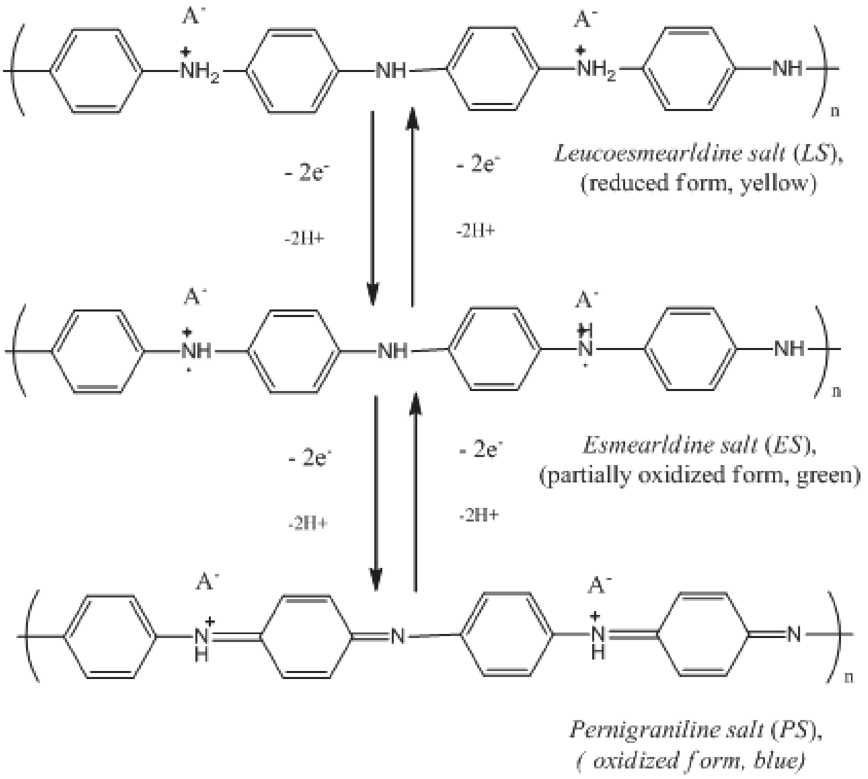

Fig.1.5 Redox reactions between the various forms of polyaniline.

Step 1. Oxidation of aniline to a radical cation, which exists in three resonance forms.

Step 2. Coupling of the radical cations, resulting in a dicationic dimer species. The coupling is predominantly “head to tail” or “para-coupling”. This dimer then undergoes re-aromatisation to its neutral state, giving the intermediate p- aminodiphenylamine known as PADPA.

Step 3. Chain propagation via coupling of the dimer radical cation (centred on the nitrogen atom) with an aniline radical cation centred in the para position and finally oxidation of the growing polymer to a radical cation and doping with HA.

The chemical polymerisation mechanism has similarities with the electrochemical polymerisation mechanism, but it also has differences in that the initial product of Step 3 in chemical polymerisation is pernigraniline salt. After full consumption of the oxidant, the pernigraniline salt is reduced by unreacted aniline to the green emeraldine salt.

As mentioned above. poly(8-anilino-1-naphthalene sulphonic acid) (PANSA) is a polyaniline derivative. As films, it shows excellent performance in the catalytic reduction of oxygen [100], anticorrosion coatings [101], and in the electrochemical determination of some biologically important compounds [102]. The monomer 8-anilino-1-naphthalene sulphonic acid contains sulfonic acid (–SO_3H) as well as amino (–NH_2) functional groups in its structure, which play an important role in various applications [103]. The existence of sulfonic acid groups helps improve solubility in common polar solvents. The polymer also acquires an intrinsic proton doping ability, leading to the formation of highly soluble self-doped homopolymers and copolymers [104]. Additionally, the presence of active functional groups,–NH_2, in the polymer chain can promote attachment to other functional groups, which can give the polymer film strong binding properties and good compatibility with other polymer layers and surfaces [105].

On the other hand, the extra benzene ring in the monomer can confer greater hydrophobicity to the polymer film leading to a lower degree of solvation, closer packing of the polymer chains, and reduced diffusion of solvated species through the film.

1.3.3.2 Polyphenazines and poly(triphenylmethanes)

Phenazine dyes are aromatic compounds consisting of a dibenzo annulated azine structure. Phenazine derivatives have methyl and/or amino groups on the benzene rings, and one N can be substituted by S (phenothiazine) or O (phenoxazine) in the azine ring [106,107]. The most common phenazines are neutral red (NR), Nile blue (NB), methylene blue (MB), methylene green (MG), brilliant cresyl blue (BCB), safranine T (ST), phenosafranine (PS), toluidine blue (TB), thionine (Thi), and azur A, B, and C (AA, AB, AC), **Fig. 1.6.**

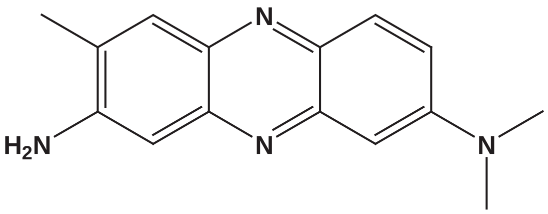

Neutral red (NR),
N,N,3-trimethylphenazine-2,8,-diamine

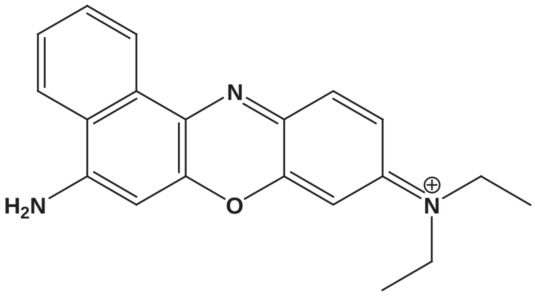

Nile blue (NB),
N-(5-amino-9H benzo[a]phenoxazin-9-ylidene-N-diethylamine

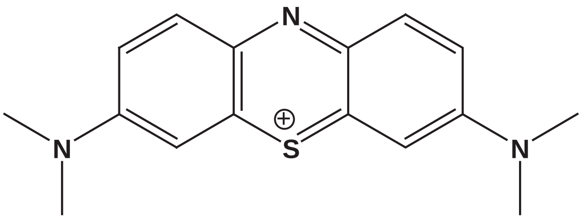

Methylene blue (MB),
7-bis (dimethylamino) phenothiazine

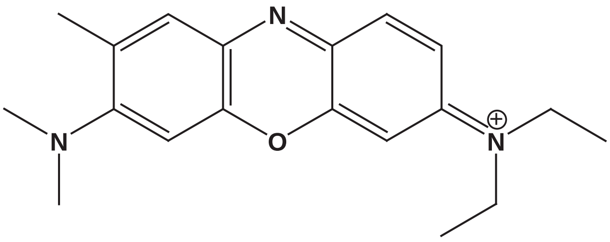

Brilliant cresyl blue (BCB),
N-(7-(dimethylamino)-8-methyl-3H-phenoxazin-3-ylidene)-N-diethylamine

Fig. 1.6 Chemical structures, trivial name with the abbreviation, IUPAC name of some phenazine monomers [110].

Phenazines are the parents of many dye compounds—such as eurhodines, toluylene red, indulines, and safranines—and such systems are widely used for various applications, such as pharmaceuticals, agrochemicals, pigments, dyes, etc. [108]. Other applications are OLEDs, solar cells (conjugated polymers and small molecules for DSSC), and sensing applications [109]. The phenazine monomers containing primary amino groups as ring substituent can release a proton upon oxidation, yielding a singly-charged cation-radical, which is responsible for the direct electrochemical polymerisation of the monomers, forming the corresponding semi-conducting polymer film [110].

Phenazine electropolymerisation can be performed in the same way as for other conducting polymers: by cycling the applied potential, applying a constant potential, or applying a constant current in the solution containing a phenazine monomer. The electrochemical reactions leading to polymer formation proceeds by monomer oxidation to form cation radicals that initiate polymerisation [111]. The number of radicals formed defines the structure of the polymer, which occurs via C-N coupling; the more radicals formed, the more branched is the polymer obtained. Polyphenazine films can be used in electrochemical sensors and biosensors. As electrode substrate, mainly carbon-based electrodes have been reported, such as glassy carbon, carbon film, and composites with graphite or carbon nanotubes.

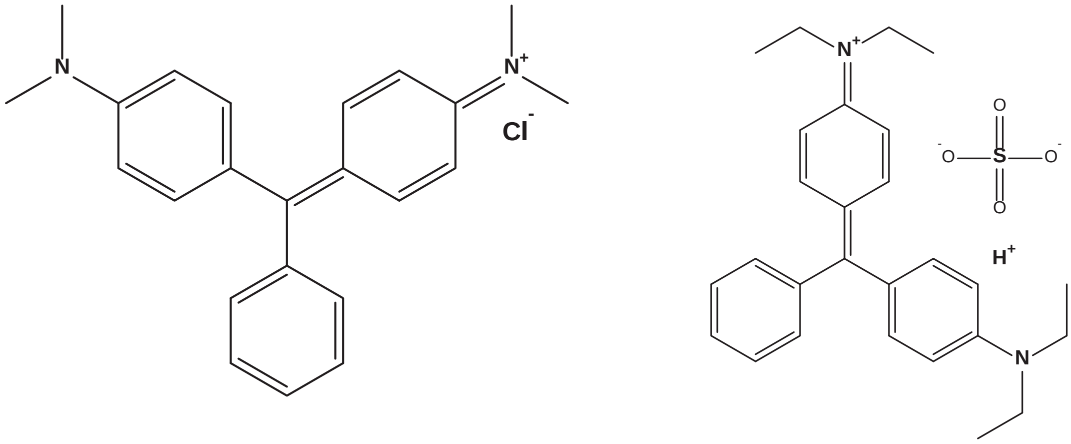

Malachite green (MCG)
4-*{[4-(Dimethylamino)phenyl]*
(phenyl)methylidene}
N,N-dimethylcyclohexa-2,5-
dien-1-iminium
chloride

Brilliant green (BG)
4-{[4-(Diethylamino)phenyl]
phenyl)methylene}-N,N-diethyl
2,5-cyclohexadien-1-iminium
hydrogen sulfate

Fig. 1.7 Chemical structures, trivial name with abbreviation, IUPAC name of malachite green and brilliant green.

Triphenylmethanes are dye compounds, that are used in textile dyeing and paper printing and as antiseptic, antifungal, and antimicrobial agents in aquaculture and in the food industry [112]. Triphenylmethane dyes are characterised by an open and ionised structure, which is expected to be a suitable building block for microporous conjugated polymers, as they are composed of three phenyl groups linked to sp^3 carbon with a rigid propeller-like configuration [113]. The fact that they have an open, ionised structure is promising for fast charge transfer and for catalytic ability in ion transport, which is very useful in the field of (bio)sensors.

However, their use in the field of sensors up to now has been rather limited and related to only two dyes: malachite green (MG) and brilliant green (BG) [114], see structures in **Fig. 1.7**.

Polymerised films of BG, in particular, are very promising for the design of new biosensor assemblies, considering that PBG film has a reported excellent performance in the detection of hydrogen peroxide, a product of most enzymatic biological reactions [115].

1.4 Enzymes and enzymatic sensors

1.4.1 Enzymes: definition and classification

Enzymes are biological catalysts that speed up biochemical reactions in living organisms. These biocatalysts are universally present in plants, animals, and microbial cells and catalyse a wide range of biological processes. Some enzymes demonstrate specificity for a group of enzyme substrates - for instance, tyrosinase. Tyrosinase is involved in two distinct reactions: the hydroxylation of a monophenol and the conversion of an o-diphenol to the corresponding o-quinone. Other enzymes exhibit much higher specificity for only one substrate, such as glucose oxidase that has almost total specificity for its substrate, β - D-glucose, and virtually no activity for any other monosaccharide. This specificity is of primordial importance in many analytical assays and biosensors that measure a specific substrate in a complex matrix (e.g., blood or urine) [116].

Table 1.2 Classification of enzymes.

Enzyme class	**Description**
EC 1 Oxidoreductases	Catalyse redox reactions and can be categorised into oxidase and reductase.
EC 2 Transferases	Catalyse the transfer or exchange of certain groups among some substrates.
EC 3 Hydrolases	Accelerate the hydrolysis of substrates.
EC 4 Lyases	Catalyse reactions involving either the cleavage or formation of chemical bonds, with double bonds either arising or disappearing. Cleavage of bond does not require water.
EC 5 Isomerases	Facilitate the conversion of iso-isomers, geometric isomers, or optical isomers.
EC 6 Ligases	Catalyse the synthesis of two molecular substrates into one molecular compound with release of energy.
EC 7 Translocases	Catalyse the movement of ions or molecules across membranes or their separation within membranes.

The nomenclature of enzymes is directly related to the substrates or the chemical reactions catalysed by them. They are classified into seven categories, as summarised in **Table 1.2**, namely isomerases, oxidoreductases, transferases, hydrolases, lyases, ligases, and translocases. Of these, hydrolases, oxidoreductases, and transferases are the most abundant types of enzyme.

1.4.2 Enzyme immobilisation methods

For an enzyme biosensor to operate successfully, the enzyme should be immobilised appropriately on the transducer surface. Immobilisation means incorporating a biomaterial in an inert support or by chemically or physically binding it to the transducer surface. Enzyme immobilisation is a critical factor to develop efficient biosensors with good operational and storage stability, high sensitivity, high selectivity, short response time, and high reproducibility. Immobilised biomolecules have to maintain their structure, function, and biological activity after immobilisation, remain tightly bound to the surface, and not be desorbed during the use of the biosensor. The choice of the most appropriate and reasonable technique also depends on the enzyme's nature, the transducer, the type of bonding involved, and the associated detection mode.

There are five basic methods of enzyme immobilisation [18,117,118]:

Adsorption

This is the simplest method and does not need any substantial pretreatment of sensor components or the use of special-purpose chemicals. Both physical adsorption and chemical adsorption can be used. In physical adsorption, the biomaterial is held on the surface by Coulomb, Van der Waals, ionic interactions, or hydrogen bonding. Chemical adsorption is based on a strong affinity and usually on a semi-covalent bond formed between a thiol group (-SH) and a gold substrate. Thus, thiol-containing enzymes, such as oxidoreductases and isomerases which contain double-catalytic site cysteine residues, can be immobilised on a gold surface via the thiol groups of their amino acid residues. These thiol-containing enzyme are either in native form or obtained through chemically modification or genetic engineering techniques, in order to provide them with reactive thiol groups. Alternatively, thiol-containing enzymes can be immobilized onto supports, which fixed with reactive disulfides or disulfide oxides, through a thiol-containing bifunctional linker which, on one end, forms disulfide bonds (S–S) to the surface, and on the other end, provides N-hydroxysuccinimide (NHS) groups that can react with the free amino groups on the enzyme. The efficiency of adsorptive immobilisation is determined mainly by the properties of the transducer surface, including its charge, the presence of polar groups, its redox potential, and its energetic uniformity.

Covalent bond

Covalent bonding is probably the most widespread immobilisation method. The sensor surface is modified to acquire a reactive group to which the biological materials can be attached. In the case of enzymatic biosensors, it is through a functional group in the enzyme, which is not essential for its catalytic activity. Usually, nucleophilic functional groups present in amino acid side chains of proteins—such as amino, carboxylic, imidazole, thiol, hydroxyl, etc.—are used for coupling. This method improves uniformity, density, and distribution of the bioelements, as well as reproducibility and surface homogeneity. Covalent immobilisation may decrease or eliminate some common problems, such as instability, diffusion, and aggregation or inactivation of biomolecules. This occurs when biomolecules are immobilised on sensor surfaces by polymer matrices.

Crosslinking

In the cross-linking method, the immobilised enzyme is prepared via cross-linking of the physical enzyme aggregates with a bifunctional or multi-functional cross-linker. The most common cross-linking methods of immobilisation are based on the formation of covalent bonds between enzyme molecules and a functionalised compound, e.g., glutaraldehyde. This involves covalent bonding of the enzyme with glutaraldehyde, usually in the presence of bovine serum albumin (BSA). BSA provides additional coupling sites without blocking the electrode surface, thus acting as an intermediate spacer arm. The glutaraldehyde reacts with lysine amino groups in the enzyme mutually cross-linking the enzyme with another protein (BSA). Higher enzyme activity and better stability can be obtained. It is a very stable method of immobilisation; however, the appropriate amount of BSA needs to be chosen to avoid the loss of enzyme activity.

Entrapment

In this case, the enzymes are not directly attached to the support surface but entrapped within a polymer gel matrix, which allows not only the movement of enzyme substrate and products but also retains the enzyme. The entrapment immobilisation process is done in two steps: (1) mixing of the enzyme into a monomer solution, followed by (2) polymerisation of the monomer solution by chemical reaction. As an enzyme is physically confined within a polymer lattice network, the enzyme does not chemically interact with the entrapping polymer. An example of this was reported by Chiorcea et al., who used oxysilane sol-gel to entrap glucose oxidase (GOx) on a highly oriented pyrolytic graphite (HOPG) electrode substrate [119].

This method could thus improve enzyme stability and reduce enzyme leaching and denaturation. Another advantage is the capability to optimise the microenvironment for the enzyme by modifying the encapsulating material to have the optimal pH, polarity, or amphiphilicity. However, a limitation is the gel matrix thickness. The enzyme substrate cannot diffuse deep into the gel matrix to reach the enzyme active site. Additionally, the entrapped enzymes may leak if the size of the pores of the support matrix is too large. The method also has low enzyme loading capability, and the support material could be altered as a result of polymerisation.

Encapsulation

Immobilisation by encapsulation represents an entrapment method in which enzymes are enclosed in a semipermeable membrane. The membrane may be lipoidal, lipoprotein, or polymer-based. The membrane allows small-sized molecules, such as enzyme substrate and product, to diffuse through the membrane while retaining larger size enzyme molecules within. The risk of enzyme leakage is minimal, and a multi-enzyme system could be developed by trapping more than one enzyme inside the membrane.

In summary, each immobilisation method presents advantages and drawbacks. Factors to consider before choosing an immobilisation technique are [120]:

(i) Applicability on different surfaces.

(ii) Immobilised biocatalyst should exhibit maximum activity.

(iii) Immobilised biocatalyst should operate over a wide pH range.

(iv) Immobilised biocatalyst should be stable.

(v) The ability to co-immobilise more than one biocomponent.

(vi) Little or no leaking of the biocomponent from the surface.

1.4.3 Enzyme kinetics

For low concentrations of substrate, nearly all enzyme-based reactions show a linear rate dependence on substrate concentration. As the concentration increases, the rate of reaction reaches saturation [121]. Enzyme kinetic models that have found wide applicability were first proposed by Michaelis and Menten in 1913 and later modified by Briggs and Haldane.

The Michaelis-Menten equation relates the initial rate of an enzyme-catalysed reaction to the substrate concentration and to a ratio of rate constants [122]. The simplest reaction involves one substrate and one enzyme with a catalytic site. The enzyme (E) and substrate (S) are in equilibrium with the enzyme substrate complex (ES), which can then dissociate to the substrate and enzyme again, or form the product (P) of the reaction and release the enzyme, as shown in equation 1.1.

$$\mathrm{S + E} \underset{k_{-1}}{\overset{k_1}{\rightleftharpoons}} \mathrm{ES} \xrightarrow{k_2} \mathrm{P + E} \tag{1.1}$$

The rate constants k_1, k_{-1}, and k_2 are used for the definition of the Michaelis-Menten constant K_M:

$$K_\mathrm{M} = \frac{k_{-1}+k_2}{k_1} \tag{1.2}$$

Assuming that the enzyme substrate complex is in rapid equilibrium with the reactant enzyme and substrate, the Michaelis-Menten equation (1.3) is obtained:

$$v_0 = \frac{v_\mathrm{max}[\mathrm{S}]}{[\mathrm{S}]+K_\mathrm{M}} \tag{1.3}$$

The initial reaction rate v_0 is related to the substrate concentration [S] and the maximum rate of the reaction v_max.

The plot of the reaction rate vs. substrate concentration is a hyperbolic curve, **Fig. 1.8 (A)**, in which the K_M value is the substrate concentration when the reaction rate is half of v_max.

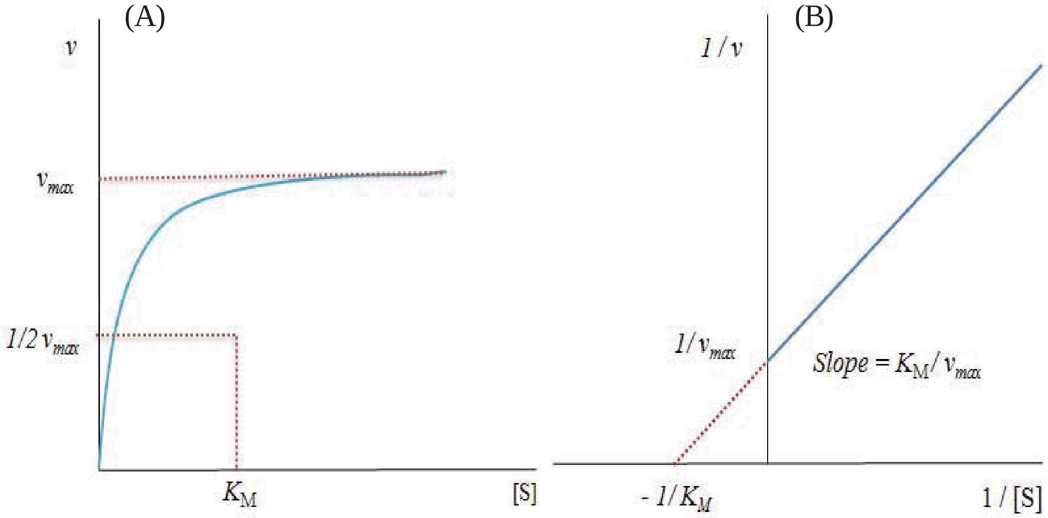

Fig. 1.8 (A) Plot of reaction rate vs. substrate concentration [S] according to the Michaelis-Menten equation for fixed enzyme concentration. **(B)** Lineweaver-Burk plot of 1/v against 1/[S]. K_M and v_{max} can be determined directly by intercepts on the x- and y-axis.

The parameters also can be obtained by rearranging the Michaelis-Menten equation, to give the *Lineweaver-Burk* equation (1.4):

$$v_0 = \frac{1}{v_{max}} + \frac{K_M}{[S]}\frac{1}{v_{max}} \tag{1.4}$$

The parameters v_{max} and K_M can be determined directly from this representation by the intercept on the y-axis and the slope of the plot, see **Fig. 1.8 (A)**.

Studies of enzyme inhibition can furnish knowledge about enzyme specificity, the properties of the enzyme active site, and the mechanism of the enzyme-catalysed reaction. This is usually used as a strategy for drug development and can provide insight into the mechanism of enzyme activity, for instance, by identifying residues critical for catalysis [123].

Enzyme inhibition can occur reversibly or irreversibly. The latter occurs when the inhibitor binds tightly to the active site of the enzyme, generally covalently, and dissociates very slowly from the target.

In reversible inhibition, equilibrium exists between the inhibitor, I, and the enzyme, E,

$$E + I \rightleftharpoons EI \tag{1.5}$$

The equilibrium constant corresponding to dissociation of the enzyme-inhibitor complex is known as the inhibitor constant (K_i), given by Equation (1.6):

$$K_i = [E][I]/[EI] \tag{1.6}$$

K_i is used for calculating the affinity of the inhibitor for an enzyme, similar to the way in which K_M is a measure of the affinity of a substrate for the enzyme.

Reversible inhibition is further subdivided into competitive, non-competitive, uncompetitive, and mixed types [124], as summarised in **Fig. 1.9**. Enzyme activity is fully restored when the inhibitor is removed from the system in which the enzyme functions.

In *competitive inhibition*, the substrate and inhibitor compete for the active site of the enzyme, because the substrate and inhibitor bind to identical or overlapping sites. Due to the overlapping nature of the binding sites, a ternary complex, in which the substrate and the inhibitor simultaneously bind to the enzyme, cannot be formed. Accordingly, in the enzyme-inhibitor complex, the enzyme is completely inactive. The effect of a competitive inhibitor on the kinetics of an enzyme-catalysed reaction is illustrated in **Fig. 1.8 (A)**.

The inhibitor concentration [I] is arbitrarily chosen as K_i for comparison with the equilibrium in the absence of an inhibitor. It shows that the rate of reaction rises more slowly in the presence of an inhibitor and reaches the same v_{max} value but at a higher substrate concentration and the K_M value is increased. The *Lineweaver-Burk* plots, which have an intersection on the y-axis and an higher slope, illustrate the fact that v_{max} is unaffected by a competitive inhibitor.

A *non-competitive inhibitor* can bind to an enzyme with or without a substrate at different places at the same time. The conformation of the enzyme is changed, and the substrate is unable to bind to the enzyme effectively so that the enzyme activity decreases. This inhibition decreases the rate of reaction. As the inhibitor binds to both the enzyme and the enzyme substrate complex, it decreases the amount of enzyme available for catalysis, there are fewer available active sites and therefore a smaller v_{max}. Unlike competitive inhibition, raising the substrate concentration has no effect. The *Lineweaver-Burk* plots show a constant intersection on the x-axis, which means that the K_M value is unchanged by a non-competitive inhibitor, although v_{max} is decreased, **Fig. 1.9(B)**.

Uncompetitive inhibition occurs when the inhibitor binds only to the enzyme substrate complex, not to the free enzyme. Usually, the free enzyme has an inappropriate binding site for the inhibitor, but, when the substrate binds to the active site of the enzyme, a conformational change occurs in the enzyme, which makes the binding site accessible to the inhibitor, yielding a catalytically inactive ESI complex. The effect of an uncompetitive inhibitor on the enzyme kinetics, **Fig. 1.9 (C)** shows that v_{max} cannot be reached, because at any inhibitor concentration even an infinitely high substrate concentration will not drive the entire enzyme to the ES form. However, unlike the non-competitive inhibitor, the Lineweaver-Burk plots show that the intercept on the x-axis changes, but the slope remains the same, which means the K_M value is decreased, as well as v_{max}.

Mixed inhibition is the other major type of inhibition mechanism in which the inhibitor may bind to the enzyme, whether or not the enzyme has already bound the substrate, but has a greater affinity for one state or the other. It is called "mixed" because conceptually it is a mixture of competitive and uncompetitive inhibition.

Reversible enzyme inhibition requires graphical methods for diagnosing the type of inhibition and the determination of the inhibition constant K_i. Besides *Lineweaver-Burk* [125], other graphical methods are commonly used such as Dixon [126] and Cornish-Bowden [127].

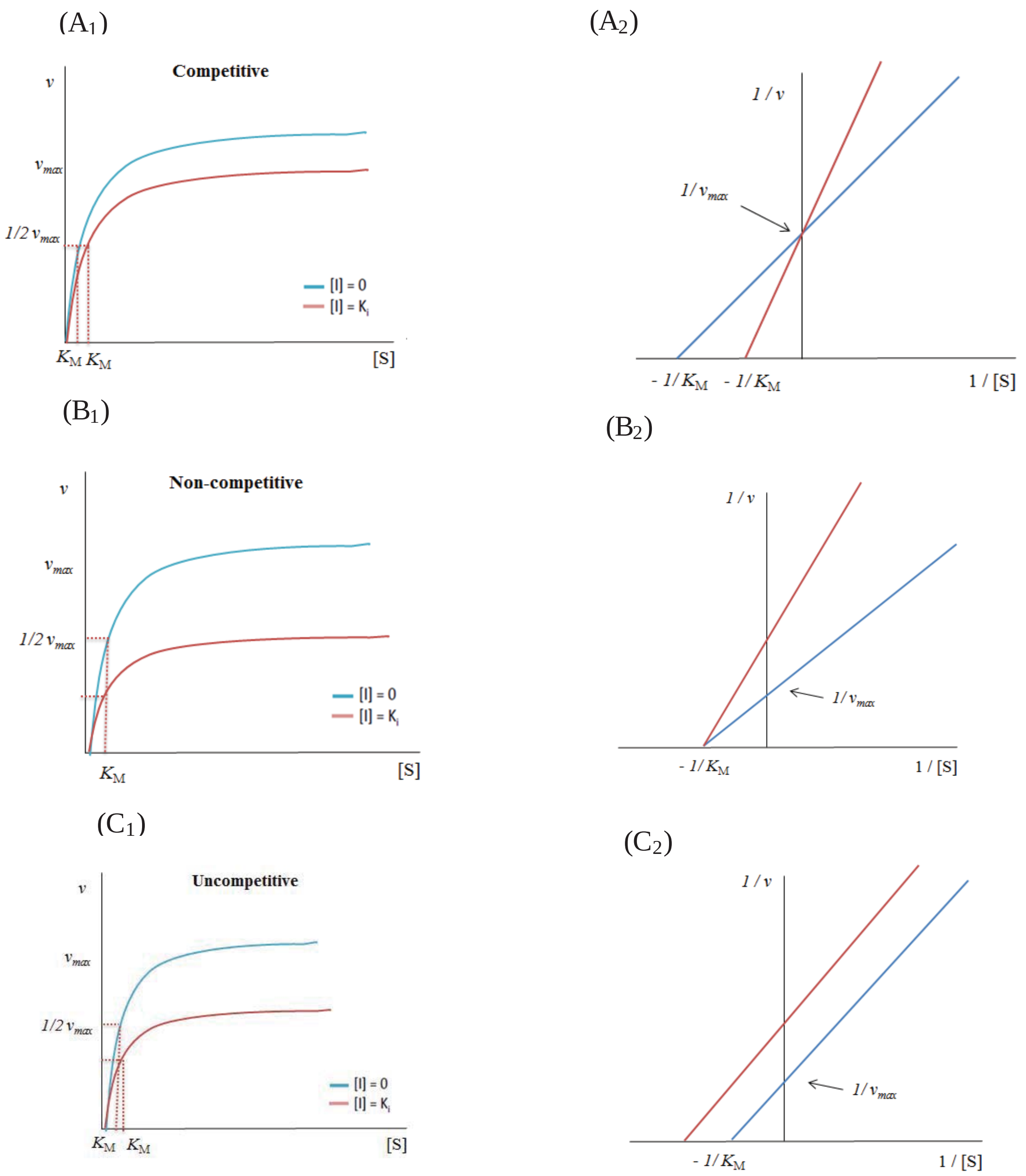

Fig. 1.9 Plots of reaction rate *v* against substrate concentration [S] according to the velocity equation in the absence and in the presence of a fixed concentration of an inhibitor for different types of inhibitions, namely: **(A_1)** competitive, **(B_1)** non-competitive, and **(C_1)** uncompetitive inhibition. *Lineweaver-Burk* plots of 1/v against 1/[S] in the absence and in the presence of three different mechanisms of inhibition: **(A_2)** competitive, **(B_2)** non-competitive, and **(C_2)** uncompetitive inhibition

It has been common to use Dixon plots to determine the inhibition type and the inhibition constants for competitive and non-competitive inhibition, but it cannot distinguish between competitive and mixed inhibition. The Cornish-Bowden method is unable to determine the inhibition constant for competitive inhibition. In this work, a new graphical strategy was used for the determination of the enzyme inhibition mechanism and will be explained in more detail in Chapter 4.

1.5 Enzymes used in this work

1.5.1 Glucose oxidase

Glucose oxidase (GOx, EC 1.1.3.4) is a flavoprotein which contains the compact non-covalently bound coenzyme flavin adenine dinucleotide (FAD) and belongs to the large group of oxidoreductase enzymes. Its molecular weight ranges from approximately 130 kD to 175 kD and consists of two identical polypeptide chain subunits having nearly equal molecular weights linked by disulphide bonds [128]. Each subunit, or monomer, folds into two domains: one domain binds to the substrate, β-D-glucose, while the other domain binds non-covalently to the FAD cofactor, which is a powerful oxidising agent. FAD is a common component in biological redox reactions.

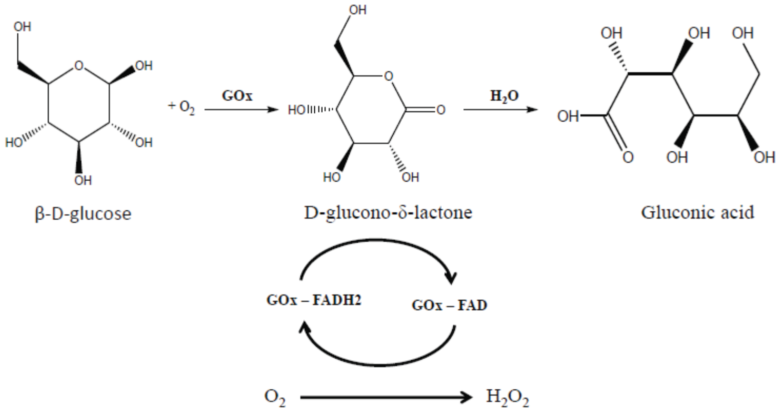

Fig. 1.10 Glucose oxidation catalysed by the enzyme glucose oxidase (GOx); when O_2 plays the role of electron acceptor.

The GOx subunit contains one mole of Fe and one mole of FAD, and contains 74% protein, 16% natural sugar, and 2% amino sugars. GOx is produced predominantly by the fungi *Aspergillus* and *Penicillium* species. GOx catalyses the oxidation of β-D-glucose to D-glucono-δ-lactone and hydrogen peroxide using molecular oxygen as an electron acceptor with the concomitant reduction of GOx [129], see **Fig. 1.10**. GOx-based biosensors are widely used in the chemical, food, beverage, pharmaceutical, and clinical industries. Such applications include glucose sensors used in clinical and environmental monitoring [130].

1.5.2 Tyrosinase

Tyrosinase (Tyr_{ase}, EC 1.14.18.1) is a metalloenzyme that contains a binuclear copper active site responsible for the enzyme existing in three oxidation states. First, it catalyses the conversion of monophenols (e.g., tyrosine) into o-diphenols (monophenolase activity), followed by the oxidation of the o-diphenols to the corresponding o-quinone derivatives (diphenolase activity), see **Fig. 1.11**. The related catechol oxidases only catalyse the second reaction, using o-diphenols as substrates [131,132]. Starting from tyrosine, the final product of the tyrosinase-catalysed reaction is dopaquinone, which is a precursor of melanin [133]. Tyr_{ase} can be produced and extracted through organisms such as bacteria, fungi, plants, and mammals and studied for specific functioning [134].

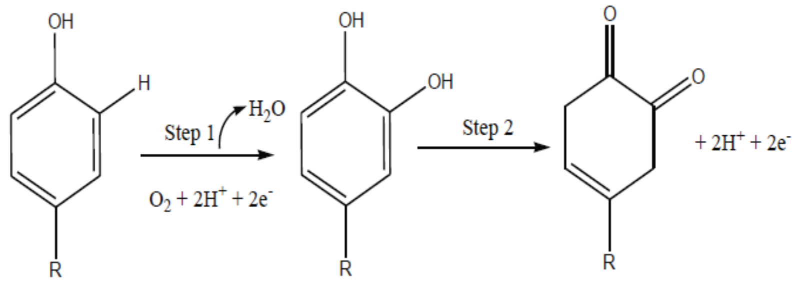

Fig. 1.11 Reactions of phenols catalysed by tyrosinase

Due to the multiple sources of tyrosinase, its structural properties are diverse in nature, along with their distribution in tissues and cells, so no common protein is observed across all species. The difference is found in primary structure, size, in post-modification sites like the active site, and in the glycosylation mechanism. The common thing in all tyrosinases is their binuclear type III copper centre containing two copper atoms, each connected with six histidine molecules in their active site. These copper atoms are linked with atmospheric oxygen that catalyses the two reactions (1) ortho-hydroxylation of monophenols and (2) oxidation of o-diphenols to o-quinones [135,136].

Tyr_{ase} is involved in the biosynthesis of melanin in melanosomes causing pigmentation of the skin, hair, and eyes in mammals, protecting against from ultraviolet radiation damage. The enzyme plays a crucial part in primary immune response and in healing of wounds in plants, various invertebrates, as well as sponges. It has significant importance in spore-forming, protecting tissues and survival after lesions or injuries in fungi. It has a vital role in the protection of bacteria. Tyr_{ase} also plays an important role in medical applications, including melanin synthesis for therapeutic purposes, production of L-DOPA production, a drug utilised to treat Parkinson’s disease, manufacturing antibiotic lincomycin, and treating various neurological disorders. Mushroom Tyr_{ase} has clinical application to treat vitiligo and produces hydroxyl tyrosol that has use as a food additive. Tyr_{ase} is also employed in the food manufacturing industries, for instance, to make the aflavins, a collection of compounds in black tea possessing anticancer and other properties [137–139].

1.5.3 Choline oxidase

Choline oxidase (ChOx, EC 1.1.3.17) is a flavoprotein which catalyses the four-electron oxidation of choline to glycine-betaine, with betaine-aldehyde as intermediate and molecular oxygen as primary electron acceptor, see **Fig. 1.12**.

The reaction occurs through two consecutive FAD-mediated oxidations of the substrate. The alcohol substrate is oxidised to betaine aldehyde in the first oxidation reaction; then, the hydrated form of betaine aldehyde, *gem*-diol choline, is oxidised to glycine betaine [140].

Choline oxidase was first described in 1977 by Ikuta et al. [141], who reported the purification and initial characterisation of the enzyme from the soil bacterium *Arthrobacter globiformis*. The study of choline oxidase is of considerable interest for several reasons.

From an applied standpoint, the development of biosensors for the detection of choline and choline ester derivatives, such as acetylcholine, in serological samples and foods renders this enzyme of medical and industrial interest.

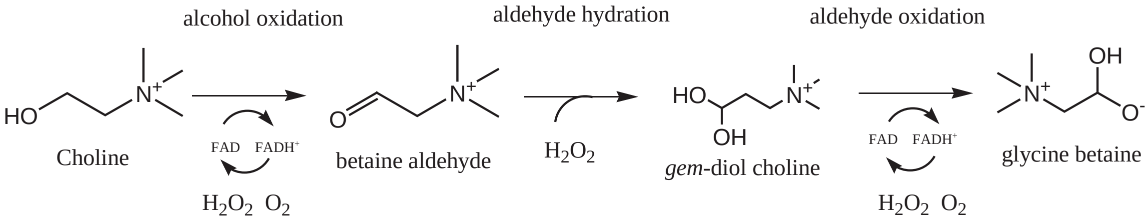

Fig. 1.12 Reactions of choline catalysed by choline oxidase.

Furthermore, the recent findings that many bacterial and plant species accumulate glycine-betaine in response to salt stress or water deficit have prompted considerable interest in research on glycine-betaine biosynthesis, with the goal of genetically engineering water/osmotic stress resistance in beneficial bacteria and crop plants.[142,143]. However, despite a wealth of studies on the biotechnological applications of the enzyme, minimal mechanistic or structural studies of choline oxidase have been reported to date.

1.6 Electrochemical techniques and microscopy

This section describes briefly the electrochemical techniques used in this work for analysis and characterisation of modified electrodes: cyclic voltammetry (CV), chronoamperometry, differential pulse voltammetry (DPV), and electrochemical impedance spectroscopy (EIS). It also describes the surface analysis techniques used for examining the nanostructure morphologies: scanning electron microscopy (SEM), transmission electron microscopy (TEM) and, X-ray diffraction (XRD).

1.6.1 Cyclic voltammetry (CV)

Cyclic voltammetry is the most common electrochemical technique used for obtaining qualitative information about electrochemical reactions. The main advantage of cyclic voltammetry results from its ability to rapidly provide crucial information on the thermodynamics of redox processes, on the kinetics of heterogeneous electron-transfer reactions, and coupled chemical reactions or adsorption processes. Furthermore, it offers fast location of redox potentials of the electroactive species and permits the convenient evaluation of the influence of the media upon the redox process [144]. It consists of scanning the potential of a stationary working electrode linearly using a triangular potential waveform, **Fig. 1.13**.

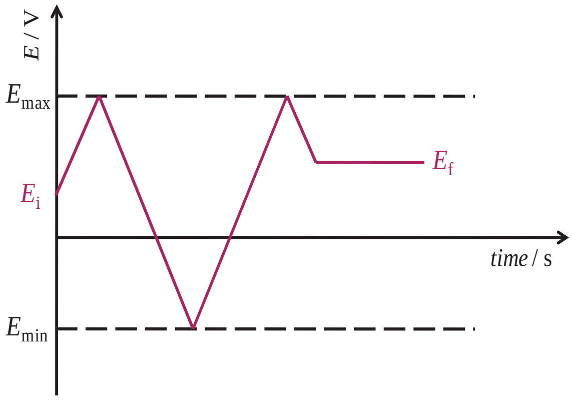

Fig. 1.13 Variation of applied potential with time in cyclic voltammetry, showing the initial potential E_{i}, the final potential E_{f}, maximum E_{max}, and minimum E_{min} potentials [145].

In cyclic voltammetry, on reaching $t = t_1$, the sweep direction is inverted and swept until E_{min}, then inverted and swept to E_{max}, etc. The important parameters are:

- the initial potential, E_{i}
- the final potential, E_f
- the initial sweep direction
- the sweep rate, v
- the maximum potential, E_{max}
- the minimum potential, E_{min}

A faradaic current, I_{f}, due to the electrode reaction, is recorded in the relevant zone of applied potential, where the electrode reaction occurs. There is also a capacitive contribution: on sweeping the potential, due to changes in the double layer charge; this contribution increases linearly with increasing sweep rate.

The total current is:

$$I = I_c + I_f = C_d \frac{dE}{dt} + I_f = vC_d + I_f \tag{1.7}$$

For a simple electron transfer reaction (R → O + ne$^-$) with only R initially present, the faradaic current depends on the kinetics and transport by diffusion of the electroactive species. The current increases as the potential becomes more positive but then begins to be limited by the rate of diffusion of unreacted species to the electrode surface, so that a peak current appears, I_{pa}. On reversing the potential scan there is a reduction peak current I_{pc}. The theoretical description of this problem was first due to Randles and Sevčik [146,147]. For fast kinetics (reversible system) the anodic peak current is:

$$I_{\mathrm{pa}} = 2.69 \times 10^5 n^{3/2} A D_{\mathrm{R}}^{1/2} [R]_\infty v^{1/2} \tag{1.8}$$

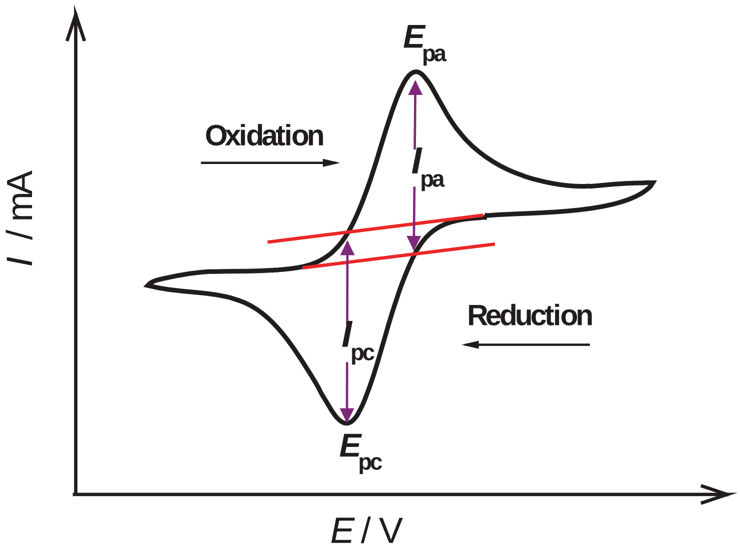

Fig. 1.14 Cyclic voltammetry with the extraction of the peak potentials (E_{pa}, E_{pc}) and the peak currents (I_{pa}, I_{pc}), used for elucidation of the mechanism of electrode reactions.

If a redox system remains in equilibrium at the electrode surface throughout the potential scan, the electrochemical reaction is said to be reversible i.e. the surface concentrations of O and R are maintained at the values required by the Nernst equation. Under these conditions, the following parameters characterise the cyclic voltammogram of the redox process at 25ºC [146]:

- $I_p \propto v^{1/2}$
- E_p independent of v
- $|E_\mathrm{p} - E_{\mathrm{p}/2}| = 56.6/n$ mV
- $E_\mathrm{p,a} - E_\mathrm{p,c} = 57.0/n$ mV
- $|I_\mathrm{p,c}/I_\mathrm{p,a}| = 1$

For irreversible processes, anodic and cathodic peaks are reduced in height and are more widely separated, due to the effect of electrode kinetics. Irreversible systems are characterised by a shift of the peak potential with the scan rate:

$$E_\mathrm{p} = E^0 - \frac{RT}{a_a\, n`F}\left[0.78 - \ln\frac{K_0}{D^{1/2}}\right] + \ln\left(\frac{a_a\, n`F}{RT}\right)^{1/2} \tag{1.9}$$

where:

- n is the number of electrons transferred in the rate-determining step
- α_a is the electrochemical charge transfer coefficient for the anodic process.

Therefore, E_p occurs at potentials higher than E^o, with the overpotential related to k_0 and α_a.

The corresponding peak current for an oxidation reaction, in amperes, is:

$$I_\mathrm{p} = 2.99 \times 10^5 n(\alpha_a n')^{1/2} A D_\mathrm{R}^{1/2}[\mathrm{R}]_\infty v^{1/2} \tag{1.10}$$

The peak current is still proportional to the bulk concentration but the peak will be lower in height (depending upon the value of α_a). Assuming $\alpha_\mathrm{a} = 0.5$, the ratio of the reversible-to-irreversible peak currents is 1.11.

Others parameters are:

- $|E_p - E_{p/2}| = 47.7/(\alpha n')$ mV
- $|dE_p/d\lg v| = 29.6/(\alpha n')$ mV
- E_p dependent on v.

For quasi-reversible systems, the current is controlled by both the charge transfer and the mass transport. As the ratio increases, the process approaches the reversible case. For smaller values, the system tends towards irreversible behaviour.

Overall, the cyclic voltammograms for a quasi-reversible system are more drawn out and exhibit a larger separation in peak potentials compared to a reversible system, **Fig. 1.15**.

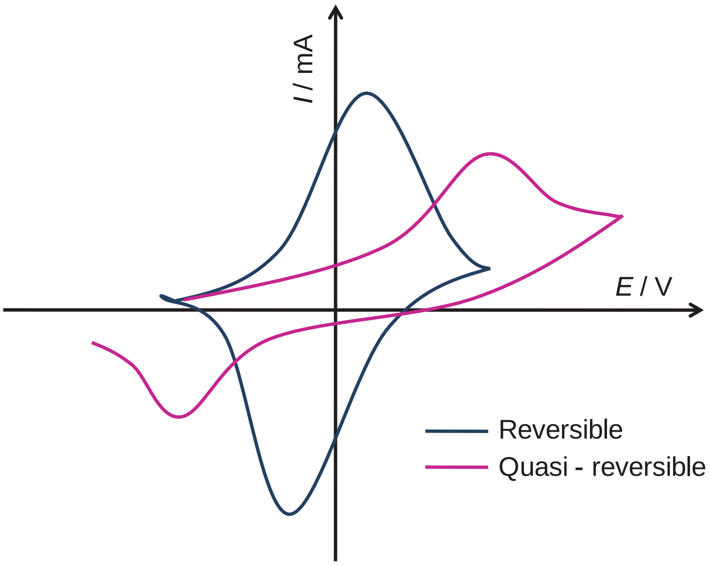

Fig. 1.15 The effect of increasing irreversibility on the shape of a CV.

If the reagent or product of an electrode reaction is adsorbed strongly or weakly on the electrode, the form of the voltammetric wave is modified. There are two types of situations:

- the rate of reaction of adsorbed species is much greater than of species in the solution;
- it is necessary to consider the reactions of both adsorbed species and those in the solution.

The current-potential curve is described by Eq. 1.11

$$I_{\mathrm{p}} = \frac{nF\sigma A\Gamma_{R,i}(b_O/b_R)\theta}{[1+(b_O/b_R)\theta]^2} \tag{1.11}$$

where

- $\Gamma_{R,\ i}$ is the surface concentration of adsorbed R species on the electrode surface of area A, before the experiment begins
- b_{O} and b_{R} express the adsorption energy of O and R

$$\sigma = \frac{nF}{RT}v$$
$$\theta = exp\left[\left(\frac{nF}{RT}\right)(E - E^{0\prime})\right]$$

The peak current for a reversible reaction, $I_{\mathrm{p},}$ is described by the equation:

$$I_{\mathrm{p}} = \frac{n^2F^2vA\Gamma_{R,i}}{4RT} \tag{1.12}$$

1.6.2 Chronoamperometry

Potential step chronoamperometry is the basis of all pulse techniques. The principle of chronoamperometry measurements involves stepping the potential of the working electrode from a value where no faradaic reaction occurs to a potential at which the surface concentration of the electroactive species is effectively zero, see **Fig. 1.16A**.

This *I-t* relationship response is comprised of two components [148]:

- the current due to charging the double-layer;
- the current due to the electron transfer reaction of the electroactive species at the electrode interface.

The extent to which both occur depends on the initial applied potential, E_{i}, and the final value, E_{s}, of the potential. When a planar electrode is used in an unstirred solution, and the applied potential is sufficient to oxidise or reduce all the electroactive species as fast as they reach the electrode surface, i.e., at a diffusion-controlled rate, the current-time curve reflects the change of the concentration gradient at the electrode surface. This is caused by a gradual increase with time of the diffusion layer thickness associated with depletion of the reactant, **Fig. 1.16B**. The current, at a planar electrode, thus decays with time, **Fig. 1.16C**, as given by the *Cottrell equation*:

$$I_t(t) = \frac{nFAD^{1/2}c_\infty}{(\pi t)^{1/2}} = kt^{-1/2} \tag{1.13}$$

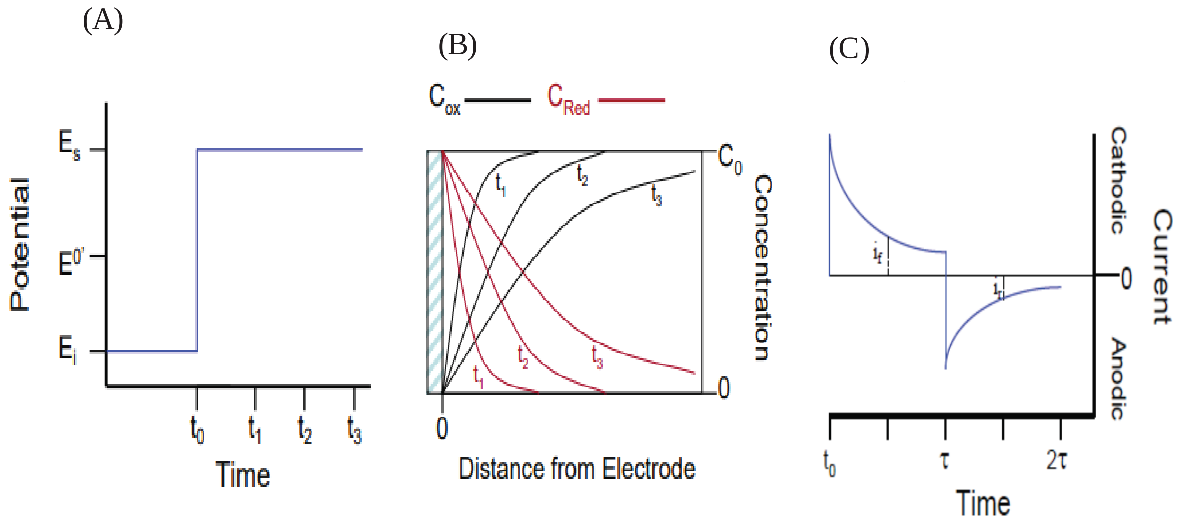

Fig. 1.16 Chronoamperometric experiments: **(A)** potential-time waveform; **(B)** change of concentration profiles with time; and **(C)** the resulting current-time response at applying successive potential steps in opposite directions.

The Cottrell equation states that the product $I\ t^{1/2}$ should be constant for a diffusion-controlled reaction at a planar electrode. Deviation from this constancy can be caused by non-planar diffusion, convection in the solution and slow charging of the interfacial region during the potential step [144].

For each of these cases, the variation of $I\ t^{1/2}$ when plotted against t is different, and the current response to a potential step always reflects the mechanism of the electrode reaction and, in principle, can be used to distinguish mechanisms of simple or coupled reactions, etc. Non-planar electrodes such as cylinders can exhibit an increase in $I\ t^{1/2}$ with increasing time [144].

1.6.3 Differential pulse voltammetry (DPV)

Differential pulse voltammetry is an extremely useful technique for measuring trace levels of organic and inorganic species. In differential pulse voltammetry, fixed height pulses—superimposed on a linear potential ramp—are applied to the working electrode at a time just before the end of the drop, **Fig. 1.17**.

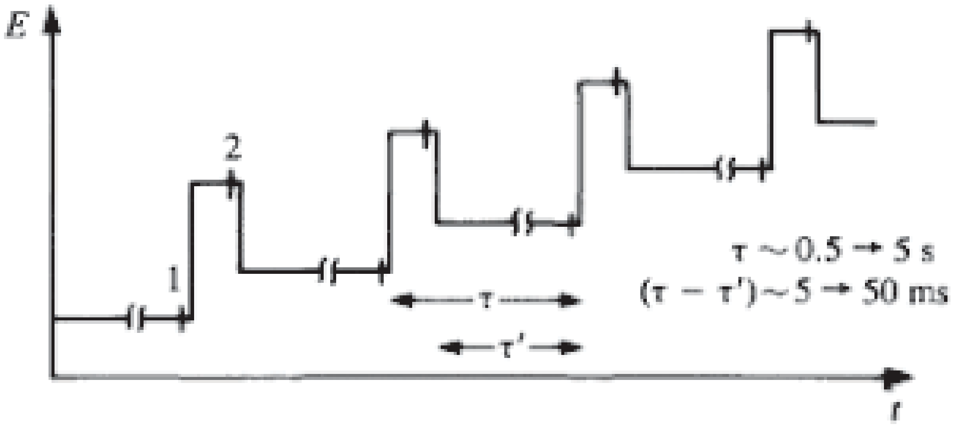

Fig. 1.17 Excitation signal for differential pulse voltammetry [146].

The current is measured twice, just before the pulse application (at 1) and again late in the pulse life (after ≅ 40 ms, at 2, when the charging current has decayed). The first current is subtracted from the second one, and this current difference [$\Delta I = I(t_2)\text{-}I(t_1)$] is plotted versus the applied potential. The resulting differential pulse voltammogram consists of current peaks, the height of which is proportional to the concentration of the corresponding analytes:

$$i_{\mathrm{p}} = \frac{nFACD^{\frac{1}{2}}}{\sqrt{\pi t_m}} \frac{(1-\sigma)}{(1+\sigma)} \tag{1.14}$$

in which $\sigma = \exp[(nF/RT)(\Delta E/2)]$ (ΔE is the pulse amplitude). The maximum value of the quotient $(1-\sigma)/(1+\sigma)$ is obtained for large pulse amplitudes.

The peak potential (E_p) can be used to identify the species, as it occurs near the half-wave potential. For an oxidation,

$$E_p = E_{1/2} - \Delta E/2 \tag{1.15}$$

Differential pulse voltammetry allows measurements at concentrations lower than 0.1 μM. DPV can also provide improved selectivity for observing different redox processes compared with cyclic voltammetry and linear sweep voltammetry [149].

The peak-shaped response of differential-pulse response measurements also results in improved resolution between two species with similar redox potential, if separated by at least 50 mV. Such a possibility depends not only upon the corresponding peak potentials but also on the peak widths. The minimum peak width at half-height, for fast electrode kinetics is given by:

$$W_{1/2} = \frac{3.52RT}{nF} \tag{1.16}$$

which corresponds to 90.1 mV for $n = 1$ (at 25 °C).

The peak-shaped response makes the technique particularly useful for analyses of mixtures. The selection of the pulse amplitude and potential scan rate usually requires a compromise between sensitivity, resolution, and speed [145,148,149]. For instance, higher pulse amplitudes result in higher and broader peaks. Pulse amplitudes of 25-50 mV, coupled with a 5 mV/s scan rate, are generally employed. Irreversible redox systems result in lower and broader current peaks compared with those for reversible systems. In addition to improvements in sensitivity and resolution, the technique can sometimes provide information about the chemical form in which the analyte appears, such as oxidation states, complexation, etc.

1.6.4 Electrochemical impedance spectroscopy (EIS)

Electrochemical impedance is the response of an electrochemical system to an applied AC potential or current; the frequency dependence of the impedance can reveal underlying chemical processes. EIS was initially applied for the determination of double-layer capacitance. It is carried out at different frequencies; that is why it is termed as impedance spectroscopy [150,151].

Applications of EIS include [152]:

(i) Interfacial processes: redox reactions at electrodes, adsorption, electrosorption, and kinetics of homogenous reactions in solution combined with redox processes.

(ii) Geometric effects: linear, spherical, cylindrical mass transfer, limited volume electrodes, porous electrodes, and determination of solution resistance.

(iii) Applications in power sources systems (batteries, fuel cells, membranes): corrosion studies, electrocatalytic reactions, self-assembly monolayers and sensors.

Electrochemical impedance is usually measured by applying a sinusoidal voltage perturbation superimposed on a fixed potential, to a working electrode and measuring the current response. The imposed perturbation can also be an applied current. The response to the applied perturbation, generally linear if the perturbation is sufficiently small, can differ in phase and amplitude from the applied signal [145].

The excitation signal is expressed as a function of time and has the form:

$$E(t) = E_0 \sin(\omega t) \tag{1.17}$$

$$I(t) = I_0 \sin(\omega t + \varphi) \tag{1.18}$$

where $E(t)$ is the potential at time t, E_0 is the amplitude of the signal, and ω is the radial frequency (expressed in radians/second) related to the frequency f (expressed in Hz):

$$\omega = 2\pi f \tag{1.19}$$

In a linear system, the response signal, $I(t)$, is shifted in phase (φ is the current-potential shift) and has a different amplitude, I_0. The impedance of the system is:

$$Z = \frac{E(t)}{I(t)} = \frac{E_0 \sin(\omega t)}{I_0 \sin(\omega t + \varphi)} = Z_0 \frac{\sin(\omega t)}{\sin(\omega t + \varphi)} \tag{1.20}$$

The impedance is expressed in terms of magnitude, Z_0, and a phase shift, φ [98, 99].

The impedance can be expressed as a complex function:

$$Z = Z' + jZ'' = |Z|\cos\varphi + j|Z|\sin\varphi \tag{1.21}$$

and the complex plane plots a representation of the imaginary part of the impedance against the real part , see **Fig. 1.18**.

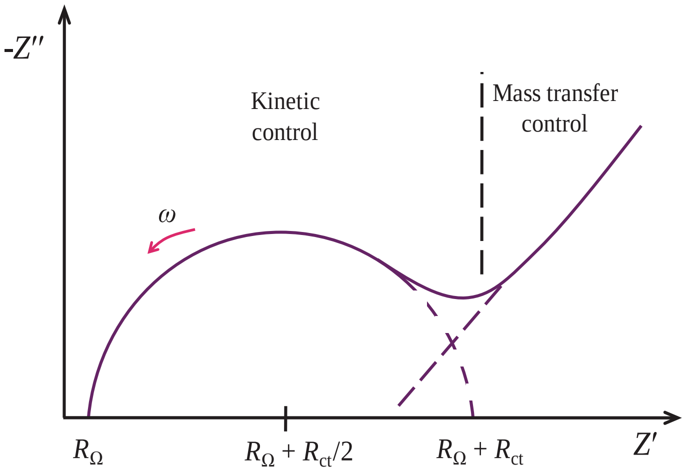

Fig. 1.18 Complex plane impedance plot of a simple electrochemical system: R + ne- → O [145].

The interpretation of the EIS measurement is often made by correlation between the impedance data and the electrochemical equivalent circuit representing the physical processes taking place in the system under investigation. For example, resistors can represent the cell resistance, R_Ω (resistance associated with the electrode material internal resistance, electrolyte solution resistance and electrode contacts), charge transfer resistance

R_{ct}, across the interface, or resistance of a film modifier. Capacitors can be correlated with the capacitance resulting from charge separation in the double layer C_{dl}, or across a surface film. Inductors, representing induced charge separation, occur at very high frequencies or in low-frequency relaxation processes [153].

All electrochemical cells can be represented in terms of an equivalent electrical circuit comprised of resistances and capacitances (inductances only for very high frequencies). Often, as in the case of this work, capacitors in EIS experiments do not behave ideally, that is, they act like a constant phase element (CPE), as defined by Eq. 1.22:

$$\mathrm{CPE} = \{(c\mathrm{i}\omega)^{\alpha}\}^{-1} \tag{1.22}$$

where C is the capacitance, ω is the frequency in rad s^{-1}, and the exponent, $0.5 < \alpha < 1$, reflects the surface non-uniformity and roughness of the modified electrodes, with $\alpha = 1$ corresponding to a complete uniform and smooth surface. A rough or porous surface can cause a capacitance to appear as a constant phase element with a value α between 0.5 and 1 [100, 101].

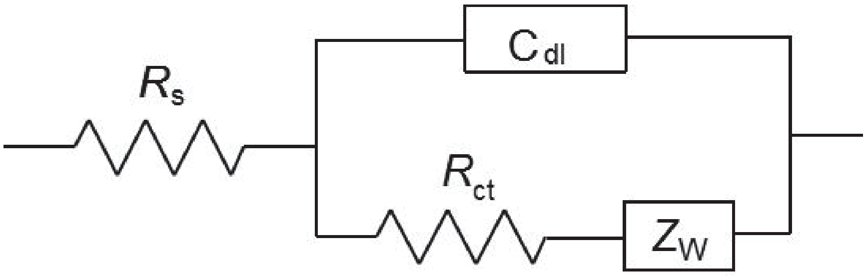

Fig. 1.19 Randles equivalent circuit for a simple charge transfer reaction

The Warburg element, Z_w, is given by $Z_w = R_D\mathrm{cth}[\tau\iota\omega)^{\alpha}]$ x $[\tau\iota\omega)^{\alpha}]$, where $\alpha < 0.5$ and is characterised by a diffusional time constant (τ), a diffusional pseudocapacitance (C_D), and a diffusional resistance ($R_D = \tau / C_D$). From the open Warburg element, the value of $\alpha_{zw} \approx 0.45$ is characteristic of a semi-infinite diffusional impedance usually found at ultrathin modified electrodes [150].

The Randles circuit, **Fig. 1.19**, is one of the simplest and most common EC models. It includes a solution resistance, R_Ω, a double layer capacitor, C_{dl} and a charge transfer or polarisation resistance, R_{ct} or R_p and a Warburg element which is used to model semi-infinite linear diffusion. In a simple situation, the Warburg element manifests itself in EIS spectra by a line with an angle of 45 degrees in the low-frequency region.

The double-layer capacity is in parallel with the impedance due to the charge transfer reaction in series with the Warburg impedance element. In addition to being a useful model, the Randles circuit model is often the starting point for other more complex models, see [150].

1.7. Electron Microscopy

An electron microscope is a type of microscope that uses a beam of electrons to create an image of the specimen. It is capable of much higher magnifications and has a greater resolving power than a light microscope, allowing it to see much smaller objects in finer detail. For topographical and morphological analysis, scanning and transmission electron microscopes have been used respectively.

1.7.1 Scanning electron microscopy (SEM)

The scanning electron microscope (SEM) uses a focused beam of high-energy electrons to generate a variety of signals at the surface of solid specimens. The signals that derive from electron-sample interactions reveal information about the sample, including external morphology (texture), chemical composition, crystalline structure and orientation of materials making up the sample. Areas ranging from approximately 1 cm to 5 μm in width can be imaged in a scanning mode using conventional SEM techniques.

When the electron is accelerated in an SEM, it carries a significant amount of kinetic energy, and this energy is dissipated as a variety of signals produced by electron-sample interactions when the incident electrons hit in the solid sample. These signals include secondary electrons, backscattered electrons, diffracted backscattered electrons, photons, visible light and heat. Secondary electrons and backscattered electrons are commonly used for imaging samples. However, secondary electrons are most valuable for showing the morphology and topography of samples, and backscattered electrons are most valuable for illustrating contrasts in elemental composition in multiphase samples. X-rays are produced by inelastic collision of the incident electrons with electrons in discrete orbital of atoms in the sample. As the excited electrons return to lower energy states, they emit X-rays of a fixed wavelength, due to the difference in energy levels of electrons in different shells for a given element [154].

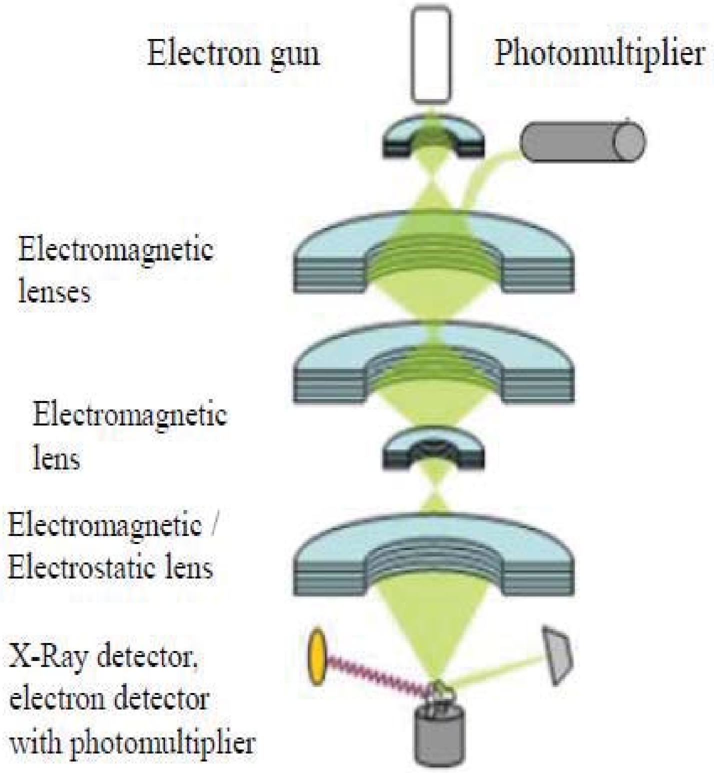

Fig. 1.20 Components of a scanning electron microscope (SEM)[155].

The column of an SEM contains an electron gun and electromagnetic lenses in such a way as to produce a very fine electron beam, which is focused on the surface of the specimen. The beam is scanned over the specimen in a series of lines and frames. Several things may happen to these electrons: (1) They may be elastically reflected from the specimen, with no loss of energy; (2) They may be absorbed by the specimen and give rise to secondary electrons of very low energy, together with X- rays; (3) They may be absorbed and give rise to the emission of visible light (cathodoluminescence), or they may give rise to electric currents within the specimen. All these effects can be used to produce an image [155,156].

By far the most common is image formation using the low-energy secondary electrons. Magnification results from the ratio of the area scanned on the specimen to the area of the image detector. Increasing the magnification in an SEM is therefore achieved by scanning the electron beam over a smaller area of the specimen.

This image formation in SEM is equally applicable to elastically scattered electrons, X-rays, or photons of visible light except that the detection systems are different in each case. Secondary electron imaging is the most common because it can be used with almost any specimen, **Fig. 1.20** shows the essential components of a scanning electron microscope.

1.7.2 Transmission electron microscopy (TEM)

Transmission electron microscopy (TEM) provides information on the atomic arrangement of atoms, due to its very higher spatial resolution (down to a few angstroms for standard microscopes). Therefore, the crystal structure of crystalline material may be accessed directly from atomically resolved TEM images, as well as, the evaluation of the size and shape of an object is also available. In TEM analysis, a high voltage (80–200 keV) focused electron beam is passed through a thin, solid sample, typically 100–200 nm in thickness, providing details about the structure's components and internal composition. Images are based on the electrons passed through the sample or primary electrons, differently from SEM in which the images are based on the electrons scattered from the sample surface or secondary electrons. Electrons can suffer coherent scattering or diffraction from lattice planes in the crystalline phase of materials, yielding phase identification [157].

The probability of scattering is described in terms of the interaction cross-section or the mean free path and can be elastic or inelastic.

The non-uniform distribution of electrons in the beam that comes out of the sample, contains all the structural information of the sample [159]. The diffracted electrons deflected away from the optical axis of the microscope are blocked using an aperture, and thus the transmitted electron beam generates a contrast on a fluorescent screen, of varying intensity. For nanomaterial analysis, the crystalline structures interact with the electron beam mainly by diffraction, rather than absorption, although the intensity of the transmitted beam depends mostly on the density and thickness of the material through which it passes.

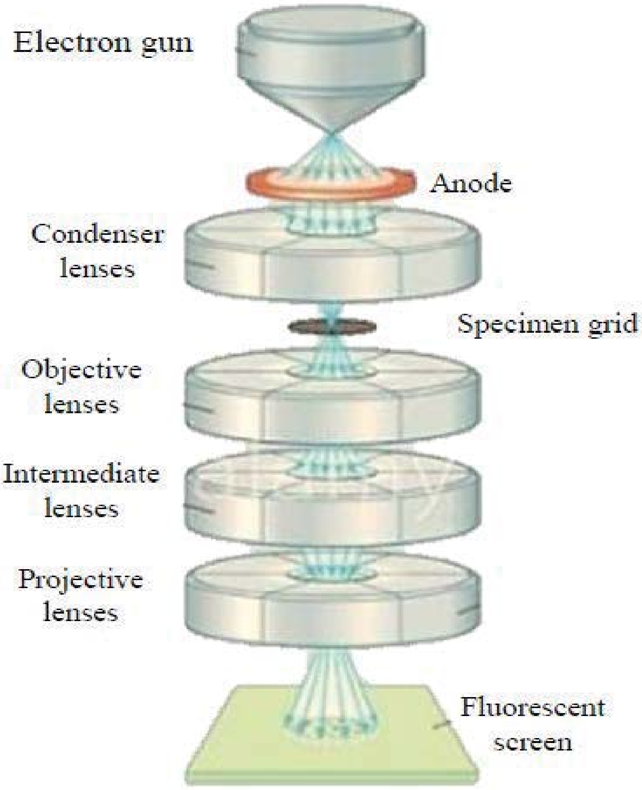

Fig. 1.21 Components of a transmission electron microscopy (TEM) [158].

The transmitted electron beam strikes the fluorescent screen and generates an image of varying contrast. The darker areas are those from which fewer electrons have been transmitted, while the areas of lower contrast display the areas in the sample which have less density or thickness, and therefore many transmitted electrons are present [158]. **Fig. 1.21** shows the layout of the various components of a transmission electron microscope.

1.8 X-ray diffraction (XRD)

Powder X-ray diffraction (XRD) is a rapid analytical technique used primarily for phase identification of a crystalline material and can provide information on unit cell dimensions. Powder X-ray diffraction is most widely used for the identification of unknown crystalline materials (e.g. minerals, inorganic compounds).

X-ray diffraction is based on constructive interference of monochromatic X-rays diffracted from the sample. These X-rays are generated by a cathode ray tube, filtered to produce monochromatic radiation, concentrated by collimation, and directed towards the sample. The interaction of the incident rays with the sample produces constructive interference (and a diffracted ray) when conditions satisfy Bragg's Law, as shown in **Fig. 1.22** [160].

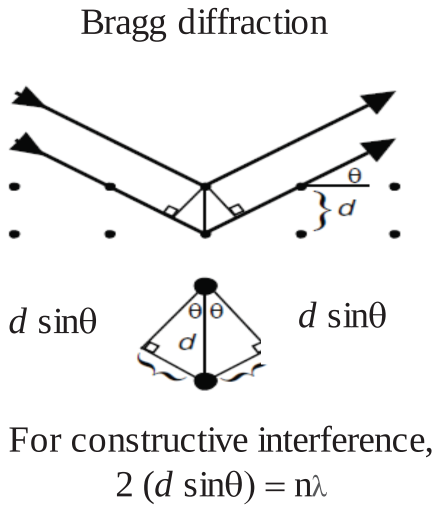

Fig. 1.22 Conditions for diffraction and derivation of Bragg's law [162].

This law relates the wavelength of electromagnetic radiation to the diffraction angle and the lattice spacing in a crystalline sample. These diffracted X-rays are then detected, processed and counted. By scanning the sample through a range of 2θ angles, all possible diffraction directions of the lattice should be attained due to the random orientation of the powdered material. Conversion of the diffraction peaks to d-spacings allows identification of the sample structure because each has a set of unique atomic spacing (d-spacings). Typically, this is achieved by comparison of d-spacings with standard reference pattern [161].

An X-ray diffractometer consists of three basic elements: an X-ray tube, a sample holder, and an X-ray detector. X-rays are generated in a cathode ray tube by heating a filament to produce electrons, accelerating the electrons toward a target by applying a voltage and bombarding the target material with electrons. When electrons have sufficient energy to dislodge inner shell electrons of the target material, characteristic X-ray spectra are produced.

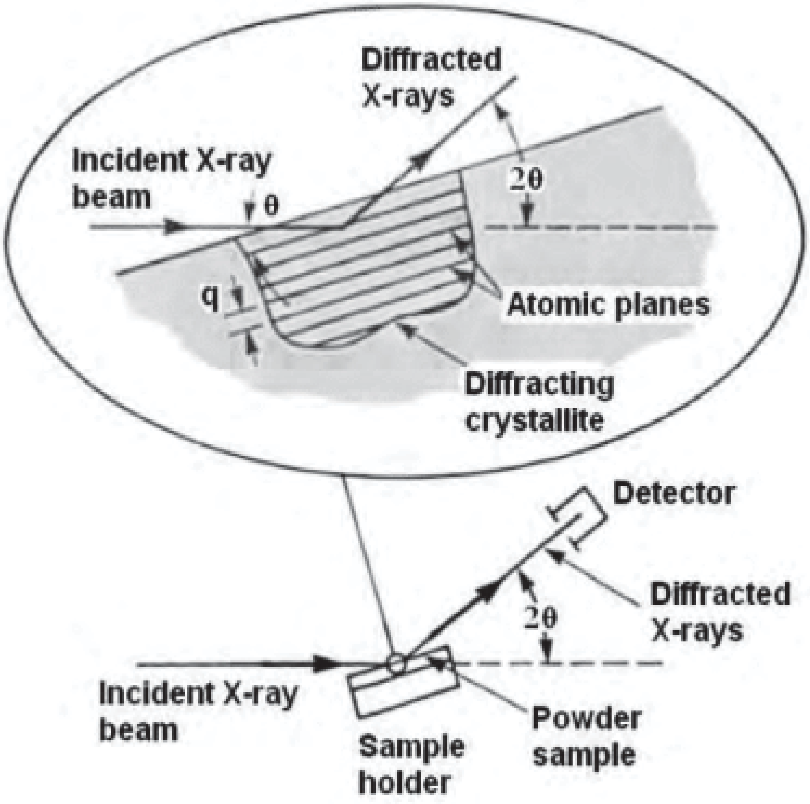

Fig. 1.23 Schematic illustration of the time-resolved X-ray spectroscopy experimental setup [163].

These spectra consist of many components, the most common being K_α and K_β. The specific wavelengths are characteristic of the target material (usually Cu, Mo, Cr, or Fe). Filtering, by foils or crystal monochromators, is necessary for obtaining monochromatic X-rays. Copper is the most common target material for single-crystal diffraction, with CuK_α radiation = 1.58 Å. As the sample and detector are rotated, the intensity of the reflected X-rays is recorded [161].

When the geometry of the incident X-rays impinging on the sample satisfies the Bragg equation, constructive interference occurs. A detector records this X-ray signal and converts the signal to a count rate. The geometry of an X-ray diffractometer is such that the sample rotates in the path of the collimated X-ray beam at an angle θ, while the X-ray detector is mounted on the arm to collect the diffracted X-rays and rotates at an angle of 2θ. For typical powder patterns, data is collected at 2θ from ~5^o to 70^o-angles that are present in the X-ray scan [164]. A typical XRD configuration is shown in **Fig. 1.23**.

This page intentionally left blank

Chapter 2

Experimental

This chapter contains information about reagents used, about the instrumentation for the electrochemical measurements and all types of the working electrodes and electrochemical cells employed. The preparation of some electrodes will be described in detail, as well as the pre-treatment and modification with redox polymers, enzymes or proteins.

2.1 Reagents and solutions

All reagents were of analytical grade and used without further purification. The reagents: Theophylline, anhydrous (purity $\geq$ 99.00 %), gold (III) chloride hydrate (purity $\geq$ 99.99 %), chitosan from crab shells, minimum 85% deacetylated, Tyramine, 99.9 %, gold (III) chloride trihydrate ($HAuCl_4 \bullet 3H_2O$), 8-anilino-1-naphthalene sulphonic acid, 97 % (ANSA). bovine serum albumin (BSA), 98 %, glutaraldehyde (GA, 25% v/v), catechol, xanthine, hypoxanthine, L-Tyrosine hydrochloride, dopamine hydrochloride, sodium hydroxide, choline chloride**,** anhydrous ethylene glycol, nitric acid (65 %), sulfuric acid (98 %), hydrochloric acid (37 %), acetic acid (99.99 %), and perchloric acid (70 %), NaH_2PO_4, $Na_2HPO_4.2H_2O$, nitric acid (65 %), hydrochloric acid (37 %), acetic acid (94.74 %), Dichlorvos PESTANAL®, analytical standard, citric acid, were all purchased from Sigma-Aldrich. Na_2HPO_4 and Sodium citrate, dehydrate (purity $\geq$ 99.00 %) were from Merck, Germany. NaH_2PO_4 and D(+) glucose were purchased from Riedel De Haën. Multi-walled carbon nanotubes (MWCNT) with ~95% purity, 30±10 nm diameter, and 1-5 μm length were from Nanolab, U.S.A. Brilliant cresyl blue dye (95 %) and Brilliant green dye (95 %) were purchased from Fluka, Switzerland. For the study of enzyme inhibition, standard 1000 mg L^{-1} solutions (Tec-Lab, Brazil) of Hg^{2+} (traceable to SRM 3133 NIST, USA), Pb^{2+} (traceable to SRM 3128 NIST, USA), Cd^{2+} (traceable to SRM 3108 NIST, USA), and Cr^{VI} (potassium dichromate from Sigma-Aldrich, Germany.

The enzyme used were: Tyrosinase (Tyr_{ase}, from mushroom, activity 2687 U mg^{-1}, CAS number: 9002-10-2), glucose oxidase (GOx, from *Aspergillus niger*, type X-S, activity 250 U mg^{-1}, CAS number: 9001-37-0), Choline oxidase (from *Arthrobacter globiformis* activity 8-20 U mg^{-1}, CAS number: 9028-67-5) were acquired from Sigma-Aldrich.

Millipore Milli-Q nanopure water (resistivity $\geq$ 18 MΩ cm) was used for the preparation of all solutions. Experiments were all performed at room temperature (25 ± 1 ºC).

2.2 Instrumentation

Cyclic voltammetry and amperometry at fixed applied potential measurements were performed at room temperature with a computer-controlled Ivium CompactStat potentiostat (version 2.024, Ivium Technologies, Netherlands) using a conventional three-electrode cell containing a glassy carbon electrode (GCE) or gold electrode AuE (both with geometric area 0.00785 cm^2) modified or not as working electrode, a platinum wire as counter electrode and an Ag/AgCl (3 M KCl) electrode was used as reference.

Electrochemical impedance measurements were carried out with a Solartron 1250 Frequency Response Analyser coupled to a Solartron 1286 Electrochemical Interface using ZPlot 2.4 software (Solartron Analytical, UK). A sinusoidal voltage perturbation of amplitude 10 mV rms was applied in the frequency range between 65 kHz and 0.1 Hz with 10 frequency steps per decade. Equivalent circuit fitting was done with ZView 3.2 software (Scribner Associates, USA).

A scanning electron microscope (SEM) (JEOL, JSM-5310, Japan) and the transmission electron microscope (TEM) (JEOL, JEM-1230, Japan) were used for morphological analysis of the nanostructures.

The pH measurements were carried out with a CRISON 2001 micropH-meter (Crison Instruments SA, Barcelona, Spain) at room temperature.

2.3 Buffer solution preparation

2.3.1 Britton-Robinson buffer (BR)

Britton-Robinson buffer (BR) is a universal pH buffer used for the range pH 2 to pH 12. Universal buffers consist of mixtures of acids of diminishing strength (increasing pK_a) so that the change in pH is approximately proportional to the amount of alkali added. The Britton-Robison (BR) buffer was prepared by mixing phosphoric acid, acetic acid and boric acid (all solutions of 0.04 M) and adjusting the pH with sodium hydroxide (0.2 M).

2.3.2 Phosphate buffer solutions (PB)

Phosphate buffer solutions (PB) is a buffer solution commonly used in biochemistry research because it is isotonic and non-toxic to biological elements such as cells, proteins and nucleic acids, etc. Phosphate buffer solutions (PB) with various pH values were prepared by mixing standard stock solutions of 0.2 M Na_2HPO_4 and 0.2 M NaH_2PO_4 and adjusting the pH with 0.1 mM hydrochloric acid or 0.1 mM sodium hydroxide.

2.4 Functionalisation of carbon nanotubes (MWCNT)

Due to the hydrophobic nature of MWCNT and the presence of some impurities obtained from the process of synthesis, its functionalisation and purification are necessary before use as a modifier. The procedure described in [165] was followed. First, an appropriate amount of MWCNT in a 5 M nitric acid aqueous solution was stirred for 24 h, in order to create defects, more edge sites and ensure a better dispersion of the carbon nanotubes by the creation of carboxylic groups. The latter refers to the creation of terminal carbons in the shortening of nanotubes, which upon oxidation are converted into carboxyl groups. Afterwards, the functionalized MWCNT were rinsed with Milli-Q water on a Millipore filter paper (0.3 μm) until a neutral pH was reached, then were collected and dried at 80 ºC overnight.

In order to ensure a stabilised and adherent MWCNT layer on the electrode surface, a dispersion of MWCNT in chitosan solution was prepared. Chitosan possesses reactive amino and hydroxyl groups; the positive amino group ensures electrostatic interaction with negative carboxyl groups of the carbon nanotubes, leading to a robust structure.

Furthermore, chitosan has a high permeation to water and ions, good mechanical strength, high film-forming ability and is an excellent matrix for biomolecule immobilisation. It has been used in enzyme biosensors as binding molecule due to the electrostatic interaction between its negative hydroxyl and positive charges of the amino groups in enzymes [166].

2.5 Preparation of gold nanoparticles (AuNP)

2.5.1 Synthesis of gold nanoparticles (AuNP) by Turkevich method

A colloidal solution of AuNP was prepared following the method described by Turkevich [167] with slight modifications. Gold nanoparticles were synthesised by reduction of $HAuCl_4{\cdot}H_2O$ with sodium citrate as follows. A volume of 200 mL of a solution of 0.01 % $HAuCl_4$ in water was brought to boiling point, to which 7.0 mL of 1.0 % sodium citrate was slowly added under stirring and left to react for 10 min. The resulting gold nanoparticle dispersion was then purified in order to remove the remaining traces of sodium citrate, and unreacted $HAuCl_4$ by centrifugation at 14,000 rpm for 20 min followed by redispersion of the precipitated solid in 200 mL of Milli-Q water.

2.5.2 Green synthesis of gold nanoparticles ($AuNP_{green}$)

The gold nanoparticles ($AuNP_{green}$) were synthesised by a green method, according to the literature [168]. First, *C. sinensis* was squeezed to extract the juice, which was then strained through a fine-mesh sieve. The filtered solution was centrifuged at 14,000 rpm for 30 min to remove all undesired impurities and to obtain a clear solution. For the synthesis of $AuNP_{green}$, 50 mL of 1 mM solution of gold (III) chloride trihydrate ($HAuCl_4.3H_2O$) was brought to boil with vigorous stirring. A volume of 5 mL of previously purified extract of *C. sinensis* was added to this solution and allowed to cool slowly. The colour changed from yellow to colourless and then to ruby red, this whole process occurring within 5 min. The colloidal solution was stirred for a further 10 min whilst cooling to room temperature. The gold nanoparticle dispersion obtained was purified by repeated centrifugation at 14,000 rpm for 20 min, followed by redispersion of the precipitated solid in 50 mL of Milli-Q water.

2.6 Preparation of AuNP-MWCNT/GCE

Different suspensions of MWCNT were prepared: 0.2, 0.5 and 1.0 w/v %. in 1% (w/v) chitosan dissolved in 1% (v/v) acetic acid and sonicated for 4 h until homogenisation. In order to prepare the AuNP-MWCNT composite, dispersions of MWCNT in chitosan (0.2, 0.5 and, 1.0 w/v %.) were mixed with equal volumes of the gold nanoparticle stock solution prepared previously, designated AuNP-MWCNT0.10, AuNP-MWCNT0.25, and AuNP-MWCNT0.50. The mixture was sonicated for 2 h and then kept at rest for 24 h before use, in order to facilitate the aggregation of gold nanoparticles in the MWCNT network. These dispersions were used for drop-casting of 2 μL on the GCE surface. AuNP/GCE and MWCNT0.25/GCE modified electrodes were also prepared by the same procedure. The modified electrodes were left to dry at room temperature for 24 h before further use.

2.7 Preparation of PANSA and AuNP$_{green}$-PANSA modified electrodes

Poly(8-anilino-1-naphthalene sulphonic acid) films were potentiodynamically electrosynthesised from a solution containing 0.1 M (anilino-1-naphthalene sulphonic acid) ANSA monomer in 0.5 M H_2SO_4. For the preparation of AuNP$_{green}$-PANSA film, a more concentrated stock solution of the monomer in a higher concentration of H_2SO_4 was prepared and this solution was mixed in a ratio of 1:3 v/v with colloidal AuNP$_{green}$ solution in order to obtain the same concentration of monomer and acid as that used for PANSA deposition. Oxygen inhibits polymer film growth; hence, in order to avoid its permeation, before polymerisation, the mixtures were degassed with N_2 for 20 min, and during polymerisation, a flux of N_2 was kept flowing on top of the cell solution. The PANSA film and AuNP$_{green}$-PANSA film were grown on bare AuE and GCE by potential cycling in the potential range 0.0 V to 1.1 V vs Ag/AgCl using 50 mV s^{-1} as scan rate for 7 cycles, as previously optimised [169]. After polymerisation, the modified electrodes were carefully rinsed with Milli-Q water for removal of unreacted monomer and dried before enzyme immobilisation. An AuNP$_{green}$/GCE and AuNP$_{green}$/AuE modified electrodes were also prepared by drop-casting 2 mL of AuNP colloidal solution on the bare and left to dry for 1 h further experiments.

2.8 Preparation of ethaline-deep eutectic solvent (DES)

Ethaline DES, consisting of a 1:2 molar ratio of choline chloride: ethylene glycol was prepared by prior heating of solid choline chloride to ~80 ºC to evaporate any water, followed by addition of ethylene glycol under stirring and heating up to 100 ºC until a homogeneous and colourless solution was obtained. After cooling down to room temperature, ethaline is ready to use for the preparation of solutions for electropolymerisation. Small amount of concentrated acids were added s doping agent to increase the rate of polymer formed.

2.9 Preparation of poly(brilliant green)(PBG) modified electrodes

PBG films were first formed in aqueous solution by potential cycling on MWCNT/GCE. The reason is that DES by itself has a low conductivity that can be made higher by increasing the ionic strength of the solution and the rate of diffusion. This can be achieved by the addition of small amounts of acid dopant to DES. Thus, the electrochemical characteristics of each type of PBG_{aq} film in the PBG/MWCNT/GCE configuration formed in aqueous medium were investigated by cyclic voltammetry and the best acid doping agent was chosen for electropolymerisation in ethaline-DES. The aqueous acid doping solutions tested were with the anions sulfate (SO_4^{2-}), nitrate (NO_3^-), chloride (Cl^-), and carboxylate (COO^-). The electropolymerisation solution contained 1.0 mM BG + 0.5 M of the acids, cycling the potential between -1.0 and 1.2 V vs. Ag/AgCl during 10 cycles at a scan rate of 50 mV s^{-1}. The best was found to be sulfuric acid.

PBG_{aq} on top of MWCNT was also prepared in an aqueous solution containing 1 mM BG in McIlvaine buffer (0.2 M disodium phosphate + 0.1M citric acid), pH 4.0 during 10 cycles at a scan rate of 150 mV s^{-1}, as in [170], which led to better film growth.

In ethaline-DES, BG was first dissolved with a concentration just above 1.0 mM in a mixture containing 10 % v/v of water : 90 % v/v ethaline, which was thoroughly stirred and sonicated in an ultrasound bath in order to completely dissolve the monomer. This was followed by the addition of a calculated volume of the concentrated sulfuric acid doping agent, to finally obtain 1.0 mM BG monomer and 0.5 M sulfuric acid, in the final mixture.

$PBG_{ethaline}$ films on MWCNT/GCE were formed by using the same potential cycling parameters as in aqueous solution; the influence of the scan rate on the formation of the films was also investigated.

2.10 Preparation of poly(brilliant cresyl blue)(PBCB) modified electrodes

PBCB films were formed in ethaline+acid in both potentiostatic and potentiodynamic mode on MWCNT/GCE, and their electrochemical behaviour was compared. A solution with a concentration just above of 0.1 mM BCB in 10 mL ethaline was prepared, to which a small volume (less than 100 μL) of different concentrated acids (HNO_3, H_2SO_4, HCl, and $HClO_4$) was added, to obtain a final concentration of 0.1 mM BCB and 0.5 M of acid.

PBCB was potentiodynamically electrodeposited on MWCNT/GCE by cycling during 30 scans in the potential range from -0.6 to +1.0 V at scan rates in the range from 50 to 200 mV s^{-1}. For comparison, PBCB was also prepared in an aqueous solution containing: 0.1 mM BCB + 0.1 M KNO_3 + 0.1 M PB (pH 7.0) at a scan rate of 50 mV s^{-1} as in [171].

PBCB films also were formed in ethaline+acid by potentiostatic mode on MWCNT/GCE. In potentiostatic electropolymerisation mode, the influence of varying the applied potential (0.8 V, 1.0 V or 1.2 V vs. Ag/AgCl), as well as the electrodeposition time (100, 300, 600, 900 s) was assessed.

PBCB films were formed in aqueous solution, $PBCB_{aq}$, with the same optimised experimental conditions as used in DES ethaline-HNO_3, in both electropolymerisation modes.

2.11 Biosensor preparation

After optimisation of the modified electrode architectures, the enzymes were immobilised on their surfaces by cross-linking, using a mixture of an optimised amount of each enzyme used with glutaraldehyde, as cross-linking agent, and BSA carrier protein. After drying, the biosensors were immersed in buffer for at least 2 h before use in order to hydrate the formed membrane and facilitate the diffusion of ionic species. When not in use, the biosensors were kept in buffer solution at 4 °C to preserve enzyme activity.

2.11.1 Biosensor for determination of tyramine (Tyr)

In order to optimise the amount of tyrosinase (Tyr_{ase}), enzyme solutions were prepared by dissolving different amounts from 0.1 to 2.0% w/v of Tyr_{ase} in 0.1 M BR buffer (pH 7.0) containing BSA (2.0% w/v). For preparation of the tyrosinase biosensors, 1 μL of the corresponding enzyme/BSA solution was mixed with 1 μL of GA (2.5% v/v) as crosslinking agent. The mixture was dropped onto the electrode surface and then left to dry for 1 h at room temperature, after which the biosensors were immersed in buffer solution (pH 7.0).

2.11.2 Biosensor for the determination of the biotoxic trace metal ions Hg^{2+}, Cd^{2+}, Pb^{2+}, and Cr^{VI} by glucose oxidase (GOx) inhibition

GOx was immobilised on the electrode surfaces by cross-linking, using a mixture of GOx with glutaraldehyde, as cross-linking agent, and BSA carrier protein. The enzyme solution was prepared by dissolving different amounts in the range 5.0 - 25 mg mL^{-1} of GOx in 0.1 M PB solution, pH 7.0. For all enzyme solutions, the same amount of BSA, 30 mg mL^{-1}, was added. For enzyme drop-coating, 1 μL of the enzyme solution containing BSA was dropped on a modified electrode surface followed by 1 μL of GA (2.5 %). The electrode assembly was left to dry for 1 h at room temperature, after which the biosensor was immersed in buffer solution (pH 7.0).

2.11.3 Nanocomposite films as enzyme electrode support for the determination of glucose and catechol

For assessing the biosensing properties of the MWCNT/GCE modified with $PBCB_{ethaline}$ films, $PBCB_{aq}$ films, and bare GCE, the enzymes, glucose oxidase (GOx) and Tyrosinase (Tyr_{ase}) were immobilised for the detection of glucose and catechol, respectively. For enzyme solution preparation, 2.0 % w/v of GOx or Tyr_{ase} was dissolved in 100 μL of 0.1 M PB solution (pH 7.0) containing BSA (2.0 % w/v). For enzyme immobilisation, 1 μL of the corresponding enzyme/BSA solution, mixed with 1 μL of GA (2.5 % v/v) as crosslinking agent, was cast on the bare or modified electrodes and then left to react at room temperature during 1h. After drying, the biosensors were immersed in PB solution (pH 7.0) for at least 2 h before use.

2.11.4 Biosensor for the determination of choline and the organophosphorus pesticide dichlorvos

Choline oxidase (ChOx) was immobilised onto the modified electrode surfaces by cross-linking with glutaraldehyde (GA) and with bovine serum albumin (BSA) as carrier protein. The enzyme solution was prepared by mixing 10 mg BSA with different amounts of ChOx, from 1.0 to 3.5 mg, in 1 mL of 0.1 M PB, pH 7.0. A volume of 1 μL of the enzyme solution containing BSA was dropped on the modified electrode surfaces, followed by dropping of 1 μL of GA (2.5 %) and was left to dry for 1 h at room temperature. The electrode assembly was left to dry for 1 h at room temperature, after which the biosensor was immersed in buffer solution (pH 7.0).

2.12. Preparation of real samples

2.12.1 Theophylline (TP)

Theophylline was measured in pharmaceutical tablets and in two types of tea (green and black tea) using the standard addition method. The samples were prepared as described below. One TP pharmaceutical tablet, labelled with 400 mg TP per tablet, was accurately weighted and grounded into powder in an agate mortar. The TP powder was dissolved in 100 mL of deionised water and used for determination. For the tea samples, 5 g of each tea was boiled in 60 mL of deionised water for 20 min in order to extract the theophylline. After filtration, the filtrate was collected and deionised water added up to a final volume of 100 mL.

2.12.2 Tyramine (Tyr)

Tyramine was measured in dairy products and fermented drinks, obtained commercially in a local supermarket. Sample preparation was as follows.

A yoghurt sample of 2.5 g was accurately weighed and diluted in 20 mL of 0.1 M BR buffer (pH 7.0). The same quantity of Roquefort cheese was weighed and treated similarly by adding the same amount of buffer; it was then homogenised until obtaining a milkylooking solution. Yoghurt and cheese dispersions were centrifuged at 14,000 rpm for 20 min and the supernatant collected and stored at 4 °C before use. A volume of 200 μL of Pilsen-type beer was degassed in an ultrasonic bath for 10 min in order to eliminate the gas and avoid the excessive formation of foam during manipulation and analysis which may compromise the measurements. The wine sample did not require any kind of preparation and was used as received without pre-treatment.

2.12.3 Trace metal ions

The determination of trace metal ions was carried out in milk samples. For this, 50 mL of milk was centrifuged at 14,000 rpm during 20 min, then the supernatants were collected, and were spiked with known amounts of Hg^{2+}, Cd^{2+}, Pb^{2+}, and Cr^{VI}. The standard addition method was used to estimate the amount of trace metal ions added in milk samples. The spiked solutions, when not in use, were kept at 4 °C.

Chapter 3

AuNP decorated MWCNT modified electrodes for the electrochemical determination of theophylline (TP)

Theophylline (TP) is a xanthine derivative commonly utilised as a clinical drug for the treatment of respiratory system diseases such as bronchial asthma and other bronchospastic conditions due to its capability of relieving bronchospasms [172]. TP induces bronchodilation and is used as an expectorant. Nevertheless, TP has to be monitored clinically to avoid serious toxicological effects because it exhibits a narrow safety range of 5-20 μg mL^{-1} (27-111 μmol L^{-1}).

This chapter describes a simpler electrode configuration which has been prepared without poly-L-lysine or another aggregation agent, consisting of gold nanoparticles, prepared by the Turkevich method (see Chapter 2, Section 2.5.1), dispersed in a multi-walled carbon nanotube-chitosan network, deposited in one step on a glassy carbon electrode substrate. Cyclic voltammetry (CV) and electrochemical impedance spectroscopy (EIS) were used for characterisation of the modified electrode and differential pulse voltammetry (DPV) for analytical determination of TP. The morphology and distribution of the nanostructures were examined by surface characterisation with transmission and scanning electron microscopy. Optimisation of the parameters influencing theophylline´s analytical determination is discussed, and application to commercial drug and tea samples is demonstrated.

The work described in this chapter has been published in reference [173], (Analytical Methods, 10 (2018) 5634-5642).

3.1. Morphological characterisation of nanostructures

The size, shape, and distribution of the AuNP, prepared by the Turkevich method (see Chapter 2), were visualized by SEM, and the aggregation of the nanoparticles on the carbon nanotube network was also verified by SEM and TEM. The SEM image of the AuNP, **Fig. 3.1A** shows nanoparticles with excellent dispersibility and also exhibiting a homogeneous surface and uniform spherical morphology.

The controlled size of the nanoparticles plays an important role as they are able to significantly enhance the electrical conductivity of the nanocomposite as compared with non-dispersed or non-homogenous nanoparticles [174]. The size distribution of the AuNP was analysed by ImageJ open source particle analysis software, in which 500 discreet nanoparticles were used as sample space. From the particle size Gaussian distribution curve, **Fig. 3.1B**, the average size of the AuNP was calculated as 18.6 ± 0.5 nm. SEM and TEM were also used to confirm the formation of the nanocomposite and for evaluating the dispersion of AuNP on the MWCNT network, **Fig. 3.1C** and **3.1D**. AuNP are well distributed in the MWCNT network with nanoparticles attached to the walls of the carbon nanotubes in a compact way, **Fig. 3.1C**.

This proves the formation of the nanocomposite and shows that the new methodology for depositing nanoparticles on carbon nanotube networks was successfully performed. **Fig. 3.1E** shows cyclic voltammetry with the modified AuNP-MWCNT$_{0.25}$/GCE in acidic media which also confirmed the presence of gold on the carbon nanotubes. A small oxidation peak, II_a, is observed, which can be ascribed to gold oxide formation. The corresponding reduction peak is coincident with that of the MWCNT reduction peak I_c.

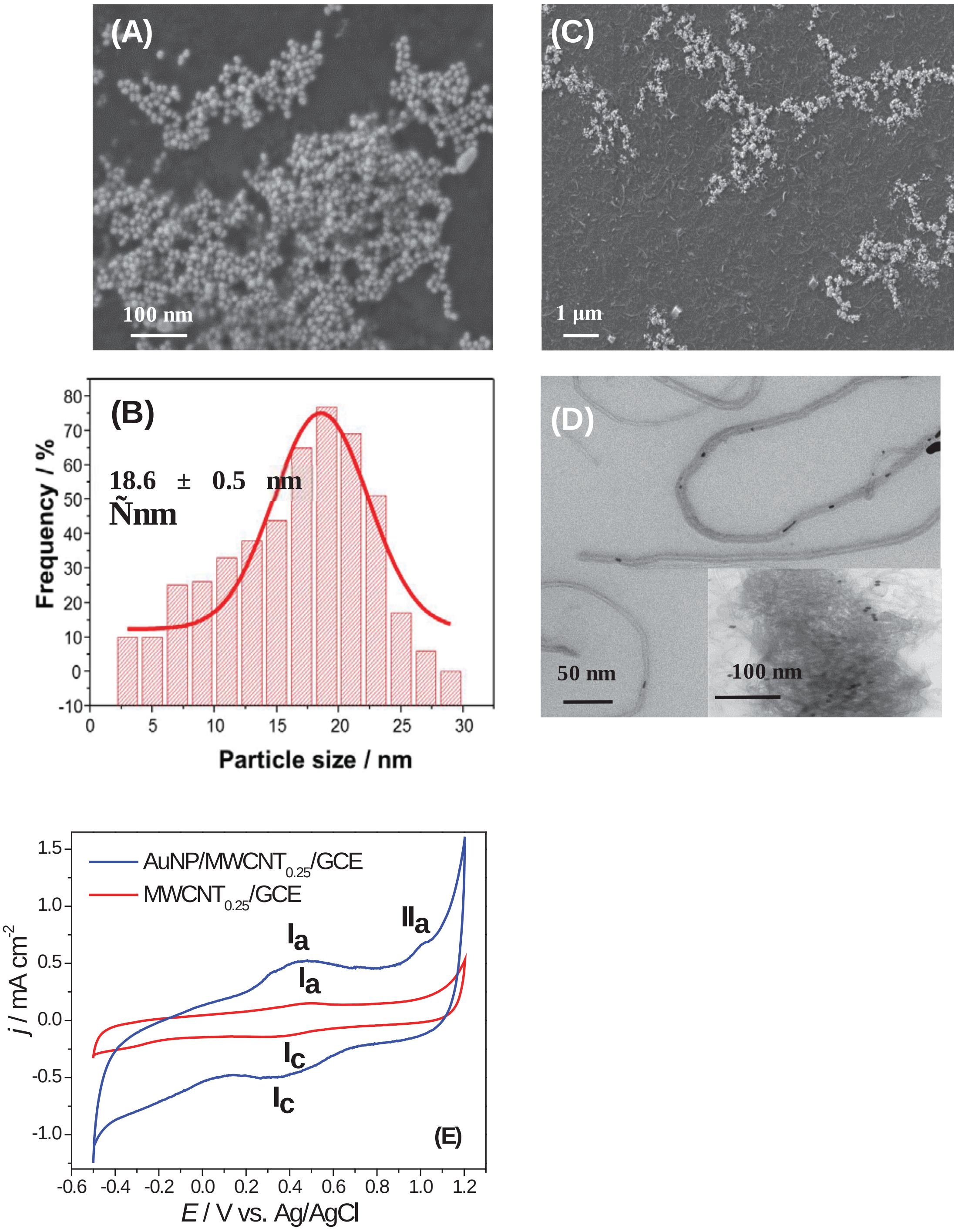

Fig. 3.1(A) SEM image of the morphology of AuNP synthesized and stabilized by sodium citrate; **(B)** Size distribution histogram of the AuNP diameter; **(C)** SEM image of MWCNT decorated by AuNP; **(D)** TEM image of individual MWCNT decorated by AuNP; inset shows network of decorated MWCNT.; **(E)** CV at (blue) AuNP-MWCNT$_{0.25}$/GCE and (red) MWCT$_{0.25}$/GCE in 0.1 M H_2SO_4. Scan rate 100 mV s^{-1}.

3.2. Electrochemical characterisation of the modified electrodes

3.2.1 Cyclic Voltammetry

Fig. 3.2 shows cyclic voltammograms at modified and unmodified GCE in 250 µM TP prepared in 0.1 M BR buffer (pH 6.0) in the potential range of +0.5 - +1.4 V, at a scan rate of 100 mV s^{-1}. One oxidation peak appears at +1.11 V for GCE and AuNP/GCE, at +1.05 V for $MWCNT_{0.25}$/GCE and at +0.98 V for AuNP-$MWCNT_{0.25}$/GCE and there is no reduction peak on the reverse scan, indicating that the oxidation process of TP at bare and modified electrodes is irreversible. Thus, the potential shifts 130 mV to a less positive value, corresponding to a significant electrocatalytic effect at AuNP-$MWCNT_{0.25}$/GCE, accompanied by a peak current enhancement compared with bare GCE.

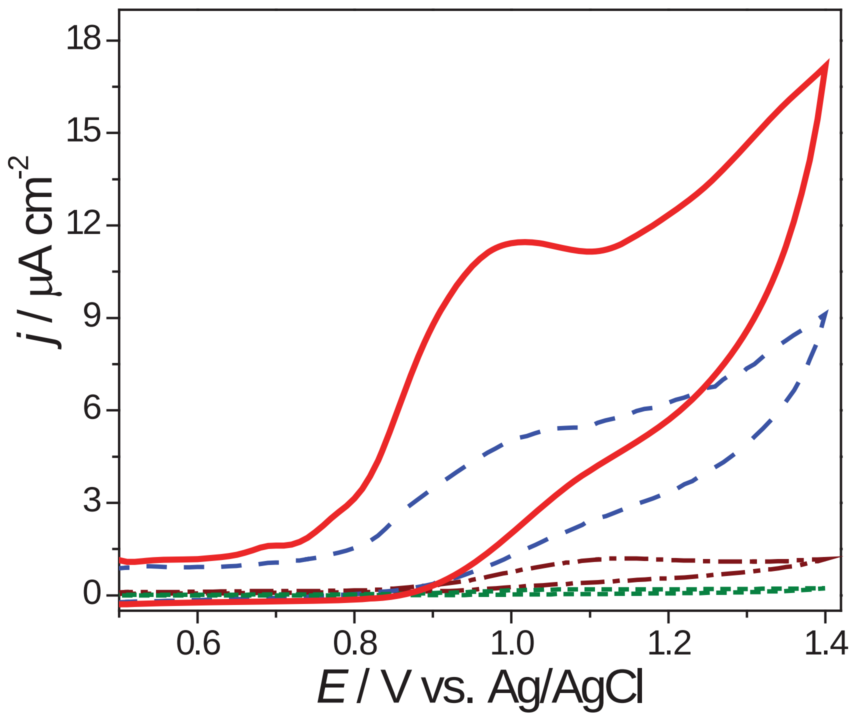

Fig. 3.2. Cyclic voltammograms for the oxidation of 250 µM TP at different electrode assemblies: (- - -) GCE; (– – –) AuNP/GCE; (– – –) $MWCNT_{0.25}$/GCE; (——) AuNP-$MWCNT_{0.25}$/GCE in 0.1 M BR buffer (pH 6.0) at a scan rate of 100 mV s^{-1}.

At AuNP-MWCNT$_{0.25}$/GCE, the response to TP increased by a factor of 60 compared with a bare electrode, while at MWCNT$_{0.25}$/GCE and AuNP/GCE the increase was much less, of 19 and 6 times, respectively. The peak shift is clear evidence of the electrocatalytic effect towards TP oxidation, which may be partly attributed to some oxygen-containing groups on the MWCNT surface (introduced during functionalisation in acid media) [175,176] and by the addition of the gold nanoparticles. The high effective electrostatic interaction promoted between TP and surface modified electrode greatly contributes to the observed electrocatalytic effect. The additional increase of the electroactive area and in conductivity on introducing AuNP explains the increased current.

The increase in the background current at AuNP-MWCNT$_{0.25}$/GCE implies that the effective surface area increases significantly after modification in comparison with the other electrode assemblies studied. It was verified that, in the second sweep, the peak current decreased significantly and this is associated with adsorption of TP´soxidation product at the electrode surface.

3.2.2 Electrochemical Impedance Spectroscopy (EIS)

Electrochemical impedance spectroscopy was used to characterise the physical and interfacial properties of the different modified electrodes, **Fig. 3.3A**. The spectra were recorded at bare GCE, AuNP/GCE, MWCNT$_{0.25}$/GCE, AuNP-MWCNT$_{0.25}$/GCE, in the presence of 250 μM TP prepared in BR buffer solution, pH 6.0 at +1.0 V *vs.* Ag/AgCl. As can be seen, all spectra had the shape of part of a semicircle and were fitted with the same electrical circuit, except for that of bare electrodes, which was simpler. The circuit used to fit all the spectra, except for bare electrodes, is that illustrated in **Fig. 3.3B**. It consists of a cell resistance (R_{Ω}) in series with two parallel combinations, one containing a constant phase element (CPE) and a resistance (R) and the other the same, but except that instead of a CPE a capacitor (C) was used. For high frequencies, the constant phase element and resistance are associated with the process occurring at the interface electrode/modifier film and inside the modifier film, CPE$_{\mathrm{f}}$ and R_{f}, respectively. For low frequencies, the capacitor and resistance describe the modifier film/solution interface and correspond to the double layer capacitance C_{dl} and charge transfer resistance, R_{ct}, respectively. For bare electrodes only, one parallel combination was used in series with R_{Ω}, describing solely the interface of the electrode with solution.

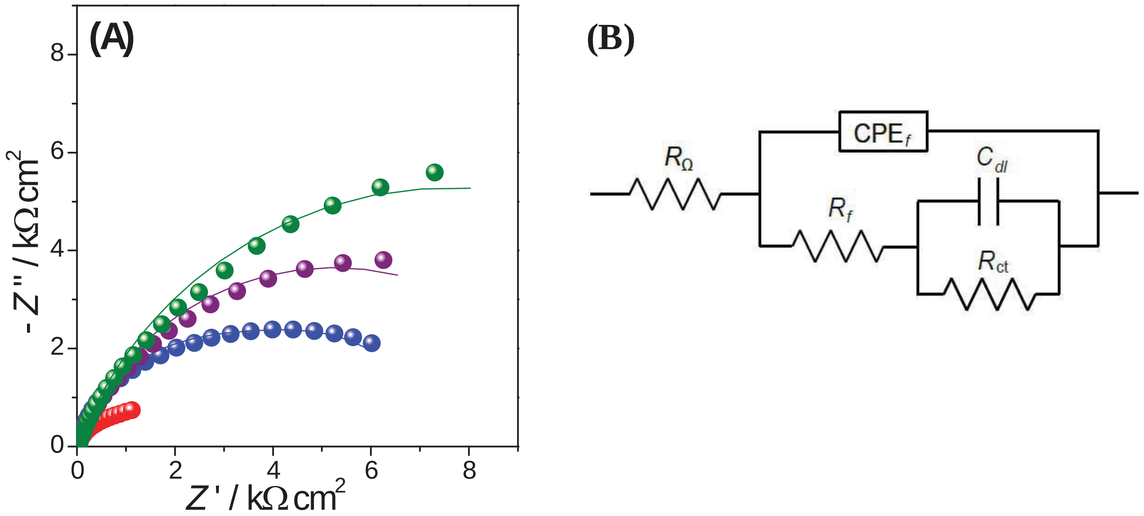

Fig. 3.3(A) Electrochemical impedance spectra at: (•) GCE, (•) AuNP/GCE, (•) MWCNT$_{0.25}$/GCE and (•) AuNP-MWCNT$_{0.25}$/GCE in the presence of 250 μM TP in BR pH 6.0 at +1.0 V *vs.* Ag/AgCl. **(B)** Equivalent electrical circuit used for fitting the impedance spectra.

The cell resistance is ~16 Ω cm^2 in all cases, and for bare electrodes R_{ct} = 15.5 kΩ cm^2, C_{dl} = 312 μF cm^{-2} s$^{\alpha-1}$ and α = 0.77; for modified electrodes the parameter values are shown in **Table 3.1**. For all modified electrodes, there is a big decrease in charge transfer resistance values compared with bare electrodes, attributed to easier electron transfer as well as increased surface area; they follow the order R_{ct}(GCE) > R_{ct}(AuNP/GCE) > R_{ct}(MWCNT$_{0.25}$/GCE) > R_{ct}(AuNP-MWCNT$_{0.25}$/GCE), showing that the fastest electron exchange occurs at AuNP-MWCNT$_{0.25}$/GCE. This is in agreement with the CV experiments, in which the sensor prepared with AuNP-MWCNT$_{0.25}$ modified GCE presented the best performance for theophylline measurement.

Table 3.1. Equivalent circuit element values obtained by fitting of the impedance spectra from **Fig. 3.3** for different electrode configurations.

Electrode configuration	R_f / kΩ cm^2	C_f / μF cm^{-2} s$^{\alpha-1}$	α_f	R_{ct} / kΩ cm^2	C_{dl} / mF cm^{-2}
AuNP/GCE	7.28	330	0.82	2.66	1.08
MWCNT$_{0.25}$/GCE	5.35	437	0.85	1.93	2.58
AuNP-MWCNT$_{0.25}$/GCE	1.33	1190	0.85	1.04	6.00

The R_{ct} decrease is accompanied by an increase in C_{dl}, due to a greater charge separation at modified electrodes. Regarding the film capacitance, its values increase with each modification of the electrode, reaching a maximum at AuNP-MWCNT$_{0.25}$, showing the highest charge accumulation at this electrode assembly. On the contrary, the film resistance decreases, indicating a lower polarisation at AuNP-MWCNT$_{0.25}$/GCE. The value of the exponent α increases with modification, indicating a smoother surface compared with bare electrodes.

3.3. Electrochemical behaviour of theophylline at modified-electrodes

3.3.1. Effect of scan rate

The electrochemical behaviour of 250 μM TP in BR buffer (pH 6.0) at GCE modified with AuNP-MWCNT$_{0.25}$ was investigated by cyclic voltammetry at different scan rates, **Fig. 3.4A**. There is a linear relationship between peak current and scan rate, v, between 5 and 100 mV s^{-1} (not shown), indicating a surface-confined process [146] expressed by:

$$I_p\ (\mu A) = 38.2\ v^{1/2} - 0.48 \qquad r = 0.9976 \qquad (3.1)$$

In addition, a plot of log I_p versus log v (Fig. 3.4 B), is linear according to:

$$\log I_p = 1.06 \log v + 3.05 \qquad r = 0.9989 \qquad (3.2)$$

The slope of 1.06 is close to the theoretically expected value of 1.0 attributed to a purely adsorption controlled process [146].

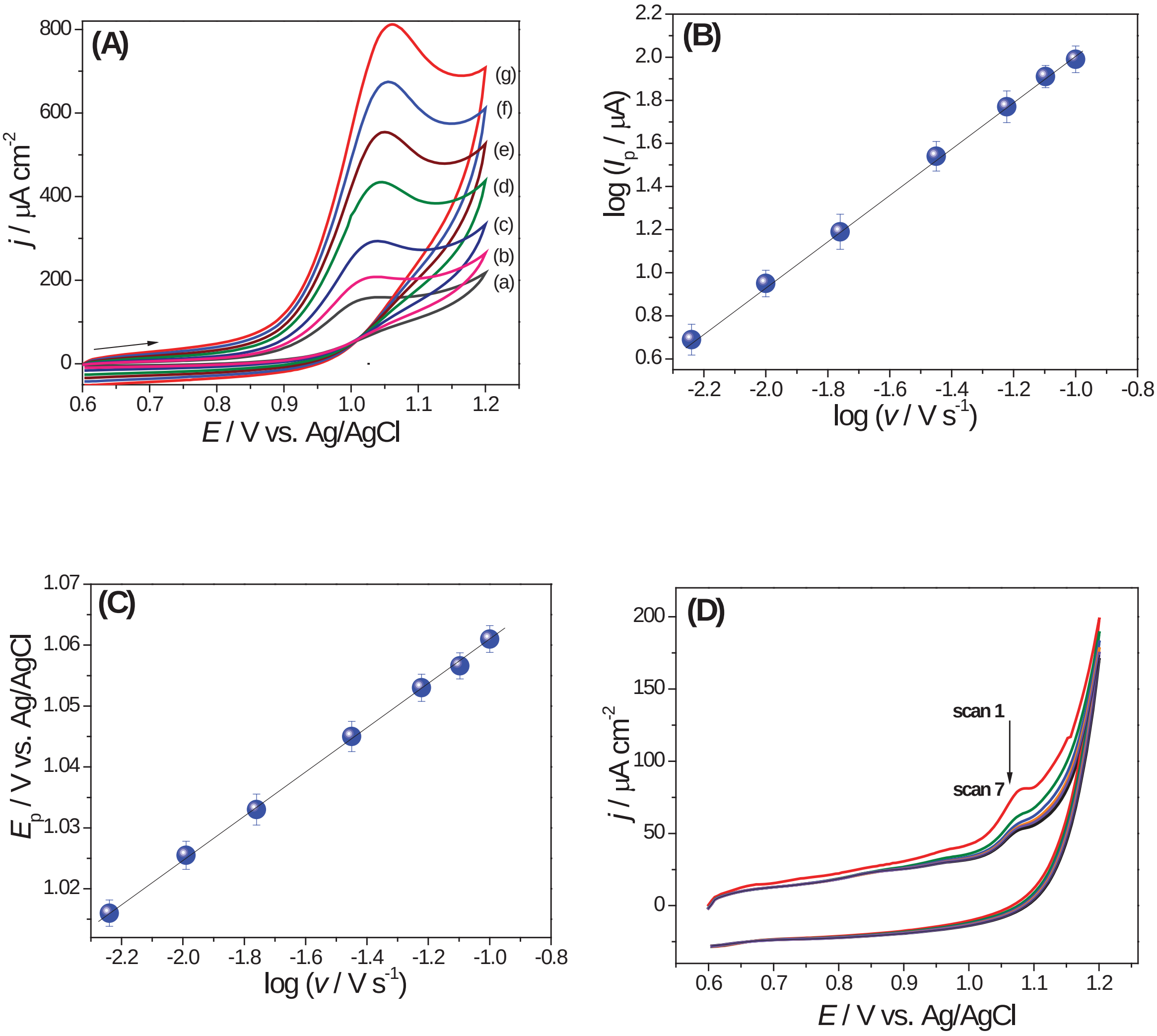

Fig. 3.4 (A) Cyclic voltammograms for the oxidation of 250 μM TP at AuNP-MWCNT$_{0.25}$/GCE at different scan rates: (a) 5; (b) 10; (c) 20; (d) 40; (e) 60; (f) 80; (g) 100 mV s^{-1}. Influence of logarithm of scan rate on the **(B)** logarithm of peak current and **(C)** peak potential. **(D)** Consecutive cyclic voltammograms at AuNP-MWCNT$_{0.25}$/GCE with 50 μM TP in 0.1 M BR buffer solution, pH 6.0, at a scan rate of 100 mV s^{-1}.

The adsorption of TP at AuNP-MWCNT$_{0.25}$ was also experimentally verified by cyclic voltammetry, **Fig 3.4D**, when performing consecutive scans in which a gradual decrease of peak current with the number of scans was observed. After carrying out CV in the presence of TP, the modified electrode was cycled in buffer solution without TP and the peak corresponding to TP was seen, also indicating adsorption at the modified electrode.

3.3.2 Influence of pH

The effect of solution pH on the oxidation of TP was investigated by DPV in the pH range from 4.0 to 9.0, **Fig. 3.5 A**.

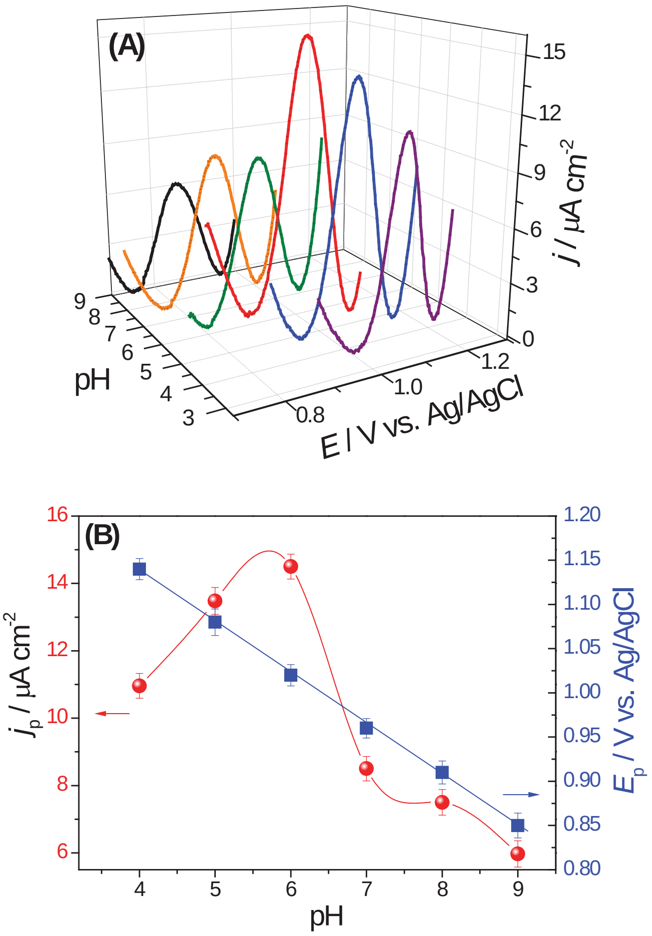

Fig. 3.5 (A) Differential pulse voltammograms of 5 µM TP at AuNP-MWCNT$_{0.25}$/GCE in BR buffer at different pH values; recorded at 5 mVs^{-1}. Amplitude 10 mV, step potential 2 mV, pulse time 10 ms. **(B)** Effect of pH on the TP oxidation peak current and peak potential.

There was an increase of oxidation peak current from pH 4.0 to 6.0, followed by a decrease from pH 6.0 to 9.0, **Fig. 3.5B**.

An explanation of this behaviour is the following. In the pH range investigated, TP molecules in the solution are mostly protonated (pK_a = 8.8) [177] and the surface of the modified electrode is rich in negative charges from AuNP, as well as from carboxyl groups from MWCNT. With the increase of pH, the extent of positive charge on TP is decreasing, leading to a decrease in the effective electrostatic interaction between the TP and the modified electrode. This causes a drop in the peak current at higher pH values [178]. In light of these results, pH 6.0 was selected as the optimum pH value for TP determination. With increasing solution pH from 4.0 to 9.0, the oxidation peak potential ($E_{p,a}$) shifted negatively and linearly, according to the equation: E/V = 1.37 – 0.058 pH (r = 0.9991) with a slope of ≅ 58 mV pH^{-1}, indicating an equal number of protons and electrons participating in the oxidation process.

3.3.3 Oxidation mechanism

The electrode reaction was irreversible, as revealed by the lack of reduction peak in the cyclic voltammograms as well as by the peak potential shifting to positive values with increasing scan rate. There was a linear dependence between peak potential and logarithm of scan rate, **Fig. 3.4C**, according to:

$$E_{p,a} = 0.036 \log v + 1.09 \qquad r = 0.9956 \quad (3)$$

Since the oxidation reaction of TP is an irreversible process, Laviron’s equation [179]', gives the slope of the plot as $2.303RT/(\alpha_a nF)$ where R is the gas universal constant, T the temperature in K, α_a is the anodic charge transfer coefficient, n the number of electrons transferred, and F the Faraday constant. At 25 ºC, the value of $\alpha_a n$ was calculated to be 1.15. It can thus be inferred that the number of electrons is 2, with α_a 0.58, in agreement with [177,180–184].

A possible mechanism for protonated TP oxidation at the pH values used here is given in **Fig. 3.6** [184].

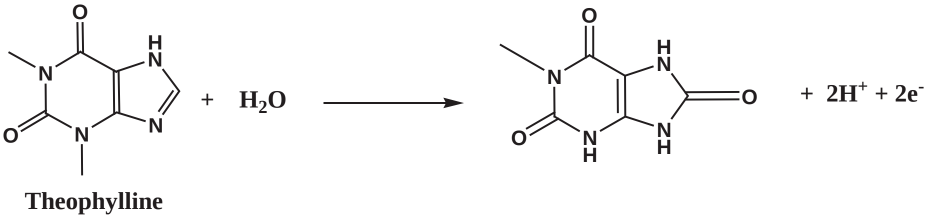

Fig. 3.6 Possible reaction mechanism for electro-oxidation of TP [184].

The proposed mechanism involves a 2-electron and 2-proton oxidation of an aromatic carbon sandwiched between electron-withdrawing nitrogen heteroatoms, as is the case of the structurally similar guanine. Therefore, the formation of the carbonyl moiety is most likely [185].

3.4. Electrochemical determination of TP at AuNP-MWCNT/GCE

The electrochemical detection of TP was carried out by DPV, which exhibits a higher sensitivity for analytical measurements than CV, and with a lower background current. Based on previous optimisation, a BR buffer solution of pH 6.0 was selected as the supporting electrolyte for the quantification of TP.

It is well known that the oxidation product of theophylline has a very strong tendency to adsorb, passivating the electrode surface. It has been suggested that pre-concentration of the analyte can overcome this problem [182,186–188]. Thus, experiments involving pre-concentration were performed, with a view to enhancing the sensitivity, decreasing the detection limit and avoiding problems arising from product adsorption. Accumulation was done at potential values in the range from +0.3 to +1.2 V during 200 s, in intervals of 0.1 V and for accumulation times of 20, 50, 60, 80, 100, 120, 150, 200, 210 and 250 s. A maximum peak current was found for an accumulation potential of +0.7 V. It is at this potential that probably enough species are attracted to the electrode surface, as observed from **Fig. 3.2 and 3.4(A)**; this is the potential where oxidation begins.

This potential ensures the maximum energy necessary for greater electrostatic interaction between the positive charges of the TP and the negatively charged carboxyl groups on the carbon nanotubes, which were introduced during acidic functionalisation. The effect of accumulation time on TP oxidation showed an increase in the oxidation peak current up to 200 s; above this time no additional increase was observed. Thus, 200 s was taken as the optimum value and used in further experiments.

The performance of AuNP-MWCNT modified glassy carbon electrodes was investigated by using different loadings of MWCNT in the dispersion solution with AuNP. The determination of TP at these different electrode configurations is presented in **Table 3.2**.

Table 3.2 Analytical parameters for determination of TP at different electrode assemblies in BR buffer solution, pH 6.

Electrode configuration	Linear range / μM	Sensitivity / μA cm^{-2} $μM^{-1}$	LOD / μM
GCE	0.5-6.0	0.48	0.50
AuNP-$MWCNT_{0.10}$/GCE	0.5-10	0.32	0.27
AuNP-$MWCNT_{0.25}$/GCE	0.5-20	1.32	0.09
AuNP-$MWCNT_{0.50}$/GCE	2.0-20	1.79	0.36

The sensitivity increased with increase in MWCNT concentration, the highest sensitivity being achieved at AuNP-$MWCNT_{0.50}$/GCE. However, this electrode presented the narrowest linear range and the highest limit of detection, LOD = 3.3(SD/slope) [21], about 4 times higher than that obtained at AuNP-$MWCNT_{0.25}$/GCE. This is probably due to a diffusion barrier caused by increased film thickness. The widest linear range and the lowest detection limit were attained at AuNP-$MWCNT_{0.25}$/GCE. This electrode also exhibited the second highest sensitivity. Taking into account the results obtained, this last configuration was chosen as optimum for further studies.

Differential pulse voltammograms obtained with increasing TP concentrations at AuNP-$MWCNT_{0.25}$/GCE are shown in **Fig. 3.7**.

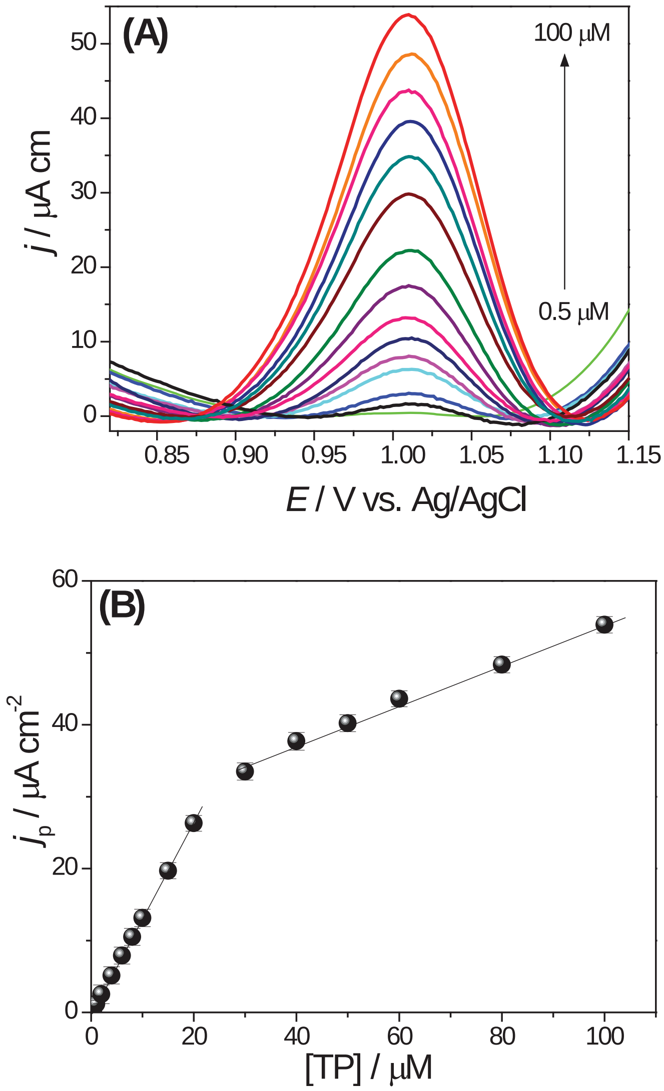

Fig. 3.7 (A) Differential pulse voltammograms at AuNP-MWCNT$_{0.25}$/GCE in BR, pH 6.0 containing different concentrations of TP, recorded at 5 mVs^{-1}. Amplitude 10 mV, step potential 2 mV, pulse time 10 ms. **(B)** Plot for variation of concentration of theophylline and peak current for the oxidation of TP.

The oxidation peak current increased linearly with theophylline concentration in the ranges of 0.5–20 μM and 30-40 μM with a detection limit of 90 nM determined from the first linear range. The equations for the linear range were j_p (μA cm^{-2}) = 1.32 C - 0.12 (r^2 = 0.999, C is in μM) and j_p (μA cm^{-2}) = 0.28 C + 25.89 (r^2 = 0.997, C is in μM).

Table 3.3. Comparison of the TP determination performance of AuNP-MWCNT$_{0.25}$/GCE with other electrode configurations

Modified electrode configuration	Technique	Peak potential / V	pH	E_{acc} / V; t_{acc} / s	Linear range / µM	Sensitivity / µA cm^{-2} µM^{-1}	LOD / nM	Ref
MWCNT-CPE	DPV	1.20 (Ag/AgCl)	3.0	OCP; 10	2.0-150	*	20	[183]
MWCNT-IL/GCE	DPV	0.83 (Ag/AgCl)	7.0	-	0.5-98	*	160	[189]
MWCNT/AuNP/PLL/SPE	SWV	0.98 (SPE)	7.5	-	10-200	*	2000	[190]
MWCNT/GCE	CV	1.08 (SCE)	5.8	OCP; 120	0.3-10	*	50	[180]
PAV3B/MWCNT/Gr/GCE	DPV	1.15 (SCE)	4.5	-	0.5-120	6.56	20	[191]
MnO$_2$/MWCNT/GCE	DPV	1.05 (SCE)	6.0	-	0.1-20	66.2	10	[192]
AT-AuNP/GCE	DPV	1.07 (Ag/AgCl)	6.0	-	20-240	0.38	-	[193]
PtNP/MWCNT-IL/GCE	CV	1.1 (SCE)	3.0	OCP, 120	0.01-10	46.1	8	[194]
PCys/N-CNT/GCE	DPV	1.17 (SCE)	1.7	-	0.1-70	1.23	33	[195]
MnO$_2$-IL-Gr/GCE	DPV	1.1 (Ag/AgCl)	5.0	-	1.0-10	*	100	[196]
PFA/Gr/GCE	DPV	1.18 (SCE)	4.5	-	0.2-10	4.84	30	[197]
AuNP-MWCNT$_{0.25}$/GCE	DPV	0.98 (Ag/AgCl)	6.0	+0.7; 200	0.5-20	1.32	90	This work

CPE-carbon paste electrode, SPE-screen printed electrode, PLL-poly-L-lysine, PAV3B-poly(Alizarin Violet 3B); Gr-graphene, AT-aminotriazole, IL-ionic liquid,PtNP-platinum nanoparticles; PCys-poly(cysteine); N-CNT- N-doped carbon nanotubes; PFA-poly(folic acid)*- no electrode area specified

In the second range, a decrease of the sensitivity (slope) was observed due to kinetic limitations, which may be attributed to the adsorption of TP´s oxidation product on the electrode surface [189].

A comparison of the proposed electrode configuration for TP determination with other similar electrochemical platforms [182,183,198,190–197] using voltammetric techniques is given in **Table 3.3**. It can be seen that the new method for preparation of AuNP-MWCNT modified GCE offered a reasonable linear range for TP determination and the low detection limit is comparable with others or even smaller and especially much smaller than the 2.0 μM achieved at similar architecture electrode with carbon nanotubes and gold nanoparticles plus poly-L-lysine [190]. Furthermore, the proposed sensor offers several advantages compared with other modified electrodes for TP determination, especially less complex architecture and rapid preparation, and lower detection potential. There is only one report of a lower potential than here [198], but it required an ionic liquid.

3.5 Determination of TP in commercial samples

In order to investigate the applicability of the proposed method, the AuNP-MWCNT$_{0.25}$/GCE was used for TP determination in commercial samples of TP tablets, green tea and black tea purchased from local market and used for quantitative analysis after preparation as described in Chapter 2, Section 2.12. Each sample was measured in triplicate, using the standard addition method, and the results are summarised in **Table 3.4**.

Table 3.4 Determination of TP in commercial samples

Samples	Original (μM)	Added (μM)	Found (μM)	Recovery (%)
TP tablets	2.26	1.00	3.39	104.0 ± 6.0
Black tea	1.37	1.00	2.40	101.3 ± 4.0
Green tea	1.13	1.00	2.18	102.3 ± 5.0

The quantity of theophylline found in the original samples is given as the value obtained in the cell after dilution; in case of the teas a 1:20 and for the tablet a 1:10000 dilution was necessary. From the results in **Table 3.4**, the detected content of TP was calculated as 407 mg per tablet (*n* =3), which is 101.7 % of the labelled value (400 mg per tablet). The concentration of TP in the green tea and black tea were calculated as 4.07 and 5.93 mg L^{-1} respectively, which is comparable with values found in the literature [186,187]. The recoveries were in the range of 101.3 % to 104.0 % with RSD less than 10 %, which clearly indicates the applicability and reliability of the proposed method.

3.6 Interferences

Under the optimum experimental conditions, the effect of potential interferents on the DPV response of 250 μM TP was evaluated by measuring the peak current corresponding to TP oxidation in the absence and presence of foreign species. The results are listed in **Table 3.5**.

Table 3.5 Influence of potential interferents on the voltammetric response to 250 μM TP in BR buffer solution, pH 6.0.

Interferents	Ratio [Interferent: TP]	Signal Change / %
Glucose	50:1	+ 3.1
Xanthine	50:1	- 6.1
Hydroquinone	50:1	- 8.1
Sucrose	50:1	+ 1.1
Zn^{2+}	100:1	- 3.1
Mg^{2+}	100:1	+ 4.3
K^{+}	100:1	+ 4.9
SO_4^{2-}	100:1	- 5.8

It was found that 50-fold higher concentrations of glucose, xanthine, hydroquinone, sucrose and 100-fold of Zn^{2+}, Mg^{2+}, K^+, SO_4^{2-}, do not interfere with the oxidation signal of TP (signal change less than 8 %) in agreement with the literature [181,192].

3.7 Repeatability, stability and selectivity at AuNP-MWCNT/GCE

The repeatability of the AuNP-$MWCNT_{0.25}$/GCE electrode was investigated by measuring the response to 250 μM TP in BR, pH 6.0; the RSD was 3.9 % with 20 successive measurements. The long-term stability of the electrode was investigated by recording its response to 250 μM TP over 45 days. When not in use, the electrode was stored at room temperature in a dark environment. After 45 days, the current response of the sensor remained at 92 % (3 sensors), which is better than that achieved in [183,184].

The results above revealed high stability and a good reproducibility and repeatability of AuNP-$MWCNT_{0.25}$/GCE for TP determination.

3.8 Conclusions

An electrochemical sensor for the rapid and sensitive determination of theophylline was constructed, consisting of gold nanoparticles (AuNP) decorated multi-walled carbon nanotubes (MWCNT) modified glassy carbon electrode (GCE). Morphological studies revealed that the synthesised gold nanoparticles exhibit excellent dispersibility and homogenous surface and uniform spherical morphology. Furthermore, a network-like structure of MWCNT with the presence of AuNP located over its surface was observed. Under optimal conditions, the proposed electrochemical sensor (AuNP-MWCNT/GCE) exhibited good promotion of the electrochemical oxidation of TP. The oxidation peak current of TP was linearly proportional to concentration in the range 0.5–20 mM and the limit of detection (LoD) was estimated to be 90 nM. The developed method showed good reproducibility and excellent selectivity. Furthermore, the sensor was successfully applied to the determination of TP in pharmaceutical tablets and tea samples with excellent recoveries.

This page intentionally left blank

Chapter 4

Impedimetric sensor and enzyme-based biosensor based on green gold nanoparticles doped poly (8-anilino-1-naphthalene sulphonic acid) modified electrodes for tyramine determination

Tyramine (Tyr) is a well-known biogenic amine produced by the decarboxylation of the amino acid tyrosine, which occurs by degradation resulting from microbial activity. It is often found in fermented foods and beverages, meat, fish, seafood and dairy products. Tyr is an indirectly-acting sympathomimetic amine which releases norepinephrine from a sympathetic nerve ending, and it has been reported that Tyr-containing foods can cause unnatural and toxic effects when ingested in large quantities[199,200]. Thus, its control and monitoring have gained attention in food safety protocols.

This chapter describes the development of two novel electrochemical approaches, namely, an impedimetric sensor and an enzyme-based biosensor for monitoring tyramine in food samples. The impedimetric sensor configuration consisted of electrodeposited poly(8-anilino-1-naphthalene sulphonic acid) (PANSA) films together with attached gold nanoparticles ($AuNP_{green}$), made by a green synthetic procedure (see Chapter 2, Section 2), on gold electrodes (AuE) by polymerisation of the monomer in the presence of $AuNP_{green}$.

The biosensor architecture is based on tyrosinase (Tyr_{ase}) immobilised on a glassy carbon electrode (GCE) modified by $AuNP_{green}$/PANSA nanocomposite films. Their characterisation and optimisation were done using X-ray diffraction (XRD), scanning electron microscopy (SEM), electrochemical impedance spectroscopy (EIS) and cyclic voltammetry (CV). Under optimal conditions, the novel electrode configurations were used for tyramine determination.

This research led to two articles in the literature, references [201] and [202], (Talanta 195 (2019) 604–612) and (Food Chemistry 282 (2019) 18–26).

4.1 Preparation of PANSA films and AuNP$_{green}$-PANSA nanocomposite films

PANSA modified MWCNT(GCE were prepared. The growth profiles of PANSA and the nanocomposite AuNP$_{green}$-PANSA films electrodeposited on AuE and GCE are shown in **Fig 4.1A-D**. Both possess two redox couples with similar voltammetric profiles to aniline polymerisation [203–205]. ANSA is an N-substituted aniline which has naphthalene sulphonic acid as a substituent in the amine ring. The redox couples I$_a$/II$_a$ and I$_c$/ II$_c$ are attributed to intrinsic redox processes during polymer formation. The couple I$_a$/II$_a$ is the result of the transformation of aniline in ANSA from the reduced leucoemeraldine state to the partly oxidised emeraldine state. The second redox couple, I$_c$/ II$_c$, is due to the transition of emeraldine to the pernigraniline state, which is accompanied by oxidation of ANSA [206,207].

The two anodic and two cathodic peaks which appeared at the initial stage of polymerisation gradually merged into one redox couple (one anodic and one cathodic peak). For both polymer and nanocomposite films, the anodic and cathodic peaks increased in height in each of the first 5 cycles indicating successful electrodeposition. However, after the 5th cycle, the cathodic peaks begin to decrease in height while the anodic peaks shift slightly to more positive values with an increasingly slower rate of electrodeposition.This behaviour indicates the self-limiting character of PANSA growth at higher cycle numbers. This has been attributed to the steric and inductive effect of the naphthalene sulphonic acid moiety [169,208]. There is also an increase in peak separation for both PANSA and AuNP$_{green}$-PANSA, indicating less reversible behaviour with increase in film thickness. This is in agreement with other work, in which it was observed that the electropolymerisation of aniline often has a self-accelerating character [169], while the naphthalene sulphonic acid moiety limits the rate of polymerisation [208]. The mid-point potential between anodic and cathodic peaks for the polymer and the nanocomposite electrodeposited on different electrode substrate were calculated. For the gold electrode (AuE), the midpoint potential, between the 2nd and 7th scan, is almost constant: $E_{\mathrm{mid,PANSA}} \approx 0.47$ V and $E_{\mathrm{mid,AuNP\text{-}PANSA}} \approx 0.450$ V. For GCE, the mid-point potential between anodic and cathodic peaks for the polymer and the nanocomposite almost does not vary between the 2nd and 7th scan (≈ 0.44 V vs. Ag/AgCl).

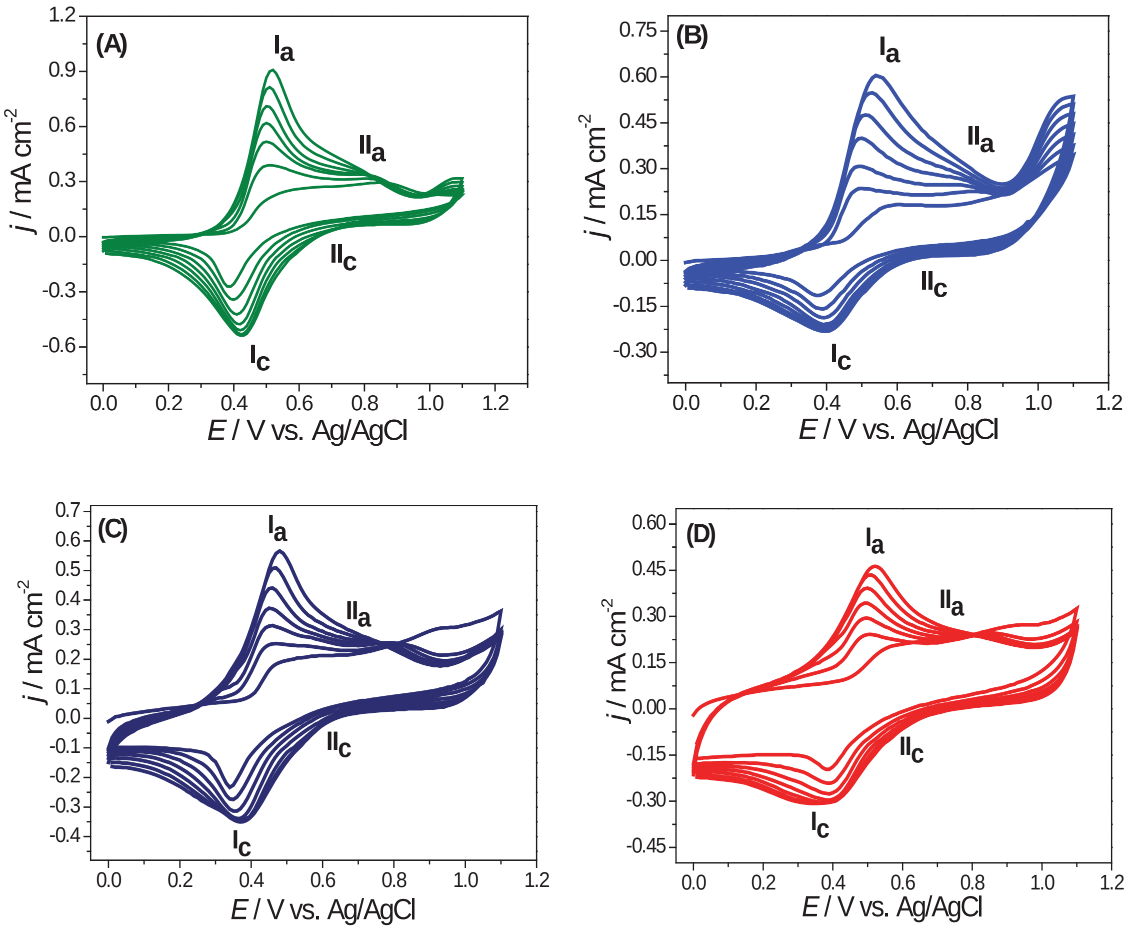

Fig. 4.1 Electrochemical synthesis of (A) PANSA/AuE, (B) AuNP-PANSA/AuE, (A) PANSA/GCE, (B) AuNP-PANSA/GCE in 0.1 M ANSA + 0.5 M H_2SO_4; scan rate 50 mVs$^{1\cdot}$.

The polymer growth voltammetric profile was very similar in both cases and was expressed as the ratio of the oxidation peak current in the seventh compared to the first cycle (I_7/I_1). For PANSA/AuE this factor was 3.21, while for AuNP$_{\text{green}}$-PANSA/ AuE it was 3.14. For PANSA/GCE the factor was calculated to be 5.6, while for AuNP AuNP$_{\text{green}}$-PANSA/GCE it was 5.9. The first cycle oxidation peak currents were also almost the same for all cases, see Fig.4.1. Thus, the addition of $AuNP_{green}$ to the monomer solution did not significantly affect the polymer growth rate. However, the inclusion of $AuNP_{green}$ in the polymer matrix was beneficial for tyramine determination as will be shown in the following sections.

4.2 Characterisation of the nanostructures

4.2.1 X-ray diffraction of $AuNP_{green}$

The colloidal solution of gold nanoparticles was dropped on glass slides and dried in an oven at 60 °C and after subjected to XRD analysis. The Bragg reflections are identified in the XRD pattern, see **Fig. 4.2A**. Gold nanoparticles synthesised from *C. sinensis,* showed Bragg reflection peaks at 36.4^o, 44.3^o, 64.9^o and 77.8^o in the 2θ range between 30^o and 90^o which can be indexed to (111), (200), (220) and (300) planes respectively in agreement with the face-centred cubic (fcc) gold crystal structure (Joint Committee on Power Diffraction Standards - JCPDS, 04-0784). The well-defined and intense peaks revealed that the $AuNP_{green}$ was successfully synthesised by the reduction of Au^+ using *C. sinensis* extracts, and shows its crystalline nature [209–211].

The mechanism for the thermal reduction of $HAuCl_4$ by citric acid from *C. sinensis* to form AuNP involves nucleation and growth processes, **Fig. 4.2B**. The coordination of citric acid with $Au^{III}Cl_4^-$ produces citrate–$Au^{III}Cl_3^-$ complexes which are activated thermostatically by constant heating of the mixture producing a reduced $Au^{II}Cl_n^{m-}$ species, along with the formation of oxidation products of citric acid such as acetoacetate, CO_2, and dicarboxyacetone. Following this, the subsequent reduction of citrate-$Au^{II}Cl_n^{m-}$ and citrate-$Au^{I}Cl_n^{m-}$complexes produce Au^0 and Au^0 nuclei, leading to the formation of $AuNP_{green}$.

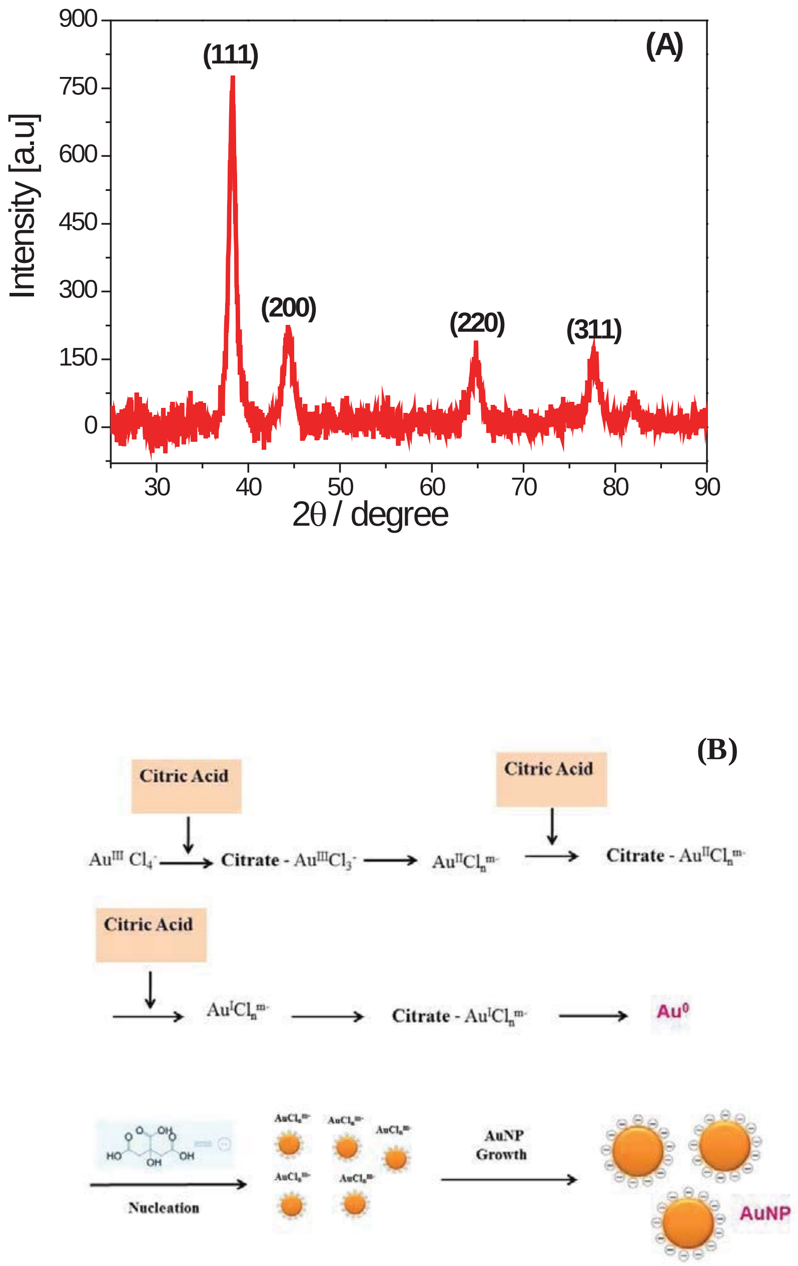

Fig. 4.2 (A) X-ray diffraction pattern recorded from drop-coated films of the colloid solution of gold nanoparticles synthesised with extract of *Citrus sinensis.* **(B)** The mechanism for the formation of $\mathrm{AuNP}_{\mathrm{green}}$ by thermal reduction using citric acid from *Citrus sinensis* at 80 °C [212].

Citrate anions are adsorbed on the AuNP surface and act as surface-stabilising agent of the nanoparticles. The negative charge of citrate suppresses $AuNP_{green}$ aggregation and leads to a more homogeneous dispersion of the nanoparticles, due to electrostatic repulsion [212].

4.2.2 Morphological characterisation of the nanostructures

The morphology of $AuNP_{green}$, formed by the green synthesis method, was examined by scanning electron microscopy (SEM), as shown in **Fig. 4.3A**. SEM reveals the predominant presence of spherical and quasi-spherical like-shaped gold nanoparticles with a relatively well-dispersed distribution. The size of $AuNP_{green}$ were analysed by ImageJ open source particle analysis software, in which 100 discreet and well-defined nanoparticles were used as sample space to measure the average size of the nanoparticles. From the Gaussian fitting curve to the histogram, **Fig. 4.3B**, the size of the nanoparticles was calculated to be 18.6 ± 2.6 nm. Similar results are found in the literature. Spherical gold nanoparticles of 30-50 nm diameter were achieved using *Penicillium sp* [213], predominantly spherically-shaped gold nanoparticles ranging from 20 nm were synthesized using biodegradable green surfactants such as VeruSOL-3 [214], quasi-spherical gold nanoparticles with diameter around 16 nm were obtained using the flower extract of *Rosa damascena* as a reducing and stabilizing agent [215].

The surface morphologies of the PANSA and the $AuNP_{green}$-PANSA nanocomposites are presented in the SEM images in **Fig. 4.AC** and **4.3B**, respectively. For both coatings, there is a rough fully-covered surface with a uniform distribution of the polymer network and globular-like formations. Evidence of the uniform distribution of the nanoparticles in the polymer network was also seen by the presence of small spherical white spots, **Fig. 4.3D**, over the whole surface.

Polymers are known to stabilise metal nanoparticles mainly by charge transfer interactions between the metal particles and the functional groups of heteroatoms on the polymer network [216].

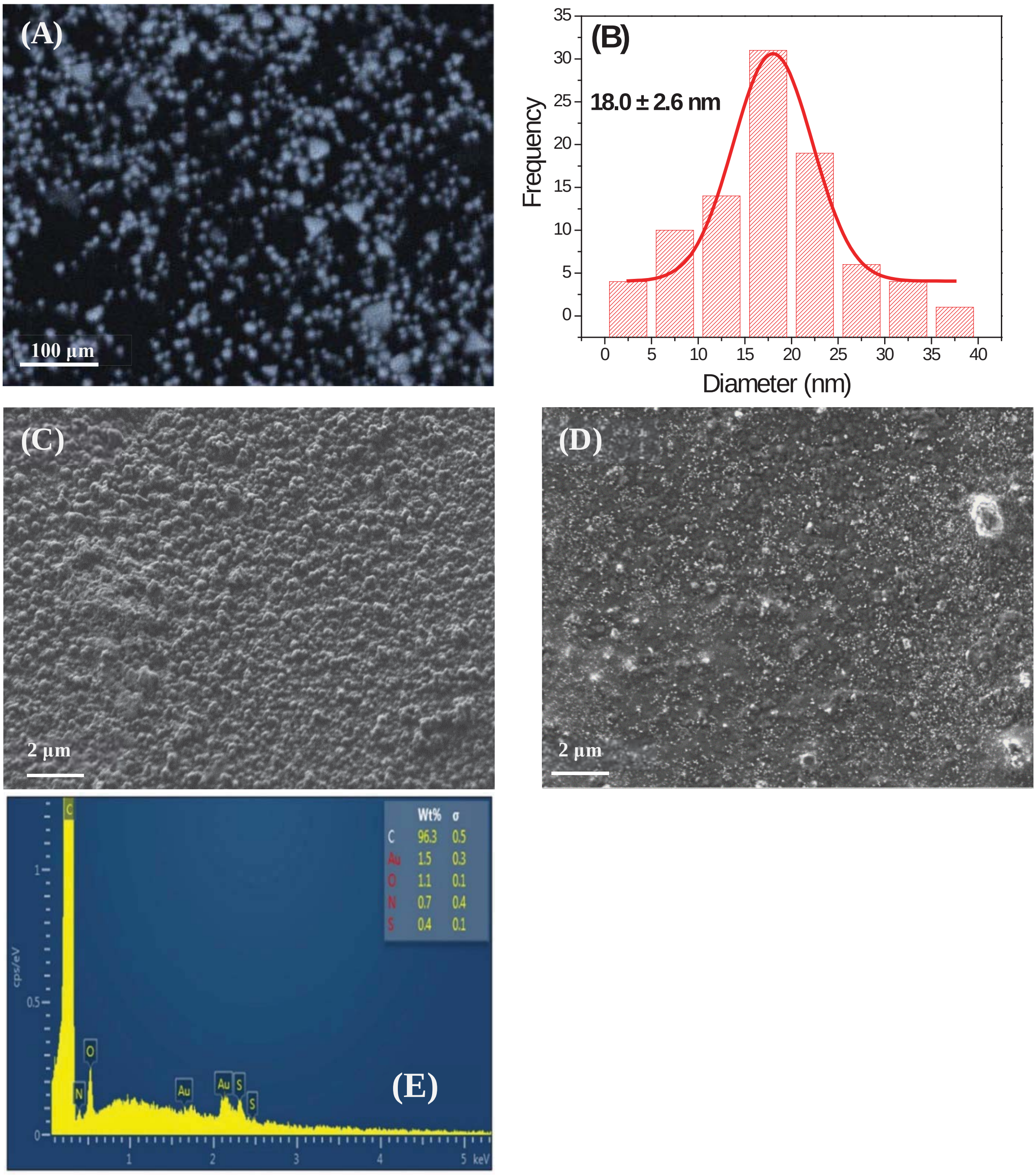

Fig. 4.4(A) Scanning electron microscopy (SEM) of the gold nanoparticles (AuNP$_{green}$) obtained by green synthesis; **(B)** Size distribution histogram of the AuNP$_{green}$; **(C)** SEM of PANSA film; **(D)** SEM of the AuNP$_{green}$-PANSA nanocomposite film; **(E)** EDS spectrum of the AuNP$_{green}$-PANSA nanocomposite film.

In the case of PANSA, a derivative of polyaniline, the aggregation and stabilisation of $AuNP_{green}$ in the polymer network is controlled by the electrostatic attraction between protonated amines in the polymer film and the negative charge of the nanoparticle citrate capping groups. This stabilisation of the $AuNP_{green}$ in the polymer matrix prevents their leaching when the modified electrode is immersed in solution. Thus, this new methodology successfully incorporates nanoparticles in the polymer network through polymerisation of the corresponding monomer in the presence of gold nanoparticles ($AuNP_{green}$) in solution.

Energy dispersive X-ray spectroscopy (EDS) obtained from a localised area of the nanocomposite film was performed for evaluating its composition, **Fig. 4.3E**. The EDS spectrum reveals the presence of carbon (C), nitrogen (N), oxygen (O) and sulphur (S) both present in the structure of the polymer. Two characteristic X-ray peaks of gold (Au) in the spectrum also proved the presence of the $AuNP_{green}$ on the nanocomposite. The EDS spectrum confirms that the new methodology for attaching nanoparticles to the polymer network is efficient.

4.3 Impedimetric sensor for tyramine

A novel impedimetric sensor for the detection of Tyr was developed based on a nanocomposite: poly-(8-anilino-1-naphthalene sulphonic acid (PANSA) and gold nanoparticle ($AuNP_{green}$) film modified gold electrode. The gold nanoparticles ($AuNP_{green}$) were incorporated within the PANSA network during electropolymerisation of the monomer on gold electrode (AuE), which contributed significantly to improvement of conductivity and sensor performance. Quantification of Tyr relied on measuring changes in the charge transfer resistance at a potential where Tyr is oxidised. Parameters such as applied potential and pH were optimised. Under the best conditions, the impedimetric sensor was used for Tyr detection.

In order to optimise the impedimetric sensor, voltammetric characterisation was first carried out.

4.3.1 Electrochemical response of different electrode configurations to tyramine (Tyr) oxidation

The effect of modifying the electrode surface on the oxidation process of Tyr was evaluated by cyclic voltammetry, as illustrated in **Fig. 4.5**. The anodic and cathodic peak current increased significantly with all modifications tested, being the highest at AuNP$_{\text{green}}$-PANSA/AuE.

The anodic peak potential shifted to a more positive value and the cathodic to a more negative value being 0.14 V and -0.22V at AuE, 0.16 V and -0.24 V at AuNP$_{\text{green}}$ /AuE, 0.18 V and -0.25 V at PANSA/AuE and 0.28 V and -0.27 V at AuNP$_{\text{green}}$ -PANSA/AuE, indicating a quasi-reversible oxidation process of tyramine at all electrodes.

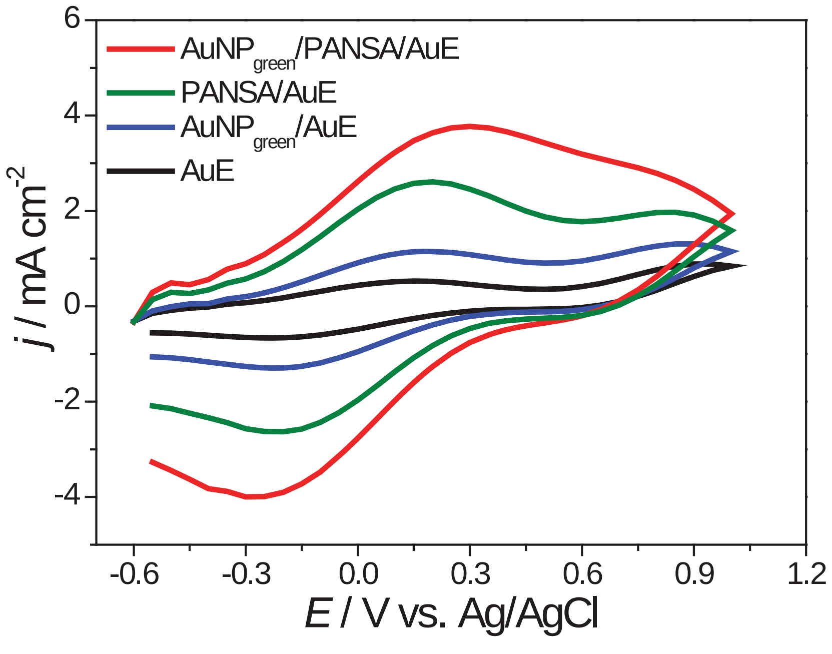

Fig. 4.5 Cyclic voltammograms for the oxidation of 200 µM Tyr in 0.1 M BR buffer solution (pH 7.0), recorded at 50 mV s-1, at (--) AuE; (--) AuNP$_{\text{green}}$ /AuE; (--) PANSA/AuE; (--)AuNP$_{\text{green}}$ -PANSA/AuE.

The significant peak current increase that occurs at $AuNP_{green}$-PANSA/AuE indicates a higher available active surface area compared with AuE, $AuNP_{green}$/AuE and PANSA/AuE. There is also a large increase in the background current at AuNP-PANSA/AuE, which can be attributed to the efficient aggregation of $AuNP_{green}$ on the polymer network. $AuNP_{green}$-PANSA/AuE is clearly superior to the other electrode configurations and was chosen to be used in all further studies.

4.3.2 Dependence of the oxidation process on the scan rate

The influence of scan rate on the voltammetric sensor response was investigated to ascertain whether it is a diffusion-controlled or a surface-confined process. CVs were recorded at $AuNP_{green}$-PANSA/AuE for 200 μM Tyr in 0.1M BR buffer pH 7.0 solution at scan rates from 10 to 100 mV s^{-1}, **Fig. 4.6A**. There is a linear relationship between the anodic peak current, I_{pa}, and the cathodic peak current, I_{pc}, with the scan rate, v, **Fig. 4.6B**, according to the equations: I_{pa} (μA) = -0.24 v + 0.05; r= 0.9980 and I_{pc} (μA) = - 0.046 v – 0.33; r= 0.9985, characteristic of a surface-confined oxidation process [146].

A plot of the logarithm of the oxidation peak current vs logarithm of scan rate (not shown) has a slope of 1.12, close to the theoretical value of 1.0 for a pure adsorption controlled electrode reaction [146].

The current also depends on the amount of Tyr in solution which demonstrates that the adsorption is reversible and that the number of adsorbed species depends on the solution concentration, and that it can be described by an isotherm. When carrying out consecutive CV scans, a current decreasing with each scan was observed, since there was not time for the adsorption/desorption equilibrium of Tyr to be reached.

In other experiments, after performing a scan in the presence of tyramine and then placing the electrode in pure buffer solution, the CV peak of tyramine oxidation appeared, also indicating that there is tyramine adsorbed on the modified electrode.

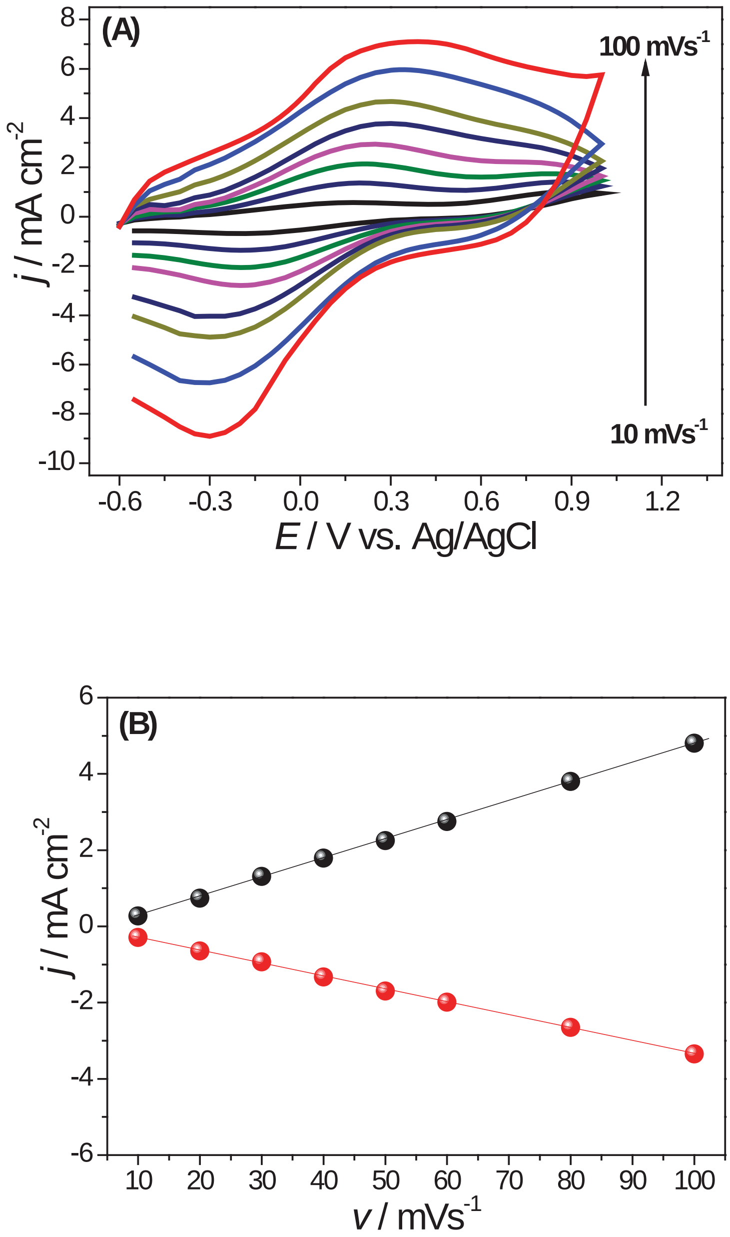

Fig. 4.6. (A) Cyclic voltammograms at AuNP$_{green}$-PANSA/AuE in 200 μM Tyr solution (0.1 M BR buffer, pH 7.0) at scan rates 10 - 100 mVs^{-1}. **(B)** The linear relationship between the peak currents and scan rate.

The separation of the anodic and cathodic peaks increases with increasing scan rate, typical for a quasi-reversible process. The dependence of the anodic peak potential, E_{pa} and the cathodic peak potential, E_{pc}, on the logarithm of scan rate are given by Laviron's equations for anodic and cathodic processes [179]:

$$E_{\mathrm{pa}} = \left(\frac{2.303RT}{\alpha_{\mathrm{a}}nF}\right)\log v \; + K$$

$$E_{\mathrm{pc}} = \left(\frac{-2.303RT}{\alpha_{\mathrm{c}}nF}\right)\log v \; + K$$

where α_{a} and α_{c} are the anodic and cathodic electron transfer coefficients, n is the number of electrons involved in the redox process, F is the Faraday constant (F = 96485 C mol^{-1}), v is the potential scan rate (V s^{-1}), R is the ideal gas constant (8.314 J K^{-1} mol^{-1}), T is the temperature (K), and K is a constant. The dependence between the peak potential and logarithm of scan rate are expressed as: E_{pa} (V) = 0.084 *log v* +0.0.94 and E_{pc} (V) = - 0.065 log v - 0.10. Taking into account the two-electron process for Tyr oxidation [217], the charge transfer coefficients were estimated to be α_{a}= 0.40 and α_{c} = 0.54.

4.3.3 Electrochemical impedance spectroscopy (EIS)

Impedance spectra were recorded at AuNP-PANSA/AuE at different potentials from 0.0 to + 0.8 V, chosen as explained below in **Section 3.5.1**. Impedance spectra at +0.6 V, the best potential for impedimetric detection as will be shown below, for different electrode configurations AuE, AuNP$_{\mathrm{green}}$ /AuE, PANSA/AuE, AuNP$_{\mathrm{green}}$-PANSA/AuE are shown in **Fig. 4.7A**.

All spectra showed a semicircle–like shape and were fitted with the same electrical equivalent circuit presented in **Fig. 4.7B**. Although it is expected that the circuit should contain contributions from the modifier film resistance and capacitance as well as from the modified electrode-solution interface, the experimental spectra are clearly dominated by one *RC* parallel combination with no other semicircles with different time constants discernible, as usually happens.

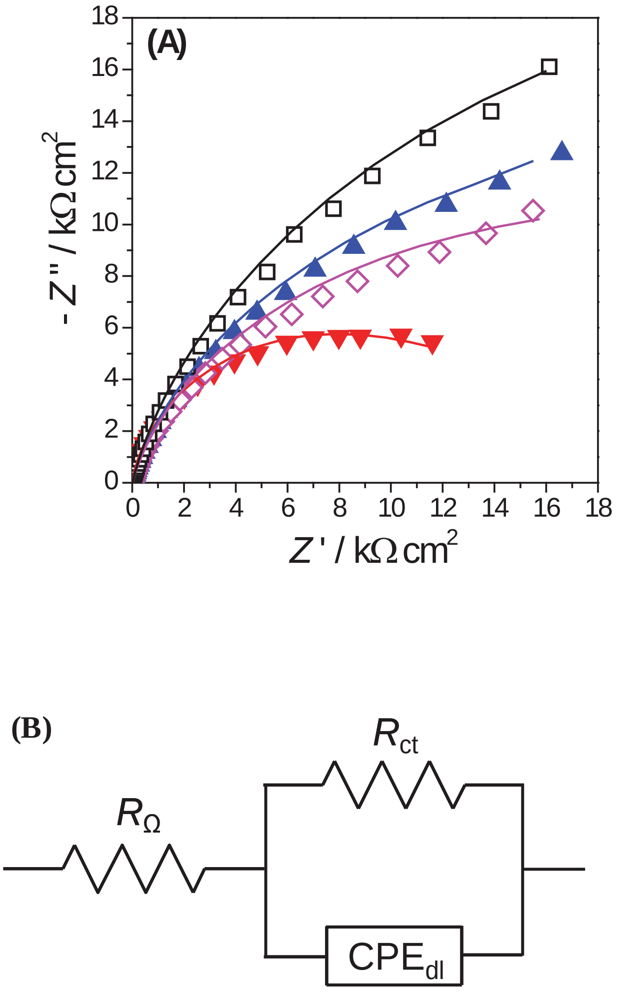

Fig. 4.7 (A) Complex plane impedance spectra recorded at different electrode configurations: (□) AuE; (▲) AuNP$_{green}$/AuE; (◇) PANSA/AuE; (▼) AuNP$_{green}$-PANSA/AuE in the presence of 100 μM tyramine in 0.1 M BR buffer (pH 7.0) at 0.6 V vs. Ag/AgCl. **(B)** Electrical equivalent circuit used to fit the impedance spectra: R_Ω cell resistance; CPE$_{dl}$ non-ideal capacitance of the double layer; R_{ct} charge transfer resistance.

Thus, the circuit comprises R_Ω, the cell resistance (solution resistance, electrical contacts etc.) in series with a parallel combination of R_{ct} and CPE_{dl}, representing the charge transfer resistance and non-ideal interfacial capacitance respectively. The CPE is modelled as a non-ideal capacitor given by $CPE = -1/(i\omega C)^\alpha$ in which the exponent α reflects the surface non-uniformity and roughness of the modified electrode assembly, where $\alpha = 1$ corresponds to a perfect uniform and smooth surface [171,218]. The results from fitting to the equivalent circuit are summarized in **Table 4.1** and are shown as continuous curves in the spectra.

Table 4.1 Values of equivalent circuit parameters obtained by fitting of the impedance spectra at different electrode configurations; +0.6 V (0.1 M BR buffer, pH 7.0). Data from **Fig. 4.7A**.

Electrode configuration	R_{ct} / kΩ cm^2	CPE_{dl} / µF cm^{-2} s$^{\alpha-1}$	α
AuE	34.4	27.3	0.84
$AuNP_{green}$/AuE	25.8	31.9	0.84
PANSA/AuE	20.9	35.1	0.85
$AuNP_{green}$-PANSA/AuE	10.8	44.7	0.90

The EIS data show that the double layer capacitance increases with modification of the electrode reaching a maximum at the $AuNP_{green}$-PANSA modified electrode. The increase in the capacitance values is accompanied by the decrease in the charge transfer resistance values. A higher value of the exponent α equal to 0.90 was obtained for AuNP-PANSA/AuE indicating that it has a more uniform surface at the nanoscale compared to the other electrode configurations, as also verified by SEM morphological studies. The R_{ct} values of the modified electrodes of 34.4, 25.8, 20.9, 10.8 kΩ cm^2 decrease in the order AuE, $AuNP_{green}$/AuE, PANSA/AuE, $AuNP_{green}$-PANSA/AuE, indicating the easiest electron transfer at the last electrode configuration. This can be explained if considering a synergetic effect of nanoparticles and polymer, which led to increase of the electroactive area and contributed to the electrocatalytic effect towards tyramine. The impedance spectra are in agreement with the cyclic voltammetry observations.

4.3.4 Optimisation of the working conditions for tyramine determination by EIS. Influence of the applied potential and solution pH

For electrochemical impedimetric as well as voltammetric measurements, the applied potential has a big influence on sensor response since it contributes to a better sensitivity for detection of the target analyte. In order to optimize the potential for detection of Tyr, impedance spectra were recorded at different potentials: 0.0, 0.2, 0.4, 0.6 and 0.8 V vs. Ag/AgCl. These potentials were chosen considering the oxidation peak potential values from CV and encompass the range of potentials where oxidation and reduction occur. Moreover, using potentials as close as possible to 0.0 V should minimise interference effects. **Fig. 4.8A** shows impedance spectra recorded at $AuNP_{green}$-PANSA/AuE in the presence of 100 μM Tyr in BR buffer solution, pH 7.0 at the various potentials. **Table 4.2** shows the results of fitting the data to the same electrical equivalent circuit used in **Fig. 4.7B**, where it can be observed that the lowest values of R_{ct} are obtained at 0.6 V, in agreement with CV experiments, where the maximum oxidation peak appears around 0.55V, **Fig. 4.6A**. Therefore, 0.6 V was taken as the best value for Tyr determination by impedance. The effect of supporting electrolyte pH on the spectra was also investigated to evaluate the optimum pH for determination of Tyr. Spectra were recorded, as shown in Fig. **4.8B**, in the presence of 100 μM Tyr in BR buffer at the pH range from 4.0-8.0 at $AuNP_{green}$-PANSA/AuE at +0.6 V. As can be seen from **Table 4.2**, the values of R_{ct} gradually decreased with increase of pH up to pH 7, then increased. The fact that R_{ct} decreases with increase of pH may reflect the lower stability of the chemical equilibrium dopamine-o-quinone by-products formed during oxidation of Tyr in acid and basic pH solution, giving a better response at neutral pH [219].

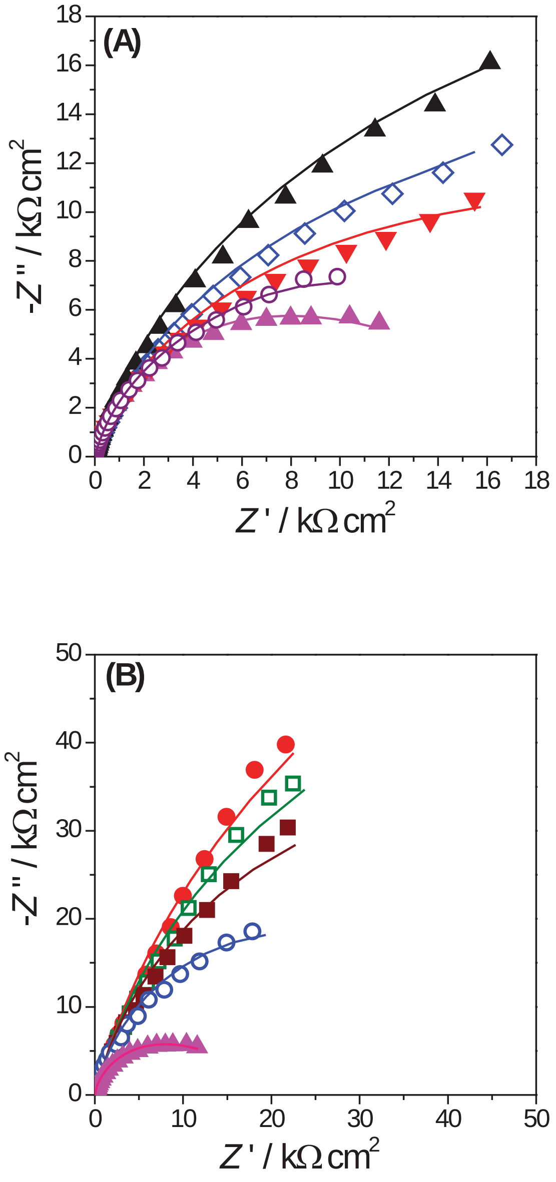

Fig. 4.6 Complex plane impedance spectra at AuNP-PANSA/AuE in the presence of 100 μM Tyr in 0.1 M BR buffer.**(A)** At pH 7.0, applied potential (◇) 0.0; (▲) 0.2; (▼) 0.4; (▲) 0.6; (○) 0.8 V vs. Ag/AgCl. **(B)** At +0.6 V vs. Ag/AgCl, pH values of (●) 4.0; (□) 5.0; (■) 6.0; (▲) 7.0; (○) 8.0.

Table 4.2 Equivalent circuit element values obtained by fitting of the impedance spectra at $AuNP_{green}$-PANSA/AuE at different potentials (pH 7.0, data from **Fig. 4.6A**) and different pH values (+0.6 V, data from **Fig. 4.6B**).

Experimental conditions		R_{ct} / kΩ cm^2	CPE_{dl} / µF cm^{-2} $s^{\alpha-1}$	α
Applied potential / V	0.0	53.2	19.3	0.85
	0.2	103.4	20.8	0.84
	0.4	84.4	18.4	0.85
	0.6	15.8	19.2	0.90
	0.8	30.7	25.0	0.88
pH	4.0	170.2	19.7	0.85
	5.0	121.3	19.9	0.83
	6.0	70.5	19.6	0.85
	7.0	15.8	19.2	0.90
	8.0	45.8	19.8	0.86

4.3.5 Impedimetric response for Tyr determination

Impedance spectra recorded under the optimum conditions determined above for Tyr sensing are shown as complex plane plots in **Fig. 4.7A**, for concentrations up to 80.0 µM. It is possible to observe a change in the shape of the spectra, associated with a decrease in the R_{ct} value, immediately with the first concentration of Tyr added, and this can be associated with a realistic limit of detection. The errors associated with fitting to electrical circuit were less than 3% and the changes in R_{ct} were much higher than this. The values of the equivalent circuit parameters after fitting the spectra are summarized in **Table 4.3**. It is clearly seen that R_{ct} decreases with increase of Tyr concentration, while the capacitance values gradually increase.

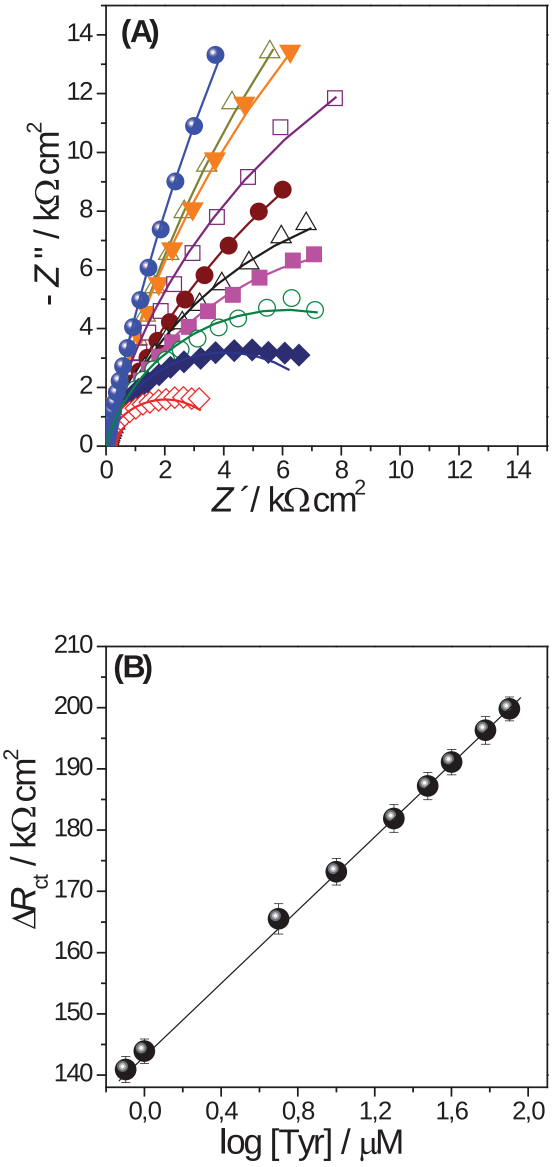

Fig. 4.7(A) Complex plane impedance spectra at AuNP$_{green}$-PANSA/AuE with different concentrations of Tyr in 0.1 M BR buffer (pH 7.0) at 0.6 V vs. Ag/AgCl: (●) 0.0; (Δ) 0.8; (▼) 1.0; (□) 5.0; (●) 10.0; (Δ) 20.0; (■) 30.0; (○) 40.0; (◆) 60.0; (◇) 80.0 μM. **(B)** Calibration curve of ΔR_{ct} versus log ([Tyr]/μM).

The calibration curve in **Fig. 4.7B** plots the change of charge transfer resistance ΔR_{ct} ($R_{ct(buffer)} - R_{ct(Tyr)}$) versus log [Tyr] according to the equation ΔR_{ct} (kΩ) = 144.1+ 29.4 (log[C/μM]) with a correlation coefficient of 0.9987. The reason for the logarithmic dependence can be attributed to the adsorption of Tyr's oxidation product on the electrode surface. The detection limit was calculated to be 0.04 μM based on three replicates. The good performance of the novel Tyr impedimetric sensor considering its ease of fabrication and simplicity of architecture is mainly attributed to a high area-volume ratio, excellent conducting capability and interface-dominated properties of $AuNP_{green}$, which, in combination with the properties of the PANSA polymer network, provide an effective modifier for Tyr oxidation.

Table 4.3 Equivalent circuit element values obtained by fitting of the impedance spectra at AuNP-PANSA/AuE with different Tyr concentrations. Data from **Fig. 4.7A**.

[Tyramine] / μM	R_{ct} / kΩ cm^2	CPE_{dl} / μF cm^{-2} s$^{\alpha-1}$	α
0.0	204	18.0	0.87
0.8	63.1	22.3	0.88
1.0	49.1	38.2	0.89
5.0	31.5	42.6	0.89
10	25.8	45.5	0.86
20	16.1	57.8	0.85
30	13.8	63.6	0.84
40	10.9	72.9	0.85
60	7.7	75.3	0.90
80	4.2	84.9	0.89

Table 4.3 Comparison of the tyramine determination performance at $AuNP_{green}$-PANSA/AuE with different electrode configurations in the literature.

*

Modified electrode configuration	Principle of detection	pH, buffer	Linear range / μM	LOD / μM	Ref
Q/fMWCNT/GCE	DPV	7.0, PBS (0.1M)	0.7-75	0.65	[217]
Carbon disc	MECC-AD	10.3, borate-NaOH (0.02M)	1-1000	0.18	[220]
fMWCNT/GCE	DPV	7.0, PBS (0.1M)	1-17	0.80	[221]
Tyrosinase/PPy/PtE	Amperometry	7.0, PBS (0.01M)	4-80	0.54	[222]
Tyrosinase/ COOfSWCNT	Amperometry	7.0, PBS(0.01M)	5-180	0.62	[223]
AuNP-PANSA/AuE	EIS	7.0, BR (0.1M)	0.8-80	0.04	This work

Q – quercetin; fMWCNT - functionalized multi-walled carbon nanotubes; GCE – glassy carbon electrodes; MECC-AD – micellar electrokinetic capillary chromatography separation with amperometric detection; DPV- Differential Pulse Voltammetry; PPy – polypyrrole; PtE – platinum electrode; COOfSWCNT – carboxyl functionalized single-walled carbon nanotubes; EIS – Electrochemical impedance spectroscopy

The analytical performance of the nanocomposite AuNP$_{green}$-PANSA/AuE for Tyr determination was compared with other electrode configurations (no reports on impedimetric sensing were found) and the results are listed in **Table 4.3**. The novel impedimetric sensor used for Tyr detection showed a superior performance to those found in the literature with the lowest limit of detection and a sufficiently broad linear range, comparable to more complex architectures that use carbon nanotubes and/or tyrosinase (Tyr$_{ase}$). Although in some configurations Tyrosinase was used [222,223], as enzyme substrate, their performance was not better than here. The sensors that used DPV for analytical Tyr determination [217,221] presented a higher limit of detection despite the high sensitivity conferred by DPV. This can be attributed to the accentuated adsorption that compromises the detection by voltammetric techniques, as verified in previous studies [217,220–223]. Hence, the proposed novel nanocomposite with impedimetric measurement has the advantage of easy and rapid preparation with a very low limit of detection.

4.3.6 Repeatability, stability, and selectivity

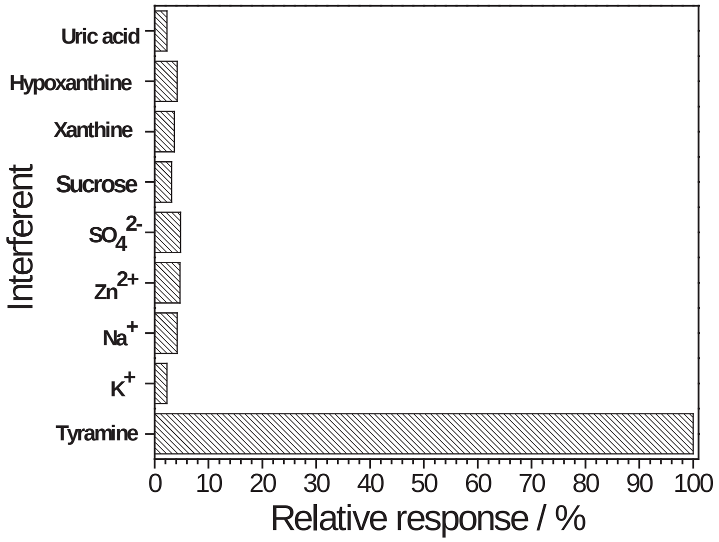

Fig. 4.8 Influence of potential interferents on the impedimetric sensor response in the presence of 100 μM Tyr, ratio with interferents (1:1).

The repeatability of impedimetric measurements at the AuNP$_{green}$-PANSA/AuE was investigated by successive measurements of the response to 100 µM Tyr in buffer BR, pH 7.0. The R_{ct} value was 95 % of the initial value after 25 successive measurements (RSD = 4.39 %; n= 3). Concerning storage stability, the EIS response of the sensor lost just 10 % of the initial signal in terms of the R_{ct} value, after a storage period of 20 days in the dry state at room temperature.

The influence of potential interferents on sensor response was also evaluated. For this, the possible interferents tested were: organic (uric acid, hypoxanthine, xanthine, sucrose) and inorganic species (SO_4^{2-}, Zn^{2+}, Na^+, K^+) in the ratio 1:1(m/m) with Tyr and the results are shown in **Fig. 4.8**. As can be seen, these species did not produce significant changes in the R_{ct} values (all less than 5 %), demonstrating good selectivity. This selectivity is comparable to that reported in the literature [224,225].

4.4 Tyr$_{ase}$/AuNP$_{green}$-PANSA/GCE biosensors for tyramine determination

In this part of the work on tyramine determination, a novel biosensor architecture based on tyrosinase (Tyr$_{ase}$) immobilised on a glassy carbon electrode modified by a nanocomposite consisting of a AuNP$_{green}$ / poly(8-anilino-1-naphthalene sulphonic acid) modified glassy carbon electrode was developed and used for amperometric detection of Tyramine. Some parameters were optimised, namely enzyme loading, pH and applied potential. Under optimal conditions, the analytical performance of the biosensor is discussed, including enzyme kinetics, calibration curve, sensitivity and limit of detection for tyramine.

4.4.1 Optimisation of the amperometric biosensor

4.4.1.1 Effect of the amount of tyrosinase

In order to determine the optimal amount of Tyr$_{ase}$ immobilized on AuNP$_{green}$-PANSA/GCE for Tyr determination, different Tyr$_{ase}$ loadings ranging from 0.1 to 3.5% (w/v) were tested, the concentrations of GA and BSA being fixed at 2.5% (v/v) and 2.0% (v/v), respectively. The amperometric response to 100 µM Tyr was tested for different enzyme loadings, using the same experimental conditions. The cathodic current increases as the amount of Tyr$_{ase}$ is increased, reaching a maximum for 2.0% (w/v) of Tyr$_{ase}$. For higher loadings, there is a decrease in biosensor sensitivity. This indicates that high amounts of enzyme compromise biosensor performance, this being attributable to diffusion limitations and to a too low concentration of dissolved oxygen, a natural cofactor for enzyme regeneration [226]. Therefore, 2.0% (w/v) of the enzyme was chosen as the best for biosensor construction.

4.4.1.2 Influence of pH solution for Tyr determination

The literature reports that the enzymatic activity of Tyr_{ase} is lost below pH 4.0 and above pH 9.0 [227,228]; hence the influence of solution pH on the oxidation of 100 μM Tyr was investigated by DPV in the pH range from 4.0 to 9.0.

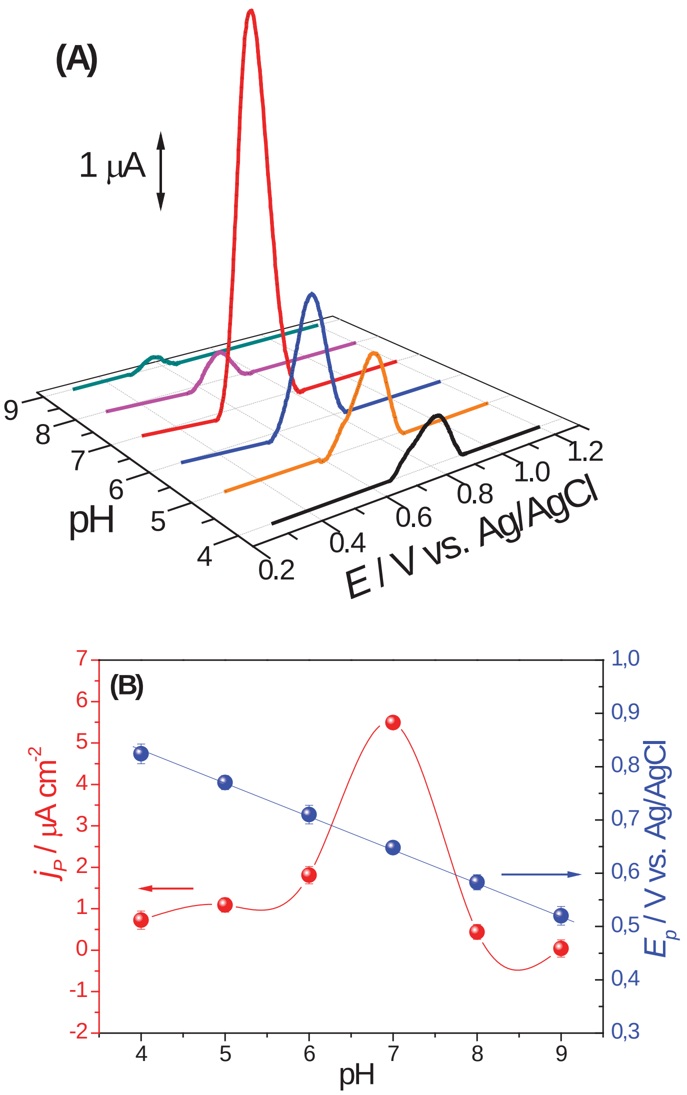

Fig. 4.9(A) Differential pulse voltammograms of 100 μM Tyr at Tyr_{ase}/$AuNP_{green}$-PANSA/CGE in 0.1 M BR buffer at different pH values recorded at 5 mVs^{-1}. Amplitude 10 mV, step potential 2 mV, pulse time 10 ms. **(B)** Effect of pH on the Tyr oxidation peak current and peak potential.

As can be seen in **Fig. 4.9A**, the maximum oxidation peak current was obtained at pH 7.0. Therefore, this pH was selected as optimum pH and used in Tyr determination. With increasing solution pH from 4.0 to 9.0, the oxidation peak potential shifted negatively and linearly, **Fig. 4.9B**, according to E_{pa} (V) = 1.06 – 0.060 pH with a correlation coefficient of 0.9987, the slope being close to the theoretical value of 59 mV pH^{-1} at 25 °C for an electrode process involving equal number of protons and electrons. The peak width at half height, $W_{1/2} = 3.52\ RT/nF$, where R is the universal gas constant, T the temperature in K, and F the Faraday constant gives an indication of the reversibility of the electrode reaction and the number of electrons involved. The minimum peak width for a reversible one-electron process is 90 mV and for a reversible two-electron process is 45 mV [146].

As seen in **Fig. 4.9A**, $W_{1/2}$ was approximately 45 mV over the pH range studied. Therefore, it can be assumed that two electrons are involved in the reaction [222,223], as proposed in the mechanism described in the following section.

4.4.1.3 Influence of the applied potential

The applied potential has a big influence on biosensor performance since it contributes to its sensitivity and selectivity. The biosensor response to 100 μM Tyr in 0.1 M BR buffer (pH 7.0) was studied between – 0.5 and + 0.3 V vs. Ag/AgCl.

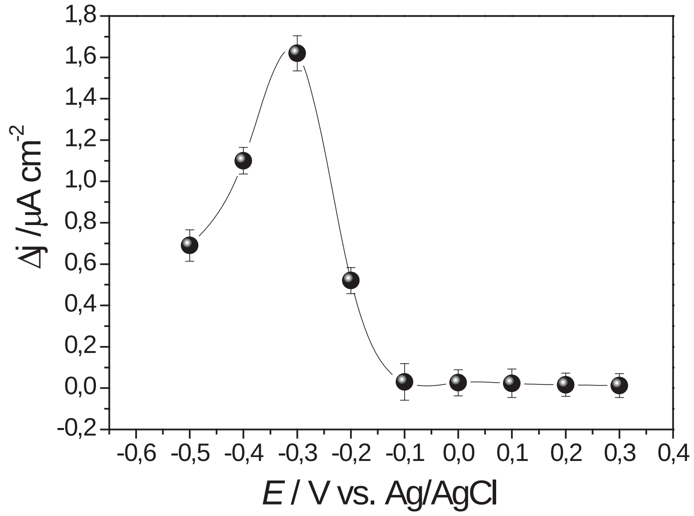

Fig. 4.10 Effect of cathodic current–applied potential dependence in 0.1M BR (pH 7.0) and 100 μM tyramine under constant stirring.

The current increases rapidly as the potential becomes less negative from – 0.5 to - 0.3 V, with a maximum at - 0.3 V and then decreases up to - 0.1 V, above which the response is almost constant, **Fig. 4.10**.

(4.1)

Tyr$_{ase}$ catalyses the hydroxylation of Tyr (eq. 4.1) as well as the oxidative conversion of the resulting dopamine to *o*-dopaquinone (eq. 4.2). The enzymatically generated o-dopaquinone by-product can easily undergo electrochemical reduction at a potential close to 0.0 V [222,223] (eq. 4.3). This reaction is verified in CVs, **Fig. 4.11B**, since a reduction peak appears at a potential close to - 0.3 V in the presence of Tyr [229]. The sensing principle of the biosensor is based on measuring the increase of the cathodic amperometric signal related to the electrochemical reduction of *o*-dopaquinone enzymatically generated on the biosensor surface that involves 2 electrons and 2 protons.

$$\text{Tyramine} + \tfrac{1}{2}\,O_2 \xrightarrow{\text{Tyrosinase}} \text{Dopamine}$$

$$\text{Dopamine} + \tfrac{1}{2}\,O_2 \xrightarrow{\text{Tyrosinase}} \text{o-Dopaquinone} + H_2O$$

$$\text{o-Dopaquinone} + 2H^+ + 2e^- \xrightarrow{\text{Tyrosinase}} \text{Dopamine}$$

Independent cyclic voltammetry measurements at tyrosinase modified glassy carbon electrodes, and AuNP$_{green}$-PANSA/CGE were carried in the presence of dopamine and tyramine, **Fig. 4.11A** and **B**.

In the presence of dopamine, two redox couples appear with midpoint potentials -0.160 V and +0.250 V; the couples II at more positive potentials is ascribed to dopamine/dopaquinone and the more negative one, I, to dopaquinone reduction. With tyramine only, an additional anodic peak III$_a$ appears, corresponding to irreversible tyramine oxidation. Thus, as can be seen, the reduction of dopaquinone occurs at - 0.3 V. In cyclic voltammetry at Tyr$_{ase}$/AuNP$_{green}$-PANSA/GCE, **Fig 4.11B**, the adsorption of tyramine and its oxidation products in the modifier films led to a very broad redox couple, and it was not possible to distinguish the processes. However, the determination of tyramine by fixed potential amperometry was carried out successfully and with better analytical parameters at the Tyr$_{ase}$/AuNP$_{green}$-PANSA/GCE biosensor than without the presence of AuNP$_{green}$-PANSA nanocomposite, see Section 4.7.

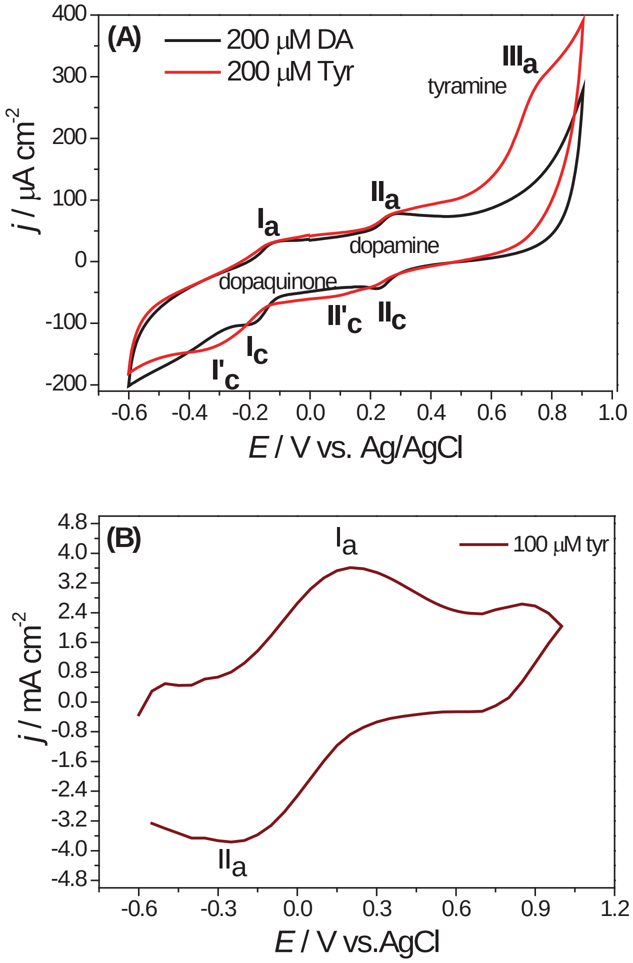

Fig. 4.11 Cyclic voltammetry at **(A)** Tyr$_{ase}$/GCE in the presence of 200 μM dopamine and 200 μM tyramine in 0.1 M BR (pH 7.0), at 50 mV s^{-1}and **(B)** Tyr$_{ase}$/AuNP$_{green}$-PANSA/CGE in the presence of 100 μM tyramine in 0.1 M BR (pH 7.0), at 50 mV s^{-1}.

Thus, in the light of the results obtained, an applied potential of - 0.30 V was selected to be used in further experiments for Tyr determination. Moreover, this potential, close to 0.0 V, minimises the likelihood of potential interferences from common electroactive species.

4.4.2 Analytical performance

The amperometric responses of Tyr$_{ase}$/AuNP$_{green}$-PANSA/GCE, Tyr$_{ase}$/PANSA/GCE, Tyr$_{ase}$/AuNP$_{green}$/GCE and, Tyr$_{ase}$/GCE biosensors for Tyr determination under the optimised conditions were evaluated. The biosensors show a rapid bioelectrocatalytic response, reaching 95% of the steady-state current within 8 s after each Tyr addition. **Fig. 4.12A** is a representative chronoamperometric profile for Tyr determination, showing a linear increase of the change in cathodic current with Tyr concentration for all the biosensor assemblies tested. **Fig. 4.12B** displays the calibration plots obtained from the amperometric responses.

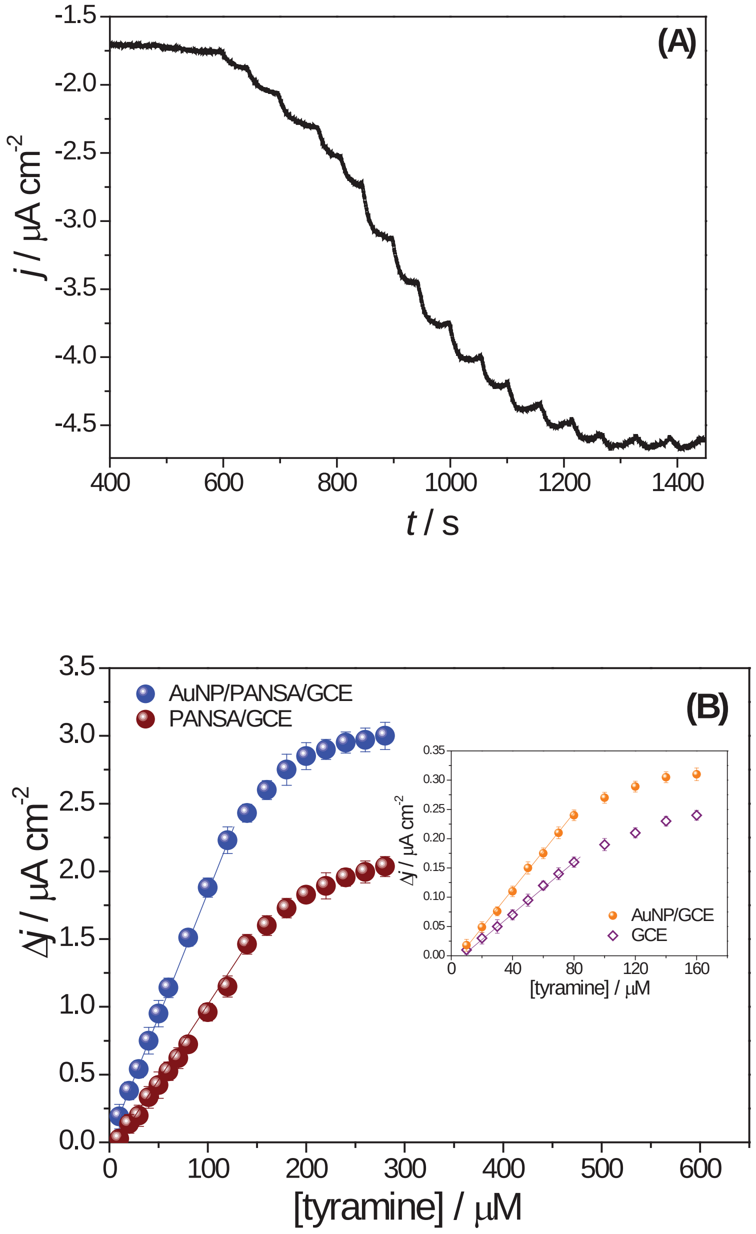

Fig. 4.12(A) Amperometric response of Tyr$_{ase}$/AuNP$_{green}$-PANSA/CGE biosensor to tyramine in 0.1 M BR buffer (pH 7.0); **(B)** Calibration curves for tyramine in 0.1 M BR buffer (pH 7.0) at −0.30 V for AuNP$_{green}$-PANSA/GCE and PANSA/GCE, the insert shows for AuNP$_{green}$/GCE and GCE.

Table 4.4 Comparative performance of different biosensor configurations for tyramine determination.

Modified electrode configuration	Principle of detection	Applied potential/ V	Linear range / µM	LOD / µM	*KM* / µM	Ref
Tyr$_{ase}$/PO$_4$-PPy/PtE	Amperometry	-0.25 (Ag/AgCl)	4.0-80	0.57	62.6	[222]
Tyr$_{ase}$–SWCNT–COOH/SPE	Amperometry	-0.20 (SPE)	5.0-180	0.62	88.5	[223]
TyOx/AgNP/L-Cys/AuE	Amperometry	+0.25 (Ag/AgCl)	17-250	10.0	-	[230]
PSAO-Nafion/MgO$_2$/CPE	Amperometry	+0.40 (Ag/AgCl)	10-300	3.0	-	[231]
Tyr$_{ase}$/TiO$_2$/CMK-3/PDDA/Nafion/GE	Cyclic voltammetry	---	6.0-130	1.5	66	[232]
SPC$_{HRP}$E	Amperometry	0.0 (SPCE)	2.0-456	2.1	-	[233]
HRP/SPCE		0.0 (SPCE)	0.2-21.4	0.2	-	
PAO/HOMFc/SPCE	Amperometry	+0.26 (Ag/AgCl)	2.0-164	2.0	-	[234]
Tyr$_{ase}$/AuNPg$_{reen}$-PANSA/GCE	Amperometry	-0.30 (Ag/AgCl)	10-120	0.71	79.3	This work

Tyr$_{ase}$/PO$_4$-Ppy/PtE - Tyrosinase/polypyrrole doped with phosphate ions on platinum disk electrode; Tyr$_{ase}$–SWCNT–COOH/SPE - screen-printed carbon electrodes modified with carboxyl functionalized Single-Walled Carbon Nanotubes; TyOx/AgNPs/L-Cys/AuE - tyramine oxidase onto citric acid-capped silver nanoparticles bound to surface of Au electrode through cysteine self-assembled monolayer; PSAO-Nafion/MgO$_2$CPE- Pea seedling amine oxidase immobilized with nafion on carbon paste modified with manganese dioxide as mediator; Tyr$_{ase}$/TiO$_2$/CMK-3/PDDA/Nafion/GE - tyrosinase immobilized into mesoporous carbon CMK-3, titania dioxide sol, poly(diallyldimethylammonium chloride) and Nafion onto graphite electrode; PAO/HOMFc/SPCE - plasma amino oxidase immobilized on screen printed carbon electrode using hidroxymethylferrocene as mediator.

The $Tyr_{ase}/AuNP_{green}$-PANSA/GCE biosensor presents the highest sensitivity of 19 nA cm^{-2} μM^{-1} and lowest limit of detection (LoD) of 0.7 µM, following the linear regression equation: Δj ($\mu A\ cm^{-2}$) = -3.58 x 10^{-3} + 1.90 x 10^{-2} [Tyr] (µM), with a correlation coefficient (R^2) equal to 0.9987. For the Tyr_{ase}/PANSA/GCE biosensor, the sensitivity was calculated to be 10 nA cm^{-2} μM^{-1} and the LoD was 1.35 µM, where Δj ($\mu A\ cm^{-2}$) = -0.10 + 1.0 x 10^{-2} [Tyr] µM, (R^2 = 0.9985). The $Tyr_{ase}/AuNP_{green}$/GCE biosensor presented a sensitivity of 3.20 nA cm^{-2} μM^{-1} and LoD of 2.91 µM, with Δj ($\mu A\ cm^{-2}$) = -0.016 + 3.2 x 10^{-3} [Tyr] µM, (R^2 = 0.9987). Finally, the Tyr_{ase}/GCE biosensor had the lowest sensitivity of 1.20 nA cm^{-2} μM^{-1} and highest LoD of 3.98 µM, where Δj ($\mu A\ cm^{-2}$) = -0.014 + 1.2 x 10^{-3} [Tyr] µM, (R^2 = 0.9987).

To evaluate the binding affinity of the immobilised enzyme (Tyr_{ase}) with its substrate Tyr, the Hill constant, h, was estimated from the slope of the relationship of log (I / I_{max}) versus log [Tyr] using the values obtained in the calibration curves. For the non-cooperative binding, the Hill constant is equal to 1.0; values of $h < 1$ indicate negative cooperative binding; this means that the binding of ligand makes the further binding more difficult. Positive cooperativity is reflected in values of $h > 1$, meaning that binding of ligand makes further binding easier.

From the Hill plot, the slopes for $Tyr_{ase}/AuNP_{green}$-PANSA/GCE, Tyr_{ase}/PANSA/GCE, Tyr_{ase}/ $AuNP_{green}$ /GCE and Tyr_{ase}/GCE biosensors were calculated to be 1.43, 1.13, 0.89 and 0.76, respectively, which indicate a strong affinity between Tyr_{ase} and Tyr at the new modified electrode support ($AuNP_{green}$-PANSA/GCE). This result indicates that the reaction between the enzyme and the target analyte (Tyr) has Michaelis-Menten type kinetics, as suggested previously [235,236]. The apparent Michaelis-Menten constant, KM, (half the maximum, saturation response of the biosensor), for $Tyr_{ase}/AuNP_{green}$-PANSA/GCE, was estimated to be 79.3 µM, a similar value to those obtained by Apetrei et al., 2013 (62.65 µM) and Apetrei et al., 2015 (88.52 µM).

A comparison of the electroanalytical properties of recently reported Tyr sensors is summarised in **Table 4.4**. The detection limit of the new platform, $Tyr_{ase}/AuNP_{green}$-PANSA/GCE was similar or lower than that of other reported biosensors. The same observation can be made for the linear range of the developed biosensor. Besides this, the novel $Tyr_{ase}/AuNP_{green}$-PANSA/GCE has several advantages, such as easy and rapid electrode modification, as well as a lower limit of detection and applied potential, compared with other biosensors for Tyr detection that have more complex architectures.

4.4.3 Repeatability and stability of Tyr$_{ase}$/AuNP$_{green}$-PANSA/GCE biosensor

The repeatability of the Tyr$_{ase}$/AuNP$_{green}$-PANSA/GCE biosensor was investigated by amperometrically measuring the response to 100 μM Tyr (BR, pH 7.0). After 20 successive assays the current was 97.5% of the initial value (RSD = 4.3%, n= 3). When not in use, the biosensors were kept in buffer (BR, pH 7.0) at 4 °C. After 20 days, the amperometric response of the biosensor for Tyr determination was 94.3% (RSD = 4.3%, n= 3) of the original, showing that the biosensor has favourable long-term stability, comparable to those reported in the literature [222,223,232].

4.4.4 Interference studies

Selectivity, a very important parameter for application to real samples, was evaluated amperometrically at -0.30 V fixed potential by the sequential addition of possible interferents after the initial addition of 100 μM Tyr. The interferents added were xanthine (100 μM), hypoxanthine (100 μM), L-tyrosine (100 μM) and dopamine (100 μM) after which a second addition of Tyr was made. The compounds xanthine, hypoxanthine, and L-Tyrosine led to a change in the current of less than 2%. Dopamine presented a reduction in current similar to Tyr, which is to be expected since it is converted to o-dopaquinone by tyrosinase. However, dopamine is not normally present in food products, the object of application of the present biosensor. For the second addition of Tyr, there was no significant change in the current response, compared with the first addition.

4.5 Determination of tyramine in food and beverages

To illustrate the practical and potential applications of the optimised electrode configuration used as impedimetric sensor (AuNP$_{green}$-PANSA/AuE) and biosensor proposed (Tyr$_{ase}$/AuNP$_{green}$-PANSA/GCE), a variety of commercial food samples including yoghurt, Roquefort cheese, red wine and beer were purchased from a local supermarket to evaluate the presence of Tyr. Amperometric and impedimetric measurements under optimal experimental conditions were applied for the quantification. Each sample was measured in triplicate, using the standard addition method, to minimise the matrix effect when analysing complex samples. The quantity of Tyr found in the original samples is given as the value obtained in the cell after dilution; which was 1:20 for dairy foods and 1:100 for fermented drinks. The results are summarised in **Table 4.5** and **4.6**.

Table 4.5 Determination of tyramine in fermented drink and dairy products at $AuNP_{green}$-PANSA/AuE.

Sample	Determined (µM)	Added (µM)	Expected (µM)	Found (µM)	RSD (%)	Recovery (%)
Roquefort cheese	4.36	2.00	6.36	6.28	2.16	98.7
Yoghurt	0.18	2.00	2.18	2.13	4.79	97.7
Red wine	1.58	2.00	3.58	3.51	3.18	98.0
Beer	1.69	2.00	3.69	3.76	4.12	101.9

Table 4.6 Determination of tyramine in fermented drink and dairy products at Tyr_{ase}/$AuNP_{green}$-PANSA/GCE.

Sample	Determined (µM)	Added (µM)	Expected (µM)	Found (µM)	RSD (%)	Recovery (%)
Roquefort cheese	4.57	2.00	6.57	6.38	3.19	97.1
Yoghurt	0.22	2.00	2.22	2.15	4.44	96.8
Red wine	1.46	2.00	3.46	3.22	4.18	93.1
Beer	1.82	2.00	3.82	3.67	4.67	96.1

For the AuNP$_{green}$-PANSA/AuE electrode, **Table 4.5**, the calculated amounts of Tyr found in Roquefort cheese and yoghurt were 59.8 mg L^{-1} and 2.47 mg L^{-1}, respectively. For the fermented drinks, it was 8.66 mg L^{-1} in red wine and 9.27 mg L^{-1} in beer samples. Recovery measurements gave values in the range from 97.7 % to 101.9 with RSDs less than 2.5%. For the Tyr$_{ase}$/AuNP$_{green}$-PANSA/GCE biosensor, it was calculated that Roquefort cheese and yoghurt contained 62.7 mg L^{-1} and 3.07 mg L^{-1} while red wine and beer contained 7.98 mg L^{-1} and 9.65 mg L^{-1}, the recovery measurements gave values in the range from 97.7 % to 101.9 % with RSD values of less than 5.0 %, **Table 4.6**. The values found in each food sample were in agreement with those expected [237–239], indicating the reliability of the two electrochemical approaches proposed for Tyr quantification and their usability for practical applications in food safety control.

4.6 Conclusions

This study has demonstrated the possibility of developing of two electrochemical approaches, namely impedimetric-based (AuNP$_{green}$/PANSA/AuE) sensor and an enzyme based-biosensor (Tyr$_{ase}$/AuNP$_{green}$/PANSA/GCE) for monitoring tyramine in food samples. Green synthesised gold nanoparticles (AuNP$_{green.}$) were attached on poly(8-anilino-1-naphthalene sulphonic acid)(PANSA) films obtained by polymerisation of the monomer in the presence of AuNP$_{green}$. The formation of AuNP$_{green}$ was initially monitored by visual observation and then characterised by using X-ray diffraction (XRD) and scanning electron microscopy (SEM). The XRD study showed that the biosynthesised AuNP are crystalline in nature and morphology of the particles synthesised consisted globally in a spheric-like structure with particle size at ~ 20 nm, similar size to the AuNP synthesised by the classical Turkevich method, see Chapter 3. SEM images also show that the nanocomposite was successfully obtained by the presence of AuNP$_{green}$ covering all PANSA network indicating the efficiency of the method used for attaching gold nanoparticles. Under optimal conditions, both electrochemical approaches showed excellent electrochemical properties for detection of tyramine in food samples. Furthermore, both electrochemical approaches have been successfully applied to determine tyramine in commercial food products with good recoveries, auguring well for their use in food safety control.

Chapter 5

Glucose biosensor based on poly (brilliant green) (PBG) - ethaline deep eutectic solvent (DES) /carbon nanotube modified electrode for biotoxic trace metal ion detection

---

This chapter describes the development of a novel biosensor based on GOx immobilised on ultra-thin poly(brilliant green) (PBG) films electrodeposited in ethaline DES on multi-walled carbon nanotube (MWCNT) modified glassy carbon electrodes (GCE) for enzyme inhibitive amperometric detection of Hg^{2+}, Cd^{2+}, Pb^{2+}, and Cr^{VI}. The influence of different acid doping agents (SO_4^{2-}, NO_3^-, Cl^-, and COO^- anions) and scan rate on the electrodeposition of PBG was probed. The performance of the nanocomposite modified GCE was evaluated by cyclic voltammetry (CV) and electrochemical impedance spectroscopy (EIS). Scanning electron microscopy (SEM) was used to examine the morphology of the nanostructures and their influence on electrochemical properties. Comparison with PBG films electrodeposited in aqueous solution was also made. In the fabrication of the biosensor, other factors were also considered, such as the degree of inhibition of the activity of GOx by injection of different trace metal ions, operational stability, sensitivity, and reproducibility. The elucidation of the mechanism of inhibition was estimated by a new graphical method, instead of the classical Dixon and Cornish-Bowden plots.

This research has been submitted for publication.

5.1 Polymerisation in aqueous media - the influence of the acid dopant on PBG film growth

The polymerisation of brilliant green was first carried out on MWCNT/GCE in aqueous medium, by cycling the potential between -1.0 and 1.2 V vs. Ag/AgCl in a 0.5 M solution of the acids H_2SO_4, HCl, HNO_3 and CH_3COOH at 50 mV s^{-1}, **Fig. 5.1**. The supporting electrolyte plays an important role in the growth of conducting polymers. In the case of PBG, this has a significant influence, since the protonic acid doping of the polymer leads to a different mechanism of nucleation. This affects both the yield and the electrochemical behaviour of the formed films, as seen in in the different voltammetric profiles in **Fig. 5.2**. The mechanism of polymerisation of BG begins with the oxidation of the secondary amino groups which form cation radicals and attack benzene rings in a free ortho-position relative to the amino group, initiating the polymerisation. In different acid solutions, **Fig. 5.1**, similar behaviour was observed for all electropolymerisations, having one redox pair with midpoint potential value at~ 0.5 V, with currents increasing in all cases, except for nitric acid solution, in which the peaks decrease. In H_2SO_4, an oxidation peak at~ 0.8 V was also observed, which is attributed to monomer oxidation [240].

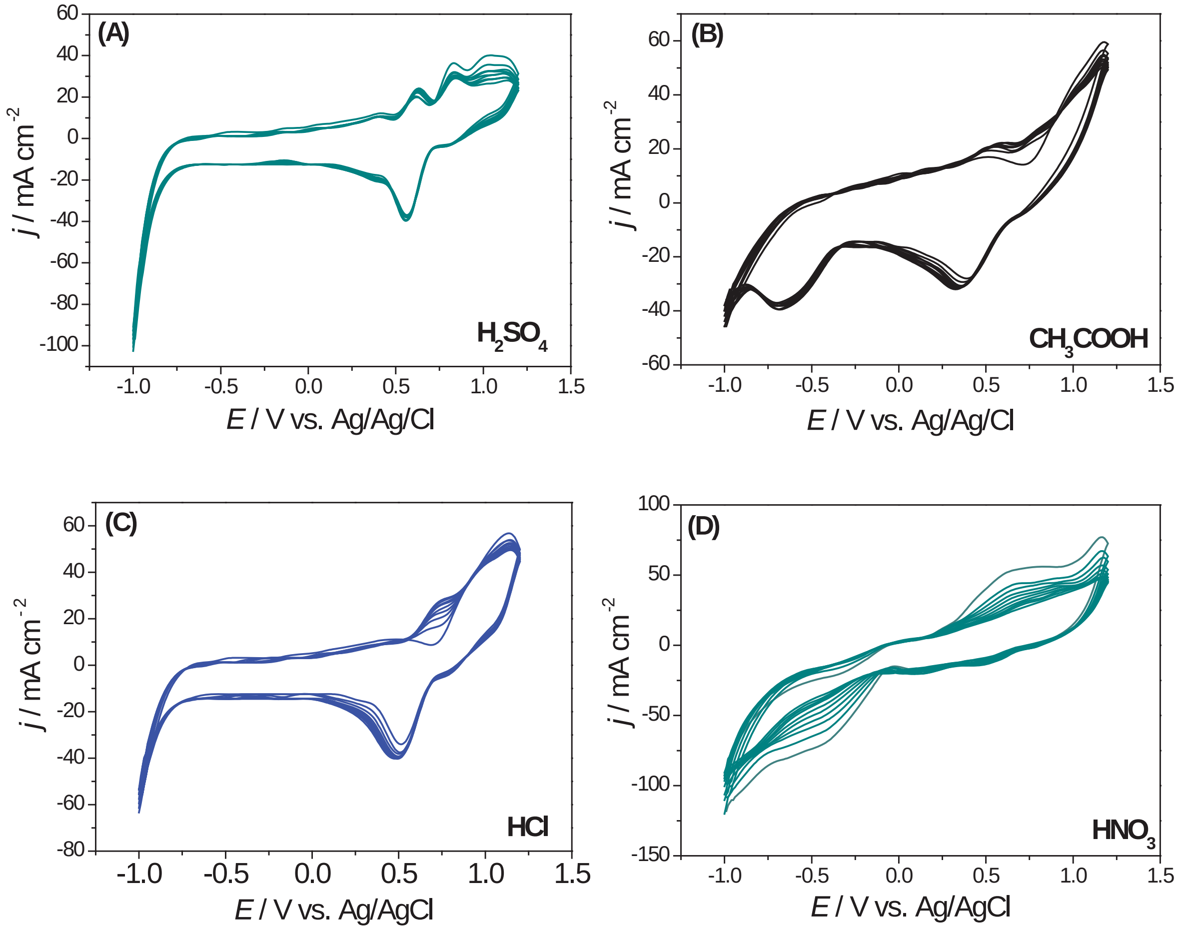

Fig. 5.1 CVs recorded during electropolymerisation of brilliant green on multi-walled carbon nanotube modified glassy carbon electrode in a solution containing 1.0 mM of BG in different acid media, 0.5M: (A) H_2SO_4; (B) CH_3COOH; (C) HCl; (D) HNO_3 aqueous solution at 50 mV s^{-1}.

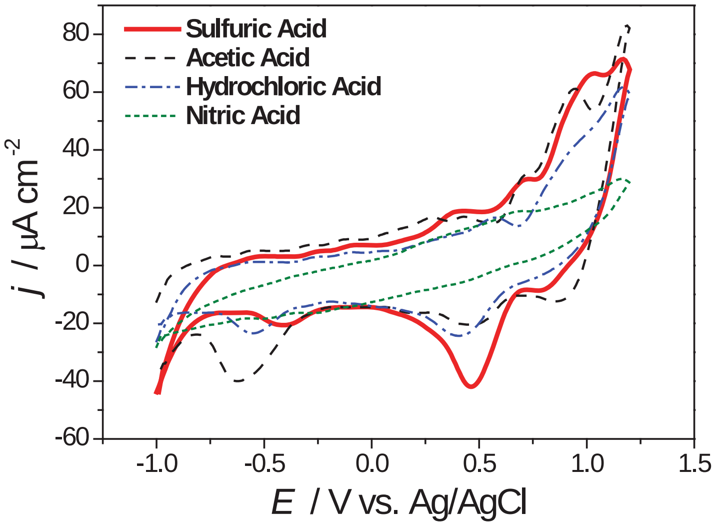

Fig. 5.2 Cyclic voltammograms of PBG/MWCNT/GCE formed in different acidic aqueous media: (———) sulfuric, (- - - -) acetic, (- · - · -) hydrochloric and (· · · · ·) nitric acid, in 0.1 M PB solution (pH 7.0) at 50 mV s^{-1} scan rate.

After electropolymerisation for 10 cycles, the anodic peak currents at ~0.5 V were found to be 10.8, 4.94, 3.98, and 0.5 µA cm^{-2}, for PBG formed in solutions of the acids H_2SO_4, HCl, HCOOH, and HNO_3, respectively. In the case of HNO_3, the polymer film was not stable as evidenced by the fact that the anodic peak current decreased with the number of cycles. Cyclic voltammograms recorded in 0.1 M PB pH 7.0 after polymerisation, **Fig. 5.2**, also showed that the current peak corresponding to the polymer,~ 0.5 V, was the highest for the film deposited in H_2SO_4. Taking into account the better-defined polymer peaks during polymerisation, the presence of monomer oxidation peak, as well as higher polymer peak currents after polymerisation the conclusion was that H_2SO_4 would be the best choice of acid-dopant for polymerisation in DES.

5.2 Influence of the scan rate on BG polymerisation in ethaline – DES

For BG electropolymerisation in DES, a solution of 1.0 mM BG with 0.5 M H_2SO_4 in a 10 % v/v of water: 90 % v/v ethaline mixture was prepared, see Chapter 2 Section 2.9, for more details. The PBG film was grown on MWCNT/GCE at scan rates in the range from 50 to 200 mV s^{-1}, during 10 cycles, sweeping the potential between -1.0 and 1.2 V vs. Ag/AgCl.

As seen in **Fig. 5.3A-D**, the peak current increased with increasing scan rate, up to the highest at 150 mV s^{-1}; the decrease above this can be ascribed to diffusion limitations [241].

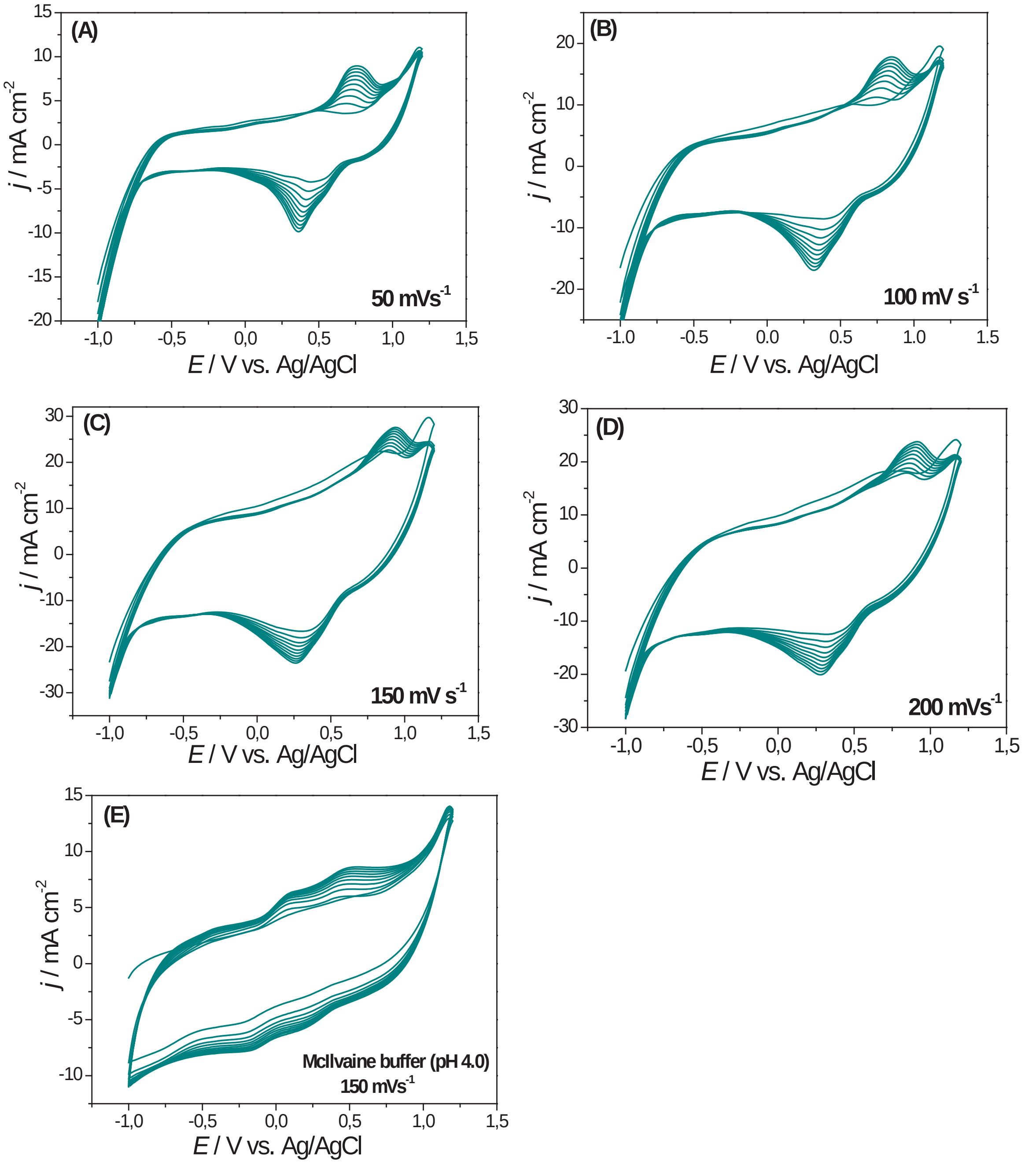

Fig. 5.3 CVs recorded during electropolymerisation of BG on MWCNT/GCE in ethaline + (0.5 M H_2SO_4 + 10 % H_2O) at scan rates: (A) 50 mV s^{-1}; (B) 100 mV s^{-1}; (C) 150 mV s^{-1}; (D) 200 mV s^{-1}; (E) electropolymerisation of BG in aqueous McIlvaine buffer solution pH 4.0 at 150 mV s^{-1}.

Cyclic voltammograms recorded in ethaline-H_2SO_4 (pH 2.0), **Fig. 5.3A-D**, for all sweep rates are quite similar, and the redox peaks are shifted toward more positive potentials compared with those of PBG_{aq} electrodeposited in McIlvaine buffer (pH 4.0) aqueous solution, **Fig. 5.3E**. This shift is directly related to the pH, with protons being inserted from the solution into the polymer during the oxidation processes, and expelled during reduction. The oxidation peak currents recorded during the first five cycles increase continuously and indicate the formation of cation radicals. However, from the 5th to 10th cycles this increase slows down, due to the polymer deposited during the first cycles impeding further oxidation of the monomer on the electrode surface, so that hardly any radical cations and/or polymer are formed at this stage. Therefore, 10 cycles were selected for further electropolymerisation studies. The same tendency is observed in the cyclic voltammograms for the polymerisation of BG in aqueous solution, McIlvaine buffer (pH 4.0), at 150 mV s^{-1}, **Fig. 5.3E**.

5.3 Characterisation of the nanostructured films

5.3.1 Cyclic voltammetry

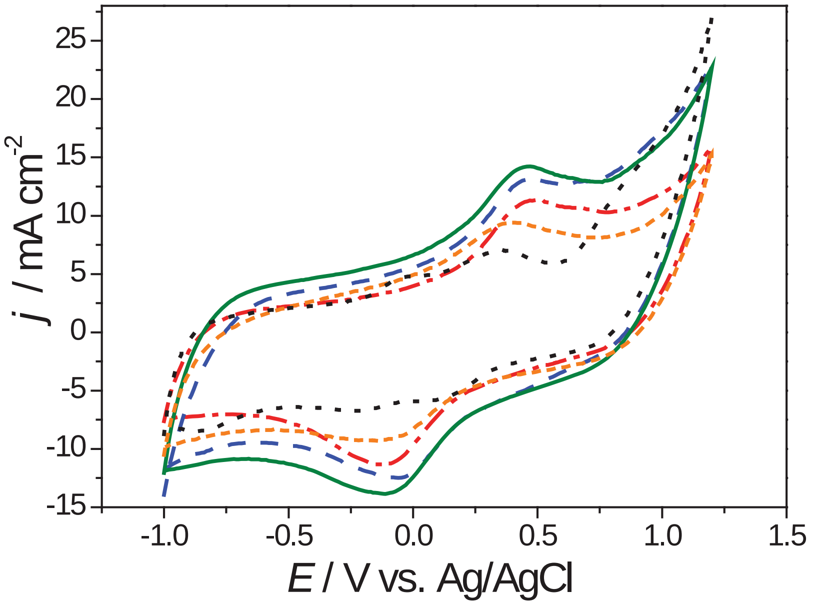

Fig 5.4 CVs of PBG/MWCNT/GCE in 0.1M PB solution (pH 7.0) at 50 mV s^{-1}: (———) $PBG_{ethaline}150$-MWCNT/GCE; (— — —) $PBG_{ethaline}200$-MWCNT/GCE; (–·–·–) $PBG_{ethaline}100$-MWCNT/GCE; (- - - - -) $PBG_{ethaline}50$-MWCNT/GCE; (· · · · ·) PBG_{aq}-MWCNT/GCE.

To evaluate the electrochemical behaviour of PBG films electrodeposited on MWCNT/GCE, cyclic voltammograms of the modified electrodes were recorded in 0.1 M PB solution (pH 7.0) at a potential scan rate of 50 mV s^{-1}.

Fig. 5.4 shows CVs of MWCNT/GCE modified with PBG_{DES} electrodeposited at different scan rates, and PBG_{aq} electrodeposited at 150 mV s^{-1}. As observed, the anodic and cathodic peak currents corresponding to PBG_{DES} films increase with the electropolymerisation scan rate, up to 150 mV s^{-1}. The decrease for PBG_{DES} films electrodeposited at 200 mV s^{-1} may be attributed to the viscosity of the DES that makes diffusion of ionic species at higher sweep rate more difficult, as seen in [242]. PBG formed in aqueous medium, McIlvaine buffer (pH 4.0), exhibits lower peak currents than PBG_{DES} films. The PBG_{DES} film electrodeposited at 150 mV s^{-1} presented the highest currents and was therefore chosen as the best electrode platform for glucose oxidase immobilisation.

5.3.2 Electrochemical impedance spectroscopy

Electrochemical impedance spectroscopy was used to analyse the interfacial properties of MWCNT/GCE modified with $PBG_{ethaline}$ films obtained at different scan rates ($PBG_{ethaline}$50-MWCNT/GCE**,** $PBG_{ethaline}$100/MWCNT/GCE, $PBG_{ethaline}$150-MWCNT/GCE, and $PBG_{ethaline}$200-MWCNT/GCE, respectively) and PBG_{aq}150-MWCNT/GCE film (PBG obtained in McIlvaine buffer solution, pH 4.0 at 150 mV s^{-1}). The applied potential was 0.5 V vs. Ag/AgCl, the approximate value of the midpoint potential of the PBG redox process in all cases, chosen from cyclic voltammograms recorded at the modified electrodes, **Fig. 5.5**. Complex plane impedance spectra are illustrated in **Fig. 5.5A** and were fitted to the equivalent electrical circuit in **Fig. 5.5B**. The circuit comprises a cell resistance, $R_{\Omega,}$ in series with a parallel combination of a resistance, R_1 and constant phase element (CPE_1) which is modelled as non-ideal capacitor expressed by $CPE = 1 / (i\omega C)^{\alpha}$, where C is the capacitance, ω is the frequency in rad s^{-1} and the exponent, $0.5 < \alpha < 1$, reflects the surface non-uniformity and roughness of the modified electrodes, $\alpha = 1$ corresponding to a perfect uniform and a smoothed surface. This is used to fit the semicircle in the high-frequency region of the spectra, describing the process occurring at the electrode/modifier film interface. The medium frequency region is modelled by a mass transport finite-diffusion Warburg element Z_W. The Warburg element, Z_w, results from the equation: $Z_w = R_D \mathrm{cth}[\tau i\omega)^{\alpha}]$ x $[\tau i\omega)^{\alpha}]$, where $\alpha < 0.5$, and is characterised by a diffusional time constant (τ), a diffusional pseudocapacitance (C_D) and a diffusional resistance ($R_D = \tau / C_D$) [153]. Finally, a second combination of a resistance,

R_2, and a second constant phase element, CPE_2, describes both the charge separation at the polymer/solution interface and the polarisation of the polymer films. This electrical circuit was also used to fit the spectra obtained from the poly(methylene blue) films electrodeposited on MWCNT in ethaline [243].

The data obtained from fitting to the equivalent circuit are summarised in **Table 5.1**. As seen in Fig **5.5A**.

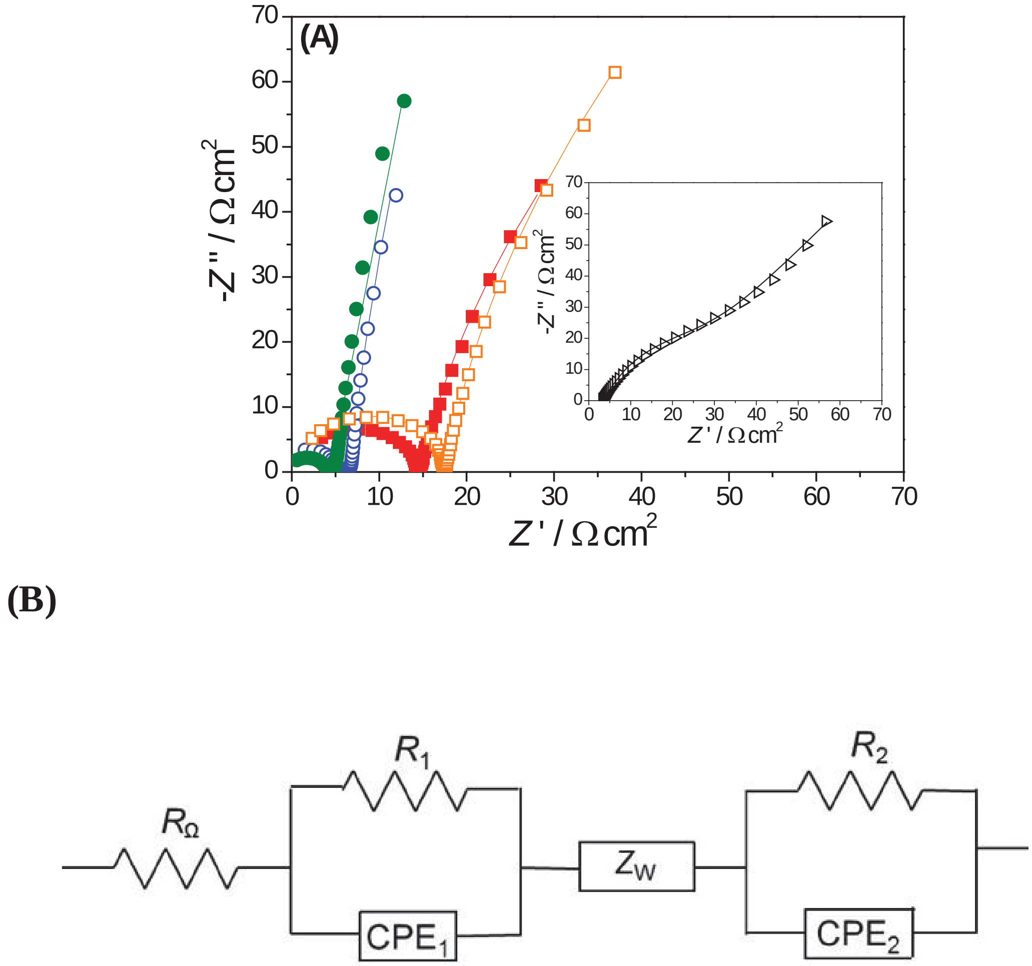

Fig. 5.5 (A) Complex plane impedance spectra recorded at (●) $PBG_{ethaline}$150-MWCNT/GCE; (○) $PBG_{ethaline}$200-MWCNT/GCE;(■) $PBG_{ethaline}$100-MWCNT/GCE; (□) $PBG_{ethaline}$50-MWCNT/GCE; (▷) PBG_{aq}150-MWCNT/GCE in 0.1M PB solution (pH 7.0) at 0.5 V vs. Ag/AgCl. **(B)** Electrical equivalent circuit used to model the spectra.

Table 5.1 Values of parameters from impedance spectra in 0.1 M PBS (pH 7.0), fitted to the electrical equivalent circuit in Fig.3C for PBG films deposited on MWCNT/GCE in ethaline, at different scan rates, and in aqueous solution.

Scan rate / mV s^{-1}	R_1 / Ω cm^2	CPE_1/ (μF cm^{-2} $s^{\alpha-1}$)	α_1	Z_w / Ω cm^2	τ / ms	α_{zw}	R_2 / Ω cm^2	CPE_2 /(mF cm^{-2} $s^{\alpha-1}$)	α_2
$PBG_{ethaline}50$	16.5	0.39	1.0	0.98	0.09	0.44	174.1	27.3	0.89
$PBG_{ethaline}100$	13.4	0.46	0.99	1.33	0.12	0.44	148.4	45.1	0.85
$PBG_{ethaline}150$	4.4	0.66	0.99	1.71	0.18	0.45	98.3	78.4	0.84
$PBG_{ethaline}200$	8.4	0.56	0.98	1.74	0.76	0.44	132.2	56.3	0.95
$PBG_{aq}150$	98.4	0.18	0.84	0.30	0.03	0.43	230.4	12.5	0.83

There is a gradual decrease of the high-frequency semicircle diameter with increase of scan rate used for the electrodeposition of $PBG_{ethaline}$, corresponding to a decrease in the charge transfer resistance. The charge separation is influenced by the polymer bulk structure, reflected by the increase of the capacitance values up to $PBG_{ethaline}$ electrodeposited at 150 mV s^{-1}, then at 200 mV s^{-1}, there is a decrease. The PBG_{aq}150/MWCNT/GCE film presents a broad semicircle at high-frequency regions with a higher charge transfer resistance and smaller capacitance value.

The values of diffusional resistance, $Z_{w,}$ for $PBG_{ethaline}$ increased up to 150 mV s^{-1} ($PBG_{ethaline}$150-MWCNT/GCE) at polymer films electrodeposited in ethaline, much higher than for that in aqueous solution (McIlvaine buffer solution, pH 4.0), which may due to the formation of thicker films, thicker with increasing electropolymerisation scan rate, as revealed by SEM, see below. The average $\alpha_{zw} \approx 0.44$, which is close to 0.5, is characteristic of a semi-infinite diffusional impedance usually found at ultrathin modified electrodes [240].

Lastly, the R_2 values of the nanostructured films are in the order: PBG_{aq}150/MWCNT/GCE > $PBG_{ethaline}$50/MWCNT/GCE > $PBG_{ethaline}$100/MWCNT/GCE > $PBG_{ethaline}$200/MWCNT/GCE > $PBG_{ethaline}$150/MWCNT/GCE. This indicates that the easiest electron transfer occurs for the final electrode configuration, in agreement with cyclic voltammetry observations.

5.3.3 Morphological characterisation of nanostructures

Fig. 5.6 displays SEM images of PBG films formed by electropolymerisation on MWCNT modified carbon film electrodes formed in aqueous McIlvaine buffer solution (pH 4.0), and in ethaline-DES at scan rates 50, 100,150 and 200 mV s^{-1}. For comparison, an image of MWCNT on the carbon electrode support without electrodeposited polymer is also shown. The SEM image in **Fig. 5.6A** shows a randomly entangled and cross-linked of MWCNT network spread over the electrode surface.

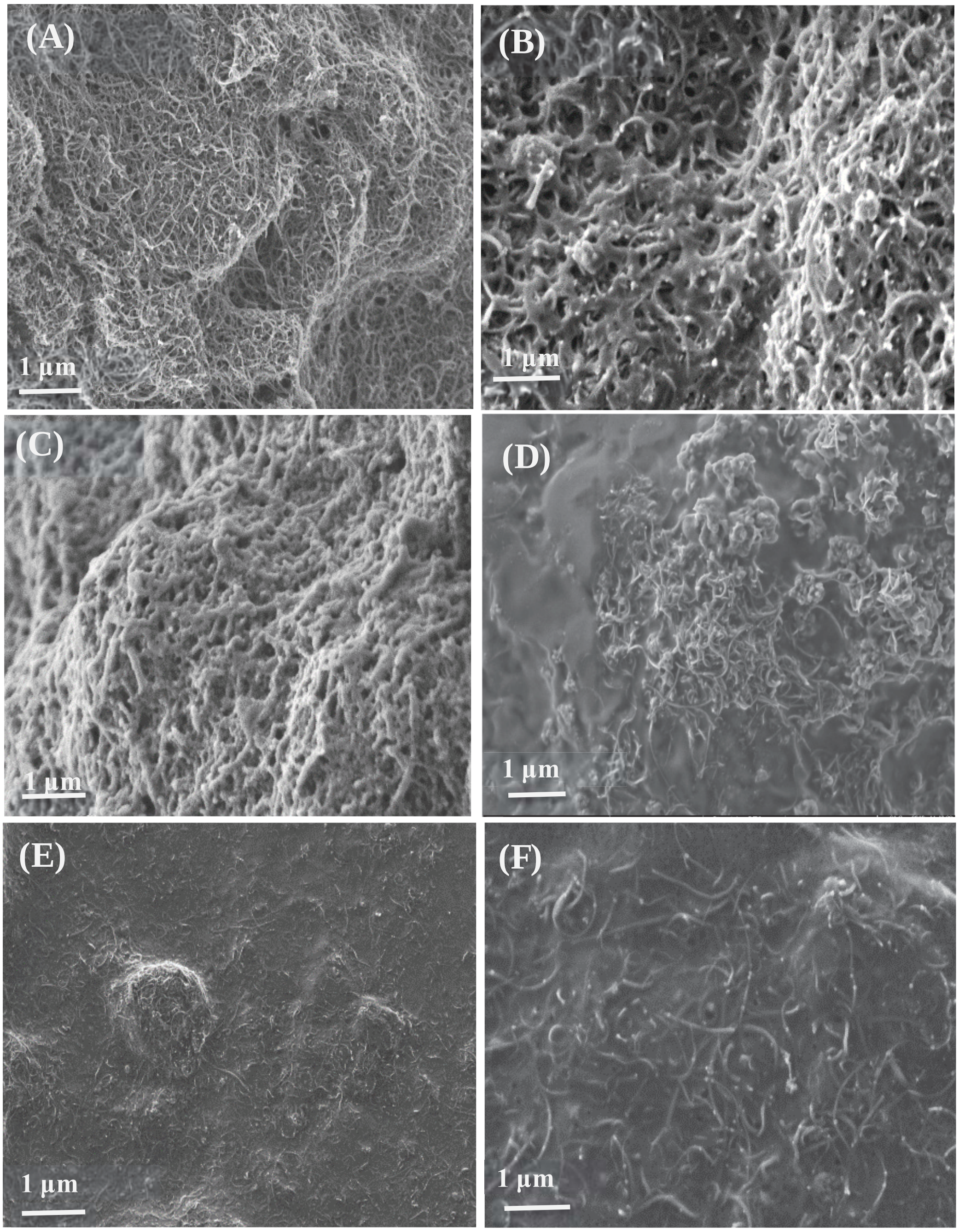

Fig. 5.6 SEM images on carbon film electrodes of **(A)** MWCNT; **(B)** PBG$_{aq}$/MWCNT (electropolymerised at 150 mV s^{-1}); **(C)** PBG$_{ethaline}$50/MWCNT; **(D)** PBG$_{ethaline}$100/MWCNT; (E) PBG$_{ethaline}$150/MWCNT; (F) PBG$_{ethaline}$200/MWCNT.

The PBG formed by electropolymerisation in aqueous McIlvaine buffer (pH 4.0), exists as a relatively thin film on the MWCNT surface, see **Fig. 5.6B**, which leads to only a slight increase in the diameter of the MWCNT.

The morphology of $PBG_{ethaline}$ films, that is those formed in ethaline, was examined as a function of the electropolymerisation scan rate, Fig. **5.6C-F**. The thickness of the polymer films is greater than that in aqueous McIlvaine buffer (pH 4.0). The $PBG_{ethaline}$ films from electropolymerisation at 50 mV s^{-1}, **Fig. 5.6C**, exhibit a visibly rough and porous surface structure; at higher scan rates, there is formation of more compact and thicker nanostructures. For the $PBG_{ethaline}$ film made at 100 mV s^{-1}, a mix of compact and smooth areas with porous structures is observed, but for the films prepared at 150 and 200 mV s^{-1}, the formation of a more uniform and smooth surface is seen. This is in agreement with the literature [244,245], and can be explained based on the relative rates of nucleation and polymer growth. At slower scan rates, the number of nucleation sites generated on the MWCNT surface is smaller and the relatively large amount of time spent in the potential range of polymer oxidation leads to rapid growth of PBG nuclei. As a result, a thinner and rougher film is formed.

On the other hand, at a higher scan rate, formation of more PBG nuclei is favoured, but less growth. As a result, **Fig. 5.6C-F**, a successively smoother and more compact surface is obtained, as the scan rate increases.

5.4 GOx/PBG_{DES}150/MWCNT/GCE biosensor for glucose determination

Enzyme biosensors for glucose determination using glucose oxidase (GOx) immobilised on the best performing PBG modified MWCNT/GCE, with PBG deposited at 150 mV s^{-1}. GOx was immobilised on the optimised modified electrode, and the novel biosensor under optimal conditions was tested for both determination of glucose and biotoxic trace metal ions by enzymatic inhibition method.

5.4.1 Influence of the applied potential – optimisation for glucose detection

The influence of the applied potential on the GOx/PBG$_{\text{ethaline}}$150/MWCNT/GCE biosensor response towards 100 μM glucose was performed in the range of -0.9 to -0.2 V vs. Ag/AgCl, **Fig. 5.7**.

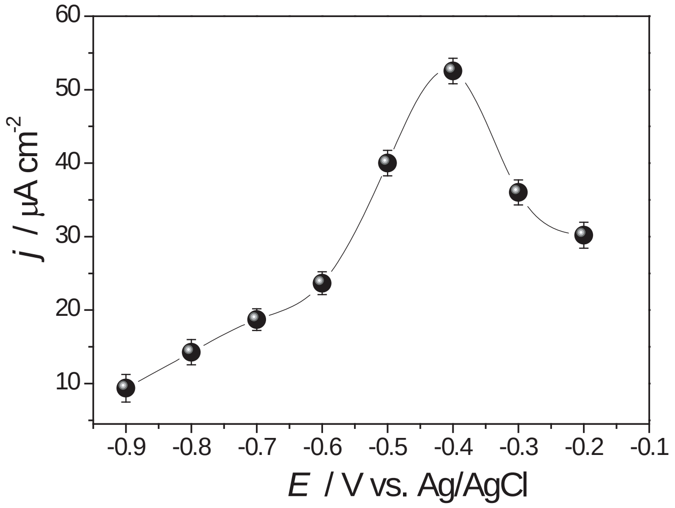

Fig. 5.7 Dependence of the glucose response at GOx/PBG$_{\text{ethaline}}$150/MWCNT/GCE on applied potential in 0.1 M PB solution (pH 7.0) in the presence of 100 μM glucose.

As can be seen, the response to glucose increments increases at a less negative potential, between -0.9 and -0.4 V, where the maximum was achieved, and then begins to decrease slightly. Therefore, an applied potential of -0.4 V vs. Ag/AgCl, was selected for further experiments.

5.4.2 Amperometric biosensing for glucose determination

Fig. 5.8A displays the amperometric response for glucose at the GOx/PBG$_{\text{ethaline}}$150/MWCNT/GCE biosensor. Stock solution of 1 mM and 2 mM glucose in 0.1 M PB (pH 7.0) were prepared for glucose determination. The measurements were performed by the addition of aliquots of the stock glucose solutions to an electrochemical cell containing 0.1 M PB (pH 7.0) electrolyte solution, under continuous stirring at an applied potential of - 0.4 V vs. Ag/AgCl. A well-defined response rapidly reaching a stable plateau was recorded after each glucose addition that was linear with glucose concentration in the range from 5 μM to 100 μM, Fig. **Fig. 5.8B**.

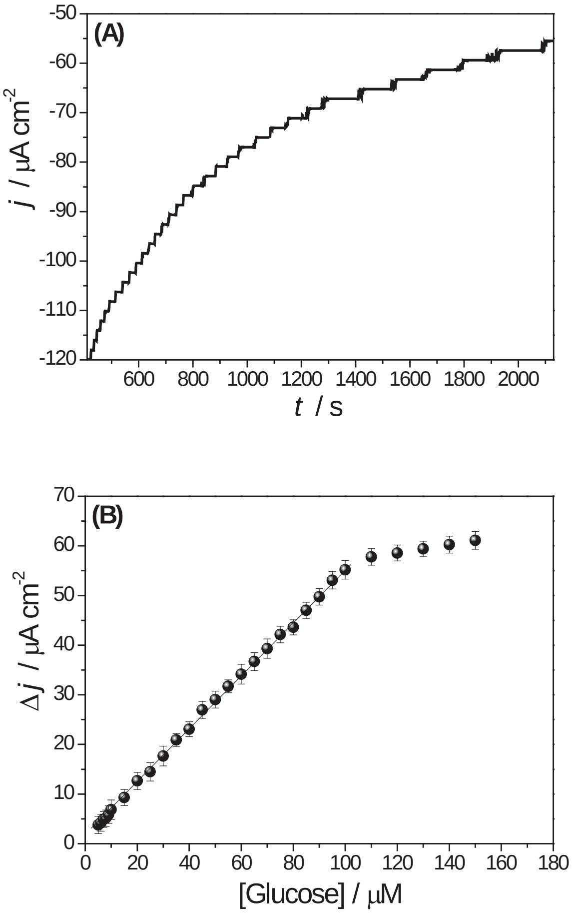

Fig. 5.8 (A) Amperometric response of GOx/PBG$_{\text{ethaline}}$150/MWCNT/GCE biosensor to glucose in 0.1 M PB solution, pH 7.0; applied potential -0.4 V vs. Ag/AgCl. **(B)** Calibration curve obtained from injection of increasing concentrations of glucose (0 -150 μM).

The calibration curve followed the equation: Δ*j* (μA cm^{-2}) = 1.33+0.54 [glucose] μM, and the limit of detection was estimated to be 2.33 μM, which is the best electrochemical performance compared with some of the most recent GOx biosensors for glucose determination in the literature [246–250]. The binding affinity of the immobilised enzyme

GOx with its substrate (glucose), the Hill constant, *h*, was estimated from the slope of the plot of log ($I/I_{\max}$) versus log [glucose]. The Hill plot slope was 1.24; this value reflects positive cooperativity, h >1, [235] meaning a high binding affinity of the immobilised enzyme (GOx) with its substrate and indicates that the reaction between enzyme and target analyte has Michaelis-Menten type kinetics. The Michaelis-Menten constant for GOx/PBG$_{\mathrm{DES}}$150/MWCNT/GCE was estimated to be 53 μM.

5.5 Optimisation of the biosensor for inhibition procedures

In order to evaluate the inhibition of the activity of glucose oxidase (GOx), amperometric measurements were made in 0.1 M PB solution (pH 7.0) at -0.4 V vs. Ag/AgCl. After stabilisation of the baseline current, a chosen glucose concentration was added, and the steady current recorded (I_0). Next, known concentrations of trace metal ions were added to inhibit the enzyme activity and the current was measured (I_1). The decrease in current is proportional to the concentration of inhibitor in solution. The percentage of inhibition, I %, is calculated according to [251]:

$$I\ \% = \frac{I_0 - I_1}{I_0} \text{ x } 100 \qquad (5.1)$$

5.5.1 Influence of the enzyme loading

The influence of the amount of immobilised enzyme was investigated at a constant concentration of BSA (30 mg mL^{-1}) and varying the concentration of GOx (5.0, 10.0, 15.0, 20.0, 25.0 and 30.0 mg mL^{-1}) immobilised on the optimised PBG$_{\mathrm{ethaline}}$150/MWCNT/GCE electrode support, as described in the experimental section. The amperometric response to 0.5 mM glucose was tested for different enzyme loadings at an applied potential of - 0.4 V vs. Ag/AgCl. The total anodic change in current increases as the amount of GOx increases, reaching a maximum at 25.0 mg mL^{-1} GOx. For higher loadings, there is a decrease in biosensor response, indicating that high concentrations of enzyme compromise biosensor response due to diffusion limitations.

The degree of inhibition for each enzyme loading was also assessed by evaluating the GOx activity in the presence of glucose by the addition of 20 nM of each metal ion in individual experiments. For all metals studied, the percentage of inhibition increased with increase in enzyme loading up to 20.0 mg mL^{-1} above which it remained the same. Therefore, 20.0 mg mL^{-1} of the enzyme was chosen as optimum.

5.5.2 Influence of the pH

The enzyme biosensor response can depend significantly on the pH of the solution. The effect of the pH was investigated by comparing the sensitivities of the calibration curves obtained from additions of each inhibitor at GOx/PBG$_{\mathrm{ethaline}}$150/MWCNT/GCE with 0.5 mM glucose as enzyme substrate, see **Table 5.2**.

Table 5.2 Effect of pH on amperometric response to 20 nM of different metal ions in 0.1 M PB (pH 7.0) at PBG$_{\mathrm{ethaline}}$150/MWCNT/GCE biosensor in the presence of 0.5 mM glucose at applied potential -0.4 V vs. Ag /AgCl.

Metal ion	Sensitivity (μA cm^{-2} nM^{-1})			Inhibition % (20 nM)		
	pH 6.0	pH 7.0	pH 8.0	pH 6.0	pH 7.0	pH 8.0
Hg^{2+}	0.98	1.26	0.78	16.5	24.2	14.9
Cd^{2+}	0.90	1.16	0.84	17.0	22.2	11.3
Pb^{2+}	0.94	1.23	0.73	5.2	8.8	3.7
Cr^{VI}	0.86	1.15	0.78	11.2	23.2	7.2

Amperometric measurements were performed at pH values between 6.0 and 8.0, at a fixed applied potential of -0.4 V vs. Ag/AgCl. The sensitivity to all trace metal ions increased from pH 6.0 to pH 7.0 and at pH 8.0 became lower again. This trend in the GOx response is the same as without the presence of inhibitors. Hence, pH 7.0 was selected as the more suitable pH value.

5.6 Determination of the mechanism of inhibition and analytical determination of Hg^{2+}, Cd^{2+}, Pb^{2+}, and Cr^{VI} ions through enzyme inhibition

The mode of interaction between the metal ions and the active site of GOx, in the mechanism of reversible inhibition of Hg^{2}, Cd^{2+}, Pb^{2+} and, Cr^{VI} was deduced from plots of the percentage of inhibition versus inhibitor concentration, for various substrate concentrations. The traditional method requires both Dixon and Cornish-Bowden plots to fully elucidate the type of inhibition because Dixon plots for mixed and competitive inhibition are similar and from the Cornish-Bowden plot it is not possible to determine the inhibition constant for competitive inhibition [126,127]. In the new method [252], the effect of different substrate concentrations on I_{50} (concentration of inhibitor necessary to inhibit 50 % of the initial response to the substrate) is evaluated. Here, three different glucose concentrations: 0.25, 0.5, and 1.0 mM were employed, as shown in **Fig. 5.9**.

For competitive inhibition, when the substrate concentration increases, the values of I_{50} also increase, and the maximum inhibition decreases, observed for Hg^{2+} and Cd^{2+}, **Fig. 5.9A** and **5.9B**. On the other hand, when the values of I_{50} decrease with increasing substrate concentration, and the maximum inhibition value increases, the mechanism is uncompetitive inhibition, as seen for Pb^{2+}, **Fig. 5.9C**. Finally, for mixed inhibition, only a slight change in I_{50} occurs, as happens with Cr^{VI}, **Fig. 5.9D**. For verification purposes, the mechanism of inhibition was also evaluated from Dixon, and Cornish-Bowden plots; the same tendency was found. The mechanism of inhibition for each metal ion agrees with that reported in the literature[253–255].

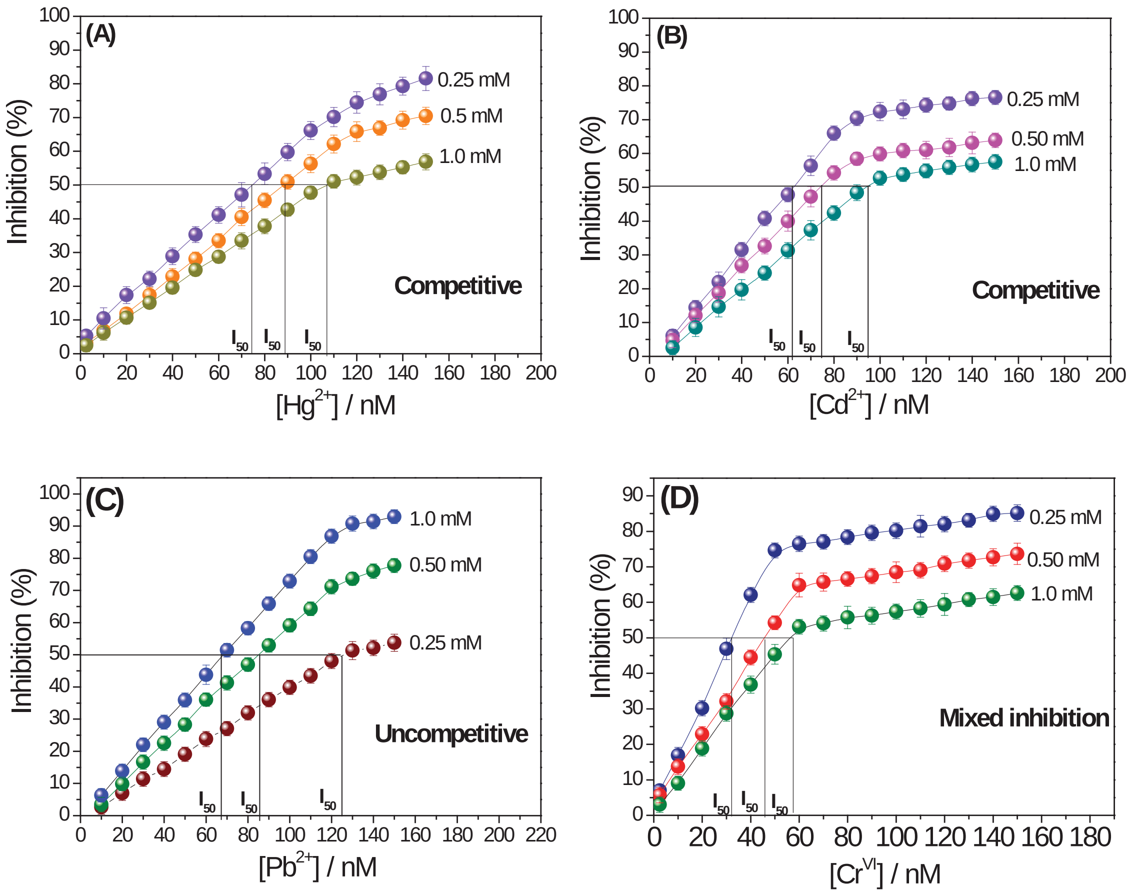

Fig. 5.9 Plots for determination of the mechanism of inhibition of the trace metal ions in 0.1 M PB solution (pH 7.0), according to [252], in the presence of three different concentrations of glucose at applied potential -0.4 V vs. Ag/AgCl.

As seen above, the concentration of the enzyme substrate needs to be carefully chosen, **Fig. 5.9**, that gives the response for 0.25, 0.5, and 1.0 mM glucose, shows that for 0.25 mM enzyme-substrate, after the first addition of inhibitor, more than 10 % inhibition occurs. On the other hand, the maximum inhibition decreases with increase in glucose concentration, except for Pb^{2+}. Hence, the intermediate concentration of 0.5 mM glucose was chosen as the best value for inhibitor quantification.

Under these conditions, the trace metal ions were determined at the GOx/PBG$_{ethaline}$150/MWCNT/GCE biosensor, and the limit of detection was calculated based on a signal-to-noise ratio of 3 (S/N=3).

Table 5.3 Parameters of inhibition obtained from the relationship between I_{50} and inhibition constant K_i. Equations from [252].

Metal ion	Mechanism of inhibition	Equation	K_i / nM	I_{10} / nM	I_{50} / nM
Hg^{2+}	Competitive	$\frac{I_{50}}{K_\mathrm{i}} = \left(1 + \frac{[\mathrm{S}]}{K_\mathrm{M}}\right)$	8.39	15.4	88.0
Cd^{2+}	Competitive	$\frac{I_{50}}{K_\mathrm{i}} = \left(1 + \frac{[\mathrm{S}]}{K_\mathrm{M}}\right)$	7.08	18.0	74.1
Pb^{2+}	Uncompetitive	$\frac{I_{50}}{K_\mathrm{i}} = \left(1 + \frac{K_\mathrm{M}}{[\mathrm{S}]}\right)$	77.3	10.9	85.4
Cr^{VI}	Mixed	$\frac{I_{50}}{K_\mathrm{i}} = 2\left(\frac{1 + \frac{[\mathrm{S}]}{K_\mathrm{M}}}{2 + \frac{[\mathrm{S}]}{K_\mathrm{M}}}\right)$	25.2	6.3	45.9

I_{10} - Concentration necessary for 10 % inhibition of the initial response of the substrate; I_{50} – Concentration necessary for 50 % inhibition of initial response of the substrate; K_i - Inhibition constant; K_M - Michaelis-Menten constant of the enzyme without the presence of inhibitor; [S] – Enzyme substrate concentration

Table 5.4 Comparison of performance of recent modified electrode-based enzyme biosensors using enzyme inhibition for trace metal ion determination.

Biosensor	Inhibitor	Mode of detection	Applied potential and pH	Linear range / µM	Detection limit / nM	Reactivation	Inhibition type	Ref.
PPy-GOx/Pt	Cd^{2+}	Amperometry	+ 0.7 V vs. (Ag/AgCl), pH 7.0	4.0 – 26	4000	EDTA, 2 mM (10 s)	competitive	[253]
	Pb^{2+}			1.6 – 7.7	1600		mixed	
	Hg^{2+}			0.48 – 3.3	480		non-competitive	
PPy-GOx/Pt	Cd^{2+}	Potentiometry	Zero current* vs.(Ag/AgCl), pH 7.0	0.04–62	44	phosphate buffer 0.05 M, (15 min)	competitive	[254]
	Pb^{2+}			0.10- 15	24		non-competitive	
	Hg^{2+}			0.025–5.0	25		non-competitive	
GOx/PANI/Fc/Pt	Cr^{VI}	Amperometry	+ 0.7 V vs. (SCE), pH 2.55	0.49 - 95.73	9.0	phosphate buffer 0.05 M, (8 min)	*	[255]
$PBG_{DES}150$-MWCNT/GCE	Hg^{2+}	Amperometry	- 0.4 V vs. (Ag/AgCl), pH 7.0	0.0025-0.100	2.30	-	competitive	This work
	Cd^{2+}			0.010-0.080	1.75		competitive	
	Pb^{2+}			0.010-0.120	2.70		uncompetitive	
	Cr^{VI}			0.0025-0.060	2.44		mixed	

From **Fig. 5.9A**, the linear range obtained for Hg^{2+} was 2.5-100 nM, with a LOD of 2.30 nM. For Cd^{2+}, **Fig. 5.9B**, the linear concentration range was 10 -100 nM and the calculated LOD was 1.75 nM. **Fig. 5.9C** shows a linear response to Pb^{2+} from 10 -120 nM presenting a LOD of 2.70 nM. Finally, for Cr^{VI}, the linear range was from 2.5-60 nM with the LOD of 2.44 nM.

The enzyme inhibition constant (K_i) was estimated from the equations of the relationship between I_{50} and K_i, valid for all type of inhibition, as proposed by Amine et al. [252], **Table 5.3**. Hg^{2+}, Cd^{2+} and Cr^{VI} show the smallest values of K_i, which indicates a greater binding affinity, in agreement with the amount of these metal ions, expressed by I_{10}, necessary to inhibit enzyme activity, demonstrating their higher toxicity. On the other hand, Pb^{2+} presented a higher value of K_i, revealing its weaker inhibitor capability [256].

The analytical performance of the novel GOx/PBG_{DES}/MWCNT/GCE biosensor for detection of these toxic trace metal ions by the enzyme inhibition strategy was compared with the most recent relevant recent reports, **Table 5.4**. The novel biosensor showed superior electroanalytical performance to those found in the literature with the lowest limit of detection until now. Furthermore, it does not require any pre-treatment after each measurement for restoring GOx activity such as immersion of the electrodes in the buffer and/or metal chelating agent (EDTA) solution for a long period.

5.7 Selectivity, repeatability, and stability

Concerning biosensor selectivity, potential interferents ions were tested, the cations (K^+, Na^+, Fe^{3+}, Zn^{2+}, Ni^{2+}, $Cu^{2+}$and Co^{2+}) and the anions (NO_3^-, SO_4^{2-} and Cl^-), **Fig. 5.10**. Inhibition at the GOx/PBG_{DES}150/MWCNT/GCE biosensor was tested in the presence of 0.5 mM glucose at the previously optimised applied potential of – 0.4 V vs. Ag/AgCl; the concentration of the interferents was 200 nM. This value corresponds to the maximum degree of inhibition achieved by all the trace biotoxic metal ions that are the object of this study. The degree of inhibition observed with the interferents had no significant influence on the initial response of glucose, less than 10%, for the high concentration of each interferent evaluated.

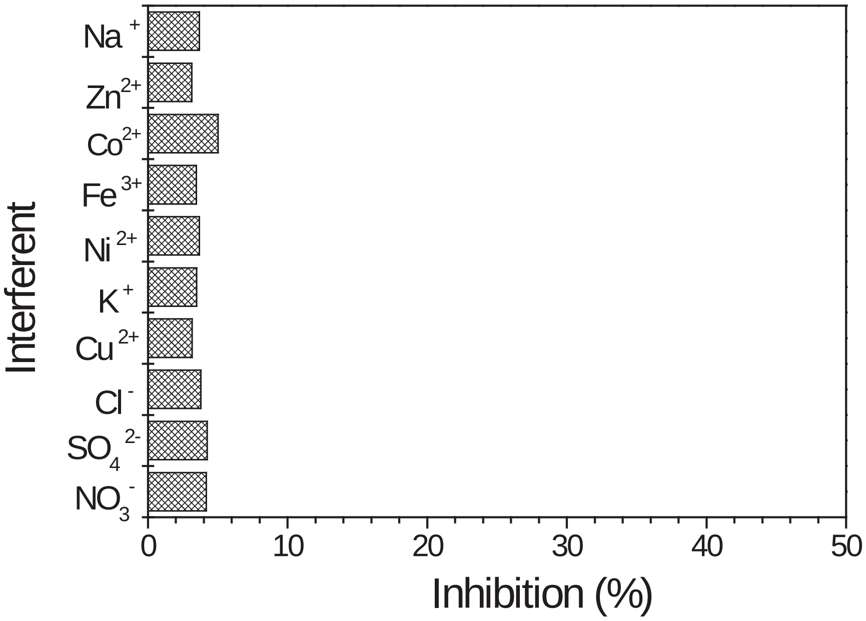

Fig. 5.10 Inhibition caused at GOx/PBG/CNT/GCE by the presence of different interferents in 0.1 M PB solution (pH 7.0) in the presence of 0.5 mM glucose at applied potential - 0.4 V vs. Ag/AgCl. Concentration of interferents: 200 nM.

The repeatability of the GOx/PBG$_{ethaline}$150/MWCNT/GCE biosensor was investigated by measuring the same concentration, 20 nM, of each trace metal ion at ten different modified electrodes prepared in the same way. The relative standard deviations were less than 4.5 %. The stability of the biosensor was monitored daily by measuring the response of glucose, during 20 days, after successive inhibition experiments for all metal ions at the same modified electrode. When not in use, the biosensors were kept in buffer (PB, pH 7.0) at 4 °C. After 20 days, the glucose response lost just 13 % of its initial value. However, such a loss of the enzyme activity does not compromise the use and the effectiveness of the inhibition biosensor.

5.8 Application of the inhibition enzyme based-biosensor for determination of trace metal ions in contaminated milk samples

To demonstrate the feasibility of the biosensor for food monitoring, the determination of trace metal ions in milk samples was carried out by the standard addition method.

Table 5.5 Determination of trace metal ions in milk samples

Metal ion	Added (nM)	Expected (nM)	Found (nM)	Recovery (%)
Hg^{2+}	20.0	20.0	19.9± 0.2	99.5
Cd^{2+}	20.0	20.0	20.2 ± 0.1	100.1
Pb^{2+}	20.0	20.0	19.8± 0.2	99.0
Cr^{VI}	20.0	20.0	19.8 ± 0.2	99.0

Milk samples were spiked with known amounts of Hg^{2+}, Cd^{2+}, Pb^{2+} and Cr^{VI} ions, and the recoveries were calculated **Table 5.5**. The average recovery was in the range 99.5 – 100.1 %, which indicates that the proposed biosensor is efficient for practical applications with an excellent level of reliability.

5.9 Conclusions

PBG polymer films with unique nanostructures have been successfully synthesised in a mixture containing 10 % v/v of water: 90 % v/v ethaline with the addition of 0.1 M H_2SO_4 in the final DES optimised mixture. The scan rate used during electropolymerisation was a crucial factor in influencing the nanostructure and morphology, and thence the electrochemical properties of the resulting $PBG_{ethaline}$ films. Comparison with PBG_{aq} revealed that all PBG films obtained from ethaline DES exhibited higher redox currents and a significantly lower charge transfer resistance than PBG_{aq}. Among the $PBG_{ethaline}$ films analysed, the more uniform observed in the SEM images was $PBG_{ethaline}$150, which can be correlated with its superior electrochemical properties, namely the polymer faradaic currents and lowest charge transfer resistance. The GOx/$PBG_{ethaline}$150/MWCNT/GCE biosensor was used for detection of trace metal ions through enzyme inhibition. The mechanism of reversible inhibition was found to be competitive for Hg^{2+} and Cd^{2+}, uncompetitive for Pb^{2+} and mixed for Cr^{VI}. The novel enzyme inhibition biosensor exhibited a lower limit of detection than the biosensors reported in the literature, with good selectivity and stability. It was successfully applied for detection in milk samples with excellent recoveries, which augurs well for its use in environmental trace metal ion monitoring.

This page intentionally left blank

Chapter 6

Poly (brilliant cresyl blue) (PBCB) - ethaline deep eutectic solvent/carbon nanotubes characterisation and biosensing applications

This chapter concerns the development, characterisation and application of a novel nanocomposite based on poly(brilliant cresyl blue) (PBCB) films formed on carbon nanotube modified glassy carbon electrodes by using fixed potential potentiostatic (PTD) and potentiodynamic cycling (PDD) electropolymerisation methods. The polymerisations were carried out in acid-doped ethaline deep eutectic solvent (DES) solution or aqueous medium. Different ionic species, i.e. NO_3^-, SO_4^{2-}, Cl^-, ClO_4^- were added to the polymerisation solution, and their influence on polymer growth was assessed. The effect of scan rate on $PBCB_{DES}$ films was also investigated. Furthermore, the influence of deposition time and applied potential on the rate of growth during potentiostatic polymerisation and on the electrochemical properties of the polymer films were also studied. The nanocomposite films produced in different experimental conditions were characterised by scanning electron microscopy, cyclic voltammetry and electrochemical impedance spectroscopy. Under optimal conditions, the $PBCB_{DES}$-acid/MWCNT and $PBCB_{aq}$/MWCNT nanocomposite films were used as electrode support for the enzymes glucose oxidase and tyrosinase for the biosensing of glucose and catechol, respectively. A comparison between biosensors with polymer films produced by both deposition methods was carried out. The best sensing platform was chosen as enzyme support for choline oxidase for biosensing of choline and of the organophosphorus pesticide dichlorvos through the enzyme inhibition strategy.

This research led to the publication of two articles, [257] and [258], (Electrochimica Acta 317(2019)766–777) and (Sensors Actuators B Chemical 12(2019) 126862 (1-9).

6.1 Potentiodynamic PBCB film deposition

6.1.1 Influence of the composition of the polymerisation solution on PBCB film growth

The electrodeposition of PBCB by potential cycling electropolymerisation can be influenced by factors that include the composition of the supporting electrolyte, pH, monomer concentration, temperature, applied potential, scan rate, etc. **Figs. 6.1A-6.1E** show CVs for the electropolymerisation of BCB on MWCNT/GCE in an ethaline-acid solution containing different acids as anion sources, H_2SO_4, HNO_3, HCl, $HClO_4$ and, for comparison, in 0.1 M PB (pH 7.0) + 0.1 M KNO_3 aqueous solution, at a scan rate of 50 mV s^{-1}. BCB species oxidise at high potentials (≈ +0.80 V), and it has been proposed that the amino group oxidises to form a cation radical. The cation radicals are cross-linked by electropolymerisation via a C-N coupling reaction forming stable PBCB [259,260]. Thus, in this work, the potential range chosen was from -0.6 V to +1.0 V vs. Ag/AgCl. In all polymerisation media, the CV shows an increase of the peak currents with increasing number of cycles indicating nucleation and growth processes [261].

For CV of BCB electrodeposited on MWCNT/GCE in ethaline-acid, **Fig. 6.1A-D**, three redox couples marked as I_a/I_c, II_a/II_c and III_a/III_c appear. The I_a/I_c couple is assigned to the oxidation/reduction of the monomer units trapped in the polymer film and the other redox pairs are due to alternating oxidised and reduced repeat units in the polymer structure. The unpaired electrons can be localized at either the nitrogen atom or the other carbon atoms in the benzene ring. The cation radicals are more concentrated near the electrode surface; their diffusion rate is high, they may find a neutral monomer to react with or, more likely, they react with other radicals forming dimers and trimers. This new structure can undergo deprotonation and form intermediate polymerisation products [262].

For BCB electropolymerised in aqueous solution, **Fig. 6.1E**, only two redox peaks are seen, I_a/I_c and II_a/II_c; the redox peaks I_a/I_c continuously decrease with the number of cycles while II_a/II_c increases and there is no formation of intermediates. Interestingly, the redox peaks of PBCB electrodeposited on MWCNT/GCE from ethaline-acidic media (pH 2.0) are at more positive potentials than those of PBCB electrodeposited in aqueous solution (pH

7.0). This means that the redox process is directly related with protons being released into the solution from the polymer during its oxidation, and vice versa for reduction. This behaviour has also been found for other polyazines e.g., poly(methylene blue), poly(brilliant green), poly(Nile blue), and for polyaniline [170,263,264].

The mechanism of electropolymerisation of BCB on MWCNT has been reported elsewhere in the literature [260,265,266]. The sidewall curvature of MWCNT, the π-π conjugative structure and highly hydrophobic surface, allow them to interact with BCB monomer, through π-π interactions and/or hydrophobic interactions. Electrostatic interactions can also occur at sufficiently high pH, due to carboxylate groups at the defects and extremities of the functionalized MWCNT attracting the positively charged amino groups of BCB. In the acidic polymerisation media used here, the former mechanism will take place. The formal potential ($E^{\ominus} = (E_{\mathrm{pa}} + E_{\mathrm{pc}})/2$) of the monomer units within the polymer film structure was calculated from the redox couple I_a/I_c, in the CVs obtained at 50 mV s^{-1} scan rate. The formal potential was calculated for the 1st cycle and 30th cycle, and the values were, vs. Ag/AgCl:

PBCB$_{\mathrm{ethaline}}$-H_2SO_4/MWCNT/GCE: $E^{\ominus}{}_1 = 0.24$ V and $E^{\ominus}{}_{30} = 0.26$ V;

PBCB$_{\mathrm{ethaline}}$-HCl/MWCNT/GCE: $E^{\ominus}{}_1 = 0.25$ V and $E^{\ominus}{}_{30} = 0.27$ V;

PBCB$_{\mathrm{ethaline}}$-HNO_3/MWCNT/GCE: $E^{\ominus}{}_1 = 0.25$ V and $E^{\ominus}{}_{30} = 0.27$ V;

PBCB$_{\mathrm{ethaline}}$$HClO_4$/MWCNT/GCE: $E^{\ominus}{}_1 = 0.15$ V and $E^{\ominus}{}_{30} = 0.16$ V;

PBCB$_{\mathrm{aq}}$/MWCNT/GCE: $E^{\ominus}{}_1 = -0.084$ V and $E^{\ominus}{}_{30} = -0.073$ V.

Only very small differences in the values of the formal potential of PBCB electrodeposited in the presence of ethaline with different acids are seen, except for $HClO_4$. The large difference in the formal potentials for PBCB electrodeposited from aqueous solution compared with PBCB electrodeposited from ethaline is due to the higher pH. Very little change in the $E^{\ominus}$ values occurs during polymer growth.

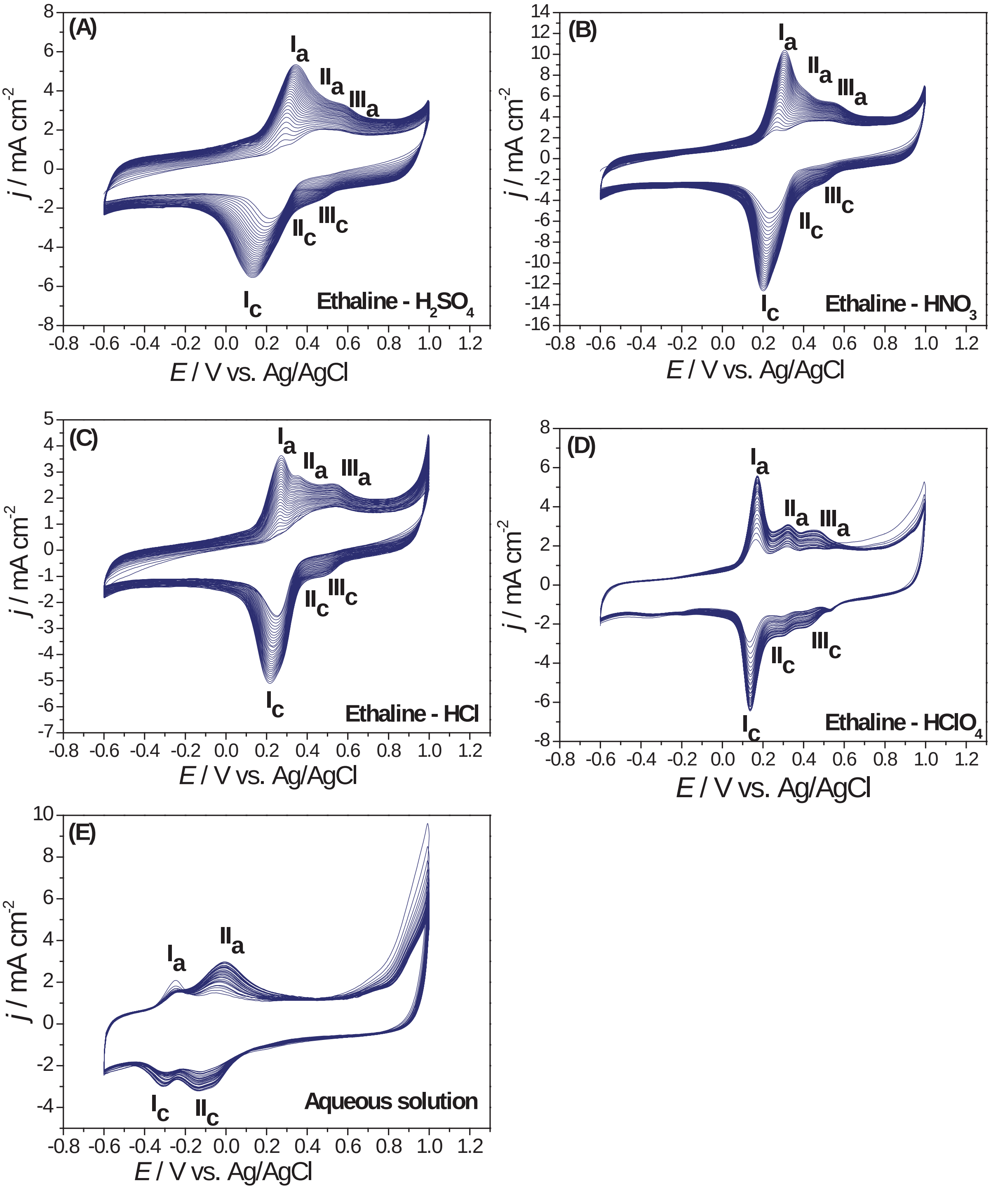

Fig. 6.1 Potential cycling electrodeposition of PBCB on MWCNT/GCE at scan rate 50 mV s^{-1} from a solution containing 0.1 M BCB in: **(A)** ethaline + 0.5 M H_2SO_4; **(B)** ethaline + 0.5 M HNO_3; **(C)** ethaline + 0.5 M HCl; **(D)** ethaline + 0.5 M $HClO_4$; **(E)** 0.1 M KNO_3 + 0.1 M PB solution (pH 7.0).

The polymer growth rate expressed as the ratio between the oxidation peak current in the thirtieth and the first cycle, I_{a30}/I_{a1} was calculated. For $PBCB_{ethaline}$-H_2SO_4/MWCNT/GCE is 10.0, for $PBCB_{ethaline}$-HCl/MWCNT/GCE is 7.3, for $PBCB_{ethaline}$-HNO_3/MWCNT/GCE is 11.7, for $PBCB_{ethaline}$-$HClO_4$/MWCNT/GCE is 3.2 and for $PBCB_{aq}$/MWCNT/GCE, is 3.9.

From this point of view, HNO_3 is the best acid dopant, closely followed by H_2SO_4. It was previously observed [171,267] that NO_3^- acts as a polymerisation accelerator, and it can also serve as a shielding agent since it neutralises the positive charge of BCB molecules. On the other hand, some other anions (ClO_4^-, BF_4^-) are known to form tight ionic pairs with BCB^+, precipitating the BCB monomer and/or produce polymer films with an irregular nanostructure [171,267,268], see **Fig. 6.5F**.

6.1.2 Influence of the scan rate on PBCB film growth

The influence of scan rate on BCB electropolymerisation in the range 50 to 200 mV s^{-1} was investigated in ethaline + HNO_3 solution since, in this medium, PBCB exhibited the best growth profile, **Fig. 6.2A-D**. The peak currents corresponding to the polymer redox processes increased with increase of scan rate from 50 to 150 mV s^{-1}, but decreased at 200 mV s^{-1}; this is in agreement with previous observations for poly(methylene blue) in [242]. This behaviour may be explained as follows. The scan rate during polymerisation influences the mass transport of the monomer from the solution to the electrode, as does the viscosity of the solution. In viscous solutions, ion movement is more difficult, but an increase in scan rate will increase the diffusion of the monomer in the solution towards the electrode surface owing to the concentration gradient created by its oxidation. However, at higher scan rates, the monomer cannot be replenished at the electrode surface sufficiently fast, due to the high viscosity, so that a decrease in monomer oxidation current will be observed. This will limit polymer growth, and the effect is already seen at 200 mV s^{-1} scan rate. The formal potential is not influenced by the scan rate, being $E^{\ominus}{}_1 = 0.25 \pm 0.02$ V and $E^{\ominus}{}_{30} = 0.27 \pm 0.02$ V.

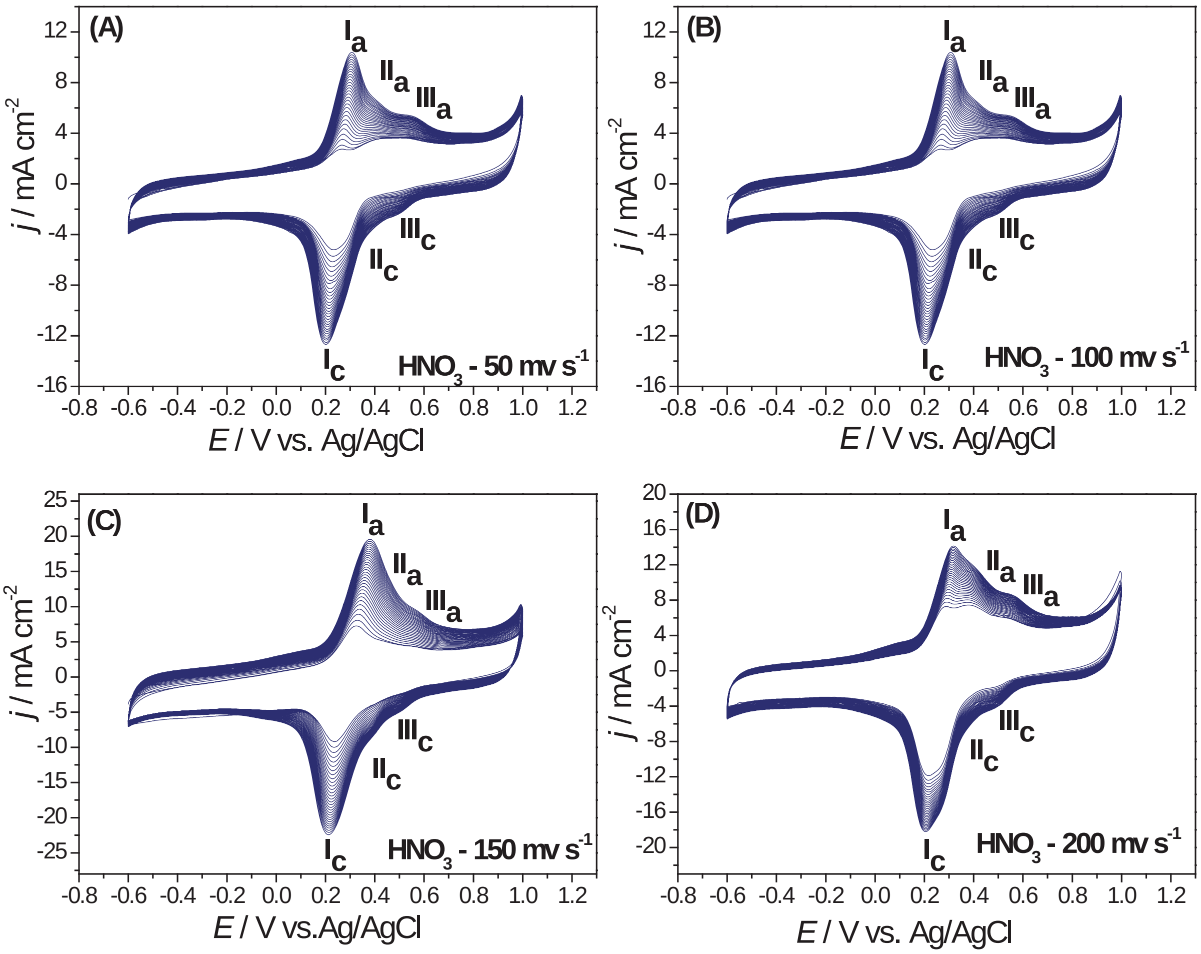

Fig. 6.2 Potential cycling electrodeposition of PBCB on MWCNT/GCE from a solution of 0.1 M BCB in ethaline + 0.5 M HNO$_3$ at different scan rates: **(A)** 50; **(B)** 100; **(C)** 150; **(D)** 200 mV s^{-1}.

The polymerisation growth rate for different scan rates (cycle 30 divided by cycle 1 peak current) was calculated as 11.7, 11.9, 12.5 and 6.4 for 50, 100, 150 and 200 mV s^{-1}, respectively. Thus, among the scan rates investigated for polymer growth, the best was 150 mV s^{-1}, in agreement with results in [242].

6.2 Electrochemical characterisation of the nanocomposite films

6.2.1 Cyclic voltammetry of the nanocomposite films

To evaluate the electrochemical behaviour of PBCB on MWCNT with a view to applications, CVs of the modified electrodes were recorded in 0.1 M BR buffer solution (pH 7.0) at a potential scan rate of 50 mV s^{-1}. **Fig. 6.3A** displays CVs of the PBCB/MWCNT nanocomposite films formed in the various media described in the previous sections.

The CV profiles of PBCB electrodeposited in ethaline containing different acids show the same two redox couples, a less well-defined I_a/I_c attributed to entrapped BCB monomer and a well-defined II_a/II_c corresponding to the polymer film, while PBCB electrodeposited in aqueous solution presents just one redox couple I_a/I_c shifted to more negative potentials; the same tendency was also verified during electropolymerisation.

The CVs clearly evidence that PBCB films obtained in ethaline containing different acids have higher peak currents, which may be attributed to a greater amount of polymer electrodeposited than that of PBCB formed in aqueous solution. The peak-to-peak separation ($\Delta E_p = E_{pa} - E_{pc}$) was calculated to be 0.08 V in aqueous solution and ~0.13 V in ethaline-acid media. The surface coverage (Γ) of the nanocomposites was estimated using the equation [179]:

$$\Gamma = Q / nFA \tag{6.1}$$

where Γ is the surface concentration (mol cm^{-2}), Q is the charge(C) obtained by integrating the corresponding area of the cathodic peak II_c; after baseline correction, n (=2) is the number of electrons transferred (calculated in Section 3.5), F is the Faraday constant (96485 C mol^{-1}), and A is the electrode geometric surface area (0.00785 cm^2).

The calculated order of increasing Γ values was $9.31 \times 10^{-8} < 1.04 \times 10^{-7} < 1.93 \times 10^{-7} < 2.31 \times 10^{-7} < 4.27 \times 10^{-7}$ mol cm^{-2}, for $PBCB_{aq}$/MWCNT, $PBCB_{ethaline}$-$HClO_4$/MWCNT, $PBCB_{ethaline}$-HCl/MWCNT, $PBCB_{ethaline}$-H_2SO_4/MWCNT and $PBCB_{ethaline}$-HNO_3/MWCNT modified GCE, respectively. The order of these values is in agreement with what is observed in Fig 6.1, in which the BCB polymerised in ethaline containing NO_3^- presented the highest increase in current during polymerisation. **Fig. 6.3B** shows CVs for PBCB$_{DES}$-$HClO_4$/MWCNT/GCE with PBCB electrodeposited at different scan rates from 50 to 200 mV s^{-1}. As expected, the peak currents increased with increase of electropolymerisation scan rate up to 150 mV s^{-1}, where the highest peak current was achieved, decreasing for 200 mV s^{-1}.

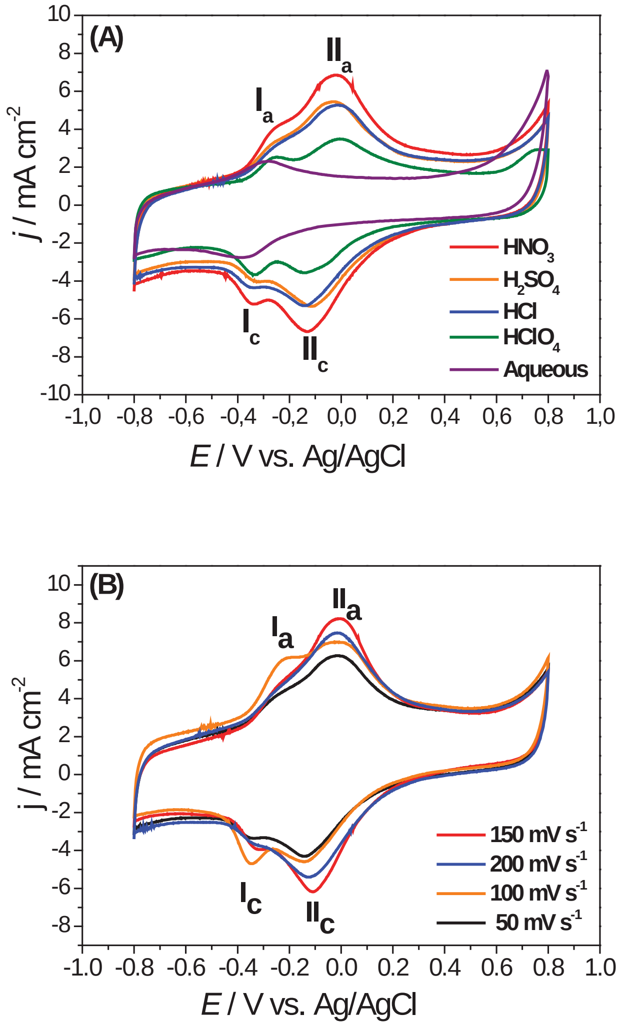

Fig. 6. 3(A) CVs of PBCB$_{ethaline}$-acid modified MWCNT/GCE in 0.1 M BR buffer solution (pH 7.0) at 50 mVs^{-1}; **(B)** CVs of PBCB$_{ethaline}$-HNO_3 modified MWCNT/GCE, for PBCB films formed at different scan rates: from 50-200 mVs^{-1} in 0.1 M BR buffer solution (pH 7.0) at 50 mVs^{-1}.

The values of ΔE_p for $PBCB_{ethaline}$-HNO_3 films were 0.133 V, 0.113 V, 0.102 V and 0.110 V for films electrodeposited at 50, 100, 150 and 200 mV s^{-1}. Mirroring the trend in polymer film growth, the ΔE_p values decrease with increasing scan rate up to 150 mV s^{-1}. The surface coverage (Γ) was estimated to be $4.27 \times 10^{-7} < 4.84 \times 10^{-7} < 5.74 \times 10^{-7} > 5.05 \times 10^{-7}$ mol cm^{-2}, for $PBCB_{DES}$-HNO_3 electrodeposited at 50, 100, 150 and 200 mV s^{-1}, respectively. Therefore, the electropolymerisation of PBCB in ethaline containing NO_3^- at 150 mV s^{-1} scan rate led to the formation of polymer/MWCNT structures with the best electrochemical properties.

6.2.2 Electrochemical impedance spectroscopy

Electrochemical impedance spectroscopy was used to examine the interfacial properties of the PBCB films electrodeposited under different experimental conditions. The measurements were carried out at an applied potential of - 0.10 V vs. Ag/AgCl, chosen from cyclic voltammograms recorded at the modified electrodes, **Fig. 6.3A**, corresponding to the approximate formal potential value for oxidation/reduction of the polymer, peaks II_a/II_c. BR buffer solution (0.10 M, pH 7.0) was used as supporting electrolyte, the same as for characterisation by cyclic voltammetry.

In all cases, the spectra obtained present three regions: a semi-circular part at high frequencies corresponding to the electron transfer processes and two linear parts at medium and lower frequencies corresponding to diffusional and charge separation phenomena, respectively. The spectra in the low-frequency region are very similar for all types of modified electrode; the main differences only appearing in the high-frequency region.

Complex plane impedance spectra are illustrated in **Fig. 6.4A**, for PBCB polymer films obtained from ethaline + different acids (H_2SO_4, HNO_3, HCl and $HClO_4$) and aqueous solution (PB+KNO_3), and **Fig. 6.4B** are spectra of PBCB films obtained at different scan rates (50, 100, 150 and 200 mV s^{-1}). The spectra were all fitted to the electrical circuit depicted in **Fig 6.4C**. The circuit comprises a cell resistance, R_Ω, in series with a parallel combination of a resistance R_1 and CPE_1 which is modelled as non-ideal capacitor expressed by $CPE = 1 / (i\omega C)^\alpha$, where C is the capacitance, ω is the frequency in rad s^{-1} and the exponent, $0.5 < \alpha < 1$, reflects the surface non-uniformity and roughness of the modified electrodes, $\alpha = 1$ corresponding to a perfect uniform and smooth surface [150]. The constant phase element (CPE_1) and the resistance (R_1) are associated with the processes which occur at the electrode/modifier interface at high frequencies. The intermediate frequency region is modelled by a mass transport finite-diffusion Warburg element Z_W. The Warburg element, Z_w, results from the equation: $Z_w = R_D\text{cth}[\tau i\omega)^{\alpha}]$ x $[\tau i\omega)^{\alpha}]$, where $\alpha < 0.5$, and is characterised by a diffusional time constant (τ), a diffusional pseudocapacitance (C_D) and a diffusional resistance ($R_D = \tau / C_D$) [150]. For low frequencies a second constant phase element was used, CPE_2, corresponding to the charge separation at the modifier film/solution interface and within the film. Values of the circuit parameters obtained by fitting the spectra are presented in **Table 6.1**.

The charge separation processes occurring at the electrode/modifier interface are influenced by the nanocomposite structures, reflected by the different values of CPE_1 obtained. For all PBCB polymer films prepared in ethaline, there is a decrease in R_1 values accompanied by an increase in C_1, attributed to greater charge separation, and easier electron transfer compared with PBCB films produced in aqueous solution. Values of R_1 decrease in the order: ($PBCB_{aq}$/MWCNT/GCE) > ($PBCB_{ethaline}$-$HClO_4$/MWCNT/GCE) > ($PBCB_{ethaline}$-HCl/MWCNT/GCE) > ($PBCB_{ethaline}$-H_2SO_4/MWCNT/GCE) > ($PBCB_{ethaline}$-HNO_3/MWCNT/GCE), the fastest electron transfer occurring at $PBCB_{ethaline}$-HNO_3/MWCNT/GCE. The average $\alpha_1 \approx 0.85$, for films obtained in ethaline, reflects a relatively high surface uniformity of the polymer films at the nanometric scale.

For PBCB films formed in aqueous solution, α_1 was 0.77, revealing a less smooth film, as also verified in SEM analysis, see below. The values of R_1 for $PBCB_{ethaline}$-HNO_3/MWCNT/GCE obtained at different electropolymerisation scan rates were in the order: 50 mV s^{-1} > 100 mV s^{-1} > 200 mV s^{-1} > 150 mV s^{-1}. Values of CPE_1 also show a scan rate dependence, in the inverse sense, with films prepared at 150 mV s^{-1} giving the highest charge separation. This is in agreement with the CV results.

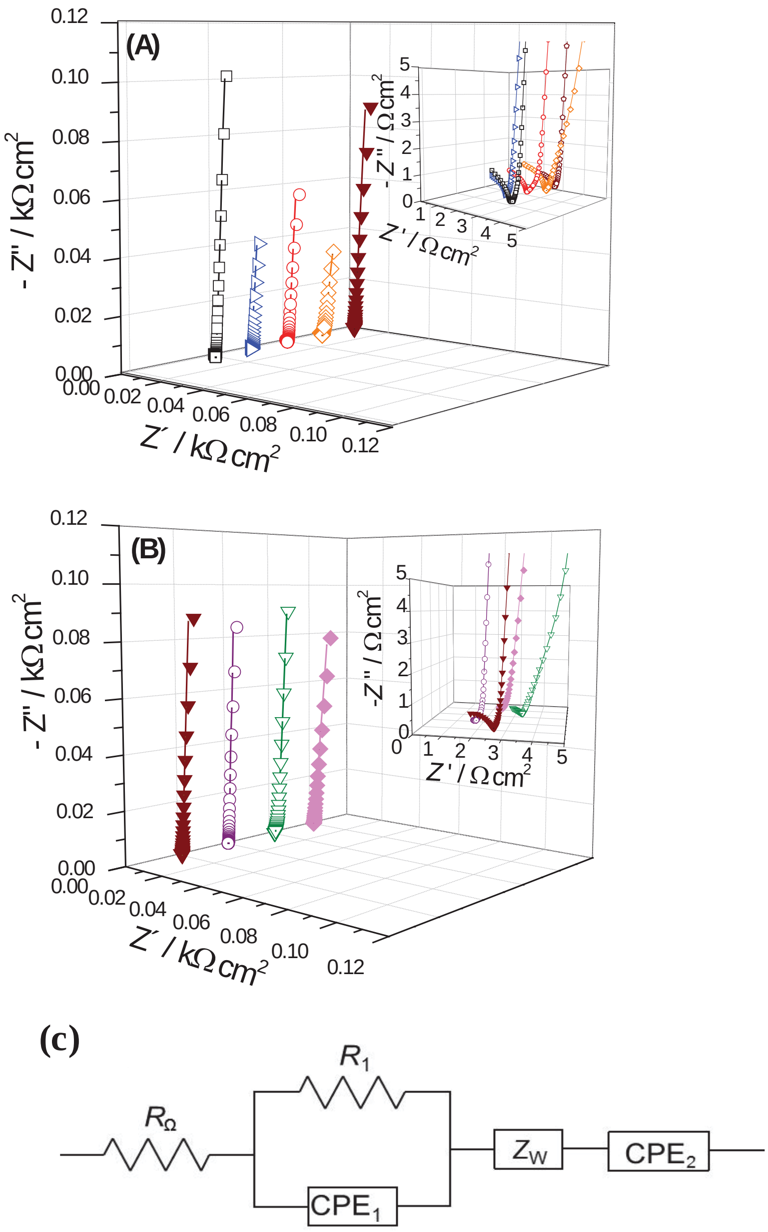

Fig. 6.4 Complex plane impedance spectra at PBCB/MWCNT/GCE in 0.1 M BR buffer solution (pH 7.0), PBCB film synthesised **(A)** at 50 mV s^{-1} in (□) 0.1 M KNO_3 + 0.1 M PB solution (pH 7.0); (▶) ethaline + 0.5 M H_2SO_4; (○) ethaline + 0.5 M HCl; (◊) ethaline + 0.5 M $HClO_4$; (▼) ethaline + 0.5 M HNO_3, **(B)** in ethaline + 0.5 M HNO_3 at scan rates: (□) 50; (▽) 100; (○) 150 and (◆) 200 mV s^{-1}. **(C)** Electrical equivalent circuit used to fit the spectra.

Table 6.1 Equivalent circuit element values obtained by fitting the impedance spectra in **Fig. 6.4A** (polymerisation scan rate 50 mV s^{-1}) and **6.4B** (different scan rates in Eth + HNO_3). Eth: ethaline.

Experimental conditions	R_1 / Ω cm^2	CPE_1/ (μF cm^{-2} $s^{\alpha-1}$)	α_1	Z_w / Ω cm^2	τ / ms	α_{zw}	CPE_2 / (mF cm^{-2} $s^{\alpha-1}$)	α_2
Aqueous	5.98	12.5	0.77	1.01	0.07	0.46	68.5	0.80
Eth + $HClO_4$	3.63	21.1	0.84	1.72	0.71	0.49	98.3	0.85
Eth + HCl	2.10	57.1	0.86	1.71	0.75	0.49	132.2	0.84
Eth + H_2SO_4	1.73	66.3	0.88	1.74	0.76	0.48	148.2	0.95
Eth + HNO_3	1.15	94.1	0.85	1.63	0.78	0.49	198.4	0.96
Scan rate / mV s^{-1}								
50	1.15	94.1	0.85	1.63	0.78	0.49	198.4	0.96
100	0.87	118.2	0.86	1.76	0.76	0.50	220.4	0.92
150	0.12	155.3	0.84	1.80	0.84	0.49	268.1	0.97
200	0.38	125.2	0.85	1.79	0.80	0.49	232.4	0.95

The values of diffusional resistance obtained from the Warburg element increased at polymer films electrodeposited in ethaline compared with those in aqueous solution, spectra in **Fig. 6.4A**, which may be attributed to a thicker film, as also observed from the values of τ, which were also a bit higher. The exponent α calculated from the Warburg element was close to 0.45, as usually found in thin films [269]. From fitting the spectra in **Fig. 6.4B**, the scan rate seems to have little influence on diffusional resistance values.

In relation to CPE_2, the trend is the same as for CPE_1. Varying the acid dopant significantly influences the values, being highest for HNO_3, and the values of α_2 also increase, being very similar for H_2SO_4 and HNO_3 dopants. There is not much influence of scan rate on CPE_2 or the α_2 values.

6.2.3 Effect of pH on peak current and peak potential at the modified electrodes

Due to the presence of amino groups in polyazines, protons are involved in the electrode reactions. Hence, the effect of solution pH at $PBCB_{DES}$-HNO_3/MWCNT/GCE, with PBCB electrodeposited at 150 mV s^{-1}, was investigated by differential pulse voltammetry (DPV) in 0.1 M BR buffer solution in the pH ranging from 3.0 to 10.0. The parameters used in DPV were: amplitude 10 mV, step potential 2 mV, scan rate 50 mV s^{-1} and pulse time 10 ms.

As seen in **Fig. 6.5A**, with increase in pH, the oxidation peak potential (E_{pa}) shifts linearly to negative potentials, according to the equation: $E_{pa}/V = 0.32 - 0.056$ pH, the slope of $\cong$ 56 mV pH^{-1}, **Fig. 6.5B**, indicating an equal number of protons and electrons participating in the oxidation process. DPV also demonstrated that the peak current increases with increase in pH up to pH 7.0, where the highest response is exhibited, and then decreases. Therefore, this pH was selected for further experiments.

The peak width at half-height ($W_{1/2}$) gives an indication of the reversibility of electrode reaction and the number of electrons involved. The value of $W_{1/2}$ in pH 7.0 BR buffer solution was estimated to be 42 ± 3 mV (three measurements), suggesting that the total number of electrons transferred in the oxidation of the electroactive centres in the polymer is equal to 2, together with 2 protons.

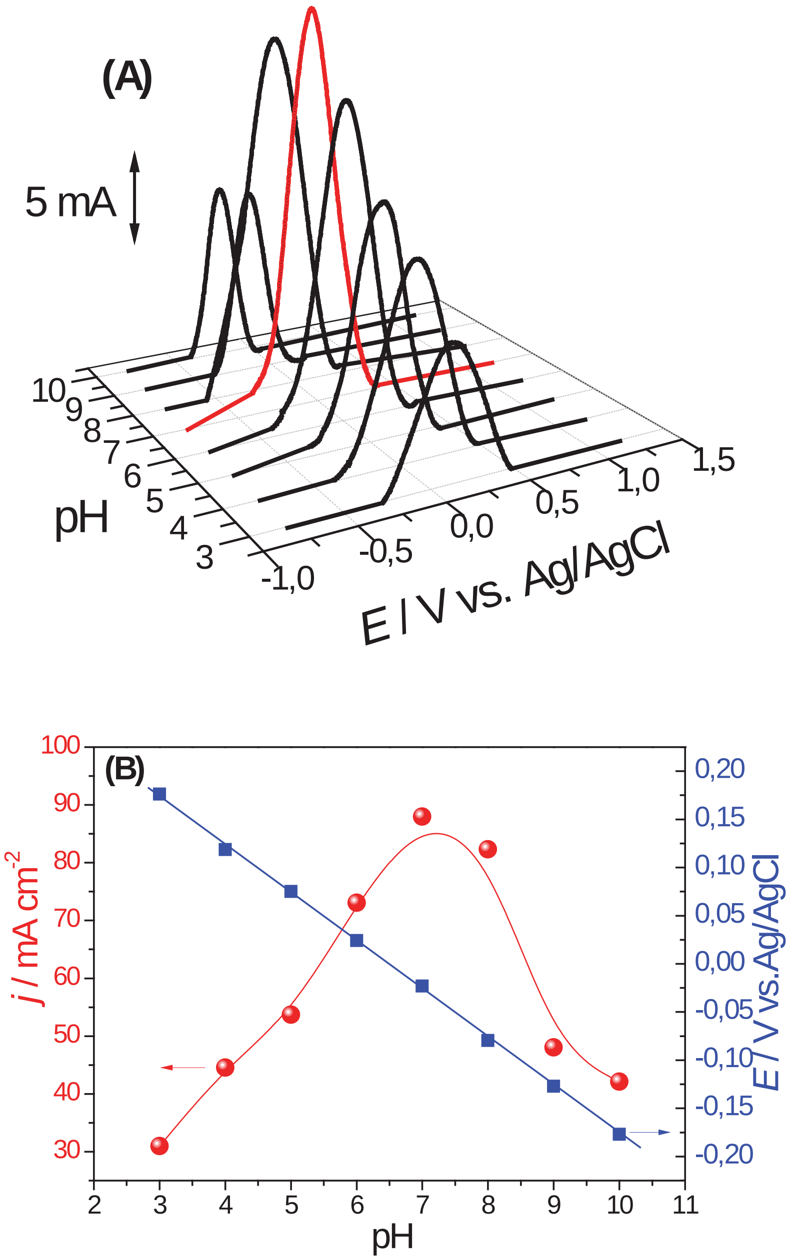

Fig. 6.5 (A) Differential pulse voltammograms at PBCB$_{DES}$-HNO$_3$/MWCNT film modified electrodes in BR buffer solution at different pH values (from 3.0 to 10), recorded at 50 mVs^{-1}. Amplitude 10 mV, step potential 2 mV, pulse time 10 ms. **(B)** Plots of oxidation peak currents and peak potentials vs. pH, data from Fig. 6.5A.

There are contradictory reports in the literature regarding the number of electrons involved in BCB oxidation, the number seeming to be dependent on the electrode support material and experimental conditions. It was found that the electron transfer is a one-electron process in [171,270], but a 2 electron process in [166,265], in agreement with what was obtained here.

6.2.4 Effect of the scan rate at modified electrodes

The effect of the scan rate in 0.1 M BR buffer solution, pH 7.0 was investigated at PBCB$_{DES}$-HNO$_3$/MWCNT/GCE with PBCB films electrodeposited at different scan rates namely, 50, 100, 150 and 200 mV s^{-1} and with PBCB$_{aq}$/MWCNT film electrodeposited at 150 mV s^{-1}.

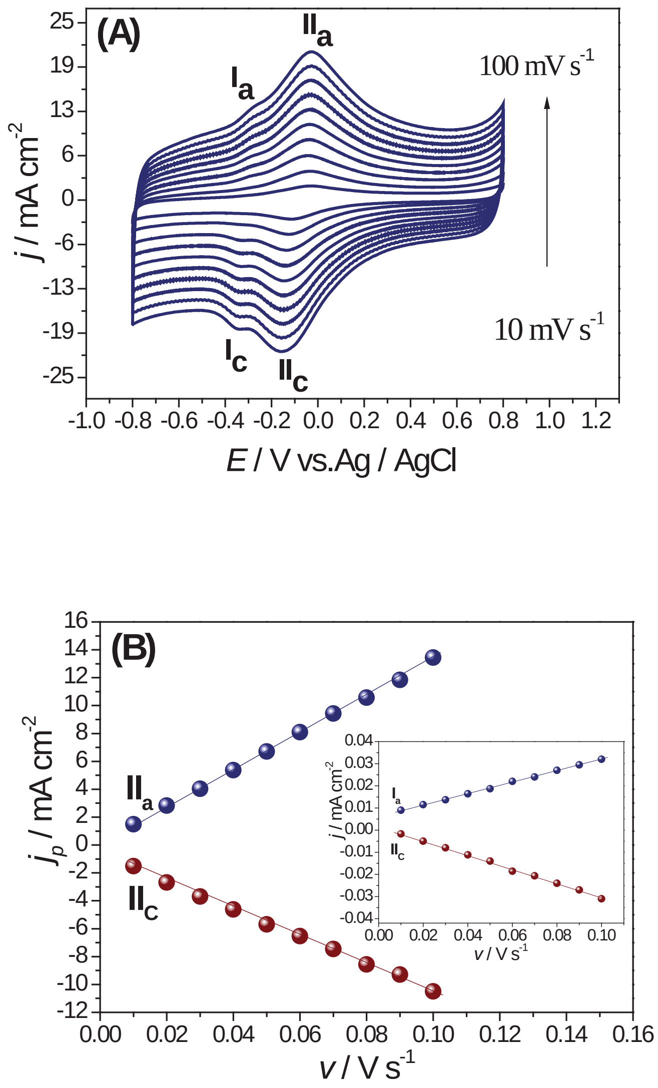

Fig. 6.6 (A) CVs for PBCB$_{ethaline}$-HNO$_3$/MWCNT modified GCE in 0.1 M BR buffer solution (pH 7.0) at scan rates 10-100 mV s^{-1}); **(B)** Plots of peak current vs. scan rate.

The anodic and cathodic peak currents increase with increase of scan rate from 10-100 mV s^{-1}, as illustrated in **Fig. 6.6A** for the PBCB$_{ethaline}$-HNO$_3$/MWCNT/GCE with film electrodeposited at 150 mV s^{-1}, and which exhibited the highest peak currents.

For all nanocomposite films, there is a linear relationship between the anodic peak current, I_{pa} and the cathodic peak current, $I_{pc,}$ with scan rate, v, **Fig. 6.6B**, as also observed in [271,272] for other PBCB modified electrodes. The following equations were obtained: for the redox couple (I_a/I_b) j_{pIa}= 0.006+0.26 v and j_{pIb}= 0.007- 0.32 v and for the redox couple (II_a/II_b) j_{pIIa}= 0.05+42.1 v and j_{pIIb} = - 0.23- 31.2 v, where the current densities (j) are expressed in mA cm^{-2} and the scan rates (v) are in V s^{-1}.

The relationship log (j_{pIIa} / mA cm^{-2}) vs log (v / V s^{-1}) (not shown) was plotted for all modified electrodes. The slopes (S) were calculated to be 0.98, for PBCB$_{aq}$/MWCNT/GCE at 150 mV s^{-1}, for PBCB$_{ethaline}$-HNO_3/MWCNT/GCE the values were 0.96 (50 mV s^{-1}); 0.96 (100 mV s^{-1}), 0.97 (150 mV s^{-1}), and 0.96 (200 mV s^{-1}), all close to the theoretical value of 1.0, characteristic of a surface-confined process [145].

6.3 Morphological characterisation of the nanostructured films

The morphology of the nanostructured PBCB films electrodeposited in ethaline in the presence of different acids as anion source and in aqueous solution was examined by SEM, **Fig. 6.7**. SEM images of MWCNT without, **Fig. 6.7A**, and with polymer electrodeposited, **Fig. 6.5B-6.5F**, were recorded. **Fig. 6.5A** shows the MWCNT morphology prior to polymer deposition, with the presence of agglomerates of MWCNT entangled bundles, of uniform diameter and smooth surface, and without any indication of metallic catalysts obtained from their synthesis, which indicates the success of the acid treatment. An SEM image of PBCB electrodeposited on MWCNT in aqueous solution is shown in **Fig. 6.7B**. The diameter of the MWCNT increases after deposition of the PBCB$_{aq}$ film, as observed by comparing the SEM images before and after PBCB electrodeposition. However, a non-uniform and very thin film is formed, that is, BCB polymerisation from aqueous solution did not change the overall morphology of the MWCNT surface revealed by the presence of some exposed MWCNT bundles in the composite film, as also reported in [273–275] for other polyazines synthesised in aqueous solution.

Figs. 6.7C-6.7F show the morphology of PBCB films electrodeposited in ethaline-DES in the presence of different acids as anion source, namely $HNO_{3,}$ H_2SO_4, HCl, and $HClO_4$. In contrast to aqueous solution, the use of DES for BCB polymerisation shows the formation of rough and compact nanostructures covering all the MWCNT bundles for all four systems evaluated.

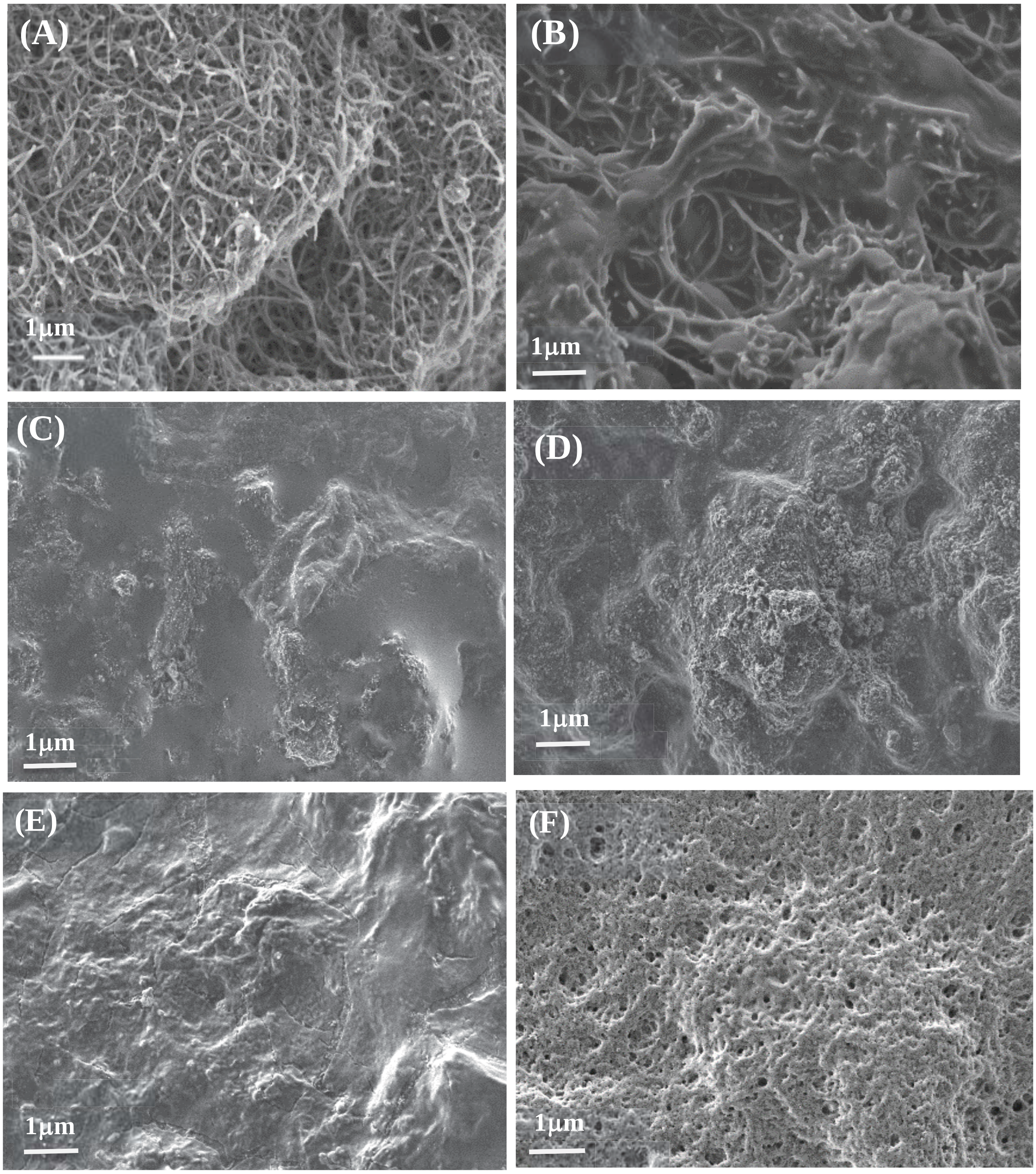

Fig. 6.7 SEM micrographs on carbon film electrodes of **(A)** Multi-walled-carbon nanotubes (MWCNT); **(B)** PBCB$_{aq}$/MWCNT nanocomposite film; **(C)** PBCB$_{ethaline}$-HNO$_3$/MWCNT nanocomposite film; **(D)** PBCB$_{ethaline}$-H$_2$SO$_4$/MWCNT nanocomposite film; **(E)** PBCB$_{ethaline}$-HCl/MWCNT nanocomposite film; **(F)** PBCB$_{ethaline}$-HClO$_4$/MWCNT nanocomposite film.

This can explain their enhanced electrochemical properties, namely the higher polymer oxidation and reduction currents in CVs and the lower charge transfer resistance in EIS compared with PBCB synthesised in aqueous solution, **Fig. 6.3A** and **Table 6.1**.

Furthermore, the use of different anion sources played an important role in the nanocomposite film morphology. $PBCB_{ethaline}$-HNO_3/MWCNT presents a more uniform surface than the other nanocomposite films that may explain the best electrochemical performance. $PBCB_{ethaline}$-H_2SO_4/MWCNT nanocomposite film reveals the presence of a thicker film and less uniform surface with the presence of agglomerates. $PBCB_{ethaline}$-HCl/MWCNT nanocomposite film has a relatively smooth surface but appears brittle, that may be responsible for its lower stability and less good electrochemical performance than $PBCB_{ethaline}$-HNO_3/MWCNT and $PBCB_{ethaline}$-H_2SO_4/MWCNT. $PBCB_{ethaline}$-$HClO_4$/MWCNT presents an irregular sponge-like surface, which may be due to a change in the mechanism of polymer deposition in the presence of ClO_4^- that, during the initial formation of the polymer film, hinders direct access of unreacted monomers to the electrode surface leading to formation of an irregular, thinner and less conductive film than the other polymer films prepared in ethaline [276].

6.4 Application of the $PBCB_{DES}$-HNO_3/MWCNT nanocomposite film in enzyme biosensors

After optimisation of the best conditions for PBCB electrodeposition in DES and corresponding film characterisation, application of the nanocomposite-modified electrode (with PBCB electropolymerised at scan rate 150 mV s^{-1}) in enzyme biosensors was investigated. Fixed potential amperometry was carried out by successive addition of glucose or catechol aliquots in buffer, and the corresponding enzyme (GOx or Tyr_{ase} immobilised on $PBCB_{ethaline}$-HNO_3/MWCNT/GCE) catalysed response measured, see **Fig 6.8A** and **6.9A**, respectively. For comparison, the enzymes were also immobilised on $PBCB_{aq}$/MWCNT/GCE and unmodified GCE, as described in the experimental section. All experiments were repeated three times; each set of measurements consists of 16 successive analyte injections. No enzyme leaching from the electrode was observed after these measurements.

6.4.1 Amperometric enzyme biosensor for glucose determination

Fig. 6.8B displays calibration plots at the glucose oxidase biosensors following sequential additions of glucose under continuous stirring at an applied potential of - 0.4 V vs. Ag/AgCl in 0.1 M PB solution (pH 7.0), as in [277]. To compare the sensitivity of the three biosensor configurations GOx/PBCB$_{\text{ethaline}}$-HNO$_3$/MWCNT/GCE, GOx/PBCB$_{\text{aq}}$/MWCNT/GCE and GOx/GCE, the same amount of glucose oxidase was immobilised on all types of electrode.

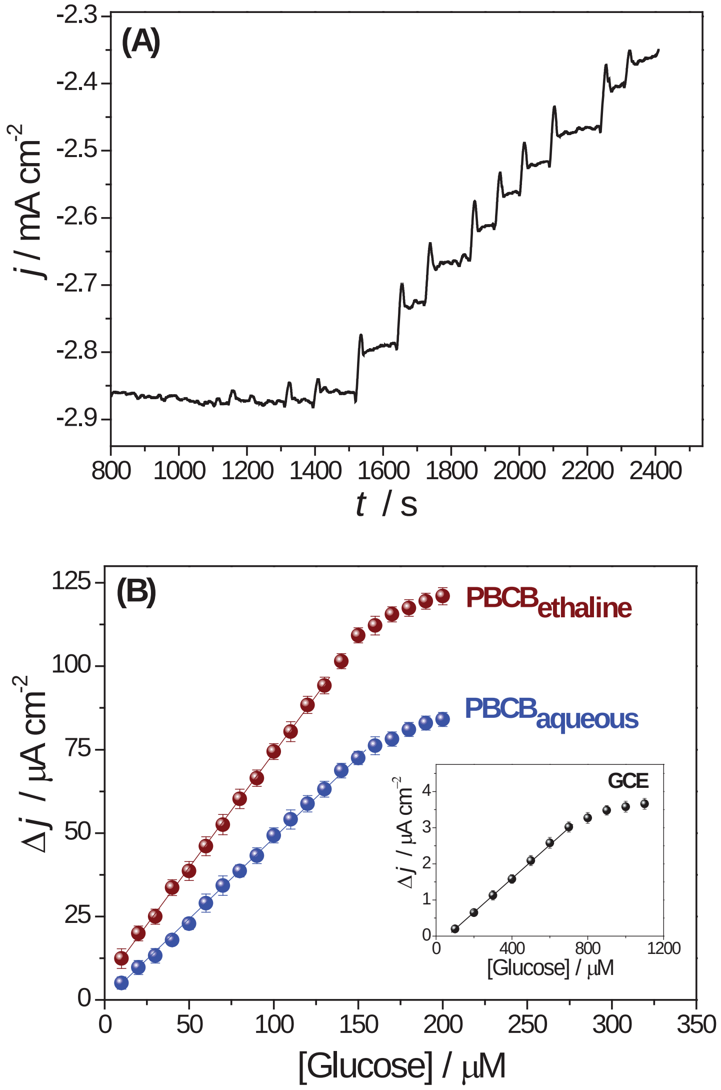

Fig. 6.8 Typical amperometric response of **(A)** GOx/PBCB$_{\text{ethaline}}$/MWCNT/GCE biosensor to glucose at -0.4 V, and **(B)** Corresponding calibration plots for the biosensors with enzyme immobilised on PBCB$_{\text{ethaline}}$ and PBCB$_{\text{aq}}$ modified MWCNT/GCE. Insert: GOx /GCE.

The first biosensor assembly, with PBCB deposited in DES, exhibited the highest sensitivity of 700 μA cm^{-2} mM^{-1} and the lowest limit of detection of 2.9 μM. The second, with PBCB deposited in aqueous solution, had a 30 % lower sensitivity of 500 μA cm^{-2} mM^{-1} and higher limit of detection of 4.2 μM. GOx/GCE showed significantly inferior analytical parameters: a sensitivity of 5.0 μA cm^{-2} mM^{-1} and limit of detection of 12.1 μM. The apparent Michaelis-Menten constant, K_M, is the concentration corresponding to half the maximum, saturation response of the biosensor. K_M can be estimated as around 80 μM for the first two biosensor assemblies with PBCB and around 400 μM for the GCE without it.

Comparison of the analytical parameters of GOx/$PBCB_{ethaline}$-HNO_3/MWCNT/GCE with the most recent glucose oxidase-based electrochemical biosensors was made. The novel approach offers better characteristics (limit of detection and sensitivity) than other glucose biosensors recently reported in the literature. For example, when GOx was adsorbed onto a nanoporous TiO_2 film layer on the surface of an iron phthalocyanine (FePc) vertically-aligned CNT-modified electrode, the biosensor exhibited a sensitivity of only 8.25 μA cm^{-2} mM^{-1}, the linear range was from 50 μM to 4.0 mM and a much higher detection limit of 30 μM [278].

Mani et al. [279] developed a biosensor for glucose, by immobilisation of GOx on electrochemically reduced graphene oxide–MWCNT hybrid modified GCE; the sensitivity of this biosensor was 7.95 μA cm^{-2} mM^{-1}, the linear range was 10 μM – 6.5 mM and the limit of detection was 4.70 μM. Luo et al. [280] proposed a glucose biosensor, by immobilisation of GOx on a reduced graphene oxide/PAMAM–silver nanoparticles nanocomposite (RGO–PAMAM–Ag), the sensitivity being 75.75 μA cm^{-2} mM^{-1}, the linear range was between 320 μM and 6.5 mM and the limit of detection 4.50 μM, higher than in this work.

6.4.2 Amperometric enzyme biosensor catechol determination

The same platforms were used to prepare Tyr_{ase} biosensors for the amperometric detection of catechol. Amperometric measurements were carried out in 0.1 M PB solution (pH 7.0), at an applied potential of -0.2 V vs. Ag/AgCl, as in [281]. Aliquots of known concentration of catechol were injected into the electrochemical cell under stirring, as for glucose and **Fig. 6.9B** shows the corresponding calibration plots. The Tyr_{ase}/$PBCB_{ethaline}$-HNO_3/MWCNT/GCE presented the best performance for catechol determination, as occurred for glucose with GOx, with the highest sensitivity of 750 μA cm^{-2} mM^{-1} and lowest limit of detection of 3.9 μM. The Tyr$_{ase}$/PBCB$_{aq}$/MWCNT/GCE biosensor exhibited a sensitivity of 330 μA cm^{-2} mM^{-1} and a limit of detection of 5.3 μM whereas Tyr/GCE presented a sensitivity of 30 μA cm^{-2} mM^{-1} and a limit of detection of 43 μM. The values of K_M are around 80 μM for the first two biosensor assemblies with PBCB and around 1000 μM for GCE without PBCB.

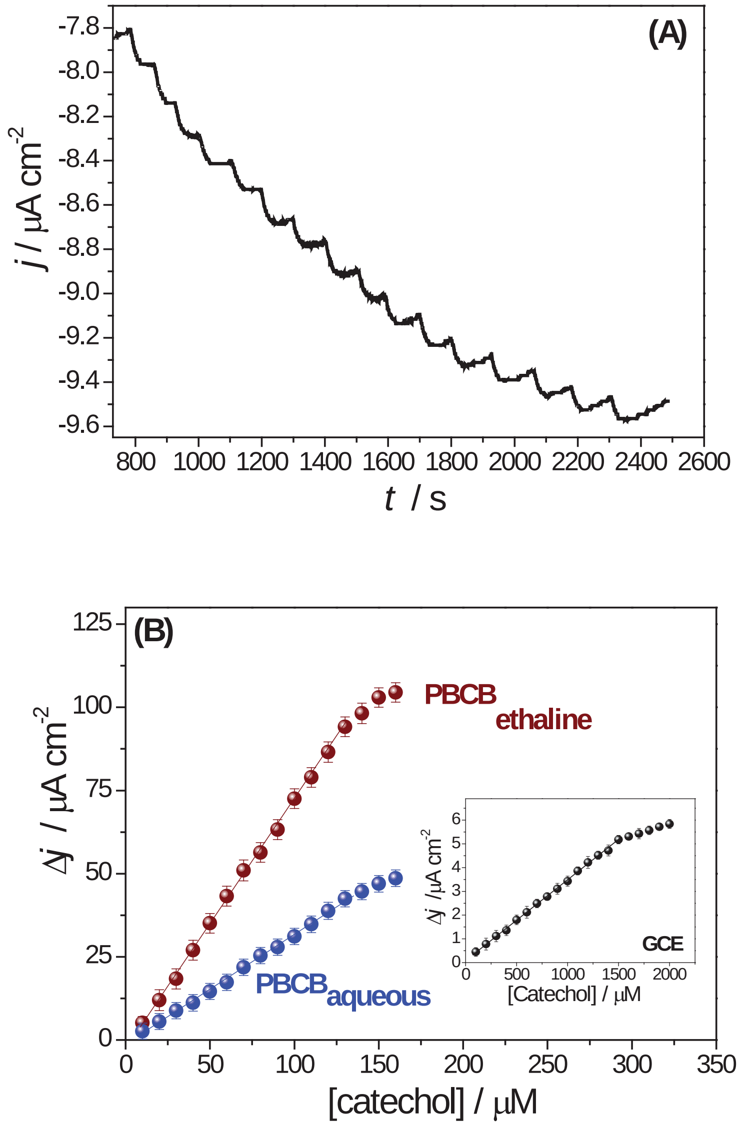

Fig. 6.9 Typical amperometric response of **(A)** Tyr$_{ase}$/PBCB$_{ethaline}$/MWCNT/GCE biosensor to catechol at -0.2 V vs. Ag/AgCl in PB (pH 7.0). **(B)** Corresponding calibration plots for the biosensors with enzyme immobilised on PBCB$_{ethaline}$ and PBCB$_{aq}$ modified MWCNT/GCE. Insert: Tyr$_{ase}$ /GCE.

The analytical parameters of the $Tyr_{ase}/PBCB_{ethaline}$-$HNO_3$/MWCNT/GCE biosensor were also compared with the most recent biosensors reported in the literature. Tembe et al. [282] developed an electrochemical biosensor for catechol using Tyrosinase enzyme entrapped in an agarose–guar gum composite matrix with sensitivity 1 μA cm^{-2} mM^{-1}, the linear range was 65 μM – 1.0 mM and a limit of detection of 6 μM. López and Ruiz [283] proposed a biosensor based on the immobilisation of Tyr_{ase} onto microparticles prepared by polymerisation of the ionic liquid 1-vinyl-3-ethyl-imidazolium bromide ($ViEtIm^+Br^-$) for catechol determination having a sensitivity of 17.96 μA cm^{-2} mM^{-1}, the linear range was from 39 μM to 2.5 mM and a limit of detection of 20 μM. López and Merkoçi [284] also developed a biosensor for catechol determination using Tyr_{ase} immobilised on MWCNT decorated by magnetic nanoparticles modified screen-printed electrode with a sensitivity of 4.8 μA cm^{-2} mM^{-1}, the linear range was between 10 μM – 120 μM and limit of detection of 7.61 μM.

Additional experiments were performed to evaluate if the absence of oxygen influences the electroactivity of the $PBCB_{DES}$-HNO_3/MWCNT for both GOx and Tyr_{ase} for glucose and catechol biosensing. Cyclic voltammograms were recorded in the presence and absence of oxygen, and no significant changes were observed, either in the voltammograms shape or in the peak current. Compared with other sensors used for biosensing glucose and catechol, the proposed platform exhibited the lowest limit of detection, highest sensitivity and comparable linear range. These results also suggest that the novel $PBCB_{DES}$-HNO_3/MWCNT platform has the best affinity for enzyme immobilisation, presenting an excellent performance for enzyme electrochemical biosensors.

6.5 Potentiostatic PBCB film deposition

Poly(brilliant cresyl blue) films were also formed on MWCNT/GCE potentiostatically at a fixed applied potential, and a comparison was carried out with PBCB films electrodeposited potentiodynamically by potential cycling at 150 mV s^{-1}, as optimised in Sections 6.1 to 6.3. The following terminology will be used to distinguish the electropolymerisation methods: $PBCB^{PTD}$ (potentiostatic deposition of polymer film) and $PBCB^{PDD}$ (potentiodynamic deposition of polymer film). Polymerisation was carried out in ethaline DES-HNO_3 solutions and aqueous solution. For the optimisation of the best conditions for PBCB film electrodeposition in potentiostatic mode, the influence of composition of the polymerisation solutions, applied potential and deposition time were investigated.

6.5.1 Influence of the applied potential and deposition time

The applied potential used for the potentiostatic, fixed potential, polymer synthesis has a significant influence on the amount of polymer film formed. **Fig. 6.10** shows chronoamperometric curves (*j* – *t*) of PBCB$_{\text{ethaline}}^{\text{PTD}}$-HNO$_3$ film electrodeposition at values of the applied potential of 0.8, 1.0 and 1.2 V vs. Ag/AgCl, during 300 s (the PBCB$_{\text{ethaline}}^{\text{PTD}}$-HNO$_3$ films did not grow when less positive potentials were employed).

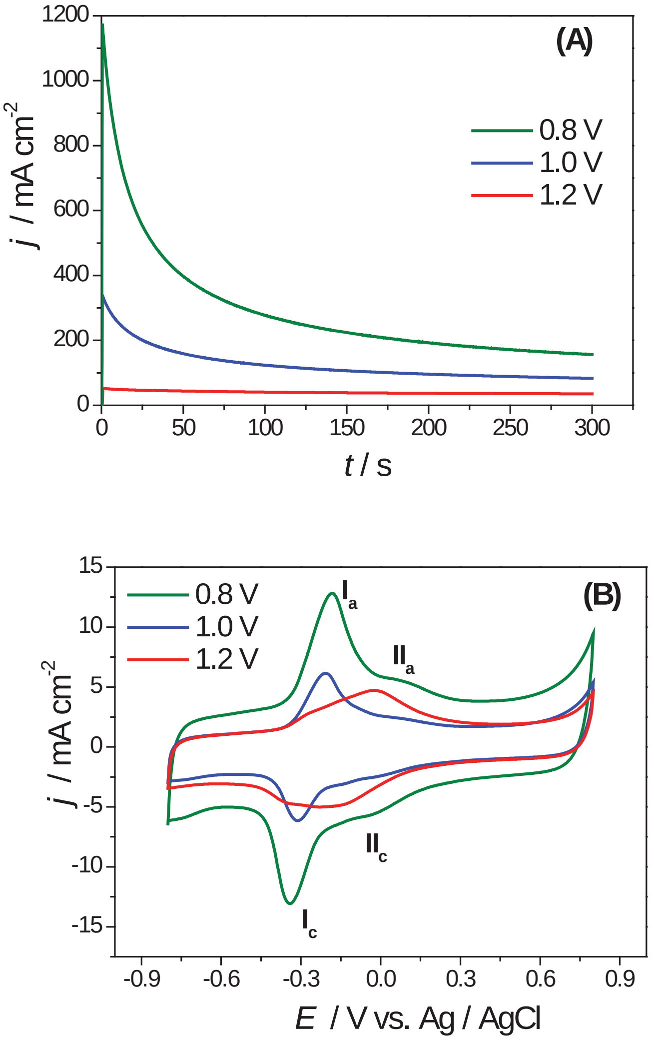

Fig. 6.10 Potentiostatic formation of PBCB films on MWCNT/GCE from solutions containing 0.1 mM BCB in 0.5 M HNO$_3$ – ethaline **(A)** at different applied potentials (0.8, 1.0 and 1.2 V vs. Ag/AgCl) for 300 s. **(B)** CVs of PBCB films in 0.1 M PB (pH 7.0) at 50 mV s^{-1} formed at different applied potentials.

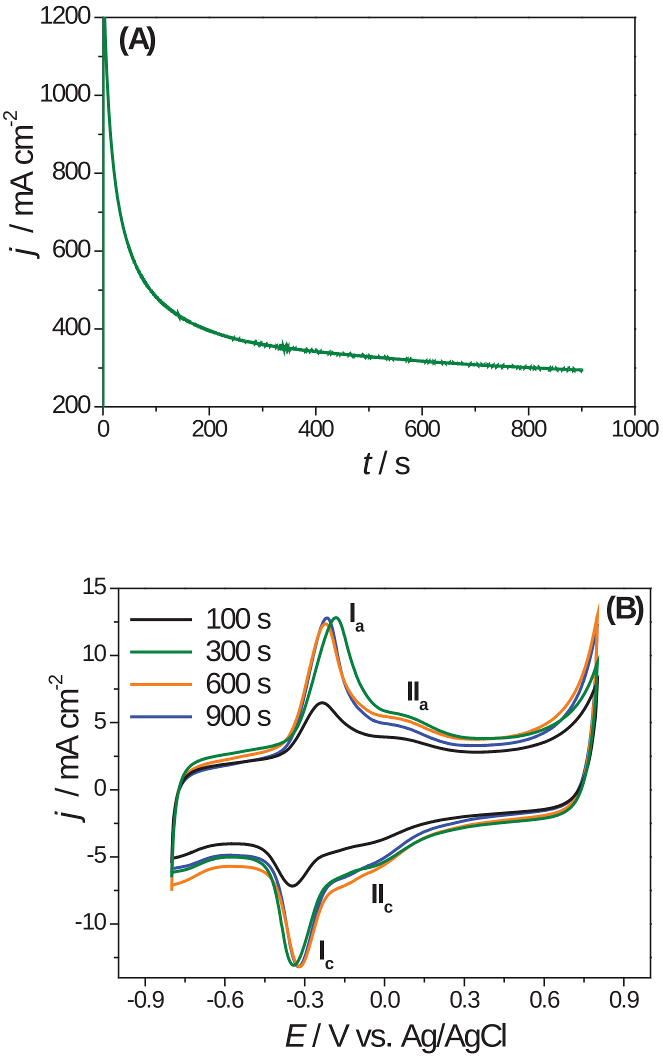

Fig. 6.11 Potentiostatic formation of PBCB films on MWCNT/GCE from solutions containing 0.1 mM BCB in 0.5 M HNO_3 – ethaline **(A)** for 900 s deposition time. **(B)** CVs of PBCB films during different electropolymerisation times.

The curves show the characteristic profile of potentiostatic polymerisation. First, there is a rapid increase in current attributed to double layer charging and oxidation of monomer close to the electrode surface and following this, when the current begins to decay, nucleation takes place accompanied by continuous and gradual polymer growth.

The higher initial currents with increasing applied potential reflect a higher rate of nucleation. An increase in applied potential during potentiostatic polymerisation may result in two opposite effects. One is an increase in the polymerisation rate as mentioned above. The other effect is the enhancement of degradation processes by overoxidation at more positive potentials, influencing the polymer's electrochemical activity, equivalent to the loss of a certain amount of polymer.

That this happens is shown by the lower peak currents in the CV of the $PBCB_{DES}$-HNO_3 films, **Fig. 6.10A**, obtained at 1.0 and 1.2 V vs. For 1.2 V polymerisation potential, the peak currents in the CV profile are not as well-defined as for 1.0 V. Similar behaviour has been reported for other polymers e.g., PEDOT and polypyrrole [285,286].

The surface coverages (Γ) were calculated to be: $3.72 \times 10^{-7} < 4.23 \times 10^{-7} < 5.05 \times 10^{-7}$ mol cm^{-2}, for $PBCB_{DES}$-HNO_3 electrodeposited at 1.2, 1.0 and 0.8 V respectively. The electrochemical response of the $PBCB_{ethaline}$-HNO_3 films obtained at 0.8 V vs. Ag/AgCl was higher and was chosen as the best.

The influence of the deposition time on the amount of $PBCB_{DES}$-HNO_3 film formed was also assessed. $PBCB_{DES}$-HNO_3 films were electrodeposited at 0.8 V vs. Ag/AgCl, as previously optimised, **Fig. 6.11A** and deposition were stopped after periods of 100, 300, 600 and 900 s. The CV profile of the polymer films, **Fig. 6.11B**, all present two redox couples (I_a/I_c and II_a/II_c), in which on increasing the deposition time from 100 to 300 s, a significantly greater amount of polymer film is deposited, as revealed by higher peak currents. For longer deposition times of 600 and 900 s, the peak currents have almost the same magnitude as for 300 s, indicating little further deposition. The surface coverage (Γ) was calculated to be 2.15×10^{-7}, 5.80×10^{-7}, 5.82×10^{-7}, and 5.85×10^{-7} mol cm^{-2} for 100, 300, 600, and 900 s deposition time, respectively. Thus, a deposition time of 300 s was chosen as optimum.

6.5.2 Influence of the electrodeposition mode on PBCB film morphology

Fig. 6.12 shows SEM images of PBCB films on MWCNT-modified carbon film electrodes produced under the optimized conditions described previously. The morphology of the PBCB films depends considerably on the electropolymerisation method and the medium in which it was carried out.

In aqueous medium and for the $PBCB_{aq}^{PDD}$ film, **Fig. 6.12A**, only a small amount of polymer is electrodeposited with incomplete coverage. The overall morphology of the MWCNT surface did not change, revealed by the presence of some exposed MWCNT bundles in the nanocomposite film, as also reported in [273,274,287]. Conversely, the $PBCB_{aq}^{PTD}$ film, **Fig. 6.12B**, revealed a thicker morphology covering all

MWCNT bundles indicating a greater polymer film mass, besides the presence of some globular-like shape nanostructures.

The difference in the morphologies of the PBCB films may be attributed to a secondary nucleation process on the previously-formed polymer, often found for potentiostatic electrodeposition [288]. Polymer films formed in ethaline DES-HNO_3 by the two electropolymerisation methods present a more compact surface than PBCB films prepared in aqueous solutions. However, in the case of $PBCB_{ethaline}$-HNO_3^{PDD} film, **Fig. 6.12C**, some irregularities are observed with a rougher surface. For the $PBCB_{ethaline}$-HNO_3^{PTD}, **Fig. 6.12D**, a completely smooth and uniform surface was obtained.

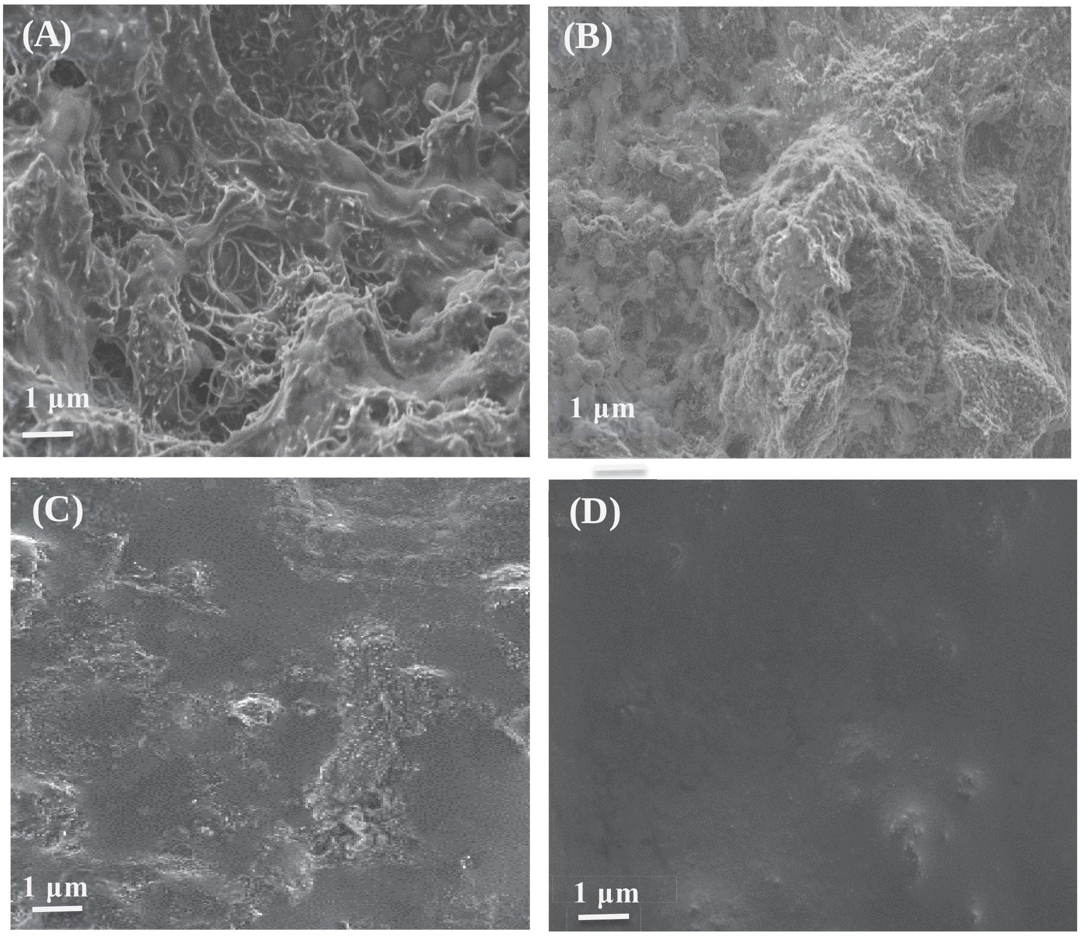

Fig. 6.12 SEM micrographs of PBCB films on MWCNT/CFE electrodeposited in: **(A)** 0.1 M KNO_3 + 0.1 M PBS (pH 7.0) at 150 mVs^{-1}; **(B)** 0.1 M KNO_3 + 0.1 M PBS (pH 7.0) at 0.8 V vs. Ag/AgCl during 300 s; **(C)** ethaline + 0.5 M HNO_3 at 150 mVs^{-1}; **(D)** ethaline + 0.5 M HNO_3 at 0.8 V vs. Ag/AgCl during 300 s.

The structures with greater roughness observed for the film grown by potentiodynamic mode are most likely associated with the effects of the entry and expulsion of counter ions during each voltammetric cycle. Under potentiostatic conditions, the polymer grows continuously at a faster rate, and the counter-ions are accumulated throughout the whole polymerisation procedure and a smoother surface is formed. These results are in agreement with the observations of Zhang et al. [288].

6.6 Application of ChOx/PBCB$_{aq}$ and ChOx/PBCB$_{DES}$-HNO$_3$ biosensor to choline detection

Choline biosensors were prepared by immobilising choline oxidase on the four types of optimised PBCB modified MWCNT/GCE, i.e., PBCB formed by potentiostatic and potentiodynamic modes and, for each, prepared in DES or aqueous medium, as discussed above. Amperometric measurements of choline for the different biosensor configurations were carried out in 0.1 M PB solution, pH 7.0, at an applied potential of -0.3 V vs. Ag/AgCl as optimised in [289], in which 3.5 mg mL^{-1} ChOx was used as enzyme loading. A typical chronoamperogram for the response to choline at ChOx/PBCB$_{DES}$-HNO$_3^{PTD}$/MWCNT/GCE is shown in **Fig. 6.13A**, evidencing an increase of the change in cathodic current with increase of choline concentration for all biosensor assemblies tested. **Fig. 6.13B** displays calibration plots for all biosensor configurations with the corresponding analytical parameters summarised in **Table 6.2**.

As observed, the highest sensitivity of 107 μA cm^{-2} mM^{-1} and lowest limit of detection (LoD) 1.55 μM was reached at the ChOx/PBCB$_{ethaline}$-HNO$_3^{PTD}$/MWCNT/GCE biosensor, following the linear regression equation: Δj(μA cm^{-2}) = 0.61 + 0.11 [choline](μM). For the ChOx/PBCB$_{ethaline}$-HNO$_3^{PDD}$/MWCNT/GCE biosensor the sensitivity was 77 μA cm^{-2} mM^{-1}and the LoD was 1.91 μM, where Δj(μA cm^{-2}) = 0.35 + 0.077 [choline](μM).

The ChOx/PBCB$_{aq}^{PTD}$/MWCNT/GCE biosensor presented a sensitivity of 41 μA cm^{-2} mM^{-1} and LoD of 2.43 μM, with Δj(μA cm^{-2}) = 0.69 + 0.041[choline](μM). Finally, the ChOx/PBCB$_{aq}$ ^{PTD}/MWCNT/GCE biosensor had the lowest sensitivity of 21 μA cm^{-2} mM^{-1} and LoD 3.41 μM, with Δj(μA cm^{-2}) = 0.05 + 0.021 [choline](μM).

The ChOx/PBCB$_{ethaline}$-HNO$_3^{PDD}$/MWCNT/GCE biosensor has the best or similar electrochemical performance compared with some of the most recent ChOx biosensors for choline determination found in the literature.

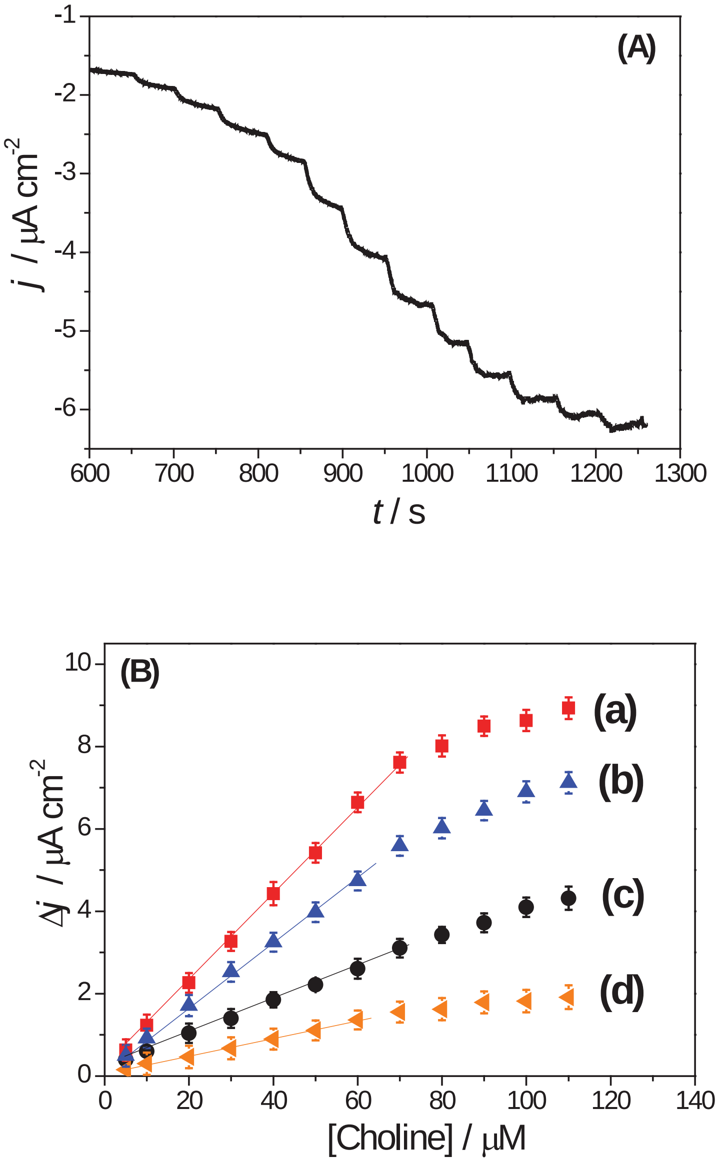

Fig. 6.13 (A) Amperometric response of ChOx/PBCB$_{ethaline}$-HNO$_3^{PTD}$ biosensor to choline. **(B)** Calibration curves for choline in 0.1 M PBS (pH 7.0) at −0.30 V for: **(a)** ChOx/PBCB$_{ethaline}$-HNO$_3^{PTD}$/MWCNT/GCE biosensor; **(b)** ChOx/PBCB$_{ethaline}$-HNO$_3^{PDD}$/MWCNT/GCE biosensor; **(c)** ChOx/PBCB$_{aq}^{PTD}$/MWCNT/GCE biosensor; **(d)** ChOx/PBCB$_{aq}^{PDD/}$ MWCNT/GCE biosensor.

Table 6.2. Analytical performance of different biosensor configurations towards choline.

Biosensor Configuration on MWCNT/GCE	LOD / µM	Sensitivity / µA cm^{-2} mM^{-1}
ChOx/$PBCB_{aq}$ ^{PDD}	3.41	21
ChOx/$PBCB_{aq}$ ^{PTD}	2.43	41
ChOx/ $PBCB_{ethaline}$-HNO_3^{PDD}	1.91	77
ChOx/ $PBCB_{ethaline}$-HNO_3^{PTD}	1.55	107

^{*PDD} - polymer films electrodeposited by potential cycling, 30 cycles

^{*PDT} - polymer films electrodeposited at fixed potential: 0.8V during 300s

For instance, an amperometric choline biosensor consisting of choline oxidase immobilised on a PB–$FePO_4$ nanocomposite modified GCE, exhibited a sensitivity of 75.2 µA mM^{-1} cm^{-2} and LoD of 0.4 µM [290]. Yang et al. [291], developed a bi-enzymatic biosensor for choline determination based on ChOx and horseradish peroxidase (HRP) immobilised on polythionine film modified carbon paste electrodes; the sensitivity of this biosensor was 0.75 µA mM^{-1} cm^{-2} and LoD was 3.0 µM. Rahimi et al. [292], proposed a choline biosensor by immobilisation of ChOx on RTIL/NH_2-MWCNT/GCE; the sensitivity being 125.8 µA mM^{-1} cm^{-2} and with LoD of 3.85 µM. Yu et al. [293], also developed a biosensor based on the immobilisation of ChOx on manganese dioxide (MnO_2) nanoparticle modified GCE, which exhibited a sensitivity of 7.86 8 µA mM^{-1} and LoD of 5.0 µM. Thus, ChOx/$PBCB_{ethaline}$-HNO_3^{PDD}/MWCNT/GCE was chosen as the best biosensor configuration for inhibition studies.

6.7 Inhibition measurements

6.7.1 Influence of the pH, applied potential, and enzyme loading

The dependence of the degree of inhibition on pH was assessed in the pH range from 6.0 to 8.0. The response of the biosensor to 20 nM dichlorvos, in the presence of 0.5 mM choline, varied significantly with pH as illustrated in **Fig. 6.14A**. The inhibition measurements were initially carried out at an applied potential of -0.3 V vs. Ag/AgCl and 3.8 mg mL^{-1} enzyme loading. As can be observed, the change in amperometric response due to inhibition rises with increase of pH from 6.0 to 7.0, where the maximum is reached, and then decreases again. Thus, pH 7.0 PB solution was chosen for further inhibition experiments.

The influence of the applied potential was also assessed by measuring the amperometric response to 20 nM dichlorvos using the same concentration of choline and ChOx at fixed potentials ranging from -0.4 to + 0.2 V vs. Ag/AgCl, **Fig. 6.14B**. The response to dichlorvos increases from -0.4 to -0.3 V vs. Ag/AgCl and then decreases as the applied potential was shifted to less negative potential values. The highest degree of inhibition is exhibited at -0.3 V vs. Ag/AgCl, which was chosen as optimum.

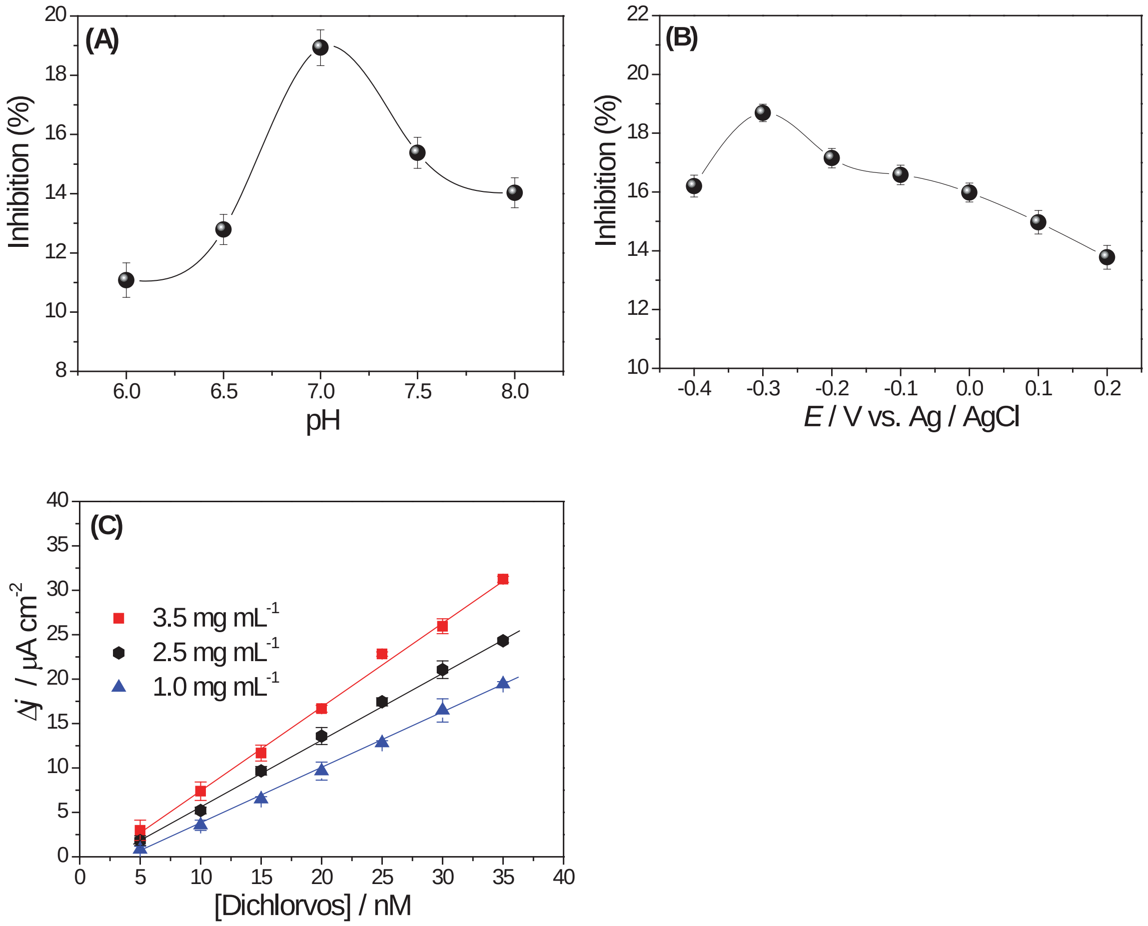

Fig. 6.14 Influence of **(A)** pH and **(B)** applied potential on the amperometric response to 20 nM dichlorvos in 0.1 M PBS at ChOx/PBCB$_{ethaline}$HNO$_3^{PTD}$/MWCNT/GCE biosensor in the presence of 0.5 mM choline. **(C)** Calibration plots for the determination of dichlorvos in 0.1 M PBS pH 7.0 for three different ChOx concentrations in the presence of 0.5 mM choline. Applied potential - 0.3 V vs Ag/AgCl.

The enzyme concentration can also influence the enzymatic activity under inhibition conditions. The effect successive additions of dichlorvos on the response to 0.5 mM choline was tested by measuring the activity for three different loadings of choline oxidase (ChOx) (1.0, 2.5 and 3.5 mg mL^{-1}) immobilised on PBCB$_{\text{ethaline}}$-HNO$_3^{\text{PTD}}$ MWCNT/GCE. **Fig. 6.14B** shows calibration plots and an increase of the sensitivity to inhibitor is clearly observed when the ChOx concentration was increased: 628, 764 and 950 μA cm^{-2} μM^{-1} for 1.0, 2.5 and 3.5 mg mL^{-1} enzyme loading, respectively. The highest sensitivity was achieved for 3.5 mg mL^{-1} ChOx immobilised on PBCB$_{\text{ethaline}}$-HNO$_3^{\text{PTD}}$MWCNT/GCE and therefore was chosen as optimum and used in further enzyme inhibition experiments.

6.7.2 Mechanism of inhibition and analytical performance of the inhibition biosensor for dichlorvos detection

To study the mode of interaction between the dichlorvos and the active site of ChOx, the same graphical method used at PBG$_{\text{ethaline}}$150/MWCNT/GCE biosensor for the determination of reversible inhibition type was employed. Three choline concentrations, namely 0.3, 0.5 and 1.0 mM, were used, as shown in **Fig. 6.15A**. After successive additions of known concentration of dichlorvos in the presence of different concentrations of choline; the values of I_{50} decreases whilst the substrate concentration increases, and maximum inhibition increases, tendency characteristic of an uncompetitive mechanism of inhibition [252]. The mechanism of inhibition was also evaluated from the classical Dixon and Cornish-Bowden plots. The Dixon plot, **Fig. 6.15B1** showed parallel lines and Cornish-Bowden plots, **Fig. 6.15B2**, showed an intersection of the lines on the left side of the y-axis, above the inhibitor axis, both in agreement with the uncompetitive inhibition mechanism.

The enzyme inhibition constant (K_i) was estimated by equation 6.3, from the relationship between I_{50} and K_i, for an uncompetitive inhibition mechanism, as proposed by Amine et al [252].

$$\frac{I_{50}}{K_i} = \left(1 + \frac{K_\text{M}}{[\text{S}]}\right) \qquad 6.3$$

where K_M = 39.2 μM, is the Michaelis-Menten constant of the enzyme without the presence of inhibitor and [S] = 0.5 mM, is the substrate concentration.

The enzyme inhibition constant (K_i) was calculated to be 19.8 nM, close to the value obtained from the intercepts of the curves of the Cornish-Bowden plots, 19.2 nM, corresponding to good agreement between the two approaches.

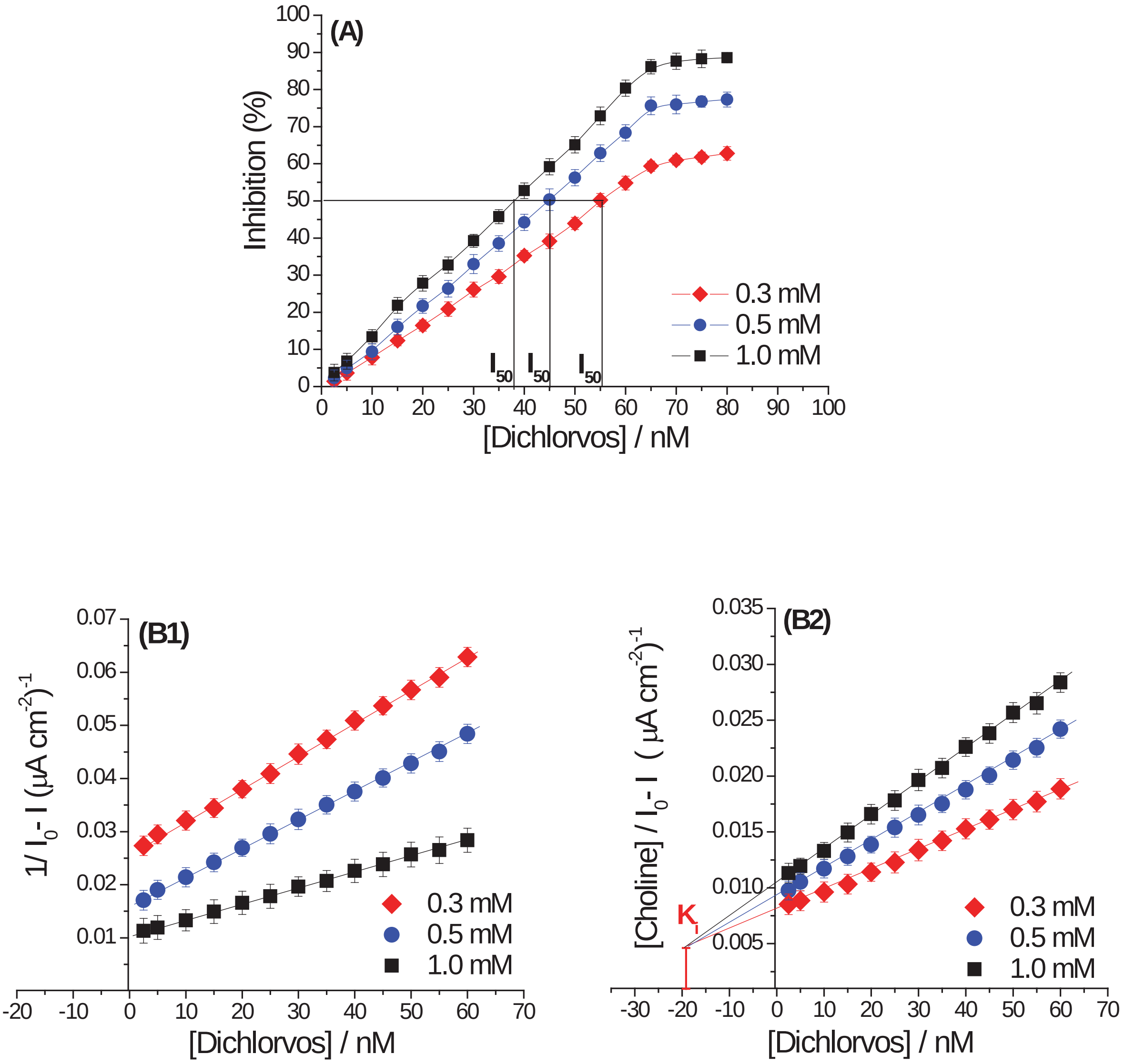

Fig. 6.15 (A) Plots for determination of the mechanism of inhibition of dichlorvos in 0.1 M PB (pH 7.0), according to [252], for three different concentrations of choline. **(B)** Cornish-Bowden **(B1)** and Dixon **(B2)** plots for three different concentrations of choline. Applied potential -0.3 V vs. Ag/AgCl.

Amperometric measurements of dichlorvos at the ChOx/PBCB$_{ethaline}$-HNO$_3$^{PTD}MWCNT/GCE were carried out in 0.1 M PB, pH 7.0 at an applied potential of - 0.3 V vs. Ag/AgCl, as previously optimised. As seen above, the concentration of the enzyme substrate can greatly influence the degree of inhibition for each inhibitor aliquots injected. Thus, the concentration of the enzyme substrate needs to be carefully chosen. Independently of the mechanism of inhibition, a higher concentration of the enzyme substrate can lead to a decrease of enzyme inhibition by the inhibitor. On the other hand, when the concentration of the substrate is low, saturation of the enzyme activity is observed in the presence of low inhibitor concentrations, compromising its response. To minimise these effects, an intermediate value of 0.5 mM choline, **Fig. 6.15A**, was chosen for calibration plots.

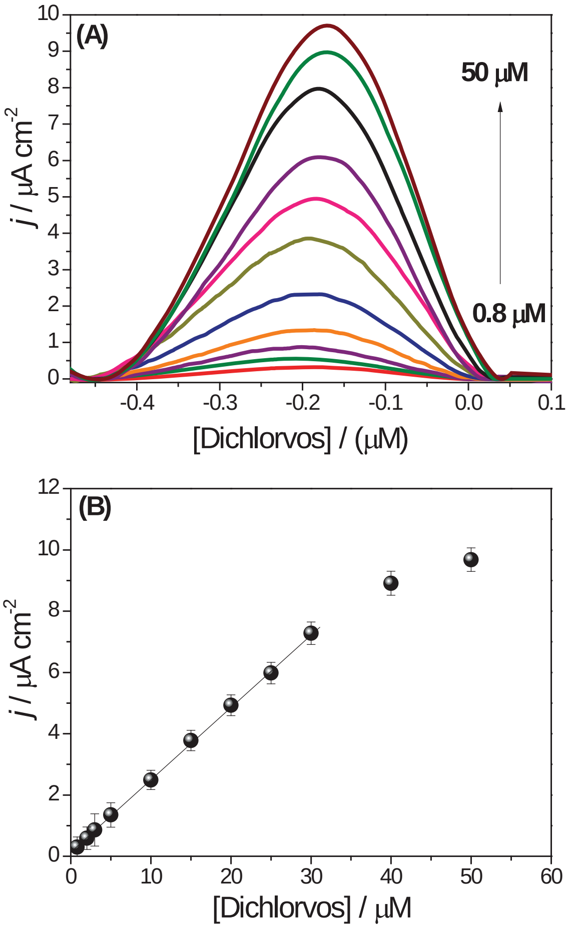

Fig. 6.19 (A) Differential pulse voltammetry for oxidation of dichlorvos at PBCB$_{ethaline}$-HNO$_3$^{PTD}MWCNT/GCE in 0.5 M Na$_2$SO$_4$, recorded at 5 mVs^{-1}. Amplitude 10 mV, step potential 2 mV, pulse time 10 ms. **(B)** Calibration plots for voltammetric determination of dichlorvos.

Table 6.3. Comparison of the analytical performance of the ChOx/PBCB$_{ethaline}$-HNO$_3^{PTD}$ for dichlorvos determination with other inhibition biosensor configurations.

Biosensor configuration	Mode of detection	Applied potential and pH	Linear range / nM	Detection limit / nM	method	Ref.
AChE/CS@TiO$_2$-CS/rGO/GCE	Differential pulse voltammetry	E_p ~ 0.65 V vs. (Ag/AgCl), PB (pH 7.4)	36 - 22.6 x10^3	29	incubation	[294]
AChE–Er-GRO–Nafion/GCE	Amperometry	0.5 V vs. (Ag/AgCl), PB (pH 7.0)	22.6 - 453	9.05	incubation	[295]
AChE/Cyt c / SiL/ITO	Amperometry	-0.5 V vs. (Ag/AgCl), PB (pH7.0)	10 - 1 x10^6	3.01	incubation	[296]
AChE/Al$_2$O$_3$ / SPE	Amperometry	0.25 V vs. (Ag/AgCl), PB (pH 7.0)	100-80 x10^3	10	incubation	[297]
ChOx/PBCB$_{DES}$ -HNO$_3^{PTD}$	Amperometry	-0.5 V vs. (Ag/AgCl), PB (pH 7.0)	2.5-60	1.6	injection	This work

AChE/CS@TiO$_2$-CS/rGO/GCE - acetylcholinesterase (AChE) adsorbed on chitosan (CS), TiO$_2$ sol-gel, and reduced graphene oxide (rGO) based multi-layered immobilisation matrix modifying glassy carbon electrode; AChE–Er-GRO–Nafion/GCE - AChE immobilized on electrochemically reduced graphene oxide and Nafion hybrid nanocomposite modified glassy carbon electrode; AChE/Cyt c/SiL/ITO - AChE and cytochrome c (Cyt c) incorporated into mesoporous silica thin films modifying indium tin oxide; AChE/Al$_2$O$_3$/SPE - ACHE entrapped in Al$_2$O$_3$ screen-printed sol-gel matrix

In some inhibition studies, the limit of detection is calculated based on a signal-to-noise ratio of 3 (S/N=3) and others consider I_{10} value (concentration necessary for 10 % inhibition of the initial response of the substrate). The LoD and I_{10} were calculated to be 1.59 and 9.96 nM, respectively. From the linear response between 2.5 and 60 nM, the following equation was obtained: Δj (μA cm^{-2}) = -1.47+1.15 [dichlorvos] (nm). Independently of the method of calculation, the present biosensor exhibited the lowest of the detection limits reached until now for dichlorvos detection, see **Table 6.3**.

Besides this, the novel ChOx/PBCB$_{ethaline}$-HNO3^{PTD} /MWCNT/GCE biosensor has several advantages, such as easy preparation, fast response, and low applied potential compared with the other biosensors for dichlorvos detection in **Table 6.3**.

Furthermore, it did not require any kind of special procedure for restoring the ChOx activity such as immersion of the electrodes in buffer solution and/or successive potential scans, to restore the original activity.

Additional experiments were also carried out for direct detection of dichlorvos by differential pulse voltammetry, **Fig. 6.19A**. The peak current increased linearly with dichlorvos concentration in the range from 0.8 to 30 μM, **Fig. 6.19A**. The linear equation was calculated as Δj (μA cm $^{-2}$) = 0.16+0.26 [dichlorvos] (μM) with a limit of detection of 0.65 μM. However, the limit of detection achieved is not as low as the nanomolar detection limit obtained by the enzyme inhibition method, that can quantify concentration values less than those considered hazardous for living organisms.

6.8 Repeatability, stability, and selectivity

Repeatability and stability are also important factors for practical application of enzyme biosensors. Good repeatability with a relative standard deviation (RSD) less than 5.0 % was obtained by evaluation of five different ChOx/PBCB$_{ethaline}$-HNO$_3$^{PTD}/MWCNT/GCE biosensors by the injection of the same concentration of dichlorvos, 20 nM. Additionally, the stability of the ChOx biosensor was assessed by monitoring the 0.5 mM choline amperometric response after 10 consecutive injections of 20 nM dichlorvos every day for 20 days. After 20 days the choline response still retained 95.6 % of the initial response, demonstrating excellent stability of the biosensor. To identify potential interferents and selectivity of the ChOx/PBCB$_{ethaline}$-HNO$_3$^{PTD}/MWCNT/GCE biosensor, interference studies were carried out in the presence of several interfering species, which are known to be able to inhibit enzyme activity and which could be present in waters or agricultural produce. These were trace metals ions (Cu^{2+}, Fe^{2+}, Ni^{2+}, Co^{2+}, Cd^{2+}, Hg^{2+}, and Cr^{VI}) and the pesticides cyanazin and terbutryn, **Fig. 6.16**.

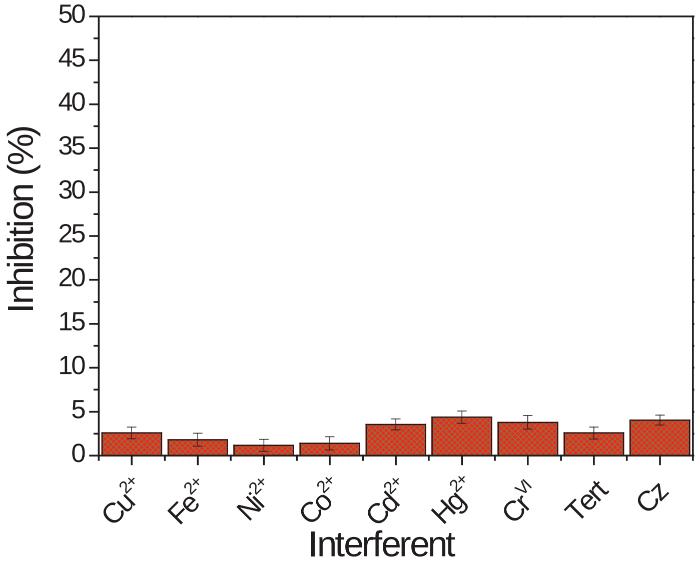

Fig. 6.16 Inhibition caused at ChOx/$PBCB_{ethaline}$-HNO_3^{PTD}/MWCNT/GCE by the presence of different interferents in 0.1 M PB (pH 7.0) in the presence of 0.5 mM choline at applied potential - 0.3 V vs. Ag/AgCl. Concentration of interferents: 100 nM.

The inhibition caused by each interferent was evaluated in independent experiments in relation to the initial response to 0.5 mM choline at an applied potential of – 0.3 V vs. Ag/AgCl, as previously optimised; the concentration of each interferent injected in the electrochemical cell was 100 nM. The degree of inhibition for all interferents tested had no significant influence over the initial response of choline, less than 5%. In general, the ChOx/$PBCB_{DES}$-HNO_3^{PTD}/MWCNT/GCE biosensor exhibited good selectivity towards the dichlorvos response, which suggests its use for monitoring trace dichlorvos in agricultural produce, and for monitoring in water.

6.9 Application of ChOx/ $PBCB_{ethaline}$-HNO_3^{PTD} biosensor for dichlorvos determination in orange juice

To evaluate the feasibility of the biosensor for environmental monitoring, application to the determination of dichlorvos in orange juice by the standard addition method was examined. Prior to measurements, the extracted orange juice was strained through a fine mesh sieve.

Table 6.4. Recovery test of dichlorvos spiked in orange juice.

Sample	Added / nM	Expected / nM	Found / nM	Recovery (%)
1	10	10	10.22 ± 0.04	102.2
2	20	20	19.94 ± 0.02	99.7
3	30	30	31.05 ± 0.04	101.5

Afterwards, the orange juice was centrifuged at 14,000 rpm for 20 min, then the supernatants were collected and kept at 4 °C before use. The juice samples, after pre-treatment, were spiked with three known concentration of dichlorvos, **Table 6.4**. The average recovery was in the range of 99.7 – 103.2%, which indicates the efficient applicability of the biosensor for practical analysis.

6.10 Conclusions

$PBCB_{DES}$ films were electrodeposited by fixed potential and potentiodynamic cycling electropolymerisation. SEM studies demonstrated that morphology of the nanostructures obtained are greatly dependent on the composition of the polymerisation solutions and electrodeposition mode, which the polymer films produced from ethaline-HNO_3 in potentiostatic mode showed a smoother and more compact surface. The enzymes GOx and Tyr_{ase} were immobilised on $PBCB_{ethaline}$-HNO_3/MWCNT/GCE ($PBCB_{DES}$ film electrodeposited by potentiodynamic cycling electropolymerisation), presenting excellent biosensing performance for glucose and catechol. $PBCB_{DES}$ electrodeposited by fixed potential also demonstrated excellent biosensing properties towards choline and this configuration was used for detection of dichlorvos through ChOx enzyme inhibition. The novel enzyme inhibition biosensor exhibited a lower limit of detection, in the nanomolar range, with good selectivity and stability, than those in the literature. These results demonstrated that the novel nanocomposite developed is a promising sensing platform for enzyme immobilisation and fabrication of novel enzyme biosensors.

This page intentionally left blank

Chapter 7

Conclusions and Perspectives

The research undertaken in this work concerned the development of novel electrode architectures and their applications as electrochemical sensors and/or biosensors, having as goal the efficient use of the different conducting nanomaterials and preparation procedures to improve the electrochemical sensing properties of the modified electrodes proposed. Below follows a summary of the principal results obtained together with perspectives and suggestions for future research work.

A novel and simple electrode configuration based on AuNP dispersed in a MWCNT-chitosan network deposited in one step on CGE substrate is proposed to investigate the electrochemical behaviour of theophylline (TP). The optimised AuNP-$MWCNT_{0.25}$/GCE sensor showed the best electrocatalytic effect for the oxidation of TP, exhibiting the greatest enhancement of the oxidation peak current, which can be attributed to the larger effective surface area and the synergetic effect obtained by the efficient aggregation of AuNP on the MWCNT network that increased the conductivity. The sensor showed similar analytical performance to other modified electrodes but offers the important advantages of lower detection potential, easy and fast preparation and less complex architecture. It was successfully applied to determine TP in commercial samples with very good recoveries, which indicates its application to therapeutic drug monitoring of TP and in the quality control of tea.

An easy to prepare and sensitive novel nanocomposite modified electrode based on the electrochemical deposition of poly-(8-anilino-1-naphthalene sulphonic acid) together with attached $AuNP_{green}$ by polymerisation of the monomer together with the gold nanoparticles was developed. The nanocomposite was successfully electrodeposited on both gold electrode and glassy carbon electrode surfaces. The modified electrodes were used to develop an impedimetric sensor and an amperometric biosensor by the immobilisation of tyrosinase for the detection of the biogenic amine tyramine. Electrochemical impedance was demonstrated to be a very sensitive electrochemical technique for the analytical determination of tyramine. The impedimetric sensor proposed possesses good selectivity, reproducibility, stability and high selectivity, with fast response and low micromolar limit of detection. The novel amperometric biosensor exhibited a low limit of detection and a wide linear range, similar to values found for more complex architectures. From the Hill constant $h > 1$, a strong interaction between the enzyme and the electrode substrate was revealed, as well as from the Michaelis-Menten profile. The developed biosensor showed good selectivity, stability, repeatability. Furthermore, both electrochemical approaches were successfully applied to determine tyramine in commercial food products with good recoveries, auguring well for their use in food safety control.

Ethaline deep eutectic solvent (DES) was successfully used as medium for the electropolymerisation of brilliant green (BG) and brilliant cresyl blue (BCB) (PBCB prepared in both potentiodynamic and potentiostatic mode) on MWCNT modified glassy carbon electrodes. The ethaline DES permitted the formation of polymer nanostructured films with superior sensing characteristics compared with films formed in aqueous solution. The optimised sensitive nanocomposites were used as support for enzyme biosensing applications.

A glucose (GOx) inhibition biosensor for trace metal ion detection based on poly(brilliant green) – ethaline deep eutectic solvent/MWCNT exhibited a lower limit of detection, with good selectivity and stability, compared with those in the literature. The mechanism of reversible inhibition was investigated, and was found to be competitive for Hg^{2+} and Cd^{2+}, uncompetitive for Pb^{2+} and mixed for Cr^{VI}. To confirm the sensitivity and applicability of the novel biosensor approach, the modified electrode was successfully applied to trace metal ion detection in contaminated milk samples with excellent recoveries.

Brilliant cresyl blue was successfully electropolymerised in ethaline-DES permitting the formation of polymer nanostructured films with superior electrochemical performance compared with films formed in aqueous solution in both potentiostatic and potentiodynamic polymerisation modes. The composition of ethaline-acid solutions and the mode of deposition had an important role in PBCB growth, also influencing their nanoscale morphology, and thence electrochemical behaviour. For potentiodynamic deposition, the polymer films electrodeposited in ethaline-HNO_3 presented a more uniform morphology and better electrochemical performance than with the other acid dopants studied. The influence of scan rate was also an important factor in polymer electrodeposition, $PBCB_{ethaline}$ electrodeposited at 150 mV s^{-1} exhibited the best electrochemical characteristics. The enzymes GOx and Tyr_{ase} were immobilised on

PBCB$_{ethaline}$-HNO$_3$/MWCNT/GCE (PBCB$_{ethaline}$ electrodeposited at 150 mV s^{-1}), which presented excellent biosensing performance for glucose and catechol determination.

PBCB$_{ethaline}$-HNO$_3$ films electrodeposited in potentiostatic mode presented a smoother and more compact nanostructure than those prepared by potentiodynamic mode, which also influenced in its electrochemical sensing properties. These were found to be the best in the construction of a choline biosensor and its application to determine dichlorvos by enzyme inhibition. The mechanism of choline oxidase inhibition by dichlorvos was found to be uncompetitive, in agreement with the classical Dixon and Cornish-Bowden plots. The novel enzyme inhibition biosensor exhibited a lower limit of detection than reports in the literature, in the nanomolar concentration range, with good selectivity and stability, and was successfully applied to dichlorvos detection in orange juice with excellent recoveries. These properties demonstrate that this novel nanocomposite film modified electrode is very promising for future applications in electrochemical enzyme biosensors.

Future perspectives, regarding continuation of the present direction of research in sensors and biosensors as well as other related topics, could include:

- Investigation of electropolymerisation of other phenazines such as neutral red, Nile blue, methylene green, etc. in different eutectic solvents besides ethaline (e.g. reline and glyceline) on metallic and semiconductor nanoparticle or other carbon based-material modified electrodes. After characterisation and optimisation of the film preparation, their catalytic properties towards detection of various analytes can be exploited to develop novel electrode architectures for sensing applications. Moreover, due to their excellent properties as redox mediators, they could possibly be exploited as an efficient signal amplification strategy for electrochemical immunosensor and enzyme biosensor assemblies for the detection and monitoring of physiologically important analytes such as cancer and cardiac biomarkers, and neurotransmitters.

- New strategies for electrode modification, such as electrospinning of conducting polymer nanofibres modified with metal nanoparticles or carbon based-materials, leading to a web of conductive nanofibres. The nanofibres will be electrospun onto different electrode substrates, such as metals (e.g. gold, copper, platinum), boron-doped diamond electrode, glassy carbon, etc. After optimisation and appropriate chemical functionalisation; the new conducting nanomaterials will be used as electrode substrates for immobilising different oxidase enzymes for biomedical sensing applications.

- New strategies for enzyme immobilisation without loss of activity will be explored, particularly involving the encapsulation and cross-linking methods. The sol-gel technique for enzyme immobilisation will also be optimised and tested by analysing the physical properties of various oxysilane sol-gel precursor mixtures. Furthermore, the layer-by-layer (LBL) self-assembly strategy will be also assessed. A general process of LbL assembly consists in assembly between cationic polyelectrolytes and anionic proteins (enzyme) as an example. The LBL self-assembly process results in films of nanometer-scale thickness and can be conducted in an aqueous solution under mild ambient conditions. The driving force for the LbL assembly is mainly electrostatic interaction, but hydrogen bonding and metal coordination, can also be used. It should be possible to align the enzymes on the surface to maximise access to the active centre. Other advantages of this strategy include enzyme functional stability, and more efficient use of enzymes.

References

[1] D. Grieshaber, R. MacKenzie, J. Vörös, E. Reimhult, Electrochemical biosensors - Sensor principles and architectures, **Sensors** 8 (2008) 1400–1458.

[2] D. R. Thévenot, K. Toth, R. A. Durst, G. S. Wilson, Electrochemical biosensors: Recommended definitions and classification, **Biosens. Bioelectron.** 16 (2001) 121–131.

[3] A. C. A. Morri, Electroanalytical Sensor Technology, in: Electrochemistry, **IntechOpen**, Lodon, 2013.

[4] T. H. S. Dhahi, U. D. A. Bin Hashim, N. M. Ahmed, A. Mat Taib, A review on the electrochemical sensors and biosensors composed of nanogaps as sensing material, **J. Optoelectron. Adv. Mater.** 12 (2010) 1857–1862.

[5] G. S. Wilson, R. Gifford, Biosensors for real-time in vivo measurements, **Biosens. Bioelectron.** 20 (2005) 2388–2403.

[6] B. Lo, G. Z. Yang, Body sensor networks - research challenges and opportunities, **IET,** London, 2008

[7] A. P. F. Turner, Biosensors: sense and sensibility, **Chem. Soc. Rev**. 42 (2013) 3184–3196.

[8] L. Lu, X. Hu, Z. Zhu, Biomimetic sensors and biosensors for qualitative and quantitative analyses of five basic tastes, **TrAC - Trends Anal. Chem.** 87 (2017) 58–70.

[9] C. I. L. Justino, A. C. Freitas, R. Pereira, A. C. Duarte, T. A. P. Rocha Santos, Recent developments in recognition elements for chemical sensors and biosensors, **TrAC - Trends Anal. Chem.** 68 (2015) 2–17.

[10] C. I. L. Justino, T. A. Rocha-Santos, A. C. Duarte, Review of analytical figures of merit of sensors and biosensors in clinical applications, **TrAC - Trends Anal. Chem.** 29 (2010) 1172–1183.

[11] H. Mark, J. H. Kalivas, J. Ferré, R. Boqué, A. C. Olivieri, N. M. Faber, Uncertainty estimation and figures of merit for multivariate calibration (IUPAC Technical Report), **Pure Appl. Chem.** 78 (2006) 633–661.

[12] T. Kubo, Molecularly Imprinted Materials in Analytical Chemistry, **Anal. Sci.** 33 (2017) 1321–1322.

[13] Y. Picó, Chemical Analysis of Food: Techniques and Applications, **Academic Press**, Cambridge, 2012.

[14] J. Bobacka, A. Ivaska, A. Lewenstam, Potentiometric Ion Sensors, **Chem. Rev.** 108 (2008) 329–351.

[15] A. Bratov, N. Abramova, A. Ipatov, Recent trends in potentiometric sensor arrays-A review, **Anal. Chim. Acta** 678 (2010) 149–159.

[16] J. Shah, E. Wilkins, Electrochemical biosensors for detection of biological warfare agents, **Electroanalysis** 15 (2003) 157–167.

[17] D. O'Hare, K. H. Parker, C. P. Winlove, Metal-metal oxide pH sensors for physiological application, **Med. Eng. Phys. 28** (2006) 982–988.

[18] B. Eggins, Chemical Sensors and Biosensors, **John Wiley & Sons Ltd**, Northern Ireland, UK, 2007.

[19] M. Scampicchio, D. Ballabio, A. Arecchi, S. M. Cosio, S. Mannino, Amperometric electronic tongue for food analysis, **Microchim. Acta** 163 (2008) 11–21.

[20] J. Wang, Analytical Electrochemistry, **John Wiley & Sons Ltd**, New York, 2014.

[21] C. M. A. Brett, A. M. O. Brett, Electroanalysis, **Oxford University Press**, Oxford, 1998.

[22] I. Svancara, K. Kalcher, A. Walcarius, K. Vytras, I. Švancara, K. Kalcher, A. Walcarius, K. Vytras, Electroanalysis with Carbon Paste Electrodes, **CRC Press**, Boca Raton, 2012.

[23] O. Fischer, E. Fischerová, Basic principles of voltammetry, in: Exp. Tech. Bioelectrochemistry, **Birkhäuser**, Basel**,** 2013.

[24] G. Bhattacharya, A. Mathur, S. Pal, J. McLaughlin, S. S. Roy. Equivalent Circuit Models and Analysis of Electrochemical Impedance Spectra of Caffeine Solutions and BeveragesInt. **J. Electrochem. Sci.** 11 (2016) 6370 – 6386

[25] D. Chan, M. M. Bărsan, Y. Korpan, C. M. A. Brett, L-lactate selective impedimetric bienzymatic biosensor based on lactate dehydrogenase and pyruvate oxidase, **Electrochim. Acta** 231 (2017) 209–215.

[26] G. Maduraiveeran, W. Jin, Nanomaterials based electrochemical sensor and biosensor platforms for environmental applications, **Trends Environ. Anal. Chem.** 13 (2017) 10–23.

[27] A. Chen, P. Holt-Hindle, Platinum-Based Nanostructured Materials: Synthesis, Properties, and Applications, **Chem. Rev.** 110 (2010) 3767–3804.

[28] N. Baig, M. Sajid, T. A. Saleh, Recent trends in nanomaterial-modified electrodes for electroanalytical applications, **TrAC - Trends Anal. Chem.** 111 (2019) 47–61.

[29] X. Dang, H. Hu, S. Wang, S. Hu, Nanomaterials-based electrochemical sensors

for nitric oxide, **Microchim. Acta** 182 (2014) 455–467.

[30] B. R. Smith, S. S. Gambhir, Nanomaterials for in Vivo Imaging, **Chem. Rev.** 117 (2017) 3901–986.

[31] Z. Chu, Y. Liu, Y. Xu, L. Shi, J. Peng, W. Jin, In-situ fabrication of well-distributed gold nanocubes on thiol graphene as a third-generation biosensor for ultrasensitive glucose detection, **Electrochim. Acta** 10 (2015) 162–171.

[32] Z. Chu, J. Peng, W. Jin, Advanced nanomaterial inks for screen-printed chemical sensors, **Sensors Actuators, B Chem**. 243 (2017) 919–926.

[33] A. V. Nakhate, G. D. Yadav, Cu_2O nanoparticles supported hydrothermal carbon microspheres as catalyst for propargylamine synthesis, **Mol. Catal.** 451 (2018) 209–219.

[34] S. Kempahanumakkagari, A. Deep, K. H. Kim, S. Kumar Kailasa, H. O. Yoon, Nanomaterial-based electrochemical sensors for arsenic - A review, **Biosens. Bioelectron**. 95 (2017) 106–116.

[35] M. Rai, A. Yadav, A. Gade, Silver nanoparticles as a new generation of antimicrobials, **Biotechnol. Adv.** 27 (2009) 76–83.

[36] J. M. George, A. Antony, B. Mathew, Metal oxide nanoparticles in electrochemical sensing and biosensing: a review, **Microchim. Acta** 185 (2018) 35–41.

[37] A. Waheed, M. Mansha, N. Ullah, Nanomaterials-based electrochemical detection of heavy metals in water: Current status, challenges and future direction, **TrAC - Trends Anal. Chem.** 105 (2018) 37–51.

[38] T. Tangkuaram, C. Ponchio, T. Kangkasomboon, P. Katikawong, W. Veerasai, Design and development of a highly stable hydrogen peroxide biosensor on screen printed carbon electrode based on horseradish peroxidase bound with gold nanoparticles in the matrix of chitosan, **Biosens. Bioelectron.** 22 (2007) 2071–2078.

[39] W. Yin, D. H. Lee, J. Choi, C. Park, S. M. Cho, Screen printing of silver nanoparticle suspension for metal interconnects, **Korean J. Chem. Eng.** 25 (2008) 1358–1361.

[40] T. H. Le, Y. Kim, H. Yoon, Electrical and electrochemical properties of conducting polymers, **Polymers** 9 (2017) 1–32.

[41] G. Maduraiveeran, M. Sasidharan, V. Ganesan, Electrochemical sensor and biosensor platforms based on advanced nanomaterials for biological and biomedical applications, **Biosens. Bioelectron.** 103 (2018) 113–129.

[42] M. M. Bărsan, M. E. Ghica, C. M. A. Brett, Electrochemical sensors and biosensors based on redox polymer/carbon nanotube modified electrodes: A review, **Anal. Chim. Acta 881** (2015) 1–23.

[43] H. Yoon, Current Trends in Sensors Based on Conducting Polymer Nanomaterials, **Nanomaterials** 2 (2013) 524–549.

[44] C. Li, H. Bai, G. Shi, Conducting polymer nanomaterials: Electrosynthesis and applications, **Chem. Soc. Rev.** 38 (2009) 2397–2409.

[45] M. Ates, A review study of (bio)sensor systems based on conducting polymers, **Mater. Sci. Eng. C.** 33 (2013) 1853–1859.

[46] L. I. N. Tomé, V. Baião, W. da Silva, C. M. A. Brett, Deep eutectic solvents for the production and application of new materials, **Appl. Mater. Today** 10 (2018) 30–50.

[47] J. D. Mota-Morales, R. J. Sánchez-Leija, A. Carranza, J. A. Pojman, F. del Monte, G. Luna-Bárcenas, Free-radical polymerizations of and in deep eutectic solvents: Green synthesis of functional materials, **Prog. Polym. Sci.** 78 (2018) 139–153.

[48] A. P. Abbott, D. Boothby, G. Capper, D. L. Davies, R. K. Rasheed, Deep Eutectic Solvents formed between choline chloride and carboxylic acids: Versatile alternatives to ionic liquids, **J. Am. Chem. Soc.** 126 (2004) 9142–9147.

[49] K. Ghandi, A Review of Ionic Liquids, Their Limits and Applications, Green **Sustain. Chem.** 4 (2014) 44–53.

[50] T. P. Thuy Pham, C. W. Cho, Y. S. Yun, Environmental fate and toxicity of ionic liquids: A review, **Water Res.** 44 (2010) 352–372.

[51] E. L. Smith, A. P. Abbott, K. S. Ryder, Deep Eutectic Solvents (DESs) and Their Applications, **Chem. Rev.** 114 (2014) 11060−11082.

[52] F. Hollmann, Y. Dai, I. W. C. E. Arends, M. Verberne, R. Verpoorte, Y. H. Choi, J. Van Spronsen, G. J. Witkamp, Are Natural Deep Eutectic Solvents the Missing Link in Understanding Cellular Metabolism and Physiology?, **Plant Physiol.** 156 (2011) 1701–1705.

[53] M. Espino, M. A. Fernández, F. J. V. Gomez, M. F. Silva, Natural designer solvents for greening analytical chemistry, **TrAC - Trends Anal. Chem.** 76 (2016) 126–136.

[54] A. R. C. Duarte, A. S. D. Ferreira, S. Barreiros, E. Cabrita, R. L. Reis, A. Paiva, A comparison between pure active pharmaceutical ingredients and therapeutic deep eutectic solvents: Solubility and permeability studies, **Eur. J. Pharm. Biopharm.** 114 (2017) 296–304.

[55] C. M. A. Brett, Deep eutectic solvents and applications in electrochemical sensing, **Curr. Opin. Electrochem.** 10 (2018) 143–148.

[56] R. N. Goyal, S. Chatterjee, A. R. S. Rana, The effect of modifying an edge-plane pyrolytic graphite electrode with single-wall carbon nanotubes on its use for sensing diclofenac, **Carbon** 48 (2010) 4136–4144.

[57] W. Zhang, S. Zhu, R. Luque, S. Han, L. Hu, G. Xu, Recent development of carbon electrode materials and their bioanalytical and environmental applications, **Chem. Soc. Rev.** 45 (2016) 715–752.

[58] A. Chen, S. Chatterjee, Nanomaterials based electrochemical sensors for biomedical applications, **Chem. Soc. Rev.** 42 (2013) 5425–5438.

[59] P. Ramnani, N. M. Saucedo, A. Mulchandani, Carbon nanomaterial-based electrochemical biosensors for label-free sensing of environmental pollutants, **Chemosphere** 143 (2016) 85–98.

[60] T. Pasinszki, M. Krebsz, T. T. Tung, D. Losic, Carbon nanomaterial based biosensors for non-invasive detection of cancer and disease biomarkers for clinical diagnosis, Sensors 17 (2017) 2–32.

[61] M. L. Yola, T. Eren, N. Atar, A sensitive molecular imprinted electrochemical sensor based on gold nanoparticles decorated graphene oxide: Application to selective determination of tyrosine in milk, **Sensors Actuators, B Chem.** 210 (2015) 149–157.

[62] G. Eda, M. Chhowalla, Chemically derived graphene oxide: Towards large-area thin-film electronics and optoelectronics, **Adv. Mater.** 22 (2010) 2392–2415.

[63] L. Farzin, M. Shamsipur, L. Samandari, S. Sheibani, Advances in the design of nanomaterial-based electrochemical affinity and enzymatic biosensors for metabolic biomarkers: A review, **Microchim. Acta** 5 (2018) 185–276.

[64] Y. Yan, J. Miao, Z. Yang, F. X. Xiao, H. Bin Yang, B. Liu, Y. Yang, Carbon nanotube catalysts: Recent advances in synthesis, characterization and applications, **Chem. Soc. Rev.** 44 (2015) 3295–3346.

[65] P. Papakonstantinou, R. Kern, L. Robinson, H. Murphy, J. Irvine, E. McAdams, J. McLaughlin, T. McNally, Fundamental electrochemical properties of carbon nanotube electrodes, Fullerenes Nanotub. **Carbon Nanostructures** 13 (2005) 91–108

[66] N. S. Lawrence, R. P. Deo, J. Wang, Comparison of the electrochemical reactivity of electrodes modified with carbon nanotubes from different sources, **Electroanalysis** 17 (2005) 65–72.

[67] M. Hasanzadeh, N. Hashemzadeh, N. Shadjou, J. Eivazi-Ziaei, M. Khoubnasabjafari, A. Jouyban, Sensing of doxorubicin hydrochloride using graphene quantum dot modified glassy carbon electrode, **J. Mol. Liq.** 221 (2016) 354–357.

[68] L. Li, D. Liu, A. Shi, T. You, Simultaneous stripping determination of cadmium and lead ions based on the N-doped carbon quantum dots-graphene oxide hybrid, **Sensors Actuators, B Chem.** 255 (2018) 1762–1770.

[69] M. Algarra, A. González-Calabuig, K. Radotić, D. Mutavdzic, C. O. Ania, J. M. Lázaro-Martínez, J. Jiménez-Jiménez, E. Rodríguez-Castellón, M. del Valle, Enhanced electrochemical response of carbon quantum dot modified electrodes,

Talanta 178 (2018) 679–685.

[70] Q. Huang, S. Hu, H. Zhang, J. Chen, Y. He, F. Li, W. Weng, J. Ni, X. Bao, Y. Lin, Carbon dots and chitosan composite film based biosensor for the sensitive and selective determination of dopamine, **Analyst.** 138 (2013) 5417–5423.

[71] C. S. Lim, K. Hola, A. Ambrosi, R. Zboril, M. Pumera, Graphene and carbon quantum dots electrochemistry, **Electrochem. Commun.** 52 (2015) 75–79.

[72] L. Zhang, Y. Han, J. Zhu, Y. Zhai, S. Dong, Simple and sensitive fluorescent and electrochemical trinitrotoluene sensors based on aqueous carbon dots, **Anal. Chem.** 87 (2015) 2033–2036.

[73] V. Georgakilas, J. A. Perman, J. Tucek, R. Zboril, Broad Family of Carbon Nanoallotropes: Classification, Chemistry, and Applications of Fullerenes, Carbon Dots, Nanotubes, Graphene, Nanodiamonds, and Combined Superstructures, **Chem. Rev.** 115 (2015) 4744–4822.

[74] W. Chen, W. Weng, X. Niu, X. Li, Y. Men, W. Sun, G. Li, L. Dong, Boron-doped Graphene quantum dots modified electrode for electrochemistry and electrocatalysis of hemoglobin, **J. Electroanal. Chem.** 823 (2018) 137–145.

[75] H. Wang, T. Maiyalagan, X. Wang, Review on recent progress in nitrogen-doped graphene: Synthesis, characterization, and its potential applications, **ACS Catal.** 2 (2012) 781–794.

[76] S. Samuei, J. Fakkar, Z. Rezvani, A. Shomali, B. Habibi, Synthesis and characterization of graphene quantum dots/CoNiAl-layered double-hydroxide nanocomposite: Application as a glucose sensor, **Anal. Biochem.** 521 (2017) 31–39.

[77] M. H. Naveen, N. G. Gurudatt, Y. B. Shim, Applications of conducting polymer composites to electrochemical sensors: A review, **Appl. Mater. Today** 9 (2017) 419–433.

[78] V. Mody, R. Siwale, A. Singh, H. Mody, Introduction to metallic nanoparticles, **J. Pharm. Bioallied Sci.** 2 (2010) 282–289.

[79] R. Y. Zhang, H. Olin, Gold-carbon nanotube nanocomposites: synthesis and applications, **Int. J. Biomed. Nanosci. Nanotechnol.** 2 (2011) 112–135.

[80] Y. C. Yeh, B. Creran, V. M. Rotello, Gold nanoparticles: Preparation, properties, and applications in bionanotechnology, **Nanoscale** 4 (2012) 1871–1880.

[81] Z. Yang, Z. Li, X. Lu, F. He, X. Zhu, Y. M, R. He, F. Gao, W. Ni, Y. Yi, Controllable Biosynthesis and Properties of Gold Nanoplates Using Yeast Extract, **Nano-Micro Lett.** 9 (2017) 9–5.

[82] J. Wang, G. Zhu, M. You, E. Song, M.I. Shukoor, K. Zhang, M. B. Altman, Y. Chen, Z. Zhu, C. Z. Huang, W. Tan, Assembly of aptamer switch probes and photosensitizer on gold nanorods for targeted photothermal and photodynamic cancer therapy, **ACS Nano** 6 (2012) 5070–5077.

[83] B. Bhattarai, Y. Zaker, T. P. Bigioni, Green synthesis of gold and silver nanoparticles: Challenges and opportunities, **Curr. Opin. Green Sustain. Chem.** 12 (2018) 91–100.

[84] C. Han, A. Doepke, W. Cho, V. Likodimos, A. A. De La Cruz, T. Back, W. R. Heineman, H .B. Halsall, V. N. Shanov, M. J. Schulz, P. Falaras, D. D. Dionysiou, A multiwalled-carbon-nanotube-based biosensor for monitoring microcystin-LR in sources of drinking water supplies, **Adv. Funct. Mater.** 23 (2013) 1807–1816.

[85] H. S. Park, T. J. Park, Y. S. Huh, B. G. Choi, S. Ko, S. Y. Lee, W. H. Hong, Immobilization of genetically engineered fusion proteins on gold-decorated carbon nanotube hybrid films for the fabrication of biosensor platforms, **J. Colloid Interface Sci.** 350 (2010) 453–458.

[86] T. Oliveira, S. Morais, New Generation of Electrochemical Sensors Based on Multi-Walled Carbon Nanotubes, **Appl. Sci.** 8 (2018) 1925–1944.

[87] P. G. Collins, P. Avouris, Nanotubes for electronics., **Sci. Am.** 283 (2000) 62–69.

[88] A. Qureshi, W. P. Kang, J. L. Davidson, Y. Gurbuz, Review on carbon-derived, solid-state, micro and nano sensors for electrochemical sensing applications, **Diam. Relat. Mater.** 18 (2009) 1401–1420.

[89] A. T. Lawal, Synthesis and utilization of carbon nanotubes for fabrication of electrochemical biosensors, **Mater. Res. Bull.** 73 (2016) 308–350.

[90] D. A. Heller, P. W. Barone, M. S. Strano, Sonication-induced changes in chiral distribution: A complication in the use of single-walled carbon nanotube fluorescence for determining species distribution, **Carbon** 43 (2005) 651–653.

[91] S. Giordani, D. Bonifazi, P. Singh, A. Bianco, M. Prato, S. Campidelli, Organic functionalisation and characterisation of single-walled carbon nanotubes., **Chem. Soc. Rev.** 38 (2009) 2214–30.

[92] C. Gao, Z. Guo, J. H. Liu, X. J. Huang, The new age of carbon nanotubes: An updated review of functionalized carbon nanotubes in electrochemical sensors, **Nanoscale** 4 (2012) 1948–1963.

[93] H. Hu, P. Bhowmik, B. Zhao, M.A. Hamon, M. E. Itkis, R. C. Haddon, Determination of the acidic sites of purified single-walled carbon nanotubes by acid-base titration, **Chem. Phys. Lett.** 345 (2001) 25–28.

[94] H. F. Bettinger, Experimental and Computational Investigations of the Properties of Fluorinated Single-Walled Carbon Nanotubes, **ChemPhysChem.** 4 (2003) 1283–1289.

[95] A. López-Bezanilla, F. Triozon, S. Latil, X. Blase, S. Roche, Effect of the chemical functionalization on charge transport in carbon nanotubes at the mesoscopic scale, **Nano Lett.** 9 (2009) 940–944.

[96] H. Park, J. Zhao, J. P. Lu, Distinct properties of single-wall carbon nanotubes

with monovalent sidewall additions, **Nanotechnology** 16 (2005) 635–638.

[97] J. E. De Albuquerque, L. H. C. Mattoso, R. M. Faria, J. G. Masters, A. G. MacDiarmid, Study of the interconversion of polyaniline oxidation states by optical absorption spectroscopy, **Synth. Met.** 146 (2004) 1–10.

[98] J. E. Albuquerque, L. H. C. Mattoso, D. T. Balogh, R. M. Faria, J. G. Masters, A. G. MacDiarmid, Simple method to estimate the oxidation state of polyanilines, **Synth. Met.** 113 (2000) 19–22.

[99] S. K. Manohar, A. G. Macdiarmid, A. J. Epstein, Polyaniline: Pernigranile, an isolable intermediate in teh conventional chemical synthesis of emeraldine, **Synth. Met.** 41 (1991) 711–714.

[100] B. W. Zewde, S. Admassie, Electrocatalysis of oxygen reduction at poly(4-amino-3-hydroxynaphthalene sulfonic acid) and platinum loaded polymer modified glassy carbon electrodes, **J. Power Sources.** 216 (2012) 502–507.

[101] H. Bhandari, V. Choudhary, S. K. Dhawan, Influence of self-doped poly(aniline-co-4-amino-3-hydroxy-naphthalene-1-sulfonic acid) on corrosion inhibition behaviour of iron in acidic medium, **Synth. Met.** 161 (2011) 753–762.

[102] A. Geto, M. Tessema, S. Admassie, Determination of histamine in fish muscle at multi-walled carbon nanotubes coated conducting polymer modified glassy carbon electrode, **Synth. Met.** 191 (2014) 135–140.

[103] A. Geto, C. M. A. Brett, Electrochemical synthesis, characterisation and comparative study of new conducting polymers from amino-substituted naphthalene sulfonic acids, **J. Solid State Electrochem.** 20 (2016) 2969–2979.

[104] G. Ćirić-Marjanović, M. Trchová, P. Matějka, P. Holler, B. Marjanović, I. Juranić, Electrochemical oxidative polymerization of sodium 4-amino-3-hydroxynaphthalene-1-sulfonate and structural characterization of polymeric products, **React. Funct. Polym.** 66 (2006) 1670–1683.

[105] L. J. Murphy, Reduction of Interference Response at a Hydrogen Peroxide Detecting Electrode Using Electropolymerized Films of Substituted Naphthalenes, **Anal. Chem.** 70 (1998) 2928–2935.

[106] M. M. Bărsan, E. M. Pinto, C. M. A. Brett, Methylene blue and neutral red electropolymerisation on AuQCM and on modified AuQCM electrodes: An electrochemical and gravimetric study, **ChemPhysChem.** 13 (2011) 5462–5471.

[107] A. A. Karyakin, E. E. Karyakina, H. L. Schmidt, Electropolymerized azines: A new group of electroactive polymers, **Electroanalysis** 11 (1999) 149–155.

[108] S. Chhatre, A. Ichake, K. Harpale, S. Patil, A. Deshpande, M. More, P. P. Wadgaonkar, Phenazine-containing poly(phenylenevinylene): a new polymer with impressive field emission properties, **J. Polym. Res.** 25 (2018) 25–61.

[109] M. Chen, H. Nie, B. Song, L. Li, J. Z. Sun, A. Qin, B. Z. Tang, Triphenylamine-functionalized tetraphenylpyrazine: Facile preparation and multifaceted

functionalities, **J. Mater. Chem. C.** 4 (2016) 2901–2908.

[110] R. Pauliukaite, M. E. Ghica, M. M. Bărsan, C. M. A. Brett, Phenazines and polyphenazines in electrochemical sensors and biosensors, **Anal. Lett.** 43 (2010) 1588–1608.

[111] J. P. Pouget, Z. Oblakowski, Y. Nogami, P. A. Albouy, M. Laridjani, E. J. Oh, Y. Min, A. G. MacDiarmid, J. Tsukamoto, T. Ishiguro, A. J. Epstein, Recent structural investigations of metallic polymers, **Synth. Met.** 65 (1994) 131–140.

[112] V. Pifferi, M. M. Bărsan, M. E. Ghica, L. Falciola, C. M. A. Brett, Synthesis, characterization and influence of poly(brilliant green) on the performance of different electrode architectures based on carbon nanotubes and poly(3,4-ethylenedioxythiophene), **Electrochim. Acta** 98 (2013) 199–207.

[113] C. Riche, C. Pascard-Billy, Triphénylméthane, **Crystallogr. Cryst. Chem.** 30 (2002) 1874–1876.

[114] Q. Wan, X. Wang, X. Wang, N. Yang, Poly(malachite green) film: Electrosynthesis, characterization, and sensor application, Polymer (Guildf). 47 (2006) 7684–7692.

[115] M. M. Bărsan, V. Pifferi, L. Falciola, C. M. A. Brett, New CNT/poly(brilliant green) and CNT/poly(3,4-ethylenedioxythiophene) based electrochemical enzyme biosensors, **Anal. Chim. Acta** 927 (2016) 35–45.

[116] T. C. Bruice, S. J. Benkovic, Chemical basis for enzyme catalysis, **Biochemistry** 39 (2000) 6267–6274.

[117] B. Te Nijenhuis, Biosensors. Fundamentals and Applications, edited by P. F. Turner, I. Karube, G. S. Wilson, **TrAC Trends Anal. Chem.** 7 (2002) 394–395.

[118] H. Hiep Nguyen, M. Kim, An Overview of Techniques in Enzyme Immobilization, **Appl. Sci. Converg. Technol.** 26 (2017) 157–163.

[119] A. M. Chiorcea-Paquim, R. Pauliukaite, C. M. A. Brett, A. M. Oliveira Brett, AFM nanometer surface morphological study of in situ electropolymerized neutral red redox mediator oxysilane sol-gel encapsulated glucose oxidase electrochemical biosensors, **Biosens. Bioelectron.** 24 (2008) 297–305.

[120] M. E. Hassan, M. Tamer Tamer, A.M. Omer, Methods of Enzyme Immobilization, **Int. J. Curr. Pharm. Rev. Res.** 7 (2016) 385–392.

[121] S. Kurbanoglu, S. A. Ozkan, A. Merkoçi, Nanomaterials-based enzyme electrochemical biosensors operating through inhibition for biosensing applications, **Biosens. Bioelectron.** 89 (2017) 886–898.

[122] K. A. Johnson, R. S. Goody, The original Michaelis constant: Translation of the 1913 Michaelis-Menten Paper, **Biochemistry** 50 (2011) 8264–8269.

[123] A. Amine, H. Mohammadi, I. Bourais, G. Palleschi, Enzyme inhibition-based biosensors for food safety and environmental monitoring, **Biosens. Bioelectron.**

21 (2006) 1405–1423.

[124] A. Cornish-Bowden, The origins of enzyme kinetics, **FEBS Lett.** 587 (2013) 2725–2730.

[125] H. Lineweaver, D. Burk, The Determination of Enzyme Dissociation Constants, **J. Am. Chem. Soc.** 56 (1934) 658–666.

[126] M. Dixon, The determination of enzyme inhibitor constants, **Biochem. J.** 55 (1953) 170–171.

[127] A. Cornish-Bowden, A simple graphical method for determining the inhibition constants of mixed, uncompetitive and non-competitive inhibitors (*Short Communication*), **Biochem. J.** 137 (1974) 143–144.

[128] Y. Wang, M. Sun, J. Qiao, J. Ouyang, N. Na, FAD roles in glucose catalytic oxidation studied by multiphase flow of extractive electrospray ionization (MF-EESI) mass spectrometry, **Chem. Sci.** 9 (2018) 594–599.

[129] D. G. Hatzinikolaou, B. J. Macris, Factors regulating production of glucose oxidase by Aspergillus niger, **Enzyme Microb. Technol.** 17 (1995) 530–534.

[130] S. B. Bankar, M. V. Bule, R. S. Singhal, L. Ananthanarayan, Glucose oxidase - An overview, **Biotechnol. Adv.** 27 (2009) 489–501.

[131] B. Wang, J. Zheng, Y. He, Q. Sheng, A sandwich-type phenolic biosensor based on tyrosinase embedding into single-wall carbon nanotubes and polyaniline nanocomposites, **Sensors Actuators, B Chem.** 186 (2013) 417–422.

[132] X. Lai, H. J. Wichers, M. Soler-Lopez, B. W. Dijkstra, Structure and Function of Human Tyrosinase and Tyrosinase-Related Proteins, **Chem. A Eur. J.** 24 (2018) 47–55.

[133] H. Claus, H. Decker, Bacterial tyrosinases, **Syst. Appl. Microbiol.** 29 (2006) 3–14.

[134] K. Min, G. Woo Park, Y. Je Yoo, J. S. Lee. A perspective on the biotechnological applications of the versatile tyrosinase, **Bioresource Technology** 289(2019), 121-130

[135] A. M. Mayer, Polyphenol oxidases in plants and fungi: Going places? A review, **Phytochemistry** 67 (2006) 2318–2331.

[136] E. Jaenicke, H. Decker, Tyrosinases from crustaceans form hexamers, **Biochem. J.** 371 (2003) 515–523.

[137] H. Ando, H. Kondoh, M. Ichihashi, V. J. Hearing, Approaches to identify inhibitors of melanin biosynthesis via the quality control of tyrosinase, **J. Invest. Dermatol.** 127 (2007) 751–761.

[138] S.Y. Seo, V. K. Sharma, N. Sharma, Mushroom tyrosinase: Recent prospects, **J. Agric. Food Chem.** 51 (2003) 2837–2853.

[139] E. Valipour, B. Arikan, Increased production of tyrosinase from Bacillus megaterium strain M36 by the response surface method, **Arch. Biol. Sci.** 68 (2016) 659–668.

[140] R. Uluisik, E. Romero, G. Gadda, Evidence for proton tunneling and a transient covalent flavin-substrate adduct in choline oxidase S101A, BBA - Proteins and Proteomic 1865 (2017) 1470–1478.

[141] S. Ikuta, S. Imamura, H. Misaki, Y. Horiuti, Purification and characterization of Choline Oxidase from Arthrobacter globiformis, **J. Biochem.** 82 (1977) 1741–1749.

[142] M. Ohta-Fukuyama, Y. Miyake, S. Emi, T. Yamano, Identification and properties of the prosthetic group of choline oxidase from Alcaligenes sp., **J. Biochem.** 88 (1980) 197–203.

[143] H. Yamada, N. Mori, Y. Tani, Properties of choline oxidase of cylindrocarpon didymum M-l, **Agric. Biol. Chem.** 43 (1979) 2173–2177.

[144] H. H. Girault, Analytical and Physical Electrochemistry, **EPFL Press**, Lausanne, 2004

[145] C. M. A. Brett, A. M. Oliveira Brett, Electrochemistry: Principles, Methods, and Applications, Electrochemistry**, Oxford University Press**, Oxford, 1998.

[146] E. C. Potter, Electrochemistry, principles and application, **Cleaver-Hume Press**, New York, 1956

[147] J. E. B. Randles, Kinetics of rapid electrode reactions, **Faraday Discuss** 1 (1947) 11–19.

[148] A. J. Bard, L. F. R. Electrochemical methods: fundamentals and applications, **Jonh Wiley & Sons**, New York, 2001

[149] V. S Bagotsky, Fundamentals of electrochemistry, **Jonh Wiley & Sons**, Hoboken, 2006

[150] E. Barsoukov, J. R. Macdonald, Impedance Spectroscopy: Theory, Experiment, and Applications, **Jonh Wiley & Sons**, New York, 2015

[151] J. R Macdonald, Impedance Spectroscopy: Emphasizing Solid Materials and Systems, **Jonh Wiley & Sons**, New York, 1987

[152] A. Lasia, Electrochemical impedance spectroscopy and its applications, 2014. **Springer**, New York, 2014

[153] E. Barsoukov, J. R. Macdonald, Impedance Spectroscopy Theory, Experiment, and Applications, **Jonh Wiley & Sons**, Hoboken, 2018.

[154] J. I. Goldstein, D. E. Newbury, J.R. Michael, N. W. M. Ritchie, J. H. J. Scott, D. C. Joy, Scanning electron microscopy and x-ray microanalysis, **Springer**, New York, 2017.

[155] L. Reimer, Scanning Electron Microscopy: Physics of Image Formation and Microanalysis, **Wiley-VCH**, Weinheim, 1987

[156] Handbook of Sample Preparation for Scanning Electron Microscopy and X-Ray Microanalysis, **Springer**, Cambridge

[157] C. Y. Tang, Z. Yang, Transmission Electron Microscopy (TEM), **Membr. Charact.**1(2017) 145–159.

[158] C. S. S. R. Kumar, Transmission Electron Microscopy Characterization of Nanomaterials, **Springer**, Berlin, 2014.

[159] B. J. Inkson, Scanning Electron Microscopy (SEM) and Transmission Electron Microscopy (TEM) for Materials Characterization, in: Mater. Charact. Using Nondestruct. Eval. Methods, **Woodhead Publishing**, 2016.

[160] A. A. Bunaciu, E. G Udrişţioiu, H. Y. Aboul-Enein, X-Ray Diffraction: Instrumentation and Applications, **Crit. Rev. Anal. Chem.** 45 (2015) 289–299.

[161] J. R. Connolly, Introduction to X-ray Powder Diffraction, **Spring** (2007) 1–9.

[162] A. C. Hannon, Neutron Diffraction Techniques for Structural Studies of Glasses, in: Mod. Glas. Charact., **John Wiley & Sons**, 2015

[163] K. Knipe, A. C. Manero, S. Sofronsky, J. Okasinski, J. Almer, J. Wischek, C. Meid, A. Karlsson, M. Bartsch, S. Raghavan, Synchrotron X-Ray Diffraction Measurements Mapping Internal Strains of Thermal Barrier Coatings During Thermal Gradient Mechanical Fatigue Loading, **J. Eng. Gas Turbines Power.** 137 (2015) 82–506.

[164] N. Kumar, S. Kumbhat, Essentials in Nanoscience and Nanotechnology, **John Wiley & Sons**, New Jersey, 2016.

[165] M. E. Ghica, C. M. A. Brett, Simple and efficient epinephrine sensor based on carbon nanotube modified carbon film electrodes, **Anal. Lett.** 46 (2013) 1379–1393.

[166] R. Pauliukaite, M. E. Ghica, O. Fatibello-Filho, C. M. A. Brett, Comparative study of different cross-linking agents for the immobilization of functionalized carbon nanotubes within a chitosan film supported on a graphite-epoxy composite electrode, **Anal. Chem.** 81 (2009) 5364–5372.

[167] J. Turkevich, P. C. Stevenson, J. Hillier, A study of the nucleation and growth processes in the synthesis of colloidal gold, **Discuss. Faraday Soc.** 11 (1951) 55–75.

[168] M. V. Sujitha, S. Kannan, Green synthesis of gold nanoparticles using Citrus fruits (Citrus limon, Citrus reticulata and Citrus sinensis) aqueous extract and its characterization, S**pectrochim. Acta - Part A Mol. Biomol. Spectrosc.** 102 (2013) 15–23.

[169] R. F. Ngece, N. West, P. M. Ndangili, R. A. Olowu, A. Williams, N. Hendricks,

S. Mailu, P. Baker, E. Iwuoha, A silver Nanoparticle/Poly(8-Anilino-1-Naphthalene Sulphonic Acid) Bioelectrochemical Biosensor System for the Analytical Determination of Ethambutol, **Int. J. Electrochem. Sci.** 6 (2011) 1820–1834.

[170] M. E. Ghica, C. M. A. Brett, Poly(brilliant green) and poly(thionine) modified carbon nanotube coated carbon film electrodes for glucose and uric acid biosensors, **Talanta** 130 (2014) 198–206.

[171] M. E. Ghica, C. M. A. Brett, Poly(brilliant cresyl blue) modified glassy carbon electrodes: Electrosynthesis, characterisation and application in biosensors, **J. Electroanal. Chem.** 629 (2009) 35–42.

[172] E. E. Ferapontova, E. M. Olsen, K. V Gothelf, An RNA Aptamer-Based Electrochemical Biosensor for Detection of Theophylline in Serum, **J. Am. Chem. Soc.** 130 (2008) 4256–4258.

[173] W. da Silva, M. E. Ghica, C. M. A. Brett, Gold nanoparticle decorated multiwalled carbon nanotube modified electrodes for the electrochemical determination of theophylline, **Anal. Methods.** 10 (2018) 5634–5642.

[174] K. N. Rathod, Z. Joshi, D. Dhruv, K. Gadani, H. Boricha, A. D. Joshi, P.S. Solanki, N. A. Shah, Size effects on electrical properties of chemically grown zinc oxide nanoparticles, **Mater. Res. Express.** 5 (2018) 35–40.

[175] M. Musameh, J. Wang, A. Merkoci, Y. Lin, Low-potential stable NADH detection at carbon-nanotube-modified glassy carbon electrodes, **Electrochem. Commun.** 4 (2002) 743–746.

[176] H. Luo, Z. Shi, N. Li, Z. Gu, Q. Zhuang, Investigation of the electrochemical and electrocatalytic behavior of single-wall carbon nanotube film on a glassy carbon electrode, **Anal. Chem.** 73 (2001) 915–920.

[177] L. Zi, J. Li, Y. Mao, R. Yang, L. Qu, High sensitive determination of theophylline based on gold nanoparticles/l-cysteine/Graphene/Nafion modified electrode, **Electrochim. Acta** 78 (2012) 434–439.

[178] M. Mazloum-Ardakani, H. Beitollahi, B. Ganjipour, H. Naeimi, M. Nejati, Electrochemical and catalytic investigations of dopamine and uric acid by modified carbon nanotube paste electrode, **Bioelectrochemistry** 75 (2009) 1–8.

[179] E. Laviron, General expression of the linear potential sweep voltammogram in the case of diffusionless electrochemical systems, **J. Electroanal. Chem.** 101 (1979) 19–28.

[180] M. Amare, S. Admassie, Differential pulse voltammetric determination of theophylline at poly(4-amino-3-hydroxyl naphthalene sulfonic acid) modified glassy carbon electrode, **Bull. Chem. Soc. Ethiop.** 26 (2012) 73–84.

[181] R. R. H. Rajesh N. Hegde, S. T. Nandibewoor, Electrochemical Oxidation and Determination of Theophylline at a Carbon Paste Electrode Using Cetyltrimethyl Ammonium Bromide as Enhancing Agent, **Anal. Lett.** 42 (2009) 2665–2682.

[182] Y. H. Zhu, Z. L. Zhang, D. W. Pang, Electrochemical oxidation of theophylline at multi-wall carbon nanotube modified glassy carbon electrodes, **J. Electroanal. Chem.** 581 (2005) 303–309.

[183] S. J. Malode, N. P. Shetti, S. T. Nandibewoor, Voltammetric behavior of theophylline and its determination at multi-wall carbon nanotube paste electrode, **Colloids Surf. B Biointerfaces** 97 (2012) 1–6.

[184] T. Wang, E. P. Randviir, C. E. Banks, Detection of theophylline utilising portable electrochemical sensors, **Analyst.** 139 (2014) 2000–2003.

[185] R. N. Goyal, A. Dhawan, Electrochemical oxidation of inosine 5′-monophosphate in neutral aqueous solution, **J. Electroanal. Chem.** 591 (2006) 159–167.

[186] H. Yin, X. Meng, H. Su, M. Xu, S. Ai, Electrochemical determination of theophylline in foodstuff, tea and soft drinks based on urchin-like CdSe microparticles modified glassy carbon electrode, Food Chem. 134 (2012) 1225–1230.

[187] J. M. Zen, T. Y. Yu, Y. Shih, Determination of theophylline in tea and drug formulation using a Nafion®/lead-ruthenium oxide pyrochlore chemically modified electrode, **Talanta** 50 (1999) 635–640.

[188] R. N. Hedge, R. R. Hosamani, T. S. Nandibewoor, Electrochemical oxidation and determination of theophylline at a carbon paste electrode using cetyltrimetyl ammoniumbromides as enhancing agent, **Anal. Lett.** 42 (2009) 2665–2682.

[189] S. J. Malode, J. C. Abbar, N. P. Shetti, S. T. Nandibewoor, Voltammetric oxidation and determination of loop diuretic furosemide at a multi-walled carbon nanotubes paste electrode, **Electrochim. Acta** 60 (2012) 95–101.

[190] A. Peng, H. Yan, C. Luo, G. Wang, X. Ye, H. Ding, Electrochemical determination of theophylline pharmacokinetic under the effect of roxithromycin in rats by the MWCNT/Au/poly-L-lysine modified sensor, **Int. J. Electrochem. Sci.** 12 (2017) 330–346.

[191] Y. Wang, T. Wu, C. Y. Bi, Simultaneous determination of acetaminophen, theophylline and caffeine using a glassy carbon disk electrode modified with a composite consisting of poly(Alizarin Violet 3B), multiwalled carbon nanotubes and graphene, **Microchim. Acta** 183 (2016) 731–739.

[192] Y. J. Yang, W. Li, High sensitive determination of theophylline based on manganese oxide nanoparticles/multiwalled carbon nanotubes nanocomposite modified electrode, **Ionics** 21 (2015) 1121–1128.

[193] S. Kesavan, S. Abraham John, Fabrication of aminotriazole grafted gold nanoparticles films on glassy carbon electrode and its application towards the simultaneous determination of theophylline and uric acid, S**ensors Actuators, B Chem.** 205 (2014) 352–362.

[194] L. Liu, F. Xiao, J. Li, W. Wu, F. Zhao, B. Zeng, Platinum nanoparticles decorated multiwalled carbon nanotubes - ionic liquid composite film coated

glassy carbon electrodes for sensitive determination of theophylline, **Electroanalysis** 20 (2008) 1194–1199.

[195] Y. Wang, Y. Ding, L. Li, P. Hu, Nitrogen-doped carbon nanotubes decorated poly (L-Cysteine) as a novel, ultrasensitive electrochemical sensor for simultaneous determination of theophylline and caffeine, **Talanta**178 (2018) 449–457.

[196] X. Zhuang, D. Chen, S. Wang, H. Liu, L. Chen, Manganese dioxide nanosheet-decorated ionic liquid-functionalized graphene for electrochemical theophylline biosensing, **Sensors Actuators, B Chem.** 251 (2017) 185–191.

[197] X. Shu, F. Bian, Q. Wang, X. Qin, Y. Wang, Electrochemical sensor for simultaneous determination of theophylline and caffeine based on novel poly(folic acid)/graphene composite film modified electrode, I**nt. J. Electrochem. Sci.** 12 (2017) 4251–4264.

[198] M. B. Gholivand, M. Khodadadian, Simultaneous voltammetric determination of theophylline and guaifenesin using a multiwalled carbon nanotube-ionic liquid modified glassy carbon electrode, **Electroanalysis** 26 (2014) 1975–1983.

[199] A. S. Hernández-Cázares, M. C. Aristoy, F. Toldrá, An enzyme sensor for the determination of total amines in dry-fermented sausages, **J. Food Eng.** 106 (2011) 166–169.

[200] I. Al Bulushi, S. Poole, H. C. Deeth, G. A. Dykes, Biogenic amines in fish: Roles in intoxication, spoilage, and nitrosamine formation-A review, **Crit. Rev. Food Sci. Nutr.** 49 (2009) 369–377.

[201] W. da Silva, M.E. Ghica, R. F. Ajayi, E. I. Iwuoha, C. M. A. Brett, Impedimetric sensor for tyramine based on gold nanoparticle doped-poly(8-anilino-1-naphthalene sulphonic acid) modified gold electrodes, **Talanta** 195 (2019) 604–612.

[202] W. da Silva, M. E. Ghica, R. F. Ajayi, E. I. Iwuoha, C. M. A. Brett, Tyrosinase based amperometric biosensor for determination of tyramine in fermented food and beverages with gold nanoparticle doped poly(8-anilino-1-naphthalene sulphonic acid) modified electrode, **Food Chem.** 282 (2019) 18–26.

[203] L. F. Marchesi, S. C. Jacumasso, R. C. Quintanilha, H. Winnischofer, M. Vidotti, The electrochemical impedance spectroscopy behavior of poly(aniline) nanocomposite electrodes modified by Layer-by-Layer deposition, **Electrochim. Acta** 174 (2015) 864–870.

[204] C. Chen, Z. Gan, C. Xu, L. Lu, Y. Liu, Y. Gao, Electrosynthesis of poly(aniline-co-azure B) for aqueous rechargeable zinc-conducting polymer batteries, **Electrochim. Acta** 252 (2017) 226–234.

[205] G. Milczarek, Electrochemical conversion of poly-aniline into a redox polymer in the presence of nordihydroguaiaretic acid, **J. Electroanal. Chem.** 626 (2009) 143–148.

[206] T. Lindfors, A. Ivaska, Potentiometric and UV-vis characterisation of N-substituted polyanilines, **J. Electroanal. Chem.** 535 (2002) 65–74.

[207] E. I. Iwuoha, S. E. Mavundla, V. S. Somerset, L. F. Petrik, M. J. Klink, M. Sekota, P. Bakers, Electrochemical and spectroscopic properties of fly ash-polyaniline matrix nanorod composites, **Microchim. Acta** 155 (2006) 453–458.

[208] R. Mažeikiene, G. Niaura, A. Malinauskas, Raman spectroelectrochemical study of self-doped copolymers of aniline and selected aminonaphthalenesulfonates, **Electrochim. Acta** 51 (2006) 1917–1924.

[209] P. Khademi-Azandehi, J. Moghaddam, Green synthesis, characterization and physiological stability of gold nanoparticles from Stachys lavandulifolia Vahl extract, **Particuology** 19 (2015) 22–26.

[210] F. U. Khan, Y. Chen, N. U. Khan, A. Ahmad, K. Tahir, Z. U. H. Khan, A. U. Khan, S.U. Khan, M. Raza, P. Wan, Visible light inactivation of *E. Coli*, Cytotoxicity and ROS determination of biochemically capped gold nanoparticles, **Microb. Pathog.** 107 (2017) 419–424.

[211] A. K. Suresh, D. A. Pelletier, W. Wang, M. L. Broich, J. W. Moon, B. Gu, D. P. Allison, D. C. Joy, T. J. Phelps, M. J. Doktycz, Biofabrication of discrete spherical gold nanoparticles using the metal-reducing bacterium Shewanella oneidensis, **Acta Biomater.** 7 (2011) 2148–2152.

[212] Y. Shiraishi, H. Tanaka, H. Sakamoto, S. Ichikawa, T. Hirai, Photoreductive synthesis of monodispersed Au nanoparticles with citric acid as reductant and surface stabilizing reagent, **RSC Adv.** 7 (2017) 6187–6192.

[213] L. Du, L. Xian, J. X. Feng, Rapid extra/intracellular biosynthesis of gold nanoparticles by the fungus *Penicillium sp.*, **J. Nanoparticle Res.** 13 (2011) 921–930.

[214] M. N. Nadagouda, G. Hoag, J. Collins, R.S. Varma, Green synthesis of Au nanostructures at room temperature using biodegradable plant surfactants, **Cryst. Growth Des.** 9 (2009) 4979–4983.

[215] S. M. Ghoreishi, M. Behpour, M. Khayatkashani, Green synthesis of silver and gold nanoparticles using Rosa damascena and its primary application in electrochemistry, **Phys. E Low-Dimensional Syst. Nanostructures** 44 (2011) 97–104.

[216] O. P. Dimitriev, Doping of polyaniline by transition-metal salts, **Macromolecules** 37 (2004) 3388–3395.

[217] J. B. Raoof, R. Ojani, M. Amiri-Aref, M. Baghayeri, Electrodeposition of quercetin at a multi-walled carbon nanotubes modified glassy carbon electrode as a novel and efficient voltammetric sensor for simultaneous determination of levodopa, uric acid and tyramine, **Sensors Actuators, B Chem.** 167 (2012) 508–518.

[218] D. R. Kumar, S. Kesavan, M. L. Baynosa, J. J. Shim, 3,5-Diamino-1,2,4-

triazole@electrochemically reduced graphene oxide film modified electrode for the electrochemical determination of 4-nitrophenol, **Electrochim. Acta** 246 (2017) 1131–1140.

[219] M. Cheng, X. Zhang, M. Wang, H. Huang, J. Ma, A facile electrochemical sensor based on well-dispersed graphene-molybdenum disulfide modified electrode for highly sensitive detection of dopamine, **J. Electroanal. Chem.** 786 (2017) 1–7.

[220] Q. Wang, H. Yu, H. Li, F. Ding, P. He, Y. Fang, Simultaneous determination of food-related biogenic amines and precursor amino acids by micellar electrokinetic capillary chromatography with electrochemical detection, **Food Chem.** 83 (2003) 311–317.

[221] J. B. Raoof, R. Ojani, M. Baghayeri, M. Amiri-Aref, Application of a glassy carbon electrode modified with functionalized multi-walled carbon nanotubes as a sensor device for simultaneous determination of acetaminophen and tyramine, **Anal. Methods.** 4 (2012) 1579–1587.

[222] I .M. Apetrei, C. Apetrei, Amperometric biosensor based on polypyrrole and tyrosinase for the detection of tyramine in food samples, **Sensors Actuators, B Chem.** 178 (2013) 40–46.

[223] I. M. Apetrei, C. Apetrei, The biocomposite screen-printed biosensor based on immobilization of tyrosinase onto the carboxyl functionalised carbon nanotube for assaying tyramine in fish products, **J. Food Eng.** 149 (2015) 1–8.

[224] J. Huang, X. Xing, X. Zhang, X. He, Q. Lin, W. Lian, H. Zhu, A molecularly imprinted electrochemical sensor based on multiwalled carbon nanotube-gold nanoparticle composites and chitosan for the detection of tyramine, **Food Res. Int.** 44 (2011) 276–281.

[225] Y. Li, C. H. Hsieh, C. W. Lai, Y. F. Chang, H. Y. Chan, C. F. Tsai, J. A. Ho, L. C. Wu, Tyramine detection using PEDOT:PSS/AuNPs/1-methyl-4-mercaptopyridine modified screen-printed carbon electrode with molecularly imprinted polymer solid phase extraction, **Biosens. Bioelectron.** 87 (2017) 142–149.

[226] L. Lu, L. Zhang, X. Zhang, S. Huan, G. Shen, R. Yu, A novel tyrosinase biosensor based on hydroxyapatite-chitosan nanocomposite for the detection of phenolic compounds, **Anal. Chim. Acta** 665 (2010) 146–151.

[227] F. C. Vicentini, B. C. Janegitz, C. M. A. Brett, O. Fatibello-Filho, Tyrosinase biosensor based on a glassy carbon electrode modified with multi-walled carbon nanotubes and 1-butyl-3-methylimidazolium chloride within a dihexadecylphosphate film, **Sensors Actuators, B Chem.** 188 (2013) 1101–1108.

[228] Y. Tan, J. Kan, S. Li, Amperometric biosensor for catechol using electrochemical template process, **Sensors Actuators, B Chem.** 152 (2011) 285–291.

[229] J. Njagi, M. M. Chernov, J. C. Leiter, S. Andreescu, Amperometric detection of dopamine in vivo with an enzyme based carbon fiber microbiosensor, **Anal.**

Chem. 82 (2010) 989–996.

[230] B. Batra, S. Lata, R. Devi, S. Yadav, C. S. Pundir, Fabrication of an amperometric tyramine biosensor based on immobilization of tyramine oxidase on AgNPs/l-Cys-modified Au electrode, **J. Solid State Electrochem.** 16 (2012) 3869–3876.

[231] D. Telsnig, V. Kassarnig, C. Zapf, G. Leitinger, K. Kalcher, A. Ortner, Characterization of an amperometric biosensor for the determination of biogenic amines in flow injection analysis, **Int. J. Electrochem. Sci.** 7 (2012) 10476–10486.

[232] J. Kochana, K. Wapiennik, P. Knihnicki, A. Pollap, P. Janus, M. Oszajca, P. Kuśtrowski, Mesoporous carbon-containing voltammetric biosensor for determination of tyramine in food products, **Anal. Bioanal. Chem.** 408 (2016) 5199–5210.

[233] A. Calvo-Pérez, O. Domínguez-Renedo, M. A. Alonso-Lomillo, M. J. Arcos-Martínez, Disposable Horseradish Peroxidase Biosensors for the Selective Determination of Tyramine, **Electroanalysis** 25 (2013) 1316–1322.

[234] A. Calvo-Pérez, O. Domínguez-Renedo, M. A. Alonso-Lomillo, M. J. Arcos-Martínez, Disposable amperometric biosensor for the determination of tyramine using plasma amino oxidase, **Microchim. Acta** 180 (2013) 253–259.

[235] J. M. Berg, J. L. Tymoczko, L. Stryer, Biochemistry (5th edition), **W. H. Freenman&Co. Ltd**, New York, 2011

[236] J. Feher, Quantitative Human Physiology, **Academic Press**, Cambridge, 2016.

[237] J. L. Ordóñez, A. M. Troncoso, M. D. C. García-Parrilla, R. M. Callejón, Recent trends in the determination of biogenic amines in fermented beverages – A review, **Anal. Chim. Acta** 939 (2016) 10–25.

[238] S. Novella-Rodríguez, M. T. Veciana-Nogués, M. Izquierdo-Pulido, M. C. Vidal-Ca, Distribution of Biogenic Amines and Polyamines in Cheese, **J. Food Sci.** 68 (2003) 750–755.

[239] C. M. Mayr, P. Schieberle, Development of Stable Isotope Dilution Assays for the Simultaneous Quantitation of Biogenic Amines and Polyamines in Foods by LC-MS/MS, **J. Agric. Food Chem.** 60 (2012) 3026–3032.

[240] M .E. Ghica, R. Pauliukaite, O. Fatibello-Filho, C.M.A. Brett, Application of functionalised carbon nanotubes immobilised into chitosan films in amperometric enzyme biosensors, **Sensors Actuators, B Chem.** 142 (2009) 308–315.

[241] W. A. Badawy, K. M. Ismail, S. S. Medany, Optimization of the electropolymerization of 1-amino-9,10-anthraquinone conducting films from aqueous media, **Electrochim. Acta** 51 (2006) 6353–6360.

[242] O. Hosu, M. M. Bărsan, C. Cristea, R. Săndulescu, C. M. A. Brett, Nanostructured electropolymerized poly(methylene blue) films from deep

eutectic solvents. Optimization and characterization, **Electrochim. Acta** 232 (2017) 285–295.

[243] O. Hosu, M. M. Bărsan, C. Cristea, R. Săndulescu, C. M. A. Brett, Nanocomposites based on carbon nanotubes and redox-active polymers synthesized in a deep eutectic solvent as a new electrochemical sensing platform, **Microchim. Acta** 184 (2017) 3919–3927.

[244] S. Mu, Y. Yang, Spectral characteristics of polyaniline nanostructures synthesized by using cyclic voltammetry at different scan rates, **J. Phys. Chem. B.** 112 (2008) 11558–11563.

[245] A. Kellenberger, D. Ambros, N. Plesu, Scan Rate Dependent Morphology of Polyaniline Films Electrochemically Deposited on Nickel, **Int. J. Electrochem. Sci.** 9 (2014) 6821–6833.

[246] R. Devasenathipathy, V. Mani, S. M. Chen, S. T. Huang, T. T. Huang, C. M. Lin, K.Y. Hwa, T. Y. Chen, B. J. Chen, Glucose biosensor based on glucose oxidase immobilized at gold nanoparticles decorated graphene-carbon nanotubes, **Enzyme Microb. Technol.** 78 (2015) 40–45.

[247] A. P. Periasamy, Y. J. Chang, S. M. Chen, Amperometric glucose sensor based on glucose oxidase immobilized on gelatin-multiwalled carbon nanotube modified glassy carbon electrode, **Bioelectrochemistry** 80 (2011) 114–120.

[248] S. Palanisamy, C. Karuppiah, S. M. Chen, Direct electrochemistry and electrocatalysis of glucose oxidase immobilized on reduced graphene oxide and silver nanoparticles nanocomposite modified electrode, **Colloids Surf. B Biointerfaces** 114 (2014) 164–169.

[249] F.Y. Kong, S. X. Gu, W. W. Li, T. T. Chen, Q. Xu, W. Wang, A paper disk equipped with graphene/polyaniline/Au nanoparticles/glucose oxidase biocomposite modified screen-printed electrode: Toward whole blood glucose determination, **Biosens. Bioelectron.** 56 (2014) 77–82.

[250] T. Homma, D. Sumita, M. Kondo, T. Kuwahara, M. Shimomura, Amperometric glucose sensing with polyaniline/poly(acrylic acid) composite film bearing covalently-immobilized glucose oxidase: A novel method combining enzymatic glucose oxidation and cathodic O_2 reduction, **J. Electroanal. Chem.** 712 (2014) 119–123.

[251] B. Elsebai, M. E. Ghica, M. N. Abbas, C. M. A. Brett, Catalase based hydrogen peroxide biosensor for mercury determination by inhibition measurements, J. Hazard. Mater. 340 (2017) 344–350.

[252] A. Amine, L. El Harrad, F. Arduini, D. Moscone, G. Palleschi, Analytical aspects of enzyme reversible inhibition, **Talanta** 118 (2014) 368–374.

[253] J. G. Ayenimo, S. B. Adeloju, Rapid amperometric detection of trace metals by inhibition of an ultrathin polypyrrole-based glucose biosensor, **Talanta** 148 (2016) 502–510.

[254] J. G. Ayenimo, S. B. Adeloju, Inhibitive potentiometric detection of trace metals with ultrathin polypyrrole glucose oxidase biosensor, **Talanta** 137 (2015) 62–70.

[255] G. M. Zeng, L. Tang, G. L. Shen, G. H. Huang, C. G. Niu, Determination of trace chromium (VI) by an inhibition-based enzyme biosensor incorporating an electropolymerized aniline membrane and ferrocene as electron transfer mediator, I**nt. J. Environ. Anal. Chem.** 84 (2004) 761–774.

[256] F. Ramírez-Sánchez, Karla; Alvarado Hidalgo, Enzymatic Inhibition Constant of Acetylcholinesterase for the Electrochemical Detection and Sensing of Chlorpyrifos Article history, **J. Nat. Resour. Dev.** 8 (2018) 9–14.

[257] W. da Silva, M.E. Ghica, C. M. A. Brett, Novel nanocomposite film modified electrode based on poly(brilliant cresyl blue)-deep eutectic solvent/carbon nanotubes and its biosensing applications, **Electrochim. Acta** 317 (2019) 766–777.

[258] W. da Silva, M. E. Ghica, C. M. A. Brett, Choline Oxidase Inhibition Biosensor Based on Poly(Brilliant Cresyl Blue) – Deep Eutectic Solvent / Carbon Nanotube Modified Electrode for Dichlorvos Organophosphorus Pesticide, **Sensors Actuators B Chem.** 12 (219) 62–68.

[259] A. Balamurugan, S. M. Chen, Electrochemical preparation of composite of poly brilliant cresyl blue (PBCB)-poly 5-amino-2-napthalenesulfonic acid electrode and electrocatalytic application, **J. Solid State Electrochem.** 14 (2010) 35–41.

[260] M. Chen, J. Q. Xu, S. N. Ding, D. Shan, H. G. Xue, S. Cosnier, M. Holzinger, Poly(brilliant cresyl blue) electrogenerated on single-walled carbon nanotubes modified electrode and its application in mediated biosensing system, **Sensors Actuators, B Chem.** 152 (2011) 14–20.

[261] L. Shen, X. Huang, Electrochemical polymerization of aniline in a protic ionic liquid with high proton activity, **Synth. Met.** 245 (2018) 18–23.

[262] N. Yi, M. R. Abidian, Conducting polymers and their biomedical applications, in: Biosynthetic Polym. Med. Appl., **Woodhead Publishing**, Cambrige, 2015

[263] V. Pfaffen, P. I. Ortiz, S. I. Córdoba de Torresi, R. M. Torresi, On the pH dependence of electroactivity of poly(methylene blue) films, Electrochim. Acta 55 (2010) 1766–1771.

[264] A. Malinauskas, G. Niaura, S. Bloxham, T. Ruzgas, L. Gorton, Electropolymerization of preadsorbed layers of some azine redox dyes on graphite, **J. Colloid Interface Sci.** 230 (2000) 122–127.

[265] D. W. Yang, H. H. Liu, Poly(brilliant cresyl blue)-carbonnanotube modified electrodes for determination of NADH and fabrication of ethanol dehydrogenase-based biosensor, **Biosens. Bioelectron.** 25 (2009) 733–738.

[266] M. M. Bărsan, M. E. Ghica, C. M. A. Brett, Electrochemical sensors and biosensors based on redox polymer/carbon nanotube modified electrodes: A review, **Anal. Chim. Acta** 881 (2015) 1–23.

[267] R. Pauliukaite, C. M. A. Brett, Poly(neutral red): Electrosynthesis, characterization, and application as a redox mediator, **Electroanalysis** 20 (2008) 1275–1285.

[268] R. Pauliukaite, A. Selskiene, A. Malinauskas, C. M. A. Brett, Electrosynthesis and characterisation of poly(safranine T) electroactive polymer films, **Thin Solid Films** 517 (2009) 5435–5441.

[269] R. Pauliukaite, M. E. Ghica, O. Fatibello-Filho, C. M. A. Brett, Electrochemical impedance studies of chitosan-modified electrodes for application in electrochemical sensors and biosensors, **Electrochim. Acta** 55 (2010) 6239–6247.

[270] K. C. Lin, J. Y. Huang, S. M. Chen, Poly(brilliant cresyl blue) electrodeposited on multi-walled carbon nanotubes modified electrode and its application for persulfate determination, **Int. J. Electrochem. Sci.** 7 (2012) 9161–9173.

[271] R. Pauliukaite, A. Selskiene, A. Malinauskas, C. M. A. Brett, Electrosynthesis and characterisation of poly(Nile blue) films, **J. Electroanal. Chem.** 662 (2011) 328–333.

[272] D.W. Yang, H. H. Liu, Poly(brilliant cresyl blue)-carbonnanotube modified electrodes for determination of NADH and fabrication of ethanol dehydrogenase-based biosensor, **Biosens. Bioelectron.** 25 (2009) 733–738.

[273] H. Yi, D. Zheng, C. Hu, S. Hu, Functionalized multiwalled carbon nanotubes through in situ electropolymerization of brilliant cresyl blue for determination of epinephrine, **Electroanalysis** 20 (2008) 1143–1146.

[274] H. Liu, G. Wang, J. Hu, D. Chen, W. Zhang, B. Fang, Electrocatalysis and determination of uracil on polythionine/multiwall carbon nanotubes modified electrode, **J. Appl. Polym. Sci.** 107 (2008) 3173–3178.

[275] Y. Xu, Y. Z. Fang, Y. Wang, Y. Fang, Enhancement of Electrochemical Capacitance of Carbon Nanotubes by Polythionine Modification, **Chinese J. Chem.** 28 (2010) 417–421.

[276] A. Geto, C. M. A. Brett, Electrochemical synthesis, characterisation and comparative study of new conducting polymers from amino-substituted naphthalene sulfonic acids, **J. Solid State Electrochem.** 20 (2016) 2969–2979.

[277] M. M. Bărsan, C. M. A. Brett, A new modified conducting carbon composite electrode as sensor for ascorbate and biosensor for glucose, **Bioelectrochemistry** 76 (2009) 135–140.

[278] H. F. Cui, K. Zhang, Y. F. Zhang, Y. L. Sun, J. Wang, W. De Zhang, J. H. T. Luong, Immobilization of glucose oxidase into a nanoporous TiO_2 film layered on metallophthalocyanine modified vertically-aligned carbon nanotubes for efficient direct electron transfer, **Biosens. Bioelectron.** 46 (2013) 113–118.

[279] V. Mani, B. Devadas, S.M. Chen, Direct electrochemistry of glucose oxidase at electrochemically reduced graphene oxide-multiwalled carbon nanotubes hybrid

material modified electrode for glucose biosensor, **Biosens. Bioelectron.** 41 (2013) 309–315.

[280] Z. Luo, L. Yuwen, Y. Han, J. Tian, X. Zhu, L. Weng, L. Wang, Reduced graphene oxide/PAMAM-silver nanoparticles nanocomposite modified electrode for direct electrochemistry of glucose oxidase and glucose sensing, **Biosens. Bioelectron.** 36 (2012) 179–185.

[281] M. Cerrato-Alvarez, E. Bernalte, M. J. Bernalte-García, E. Pinilla-Gil, Fast and direct amperometric analysis of polyphenols in beers using tyrosinase-modified screen-printed gold nanoparticles biosensors, **Talanta** 193 (2019) 93–99.

[282] S. Tembe, S. Inamdar, S. Haram, M. Karve, S. F. D’Souza, Electrochemical biosensor for catechol using agarose-guar gum entrapped tyrosinase, **J. Biotechnol.** 128 (2007) 80–85.

[283] M. Sánchez-Paniagua López, B. López-Ruiz, Electrochemical biosensor based on ionic liquid polymeric microparticles. An analytical platform for catechol, **Microchem. J.** 138 (2018) 173–179.

[284] B. Pérez-Lõpez, A. Merkoçi, Magnetic nanoparticles modified with carbon nanotubes for electrocatalytic magnetoswitchable biosensing applications, **Adv. Funct. Mater.** 21 (2011) 255–260.

[285] X. Du, Z. Wang, Effects of polymerization potential on the properties of electrosynthesized PEDOT films, **Electrochim. Acta** 48 (2003) 1713–1717.

[286] N. C. T. Martins, T. Moura e Silva, M. F. Montemor, J .C. S. Fernandes, M. G. S. Ferreira, Electrodeposition and characterization of polypyrrole films on aluminium alloy 6061-T6, **Electrochim. Acta** 53 (2008) 4754–4763.

[287] Y. Xu, X. Zhang, Y. Wang, P. He, Y. Fang, Enhancement of electrochemical capacitance of carbon nanotubes by polythionine modification, **Chinese J. Chem.** 28 (2010) 417–421.

[288] E. Kim, N. Kang, J. J. Moon, M. Choi, A Comparative Study of Potentiodynamic and Potentiostatic Modes in the Deposition of Polyaniline, **Bull. Korean Chem. Soc.** 37 (2016) 1445–1452.

[289] H. S. Magar, M. E. Ghica, M. N. Abbas, C. M. A. Brett, A novel sensitive amperometric choline biosensor based on multiwalled carbon nanotubes and gold nanoparticles, **Talanta** 167 (2017) 462–469.

[290] H. Zhang, Y. Yin, P. Wu, C. Cai, Indirect electrocatalytic determination of choline by monitoring hydrogen peroxide at the choline oxidase-prussian blue modified iron phosphate nanostructures, **Biosens. Bioelectron.** 31 (2012) 244–250.

[291] M. Yang, Y. Yang, Y. Yang, G. Shen, R. Yu, Bienzymatic amperometric biosensor for choline based on mediator thionine in situ electropolymerized within a carbon paste electrode, **Anal. Biochem.** 334 (2004) 127–134.

[292] P. Rahimi, H. Ghourchian, S. Sajjadi, Effect of hydrophilicity of room temperature ionic liquids on the electrochemical and electrocatalytic behaviour of choline oxidase, **Analyst.** 137 (2012) 471–475.

[293] G. Yu, Q. Zhao, W. Wu, X. Wei, Q. Lu, A facile and practical biosensor for choline based on manganese dioxide nanoparticles synthesized in-situ at the surface of electrode by one-step electrodeposition, **Talanta** 146 (2016) 707–713.

[294] , H. F. Cui, W. W. Wu, M. M. Li, X. Song, Y. Lv, T. T. Zhang, A highly stable acetylcholinesterase biosensor based on chitosan-TiO_2-graphene nanocomposites for detection of organophosphate pesticides, **Biosens. Bioelectron.** (2018) 223–229.

[295] S. Wu, F. Huang, X. Lan, X. Wang, J. Wang, C. Meng, Electrochemically reduced graphene oxide and Nafion nanocomposite for ultralow potential detection of organophosphate pesticide, **Sensors Actuators, B Chem.** 177 (2013) 724–729.

[296] X. A. Zhang, H. H. Jia, X. F. Wang, H. L. Zhang, H. W. Yin, S. L. Chang, J. F. Wang, W.J. Wu, Biosensors based on acetylcholinesterase immobilized on mesoporous silica thin films, **Chinese Sci. Bull.** 54 (2009) 3023–3028.

[297] M. Shi, J. Xu, S. Zhang, B. Liu, J. Kong, A mediator-free screen-printed amperometric biosensor for screening of organophosphorus pesticides with flow-injection analysis (FIA) system, **Talanta** 68 (2006) 1089–1095.